Molecular beam epitaxy growth and characterisation of GaAsBi for photovoltaic applications

Author: Robert Douglas Richards

Submitted for: PhD

Department of Electronic and Electrical Engineering, University of Sheffield
Sheffield, S1 3JD, UK

Date of submission: September 2014

Acknowledgements

Firstly I would like to thank my supervisors, Professor John David and Dr John Roberts, for sharing their experience with me and for giving me guidance and feedback throughout the project. I would also like to thank Mrs Hilary Levesley for making the logistics and red tape throughout my PhD as painless as possible.

The bulk of this thesis is on molecular beam epitaxy and I owe my skills and knowledge in this area to Dr Faebian Bastiman, who has been an excellent mentor over the past three years. The tireless efforts of Mr Richard Frith also need to be acknowledged, as he has greatly contributed to the running and maintainence of the machine. I want to thank my lab partners: Chris, Rahman, Danuta and Zhize for their company, assistance and useful discussions. Thanks to all of the staff in the EEE department and the national centre who have offered me assistance over the years; special mention to Ian Wraith in this regard.

I have thoroughly enjoyed my time as part of the E-Futures program and I acknowledge the efforts of Professor Tony West, Dr Neil Lowrie and Professor Geraint Jewel in organising the scheme. I thank cohort 1, especially Krys, Rick and everyone in the E-House for their company and mutual stress venting. The Impact Ionisation Group, Cheong and Ian in particular, have offered me assistance and a sympathetic ear, which has been of great help and comfort.

I am extremely grateful for the continuous support I receive from all of my friends, in particular those with whom I make music; they have all helped me to keep my academic life in perspective. Thanks to my sister for her intuative understanding and occasional bizarre care packages. Finally I want to thank my parents, to whom I owe everything.

List of publications

Peer reviewed publications

1. T. Walther, **R. D. Richards**, F. Bastiman. Scanning transmission electron microscopy measurement of bismuth segregation in thin Ga (As, Bi) layers grown by molecular beam epitaxy. *Crystal Research and Technology*, in press.

2. A. R. Mohmad, F. Bastiman, C. J. Hunter, **R. D. Richards**, S. J. Sweeney, J. S. Ng, J. P. R. David, and B. Y. Majlis. Localization effects and band gap of GaAsBi alloys. *Physica Status Solidi (b)*, 251:12761281, 2014.

3. I. Sandall, F. Bastiman, B. White, **R. D. Richards**, J. P. R. David, C. H. Tan. Demonstration of an InAsBi photodiode operating in the mid wave infrared. *Applied Physics Letters*, 104(17):171109, 2014.

4. **R. D. Richards**, F. Bastiman, C. J. Hunter, D. F. Mendes, A. R. Mohmad, J. S. Roberts, J. P. R. David. Molecular beam epitaxy growth of GaAsBi using As_2 and As_4. *Journal of Crystal Growth*, 390:120-124, 2014.

5. L. Dominguez, D. F. Reyes, F. Bastiman, D. L. Sales, **R. D. Richards**, D. F. Mendes, J. P. R. David, D. Gonzalez. Formation of tetragonal InBi clusters in InAsBi/InAs(100) heterostructures grown by molecular beam epitaxy. *Applied Physics Express*, 6(11):112601, 2013.

6. **R. D. Richards**, F. Bastiman, C. J. Hunter, A. R. Mohmad, J. P. R. David, N. J. Ekins-Daukes. GaAsBi MQWs for multi-junction photovoltaics. *Proceedings of the IEEE 39th Photovoltaics Specialists Conference*. 303-305, 2013.

7. C. J. Hunter, F. Bastiman, A. R. Mohmad, **R. D. Richards**, J. S. Ng, S. J. Sweeney, J. P. R. David. Absorption characteristics of $GaAs_{1-x}Bi_x$/GaAs diodes in the near-infrared. *IEEE Photonics Technology Letters*, 24(23):2191-2194, 2012.

8. A. R. Mohmad, F. Bastiman, C. J. Hunter, **R. D. Richards**, S. J. Sweeney, J. S. Ng, J. P. R. David. Effects of Rapid Thermal Annealing on $GaAs_{1-x}Bi_x$ Alloys. *Applied Physics Letters*, 101(1):012106, 2012.

Oral and poster presentations

1. I. C. Sandall, F. Bastiman, B. White, **R. D. Richards**, C. H. Tan, J. P. R. David. Oral presentation: Demonstration of an InAsBi photodiode operating in the MWIR. *SPIE Security + Defence*, Amsterdam, Holland, 22-25/9/2014.

2. **R. D. Richards**, F. Bastiman, J. S. Roberts, R. Beanland, D. Walker, J. P. R. David. Poster presentation: MBE grown GaAsBi/GaAs MQW structures: structural and optical characterization. *18th International Conference on Molecular Beam Epitaxy*, Flagstaff, Arizona, USA, 7-12/9/2014.

3. **R. D. Richards**, F. Bastiman, D. Walker, R. Beanland, J. P. R. David. Oral Presentation: Strain and relaxation in GaAsBi/GaAs multiple quantum well structures. *The 5th International Workshop on Bismuth-Containing Semiconductors*, Cork, Ireland, 21-23/7/2014.

4. J. P. R. David, **R. D. Richards**, C. J. Hunter, F. Bastiman. Oral presentation: Characterisation of GaAsBi diodes. *The 5th International Workshop on Bismuth-Containing Semiconductors*, Cork, Ireland, 21-23/7/2014.

5. Z. Zhou, D. F. Mendes, **R. D. Richards**, F. Bastiman, J. P. R. David. Poster presentation: The opto-electronic characteristics of GaAs/GaAsBi/GaAs p-i-n diodes. *The 5th International Workshop on Bismuth-Containing Semiconductors*, Cork, Ireland, 21-23/7/2014.

6. **R. D. Richards**, Z. Zhou, D. F. Mendes, F. Bastiman, J. P. R. David. Oral presentation: Characterisation of bulk GaAsBi p-i-n diodes. *UK Semiconductors*, Sheffield, England, 9-10/7/2014.

7. I. C. Sandall, F. Bastiman, B. White, **R. D. Richards**, J. P. R. David, C. H. Tan. Oral presentation: InAsBi photodiode with a cut off wavelength of 3.95 μm. *UK Semiconductors*, Sheffield, England, 9-10/7/2014.

8. **R. D. Richards**, F. Bastiman, C. Hunter, A. R. Mohmad, J. S. Roberts, J. P. R. David. Oral presentation: Growth and characterisation of GaAsBi/GaAs multiple quantum well structures. *Compound Semiconductor Week*, Montpellier, France, 11-15/5/2014.

9. C. J. Hunter, **R. D. Richards**, F. Bastiman, A. R. Mohmad, J. P. R. David. Oral presentation: Growth and characterization of p-i-n diodes containing multiple quantum well GaAsBi layers. *4th International Workshop on Bismuth-Containing Semiconductors*, Fayetteville, USA, 14-17/7/2013.

10. C. J. Hunter, F. Bastiman, A. R. Mohmad, **R. D. Richards**, R. Beanland, J. P. R. David. Oral presentation: TEM characterisation of bulk GaAsBi layers. *UK Semiconductors Conference*, Sheffield, England, 3-4/7/2013.

11. **R. D. Richards**, F. Bastiman, C. J. Hunter, A. R. Mohmad, J. P. R. David. Poster presentation: GaAsBi MQWs for multi-junction photovoltaics. *39th IEEE Photovoltaics Specialists Conference*, Tampa, Florida, USA, 16-21/6/2013.

12. F. Bastiman, A. R. Mohmad, **R. D. Richards**, C. J. Hunter, D. F. Mendes, D. F. Reyes, D. L. Sales, J. S. Ng and J. P. R. David. Oral presentation: Reconstruction orientated Bi incorporation mechanisms in GaAsBi/GaAs (100). *17th European Molecular Beam Epitaxy Workshop*, Levi, Finland, 10-13/3/2013.

13. **R. D. Richards**, F. Bastiman, C. J. Hunter, A. R. Mohmad, J. P. R. David, N. J. Ekins-Daukes. Oral presentation: GaAsBi for photovoltaic applications. *Semiconductor and Integrated OptoElectronics Conference*, Cardiff, Wales, 29/4-1/5/2013.

14. A. R. Mohmad, F. Bastiman, C. J. Hunter, **R. D. Richards**, S. J. Sweeney, J. S. Ng, J. P. R. David. Oral presentation: The effect of growth parameters on the optical and structural quality of $GaAs_{1-x}Bi_x$ alloys. *17th International Conference on Molecular Beam Epitaxy*, University of Nara, Japan, 23-28/09/2012.

15. C. J. Hunter, F. Bastiman, A. R. Mohmad, **R. D. Richards**, J. S. Ng, S. J. Sweeney, J. P. R. David. Oral presentation: Optical and electrical properties of $GaAs_{1-x}Bi_x$/GaAs diodes. *3rd International Workshop on Bismuth Containing Semiconductors*, Victoria, Canada, 15-18/7/2012.

16. A. R. Mohmad, C. J. Hunter, **R. D. Richards**, S. J. Sweeney, D. F. Reyes, J. S. Ng, F. Bastiman, J. P. R. David. Oral presentation: The effect of growth parameters

on the optical and structural quality of $GaAs_{1-x}Bi_x$/GaAs alloys. *3rd International Workshop on Bismuth Containing Semiconductors*, Victoria, Canada, 15-18/7/2012.

17. **R. D. Richards**, F. Bastiman, A. R. Mohmad, C. J. Hunter, J. P. R. David. Oral presentation: Effect of As Species on Growth of GaAsBi. *3rd International Workshop on Bismuth Containing Semiconductors*, Victoria, Canada, 15-18/7/2012.

18. F. Bastiman, C. J. Hunter, A. R. Mohmad, **R. D. Richards**, J. S. Ng, S. J. Sweeney, J. P. R. David. Oral presentation: Growth and characterisation of $GaAs_{1-x}Bi_x$ p-i-n diodes. *EMRS Spring meeting*, Strasbourg, France, 14-18/5/2012.

19. A. R. Mohmad, F. Bastiman, C. J. Hunter, **R. D. Richards**, S. J. Sweeney, J. S. Ng, J. P. R. David. Oral presentation: Effects of rapid thermal annealing on the optical and structural properties of $GaAs_{1-x}Bi_x$. *Semiconductor and Integrated OptoElectronics Conference*. Cardiff, Wales, 2-4/4/2012.

20. A. R. Mohmad, F. Bastiman, C. J. Hunter, **R. D. Richards**, S. J. Sweeney, J. S. Ng, J. P. R. David. Oral presentation: Absorption characteristics of $GaAs_{1-x}Bi_x$/GaAs diodes in the near-infra red. *Semiconductor and Integrated OptoElectronics Conference*. Cardiff, Wales, 2-4/4/2012.

21. **R. D. Richards**, F. Bastiman, A. R. Mohmad, C. J. Hunter, J. P. R. David. Oral presentation: Effect of As Species on Growth of GaAsBi. *UK Semiconductors Conference*, Sheffield, England, 4-5/4/2012.

Abstract

GaAsBi is a promising candidate material for a 1 eV junction for multi-junction photovoltaics, as well as having many other potential applications in areas such as telecommunications and spintronics. The growth of GaAsBi has proven problematic due to the large size and low electronegativity of the Bi atom, and this has hindered its development. In this thesis, the growth and material characterisation of GaAsBi is presented.

A systematic series of bulk GaAsBi samples were grown by molecular beam epitaxy to investigate the effects of growth temperature, As flux and As species on the bismuth content and optical quality of the samples. Two growth regimes became apparent: a temperature limited regime in which the Bi content is limited by the miscibility of GaAs and GaBi, and a Bi flux limited regime in which the Bi incorporation coefficient approaches unity. The production of good quality GaAsBi was shown to require near a near stoichiometric Ga:As atomic flux ratio. The dependence of Bi content on As species was explained by considering the results of Foxon and Joyce, which show the necessary desorption of 50 % of the incident As_4 flux during GaAs growth. The optical quality of GaAsBi was shown to have no dependence on the As species used during growth.

Using the expertise gained from the growth of bulk GaAsBi, a series of GaAsBi/GaAs multiple quantum well p-i-n diodes was grown and characterised. Preliminary results showed that good quality structures were grown with photoluminescence peaks at around 1050 nm. The samples containing a large number of quantum wells showed signs of strain relaxation and a redshift and attenuation of their photoluminescence spectra. Calculations of the effects of strain relaxation and loss of quantum confinement on the photoluminescence emission wavelength, suggest that both factors contribute to the observed redshift. The onset of strain relaxation in these samples appeared to occur at a similar average strain to InGaAs/GaAs samples reported in the literature. These results suggest that GaAsBi could provide a competitive alternative to InGaAs for high efficiency multi-junction photovoltaics.

Contents

List of Figures

List of Tables

Chapter 1

Review of semiconductor physics and the photovoltaic effect

1.1 Introduction

This chapter introduces the fundamental working principles of solar cells, starting at basic semiconductor physics and then introducing the photovoltaic effect. Then follows a short review of solar cell technology, including the fundamental limits to efficiency and the three generations of solar cell designs. A brief overview of the thesis is given at the end of this chapter.

1.2 Band structure in crystalline solids

1.2.1 Band formation

A crystalline solid comprises many atoms with discrete electron energy levels or orbitals, bound together to form a repeating structure. The bonding of the electrons between the atoms causes the degeneracy of their energy levels to be lifted, broadening the discrete states into bands of electron states. This is shown in figure 1.1.

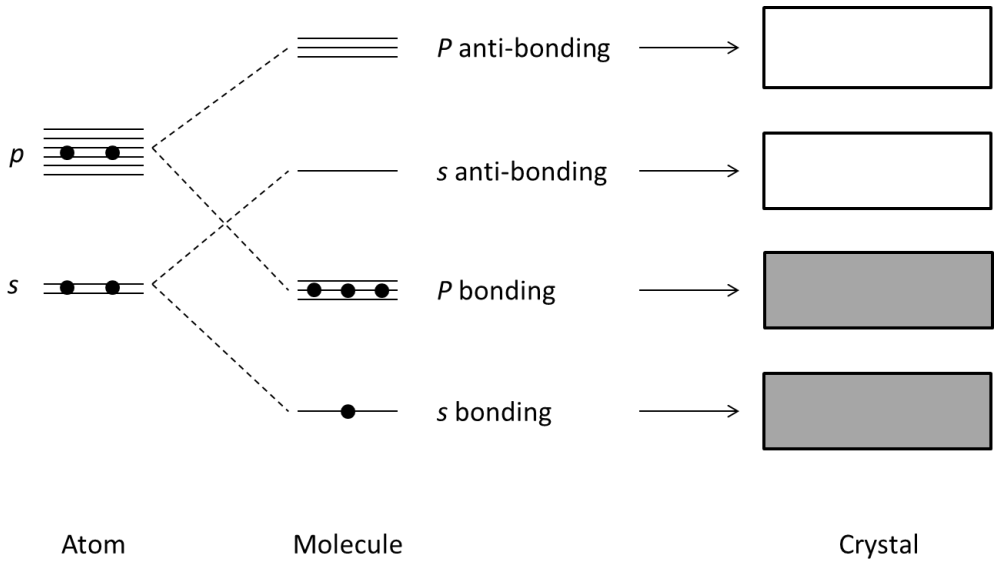

Figure 1.1: The electron orbitals of an atom are used to bond to other atoms in a molecule. The bonding orbitals have lower energy than the anti-bonding orbitals (those not used for bonding) and they fill first (shown by the black dots representing electrons); in a crystalline solid these orbitals form continuous bands of electron states (the grey regions in the crystal bands represent occupied states; the white regions represent unoccupied states). Adapted from [1].

1.2.2 Band filling

The number of electron states in each band is equal to the number of atoms in the crystal. The Pauli exclusion principle dictates that each state can only be occupied by two electrons (spin up and spin down). Therefore, the average number of valence electrons of the atoms in the crystal determines the filling of the bands. The level to which the bands are filled and the alignment of the bands determines the class of the material. This is shown in figure 1.2. In a crystalline material, the valence electron wavefunctions are delocalised, meaning the electrons are free to move through the crystal, provided that there are states available for them to move into. As such, no current can flow through the crystal in a band which is completely full or completely empty. In order for current to flow, one or more of the bands must be partially filled.

The energy gap between the highest filled band (valence band) and the next band up (conduction band) is known as the band gap (E_g). In an insulator the valence band is full and the conduction band is empty, the band gap between them being large enough to prevent

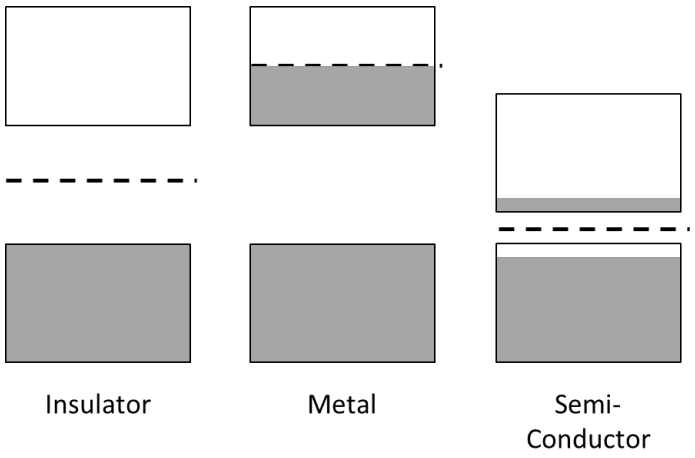

Figure 1.2: Band occupancies for different classes of material. The boxes represent bands of allowed energy states; the grey areas represent states occupied by electrons. Note that the semiconductor is the only material shown at a temperature above 0 K in order to highlight how it is different from an insulator. The small occupancy of the semiconductor conduction band is due to the thermal excitation of electrons. At 0 K it would look the same as the insulator. The metal will remain conductive down to 0 K as it contains one partially filled band. The dashed lines represent the Fermi levels of the materials as discussed in section 1.2.3. Adapted from [2].

any electrons from being thermally promoted to the conduction band at room temperature. An intrinsic semiconductor is different because its band gap is small enough to allow some thermal promotion of carriers at reasonable temperatures. Thus the difference between a semiconductor and an insulator is purely quantitative and both classes will become insulating at 0 K. In a metal, the densities of states and electrons means that the conduction band is half filled even at 0 K, explaining the excellent electrical conduction properties of metals.

1.2.3 The Fermi level

A useful way to quantify the occupancy of electron states is using the Fermi level. The Fermi level is the energy level at which the probability of an electron state being occupied is 0.5. Another way to consider the Fermi level is the level below which all of the electron states are occupied and above which all of the electron states are empty at 0 K. The dashed lines in figure 1.2 represent the Fermi levels of the materials. This thesis is concerned with the development of new semiconductor materials and, as such, the remainder of this chapter will consider semiconductors with band gaps nominally between 0.2 eV and 2 eV. The energy distribution of electrons in a non-degenerate semiconductor (i.e. a semiconductor with a

small population of electrons in the conduction band) is given by the Fermi function as shown in equation 1.1:

$$f(E) \simeq exp\left[-\frac{(E - E_F)}{k_B T}\right] \tag{1.1}$$

where $f(E)$ is the probability of a state of energy E being occupied; E_F is the Fermi energy; k_B is Boltzmann's constant; T is the temperature.

1.2.4 Electrons and holes

When an electron is promoted into the conduction band it leaves an unoccupied electron state in the valence band. It is convenient to consider an unoccupied electron state in the valence band as a particle of positive mass and positive charge known as a hole. Hence, it is common to say that electron-hole pairs are created when an electron is promoted. This process is shown schematically in figure 1.3. As the energy of an electron in a band diagram such as figure 1.3 is increased by moving vertically upwards, the energy of a hole is increased by moving vertically downwards. In these diagrams electrons "sink" and holes "float".

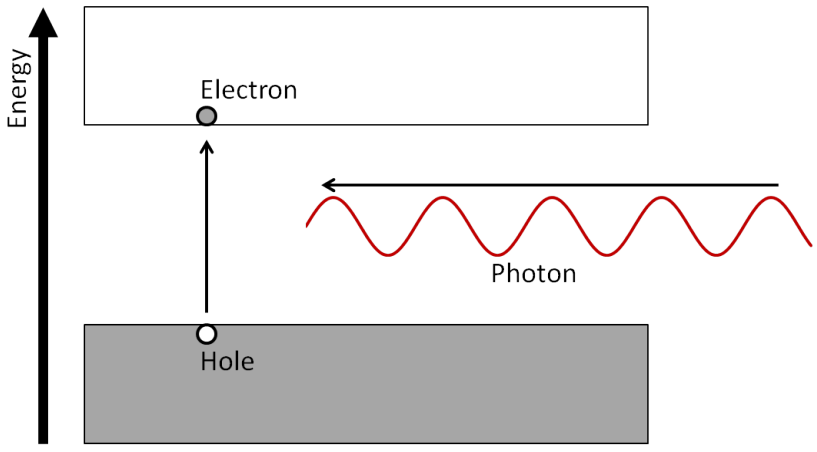

Figure 1.3: An electron can absorb energy from an incident photon of sufficiently high energy and be promoted into the conduction band. This process can also be considered as a hole being promoted into the valence band.

1.2.5 The dispersion relation

Each electron state in a crystalline solid has an associated energy and momentum. The dispersion relation between the momentum and energy of electrons in the crystal lattice produces a plot such as those in figure 1.4. The valence band maximum and conduction band minimum do not always possess the same value of momentum. Semiconductors can therefore be divided into two classes: direct gap and indirect gap. In a direct gap semiconductor the valence band maximum and the conduction band minimum possess the same momentum and an electron in the conduction band may emit a photon to return to an unoccupied state in the valence band. However, in an indirect gap semiconductor the valence band maximum is not at the same momentum as the conduction band minimum. In this case, as photons have very little momentum, an electron would need to emit a photon and simultaneously interact with a lattice vibration (phonon) in order to relax. The same principle is true for absorption. Direct and indirect absorption are shown in figure 1.4. Direct gap semiconductors absorb strongly for photon energies above the band gap but have short carrier lifetimes, as the carriers can radiatively recombine without phonon interaction. Indirect gap semiconductors exhibit weaker absorption of photons with energy above the band gap but have much longer carrier lifetimes.

Electrons in the conduction band can relax back to the valence band by one of several mechanisms. These mechanisms are discussed in section 2.2. For now it is sufficient to state that electrons have a finite excited lifetime which is dependent on the material quality of the host semiconductor.

1.3 Lattice constants, band gaps and alloying

1.3.1 Binary III-V compounds and alloying

Each semiconductor has an associated lattice constant, which is the length of one side of the unit cell of that material. As most III-V alloys have zinc-blende structures (see section 2.1.7.1), the lattice constant of all of these alloys will be considered to be independent of direction. Figure 1.5 shows the band gaps and lattice constants of several III-V semiconductors.

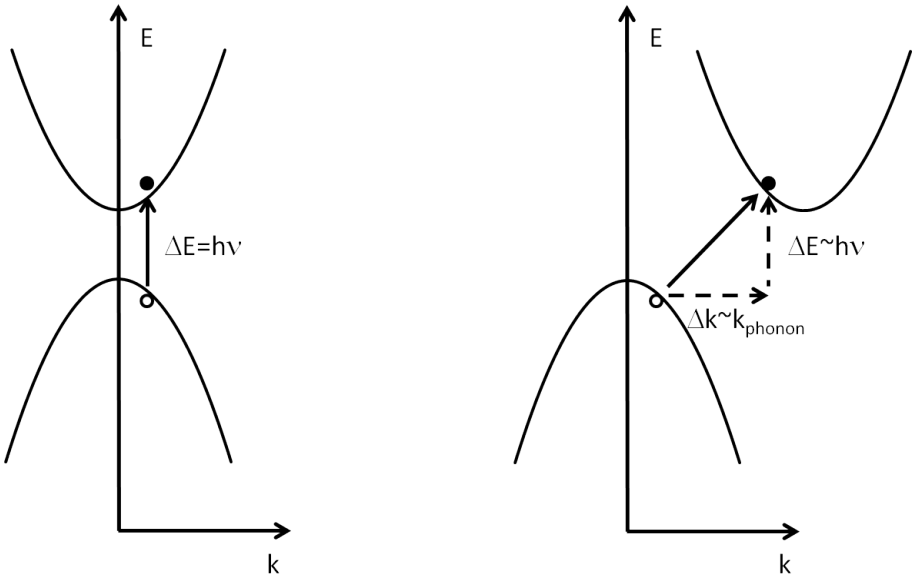

Figure 1.4: Diagram of the dispersion relations in direct and indirect band gap semiconductors. Carriers in semiconductors with direct band gaps can be promoted simply by absorbing incident photons. In indirect semiconductors, carriers can only be promoted if they interact with a lattice vibration (phonon) and simultaneously absorb a photon. The k axis represents carrier momentum and the E axis represents carrier energy.

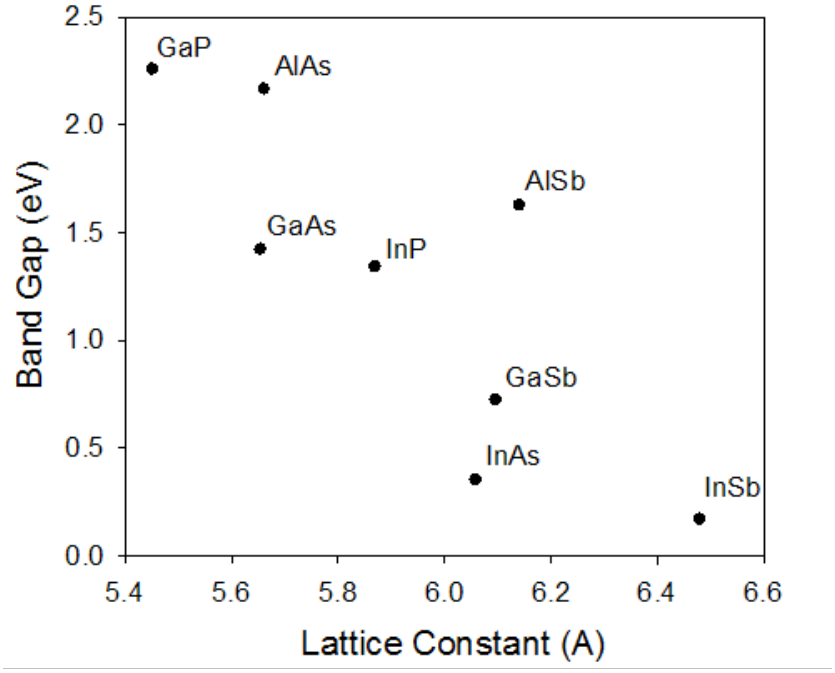

Figure 1.5: Lattice constants and band gaps for several III-V semiconductors.

It is possible to produce semiconductors with different band gaps and lattice constants by alloying these materials together. Figure 1.6 shows how the band gaps and lattice constants of these semiconductors are modified by alloying in ternary compounds.

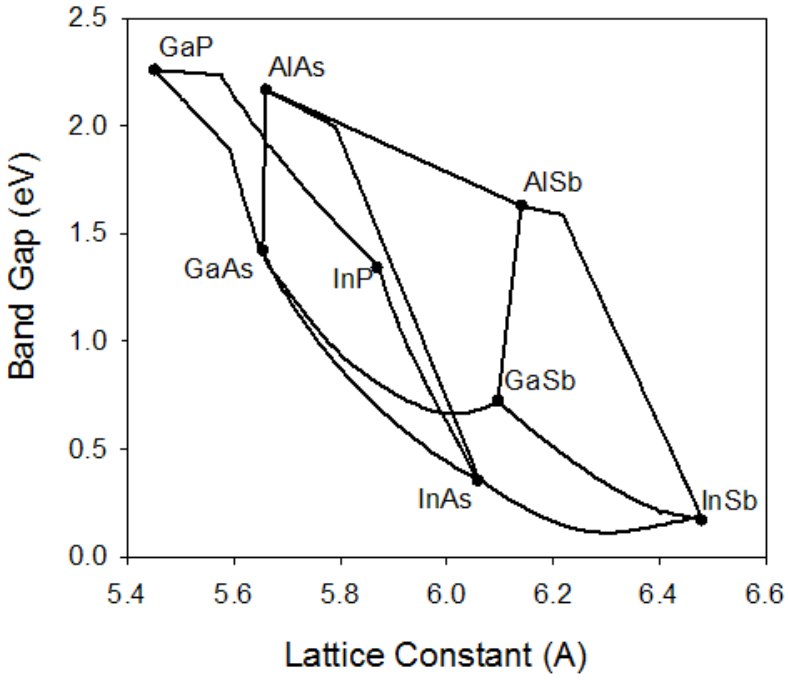

Figure 1.6: Lattice constants and band gaps for several ternary III-V semiconductors. The discontinuities in some of the alloying curves are due to the band gap changing from direct to indirect (as discussed in section 1.2.5).

III-V ternaries clearly allow significant band gap and lattice constant tailoring; however, they are still restricted to the lines in figure 1.6. The regions between the ternary alloying lines can be reached by further alloying (quaternaries, quinternaries etc...).

1.3.2 Vegard's law

The lattice constants of the ternary alloys are usually assumed to obey Vegard's law [3], which states that the lattice constant of a ternary compound can be determined by linear interpolation between the lattice constants of its end binary compounds. Vegard's law can be expressed mathematically for a compound $A_xB_{1-x}C$ as shown in equation 1.2:

$$a_{ABC} = xa_{AC} + (1 - x)a_{BC} \tag{1.2}$$

where a_{ABC} is the lattice parameter of the ternary; a_{AC} and a_{BC} are the lattice parameters of AC and BC respectively; x is the proportion of the ternary comprising AC. A similar expression can be used to describe the variation of the band gap with alloying. The expression must be modified to account for the slightly non-linear variation of band gap with alloy composition, as observed in most compounds, by incorporating a bowing parameter. The variation of band gap with alloying for most III-V compounds can be described by equation 1.3:

$$E_{ABC} = xE_{AC} + (1 - x)E_{BC} + x(1 - x)b \tag{1.3}$$

where E_{ABC} is the band gap of the ternary compound; E_{AC} and E_{BC} are the band gaps of the end binary compounds AC and BC respectively; b is the bowing parameter. Note that some of the alloying lines in figure 1.6 show abrupt changes in curvature. This is caused by the material changing from direct to indirect, meaning that these curves can be recreated by calculating the direct and indirect band gaps using equation 1.3 and taking the smaller value at each point. Compounds which have a large difference in electronegativity between the component elements, such as GaAsBi, exhibit bowing parameters which vary as a function of x. This phenomenon implies that the modified form of Vegard's law is not sufficient to describe the band gaps of these compounds. Instead they need to be described using the band anticrossing model. This will be discussed in section 3.1.2.1.

1.4 Doping and devices

1.4.1 Doping

The Fermi level, and hence the electron occupancy of band states, can be artificially modified by the inclusion of dopant atoms in the host lattice. An insulator which is made semiconducting by the addition of dopant atoms is known as an extrinsic semiconductor. A dopant atom is an atom which has a different number of valence electrons to the other atoms in the crystal and occupies one of the host lattice sites. There are two types of dopant: donor

and acceptor. A donor has more valence electrons than the atom it replaces and an acceptor has fewer. The energy levels of donor electrons or acceptor holes are usually within the band gap and very close to the conduction or valence band edge respectively. This means that they are easily thermally ionised to either donate an electron to the conduction band or accept an electron (donate a hole) from (to) the valence band. This process is shown in figure 1.7. A donor atom is known as an n-type dopant and doping a semiconductor with it produces an n-type semiconductor. An acceptor atom is known as a p-type dopant and doping a semiconductor with it produces a p-type semiconductor. By changing the doping type and level throughout a semiconductor it is possible to produce structures with specific functionalities.

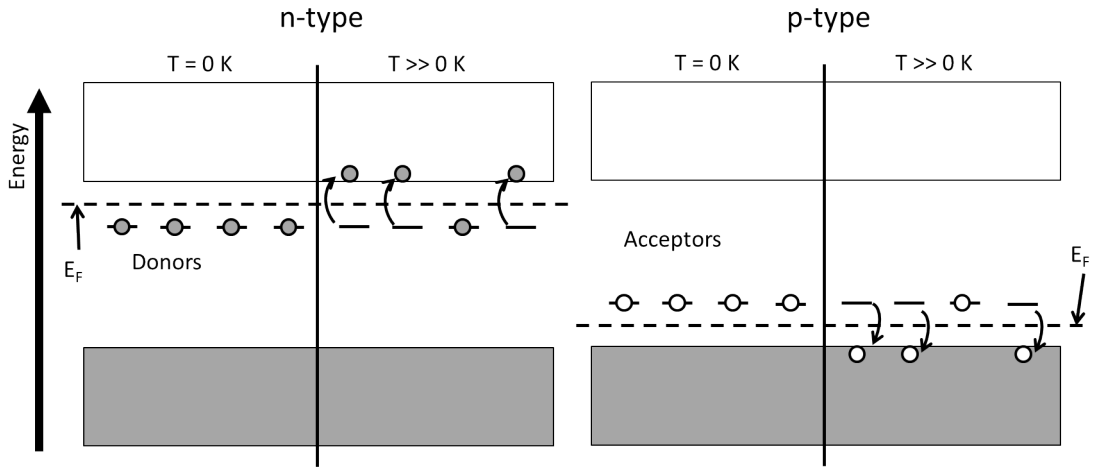

Figure 1.7: Schematic diagram of donors and acceptors in p-type and n-type semiconductors. When there is sufficient thermal energy the donors become ionised and free carriers are injected into the system. Note that the fermi level (E_f) has been modified by the addition of the dopants. At room temperature it is reasonable to assume that all of the donor impurities in an extrinsic semiconductor have been ionised as they have binding energies of a few meV [4]. However, as acceptor impurities typically have binding energies of up to 20 meV in GaAs, they tend to only be partially ionised at room temperature [4].

1.4.2 The pn junction

The fundamental building block of many semiconductor devices is the pn junction. The characteristics of a pn junction can be understood by considering joining together two layers, one n-type, the other p-type, as shown in figure 1.8. In practice this is not possible and the junctions are produced by growing or diffusing the layers on top of each other. However,

considering the joining of a p-type and an n-type layer allows one to understand the physics of the pn junction.

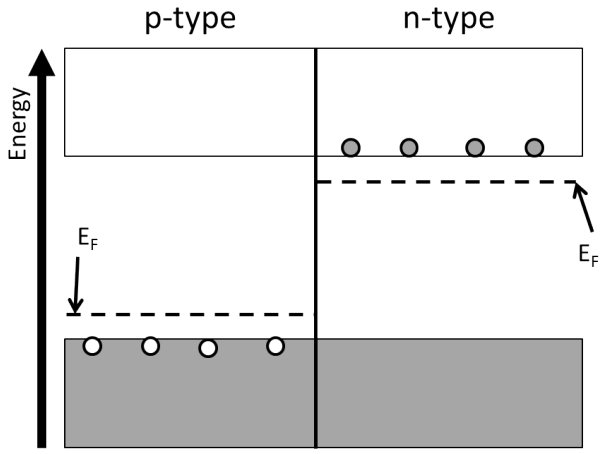

Figure 1.8: A pn junction prior to any charge transfer between the p-type and n-type layers.

At room temperature the n-type layer has an excess of free electrons and the p-type layer has an excess of free holes. Diffusion will cause electrons to migrate into the p-type layer and holes to migrate into the n-type layer. This is known as a diffusion current of majority carriers. These charge carriers then annihilate, leaving behind the ionised dopant atoms. The resulting region, which is devoid of free carriers, is known as the depletion region. The build up of negative charge in the p-type layer and positive charge in the n-type layer produces a voltage across the junction known as the built in potential. The electric field caused by the built in potential induces a current which flows in the opposite direction to the diffusion current. This current is known as the drift current. The junction reaches equilibrium when the diffusion and drift currents are equal and opposite. This theoretical sequence of events is shown in figure 1.9.

1.4.2.1 The effect of bias

It is instructive to consider the behaviour of the pn junction when an external bias is applied. When the external bias is in the same sense as the built in potential then the junction is said to be reverse biased and when the external bias acts against the built in potential the junction is said to be forward biased. Biasing the junction has the effect of changing the potential between the n and p regions.

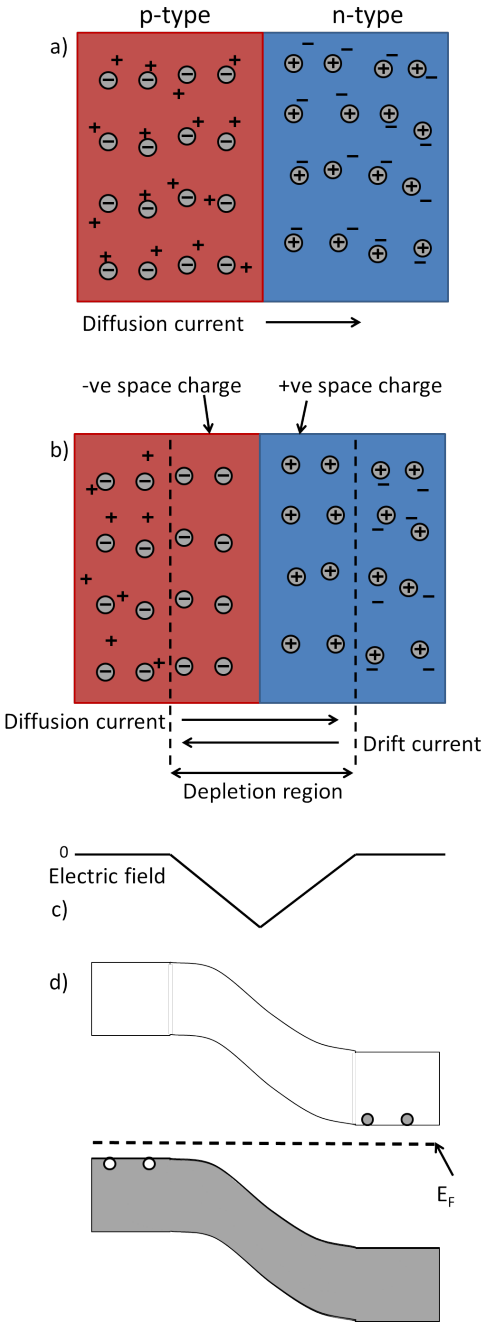

Figure 1.9: Illustration of the theoretical stages of pn junction formation. a) The two doped regions are brought into contact and no charge transfer has yet taken place b) The diffusion of the carriers produces a diffusion current; their subsequent annihilation gives rise to a depletion region within which the ionised dopant atoms produce an electric field c) The electric field throughout the junction d) The electric field causes a bending of the valence and conduction bands.

1.4.2.2 Fermi level splitting

The application of an external bias has the effect of changing the Fermi levels of the electrons and holes within the semiconductor. The two populations can no longer be described by a single Fermi level and it is necessary to separately describe the electron and hole populations. The populations of electrons and holes are said to each obey their own quasi-Fermi level (QFL). These levels are shown in figure 1.10.

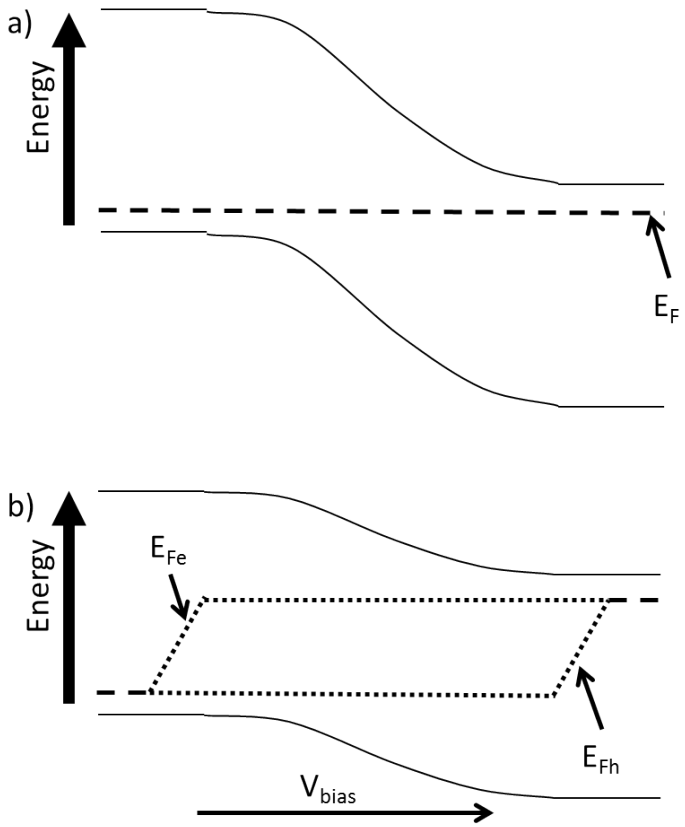

Figure 1.10: Effect of a forward bias on a pn junction. a) There is no bias and the electrons and holes can be described by a single fermi level. b) A forward bias is applied to the system and the fermi level splits into quasi-Fermi levels describing the electron (E_{Fe}) and hole (E_{Fh}) populations.

1.4.2.3 The Shockley equation

The potential between the n and p regions has negligible effect on the drift current. However, changing the magnitude of the barrier changes the proportion of majority carriers on either side of the junction that can overcome the barrier and diffuse to the other side. Reverse

biasing the junction increases the potential across the junction and reduces the diffusion current. In this simple picture, at sufficiently high reverse biases the total current across the junction will be equal to the drift current. In forward bias the potential barrier is reduced and the diffusion current increases, giving rise to an exponentially increasing total current described by the Shockley equation as shown in equation 1.4:

$$I = I_0 \left[exp\left(\frac{eV_{bias}}{k_B T} \right) - 1 \right] \tag{1.4}$$

where I is the current passing through the junction; I_0 is the drift current across the junction; e is the charge on a proton; V_{bias} is the bias voltage across the junction; k_B is Boltzmann's constant; T is the temperature.

1.4.2.4 Diode Ideality

In real devices there is another current produced by the recombination of carriers via trap states in the depletion region. The trap states can be created by many things including impurity atoms and dislocations. The recombination current can be expressed in a similar way to equation 1.4:

$$I_{rec} = I_{0_{rec}} \left[exp\left(\frac{eV_{bias}}{2k_B T} \right) - 1 \right] \tag{1.5}$$

where $I_{0_{rec}}$ is a constant. The magnitude of the recombination current is maximised when the trap states are located in the middle of the band gap, which is the reason for the factor of 2 in the denominator of the exponential in equation 1.5. The total current is the sum of the ideal and recombination currents. A good fit to experimental data can be obtained using equation 1.6:

$$I = I_0 \left[exp\left(\frac{eV_{bias}}{nk_B T} \right) - 1 \right] \tag{1.6}$$

where n is the ideality factor, which takes values between 1 and 2. An ideality factor of 1 indicates that diffusion current dominates the I-V characteristic of a device. An ideality factor of 2 indicates that recombination via defects dominates the I-V characteristic of a device. I-V characteristics with n=1 and n=2 are shown in figure 1.11.

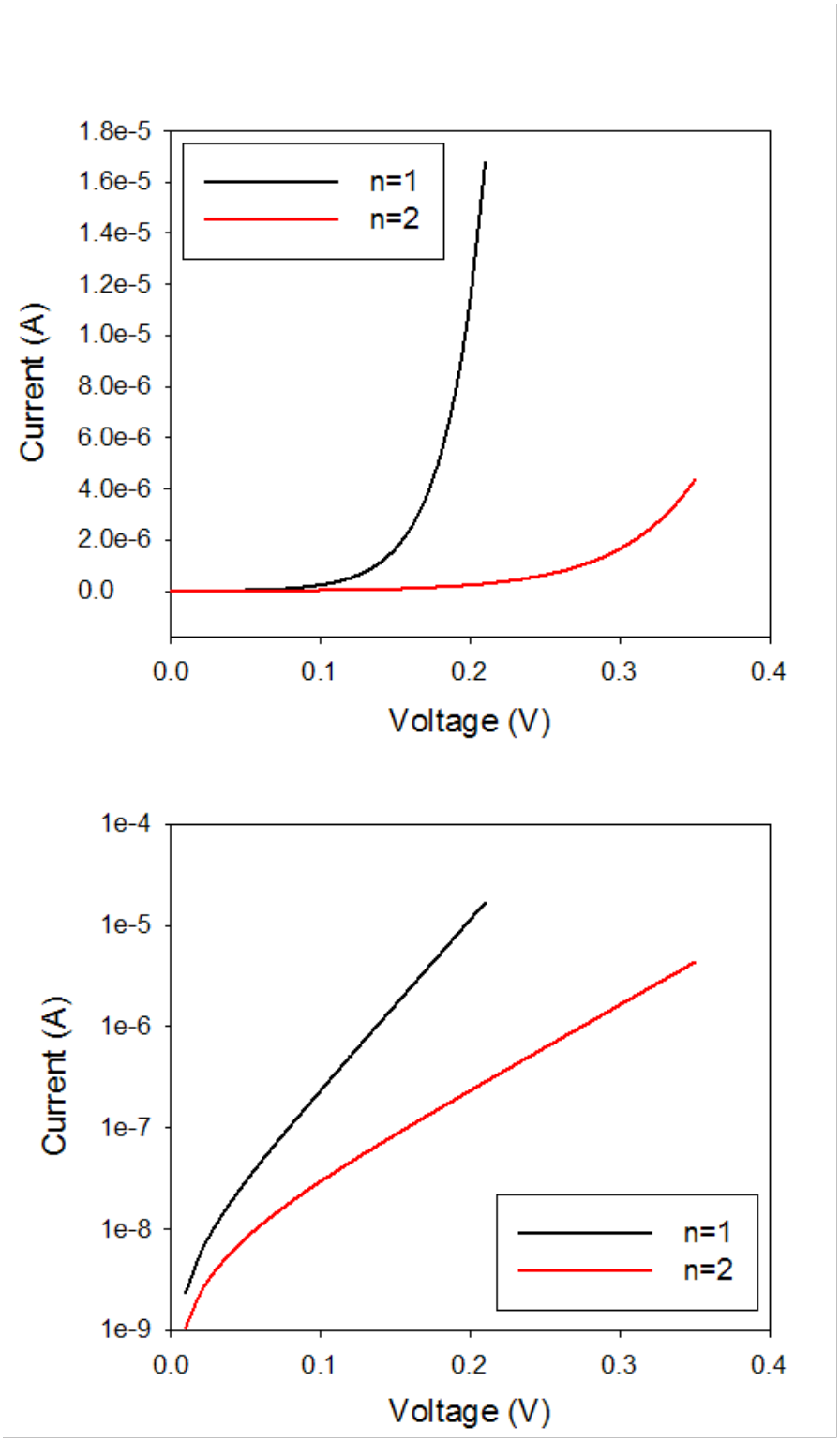

Figure 1.11: The theoretical Shockley diode curve for two diodes of ideality factors 1 (black line) and 2 (red line). The graph at the top shows the data on a linear y axis; the plot at the bottom shows the data on a log y axis.

1.4.2.5 Parasitic resistances

In reality, a diode will have parasitic resistances associated with it. The equivalent circuit of a diode taking these resistances into account is shown in figure 1.12.

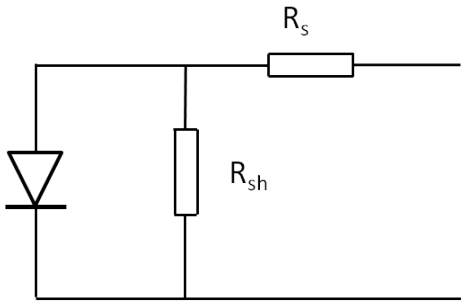

Figure 1.12: Equivalent circuit diagram of a diode including parasitic resistance.

There are two resistances shown in figure 1.12. Shunt resistance (R_{sh}), in parallel with the diode, accounts for leakage currents due to defects. The series resistance (R_s) accounts for voltage drops due to poor contacts. Equation 1.7 describes the ideal diode equation taking these resistances into account.

$$I = I_0 \left[exp\left(\frac{e(V_{bias} + IR_s)}{nk_BT} \right) - 1 \right] - \frac{V_{bias} + IR_s}{R_{sh}} \tag{1.7}$$

For best performance it is desirable to have the lowest possible series resistance (good contacts) and the highest possible shunt resistance (good material quality).

1.4.2.6 p-i-n structures

For some applications an undoped region is grown between the p and n regions in a diode to form a p-i-n structure. These structures are conceptually the same as the pn diodes discussed earlier. However, an important difference is that the electric field is maintained across a much larger region, known as the i-region, provided that it is fully depleted. For most device applications the i-region is ~ 0.5 - 1 μm thick. Excessive background doping in the i-region can reduce the width of the depleted region and impair the penetration of the electric field.

1.5 The photovoltaic effect

If the junction is subjected to incident light of sufficient energy then electron-hole pairs are created in the junction. These carriers can then be separated by the electric field across the depletion region to create a current in the circuit. Such a current is known as a photocurrent and the process is known as the photovoltaic (PV) effect. This is shown in figure 1.13.

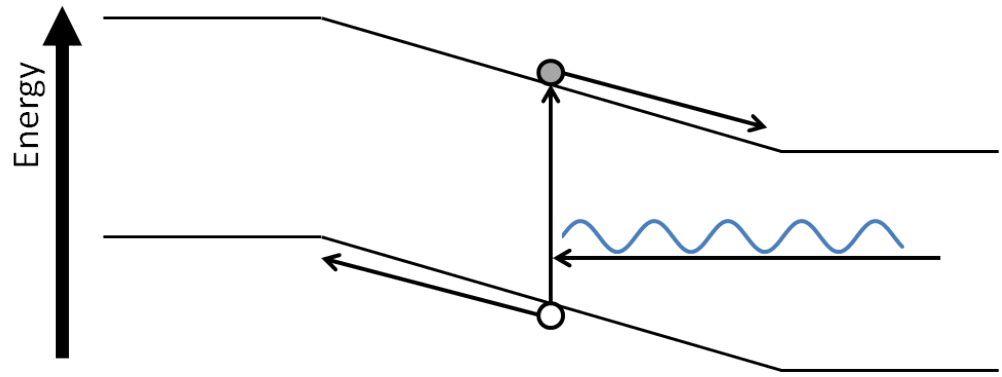

Figure 1.13: The photovoltaic effect in a p-i-n diode. In the diagram a photon with sufficient energy to promote an electron into the conduction band is absorbed in the i-region. The resulting electron-hole pair is then separated by the inbuilt electric field.

The band structure shown in figure 1.13 is a p-i-n diode. Provided the electron-hole pair is excited in the i-region it will immediately be separated by the electric field. If the junction were a pn design then the electron-hole pair would need to diffuse to the pn junction in order to be separated. The separation of of charge generated by the PV effect is the mechanism by which solar cells produce electrical power. For maximum efficiency, most solar cells contain a p-i-n junction to provide efficient separation of charge carriers throughout the device without the need for the carriers to diffuse to the pn junction.

1.5.1 Brief history

The photovoltaic effect was first observed by Bequerel in 1839 [5]. However, the effect was not utilised in a solid state device until 1883 when Fritts created a selenium solar cell [6]. The first Si cell was produced by Bell Labs in 1954 [7]. Si cells are now the most common solar cells, partly due to the abundance of Si in the earth's crust and partly due to the optimisation of Si production and processing techniques throughout the development of

computer technology. The global photovoltaic power generation capacity has increased exponentially in recent years as shown in figure 1.14.

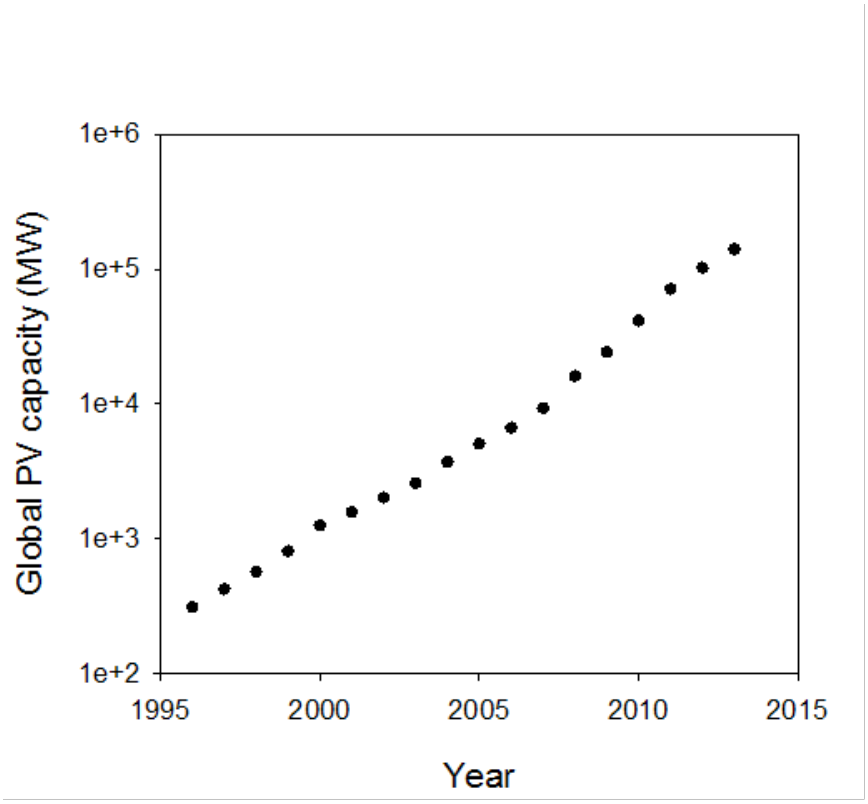

Figure 1.14: Global installed PV capacity since 1996. Data taken from [8].

There are many different solar cell designs for different applications, some of which are discussed in section 1.5.7. The operating principles and loss mechanisms are common throughout all of the various types and a general overview of these is described in the following sections.

1.5.2 Photocurrent

To a good approximation the total current output of a cell under illumination is the sum of the dark current and the photocurrent. This is shown in figure 1.15.

1.5.3 Key parameters of solar cell performance

Several key parameters of a solar cell can be extracted from the illuminated I-V curve as shown in figure 1.15. The short circuit current (I_{sc}) is the current produced by the cell when

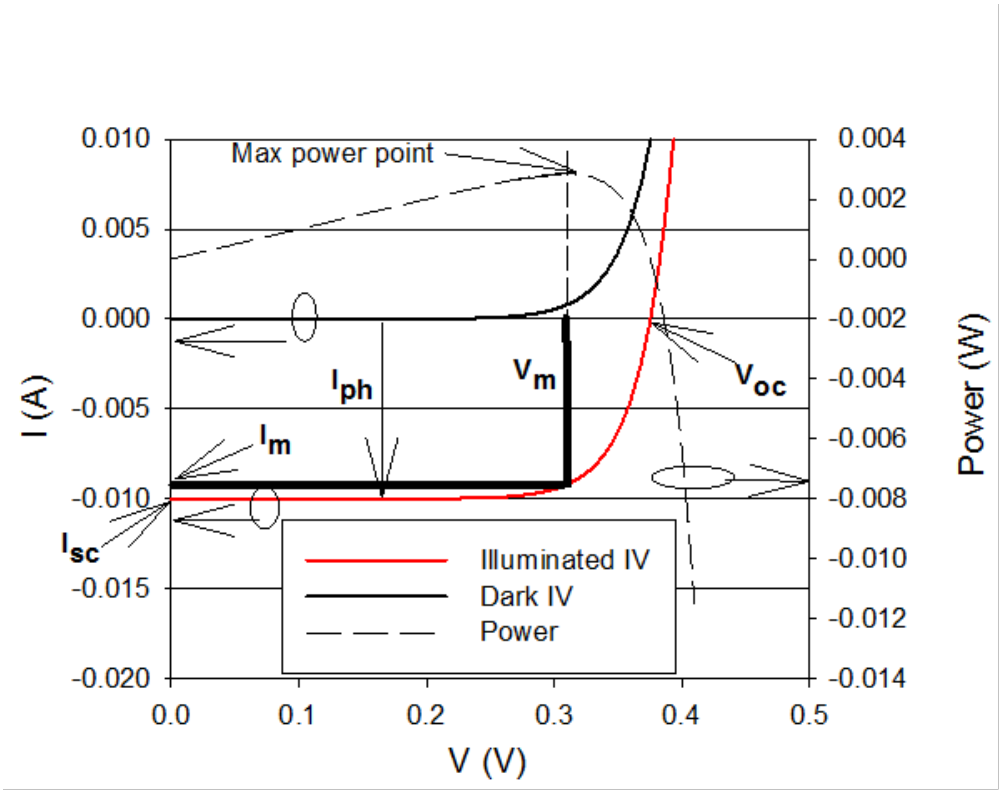

Figure 1.15: The effect of illumination on a diode I-V curve. The key parameters of a solar cell's performance are highlighted here and explained in the text.

no bias is applied and the open circuit voltage (V_{oc}) is the voltage required to reduce the cell's output current to zero. As electrical power is equal to the product of current and voltage it is clear that no power is produced at either V_{oc} or I_{sc}. In principle, one would like the short circuit current to be maintained up to the open circuit voltage, yielding a power output equal to the product of V_{oc} and I_{sc}. In practice, the I-V curve of an ideal diode as shown in figure 1.11 makes this impossible and the maximum power output is achieved at $V_m < V_{oc}$ and $I_m < I_{sc}$. This deviation from the ideal scenario can be quantified by introducing the concept of a fill factor (FF):

$$FF = \frac{I_m V_m}{I_{sc} V_{oc}} \tag{1.8}$$

which quantifies the "squareness" of the diode's light I-V curve.

The efficiency (η) of a solar cell is defined as the electrical power out divided by the optical power in:

$$\eta = \frac{I_m V_m}{P_s} = \frac{FF\, I_{sc} V_{oc}}{P_s} \tag{1.9}$$

where P_s is the incident solar power. Clearly, in order to compare the efficiencies of different cells, the incident solar power must be standardised and a standard solar spectrum is required.

1.5.4 The solar spectrum

The solar spectrum is very well described by Planck's equation for a blackbody at 5800 K. However, Earth's atmosphere introduces absorption lines into that spectrum. The solar spectrum is shown in figure 1.16.

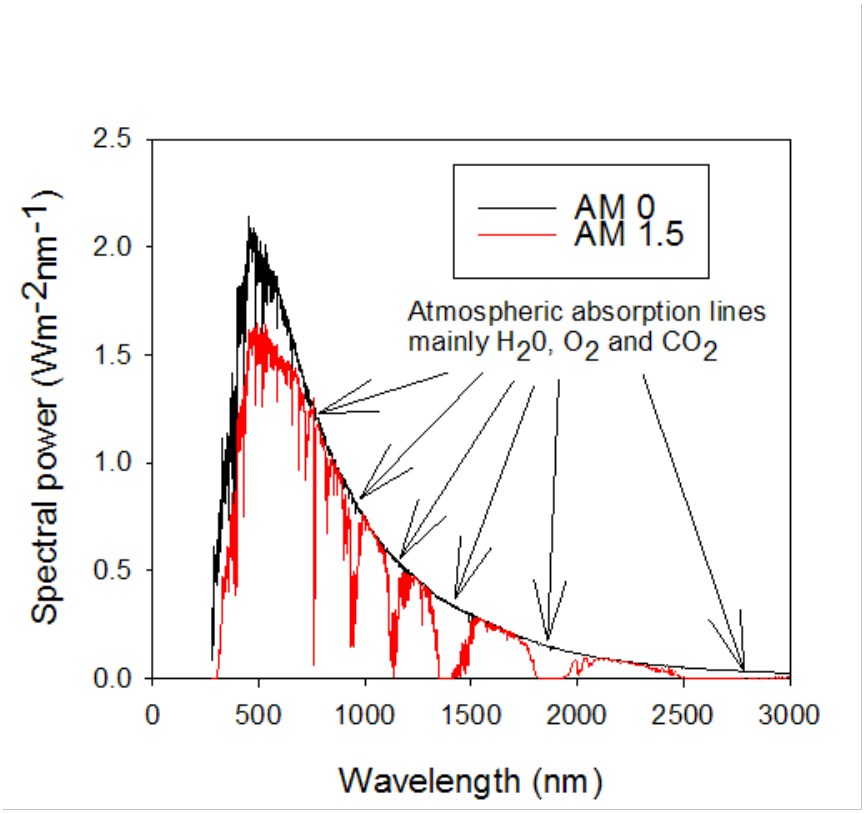

Figure 1.16: The AM 0 and AM 1.5 solar spectra. Data taken from [9].

The attenuation of the spectrum is determined by the distance travelled by the light through the atmosphere. This distance is denoted by the air mass (AM) index:

$$n_{AM} = \frac{optical\ path\ length\ to\ sun}{optical\ path\ length\ to\ sun\ if\ in\ zenith} = \csc \gamma_s \tag{1.10}$$

where γ_s is the angle of elevation of the sun.

The solar spectrum with no atmospheric absorption (i.e. as viewed from a point outside the Earth's atmosphere) is the AM 0 spectrum; the spectrum seen from the Earth's surface with the sun in the zenith is the AM 1 spectrum. The standard spectrum used for terrestrial PV characterisation is the AM 1.5 spectrum normalised to 1 kWm^{-2}, which is equivalent to the spectrum seen when $\gamma_s \sim 42\,°$. The AM 0 and AM 1.5 spectra are illustrated in figure 1.16. The variation of AM index with position is shown in figure 1.17.

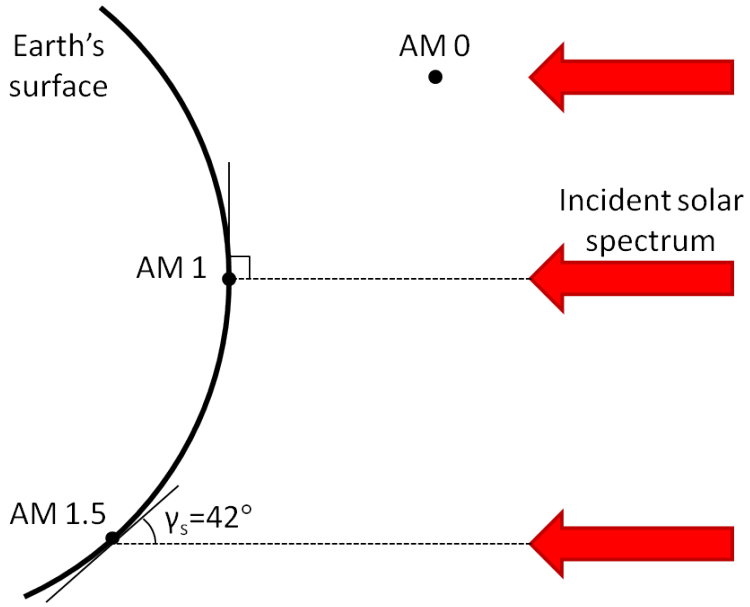

Figure 1.17: How the AM index changes with position.

1.5.5 Theoretical efficiency limits

Even if one ignores the extrinsic losses in a solar cell such as contact resistance and material defects, the theoretical efficiency of a solar cell can never be 100 %. Intrinsic losses also limit the potential performance of a cell.

There are several intrinsic loss mechanisms in solar cells. First, consider a photon with energy less than the band gap incident on the cell. Any such photon will be transmitted through the cell without being absorbed. This sub-band gap photon loss can be minimised

by reducing the band gap of the cell. The second major loss mechanism is carrier thermalisation. Any photons with energy greater than the band gap will produce carriers with excess energy. These carriers will thermalise to the band edge by emitting phonons, losing their excess energy as heat. This carrier thermalisation loss can be minimised by increasing the band gap of the cell. These two loss mechanisms are shown in figure 1.18. Clearly they cannot both be simultaneously minimised and there will be an optimum band gap at which the combined loss from both mechanisms is minimised for any given incident spectrum. This is also shown in figure 1.18.

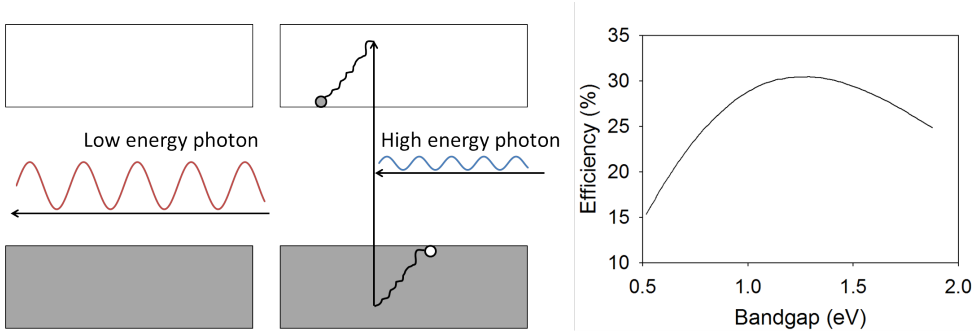

Figure 1.18: The sub-band gap photon and thermalisation loss mechanisms in solar cells. The theoretical maximum efficiency for a single junction solar cell under an AM 1.5 spectrum without concentration is shown. Taken from [10].

The intrinsic losses in a solar cell are presented in graphical form in [11] as shown in figure 1.19. Note that Below band gap transmission and thermalisation are the biggest loss mechanisms. Boltzmann loss is due to the inequality between the angle through which direct solar energy is absorbed and the angle through which the solar cell emits light due to the unavoidable radiative recombination of carriers. Boltzmann loss is discussed further in section 1.5.6. Carnot loss is due to the finite temperature difference between the Sun and the cell; it would vanish if the Sun were infinitely hot and the cell were at 0 K. Emission loss is due to Kirchoff's law, which states that any body which absorbs light must also emit light.

1.5.6 Effect of concentration

The inequality between the solid angles of light absorption and emission, that gives rise to Boltzmann loss in solar cells, is shown in figure 1.20, which also shows how the inequality

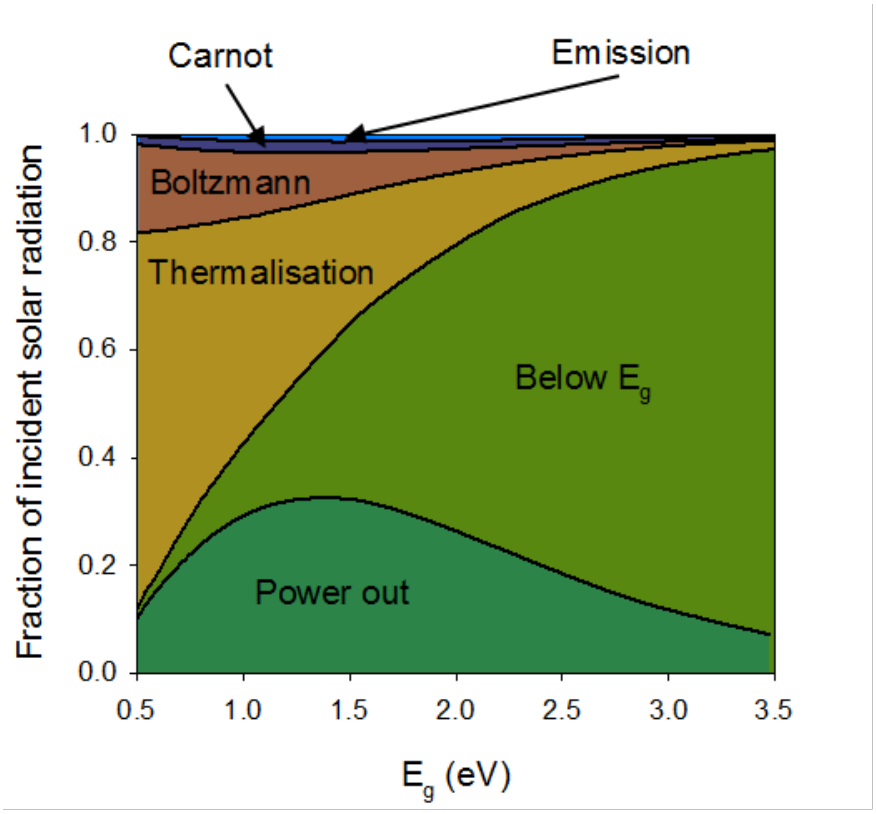

Figure 1.19: Diagram highlighting the losses from a single junction solar cell under the AM 1.5 spectrum. Adapted from [11].

between these angles can be reduced by concentrating the incident light, which reduces the Boltzmann loss.

The Boltzmann loss can also be reduced by restricting the emission angle of light from the solar cell, for example by using a reflective surface to prevent emission from the unilluminated side of the cell [12]. A small correction to the Boltzmann factor arises from the finite temperature of the cell's surroundings; the cell will not only absorb direct light from the sun, but also from all other angles. However, the flux density from the surroundings is far smaller than that from the sun and this effect is small. A final point on concentration is that it also helps to reduce the extrinsic efficiency loss due to poor material quality. Any non-radiative recombination centres in the material (as mentioned in section 2.2.2) can be saturated by injecting sufficient carriers. Thus, concentration allows the cell to approach the ideal radiative limit. The level of concentration is usually defined by the effective solid angle of direct irradiance on a cell from the sun, stated as a multiple of the solid angle of

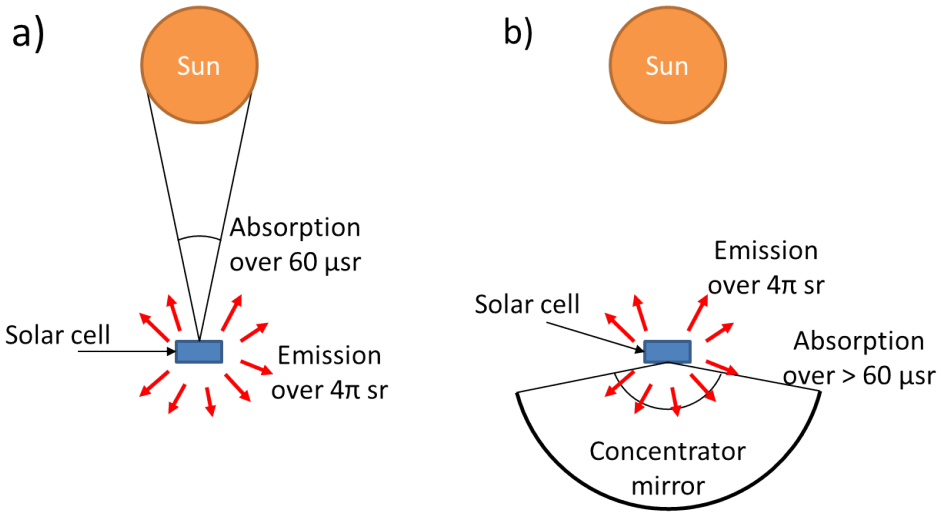

Figure 1.20: a) The disparity between light absorption and emission angles leads to radiative loss in solar cells. b) By concentrating the sunlight, that disparity can be reduced and the cell's efficiency is increased.

the sun without concentration, e.g. $\times$ 1000 suns.

1.5.7 The three generations of solar cells

Solar cell technologies can be roughly divided into three main categories known as the first, second and third generations [13]. The cost per unit power of each of these generations is shown in figure 1.21. Most of these technologies are beyond the scope of this project, so this section is limited to explaining the general concepts behind each technology.

1.5.7.1 First generation solar cells

First generation cells include Si and III-V single junction cells. The initial impetus for the development of crystalline Si cells was for space based power generation for satellites [14]. The terrestrial market was some way behind but was stimulated through reductions in cost and improvements in efficiency. They are popular due to their relative ease of installation and their proven lifetimes. The majority of PV installation is first generation.

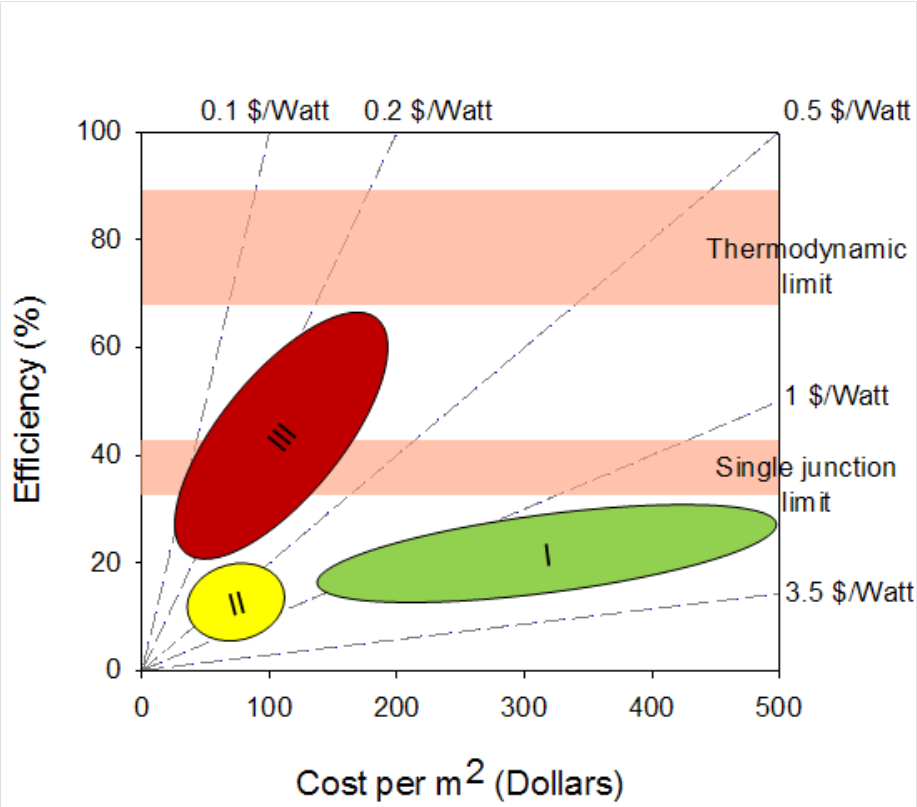

Figure 1.21: The three generations of photovoltaics. The pink bands represent the ranges of maximum theoretical efficiency achievable by single and triple junction solar cells at different levels of solar concentration. The green, yellow and red bubbles represent the regions of the plot occupied by first, second and third generation solar cells respectively. Adapted from [13].

1.5.7.2 Second generation solar cells

Second generation cells reduce the cost per Watt of devices by reducing the cost of manufacture. While the efficiencies of such cells tend to be lower than the efficiencies of first generation solar cells, the drop in efficiency is small compared to the reduction in price. These technologies include organic and thin-film cells, which are often thin enough to be flexible and are, therefore, of great interest for applications such as portable PV, building materials and window tinting. Manufacturers of second generation cells have struggled to consistently produce commercial devices with the same efficiency as their laboratory prototypes [15].

Organic solar cells are of particular interest because they can be deposited via spray coating, dramatically reducing the manufacture costs. The key issue with the technology is that the active layer reacts strongly with oxygen and water, resulting in rapid degradation of the

cell [16].

1.5.7.3 Third generation solar cells

Third generation solar cells achieve low costs by increased efficiencies. There are many different methods by which these technologies attempt to exceed the single junction maximum efficiency. The remainder of this chapter outlines some of these technologies.

Hot carrier solar cells Hot carrier solar cells tackle the thermalisation loss mechanism. By extracting carriers while the excited carrier population exhibits a higher temperature energy distribution than the lattice, the loss due to thermalisation can, in principle, be reduced. Thermalisation rates need to be reduced in order to preserve the thermal distribution of the excited carriers [17]. By using energy selective contacts, the carriers excited within the device can be collected without thermalising [18]. To date there have been no demonstrations of effective hot carrier solar cells.

Intermediate band solar cells An alternative route to reducing transmission loss is to employ an intermediate conduction band within the band gap of a solar cell as shown in figure 1.22 [19]. Incident photons can either promote carriers between the valence band and the upper conduction band; the valence band and the lower conduction band; or the lower conduction band and the upper conduction band. Provided that the two conduction bands are not in thermal equilibrium, there should be minimal energy transfer between the bands. In order to maintain thermal isolation between the two conduction bands, carriers must only be extracted from the upper conduction band. This requires energy selective contacts, as mentioned for hot carrier solar cells. There are now three band gaps absorbing the incident light, which reduces both the transmission and thermalisation losses. Optimal efficiency requires that the rate of carrier excitation from the valence band to the first conduction band equals that from the first conduction band to the second conduction band. A maximum theoretical efficiency has been predicted for this kind of solar cell at 63.1 % [20].

Multi-junction solar cells Thermalisation and sub-band gap transmission losses can simultaneously be reduced by absorbing each component of the solar spectrum with a spe-

Figure 1.22: Band layout of an intermediate band solar cell. The three boxes represent three bands. The valence band (grey to denote filling at 0 K), the conduction band (top) and the intermediate band. Provided the intermediate band and the conduction band are thermally insulated from each other, the cell acts as if it has three band gaps of energies E_g, E_{g1} and E_{g2}. Adapted from [19].

cially optimised cell. There are several different ways of achieving this, as shown in 1.23.

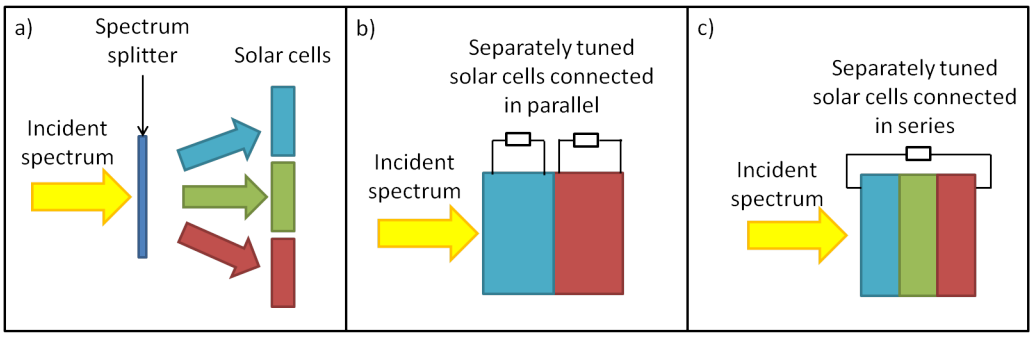

Figure 1.23: Three different implementations of a multi-junction solar cell. a) The spectrum is split prior to being incident on the cells. b) The cells are stacked on top of each other and contacted individually (known as a "four terminal tandem"). c) The cells are stacked on top of each other and work in series (known as a "two terminal multi-junction").

Each of the designs shown in figure 1.23 presents technological challenges which limit the efficiency of the design [19]. The splitting of the solar spectrum prior to absorption (as shown in figure 1.23a) is very challenging and, as such, this design has not been widely adopted. The other two designs shown in figure 1.23 involve stacking the cells with the highest band gap cell uppermost. The high energy components of the incident spectrum are absorbed by the top cell with the remaining light transmitted to the subsequent cell(s). The development of the four terminal tandem (figure 1.23b) has been limited by the difficulty in individually contacting to the cells. In principle, however, this design is capable of very high efficiencies as the power from each cell is extracted separately. The most widely used

form of multi-junction solar cell is the two contact type (figure 1.23c). The convenience of a multi-junction cell which can be incorporated into a system in the same way as a single junction cell has made this design almost ubiquitous [21]. The limitations of this cell architecture are discussed below.

Clearly, the number of junctions in any multi-junction cell will determine the maximum limiting efficiency of the cell. With each additional junction the thermalisation and below band gap transmission losses will be reduced, increasing the limiting efficiency. The limiting efficiencies for solar cells with different numbers of junctions under $1000\times$ concentration of the AM 1.5 spectrum are shown in table 1.1 [22].

Table 1.1: Maximum theoretical efficiencies for solar cells with different numbers of junctions under $1000\times$ AM 1.5 solar spectrum. Data taken from [22].

Number of junctions	Maximum efficiency (%)
1	37
2	50
3	56
36	72

Each subcell in a multi-junction solar cell is connected to the next subcell by a tunnel junction [23]. A tunnel junction is a thin layer of highly doped material. This material bends the bands in the cell to bring the conduction band of one subcell into alignment with the valence band of the next subcell such that the difference in potential between the bands is zero. The electrons and holes on either side of the junction can then tunnel through the junction and the subcells on either side of the junction can continue to produce current. The tunnelling current is limited by the density of allowed states for a carrier to tunnel into. This is limited by mis-alignment of the bands and by any inequality between the number of electrons and holes on either side of the tunnel junction. A simplified band structure diagram of a double junction solar cell is shown in figure 1.24.

As the two terminal multi-junction design is effectively several cells in series, Kirchoff's law applies, i.e. the current passing through each component of the stack must be equal. This has significant implications for the cell's design.

Figure 1.25 shows the I-V characteristics of the subcells in a tandem (two junction) solar cell. The maximum power point of each subcell is marked with a red dot. In the current matched case, the maximum power points occur at the same current, meaning that, with

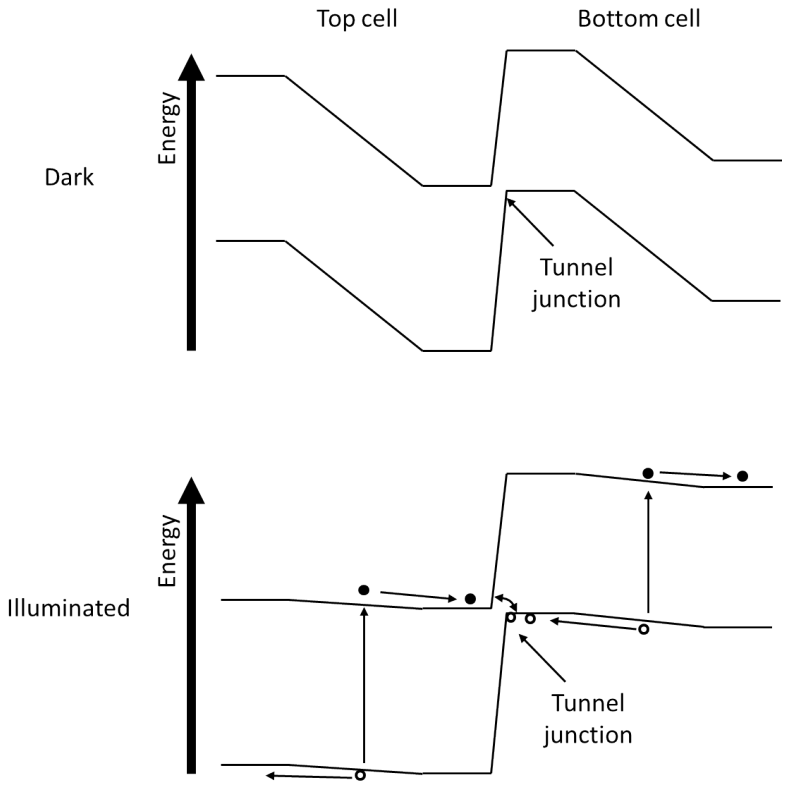

Figure 1.24: Simplified band structure of a double junction solar cell under dark and illuminated conditions (light incident from the left). The carriers are swept apart by the built in field of each subcell and tunnel through to the next junction in the cell. Based on [24].

a carefully tuned load on the cell, both subcells will be working at maximum power and the tandem cell will work at optimum efficiency. If, however, one of the subcells over - or under - supplies current (the "not current matched" case in figure 1.25) then both cells will operate away from their maximum power points and the efficiency of the tandem cell will be diminished. This effect is observed in tandem cells grown on Ge. The Ge junction overproduces current and the energy from this excess current is lost.

There are two main ways of tuning the current production of a subcell. First, one can thin the over-producing junction, reducing the total absorption in that subcell and allowing the transmitted light to produce current in the other subcells [26]. While this technique allows the system to approach current matching, it also increases thermalisation losses as the transmitted high energy photons produce high energy carriers in a low band gap material. The second approach that can be taken is to tune the band gaps of the subcells so that the current produced in each subcell is made equal with a minimal increase in thermalisation

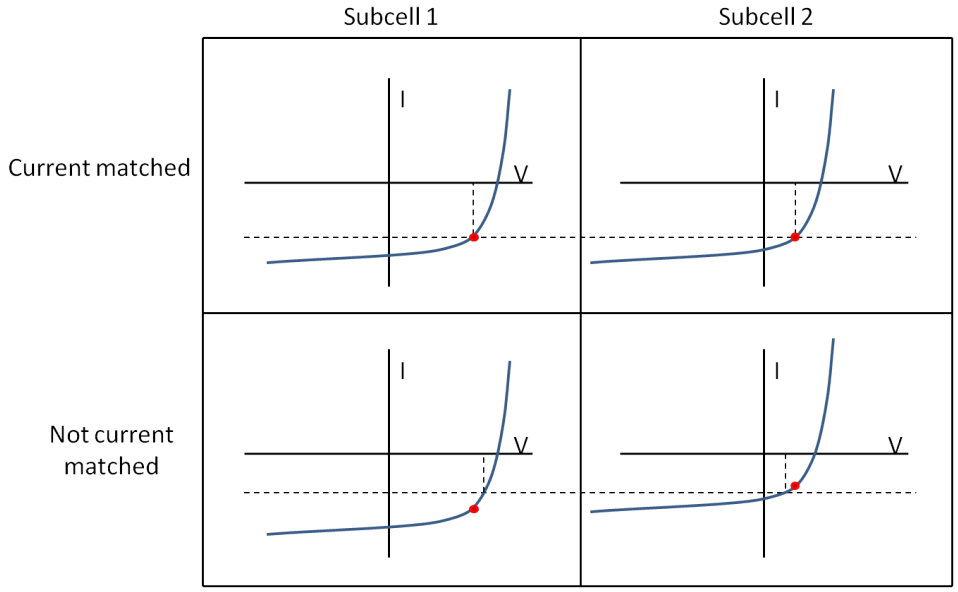

Figure 1.25: Individual I-V curves of subcells in a tandem solar cell. The maximum power point of each cell is marked with a red dot. The dashed lines indicate the current and voltage across each subcell. Note that Kirchoff's law demands that the current be equal in both subcells so the dashed line is common to both subcells in each configuration. Adapted from [25].

loss. The technical difficulty with this approach is finding a lattice matched material of the appropriate band gap. As can be seen from figure 1.6, the III-V ternary alloys do not offer a comprehensive range of band gaps at any given lattice constant. Growing non-lattice matched subcells creates strain within the multi-junction solar cell, which can lead to dislocations which promote non-radiative recombination within the device. Some groups have produced highly efficient cells by growing non-lattice matched "metamorphic" subcells and ensuring that any dislocations are formed in a layer which overproduces current [27]. This technique minimises the effect of the non-radiative recombination caused by the dislocations but it is only effective because the band gaps of the subcells are not ideal initially. There is a strong drive to develop new III-V ternary and quaternary materials to allow better tuning of multi-junction subcell band gaps. One area of particular interest is the development of a 1 eV junction, lattice matched to Ge [28]. One group of emerging candidate materials for this application is dilute nitrides [29]; however, the dramatic reduction of the optical quality of GaAs upon the incorporation of N limits the effectiveness of this material for photovoltaics [30]. An alternative material system for this application is GaAsBi, which produces the same band gap reduction per unit strain as N on GaAs [31, 32].

Multiple quantum well solar cells This topic is treated in detail in section 4.1 but will be outlined here for completeness. In 1990, Barnham et al. [33] proposed the use of a multiple quantum well (MQW) region to tune the absorption of existing III-V compounds for photovoltaic applications. The basic concept of an MQW cell is shown in figure 1.26.

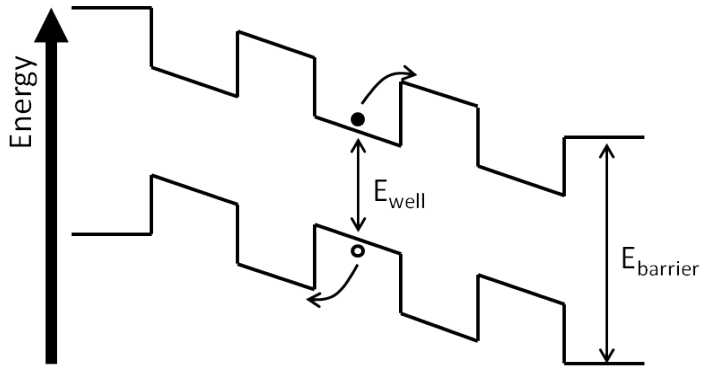

Figure 1.26: Band diagram of an MQW solar cell.

Carriers are absorbed within the wells at the ground state transition energy of the well (E_{well}) and are then thermally excited out of the wells and extracted at the voltage of the barriers. This decoupling of the I_{sc} and V_{oc} allows the cell to exceed the single junction theoretical maximum efficiency. However, the main advantage of MQW cells is realised with the application of strain balancing. For many years, researchers struggled to produce good quality MQW cells [34, 35]. The strain introduced by the wells led to dislocations which inhibited the performance of the cells. In 1999, Ekins-Daukes et al. [36] suggested using strain balancing to prevent the onset of dislocations. Strain balancing involves growing alternating compressive and tensile layers, meaning that the strain seen by the substrate averages to zero. Using the strain balancing technique, it is possible to grow very thick MQW stacks and, importantly, to independently tune the band gap and average lattice constant of the MQW. This technique allows for more precise tuning of the subcells of multi-junction solar cells. Commercially available MQW multi-junction solar cells have been produced with efficiencies of around 44 % [37].

Third generation solar cell summary The third generation technologies discussed above - i.e. hot carrier, intermediate band, multi-junction, and MQW solar cells - all work on the

same principle. In each of these designs the cell exhibits several quasi-Fermi level (QFL) separations throughout the cell. The multiple QFL separations allow carriers to be promoted and have their energy harvested without losing energy to thermal equilibration with the other QFLs throughout the cell [38].

1.6 Summary

This chapter has outlined the basics of semiconductor device physics and introduced the physics of a solar cell. The different designs and challenges associated with third generation photovoltaics have been discussed.

The purpose of this thesis is to assess the potential of GaAsBi as a candidate material for the 1 eV junction in multi-junction photovoltaics. This thesis mainly focuses on the growth of GaAsBi and uses several analytical techniques to assess material quality and device structure of the samples grown in this work.

The remainder of this thesis is arranged as follows: Chapter 2 reviews the experimental techniques used in this work, with particular attention paid to molecular beam epitaxy as it is the main focus of this thesis.

Previous work on the growth and characterisation of GaAsBi is reviewed in chapter 3, which then goes on to present an investigation into the growth of high quality bulk GaAsBi.

The device physics and development of MQW solar cells is discussed in more detail in chapter 4, which then presents work on the growth and structural characterisation of strained GaAsBi/GaAs MQW p-i-n diodes and compares their performance with reports of InGaAs/GaAs MQWs in the literature.

An overview of the results from this work and an outline of possible future work is given in chapter 5.

Bibliography

[1] M. A. Fox. *Optical properties of solids*. Oxford University Press, 2 edition, 2010.

[2] C. Kittel. *Introduction to solid state physics*, volume 5. John Wiley and sons, inc, 1976.

[3] L. Vegard. Die konstitution der mischkristalle und die raumfüllung der atome. *Zeitschrift für Physik A Hadrons and Nuclei*, 5(1):17–26, 1921.

[4] S. M. Sze and J. C. Irvin. Resistivity, mobility and impurity levels in GaAs, Ge, and Si at 300 K. *Solid-State Electronics*, 11(6):599–602, 1968.

[5] A-E. Becquerel. Mémoire sur les effets électriques produits sous linfluence des rayons solaires. *Comptes Rendus*, 9(567):1839, 1839.

[6] C. E. Fritts. On a new form of selenium cell, and some electrical discoveries made by its use. *American Journal of Science*, (156):465–472, 1883.

[7] D. M. Chapin, C. S. Fuller, and G. L. Pearson. A new silicon p-n junction photocell for converting solar radiation into electrical power. *Journal of Applied Physics*, 25(5):676–677, 1954.

[8] BP Statistical Review of World Energy 2014. Technical report, BP, June 2014. bp.com/statisticalreview.

[9] Reference solar spectral irradiance: Air mass 1.5. Technical report, NREL, 2014. http://rredc.nrel.gov/solar/spectra/am1.5/.

[10] G. L. Araújo and A. Martí. Absolute limiting efficiencies for photovoltaic energy conversion. *Solar Energy Materials and Solar Cells*, 33(2):213–240, 1994.

[11] L. C. Hirst and N. J. Ekins-Daukes. Fundamental losses in solar cells. *Progress in Photovoltaics: Research and Applications*, 19(3):286–293, 2011.

[12] N. J. Ekins-Daukes, K. H. Lee, L. Hirst, A. Chan, M. Führer, J. Adams, B. Browne, K. W. J. Barnham, P. Stavrinou, J. Connolly, J. S. Roberts, B. Stevens, R. Airey, and K. Kennedy. Controlling radiative loss in quantum well solar cells. *Journal of Physics D: Applied Physics*, 46(26):264007, 2013.

[13] G. Conibeer. Third-generation photovoltaics. *Materials Today*, 10(11):42–50, 2007.

[14] F. Treble. Milestones in the development of crystalline silicon solar cells. *Renewable Energy*, 15(1):473–478, 1998.

[15] J. Palm, V. Probst, and F. H. Karg. Second generation CIS solar modules. *Solar Energy*, 77(6):757–765, 2004.

[16] M. C. Scharber and N. S. Sariciftci. Efficiency of bulk-heterojunction organic solar cells. *Progress in Polymer Science*, 38(12):1929–1940, 2013.

[17] M. A. Green. Third generation photovoltaics: solar cells for 2020 and beyond. *Physica E: Low-dimensional Systems and Nanostructures*, 14(1):65–70, 2002.

[18] D. König, K. Casalenuovo, Y. Takeda, G. Conibeer, J. F. Guillemoles, R. Patterson, L. M. Huang, and M. A. Green. Hot carrier solar cells: Principles, materials and design. *Physica E: Low-dimensional Systems and Nanostructures*, 42(10):2862–2866, 2010.

[19] J. Nelson. *The Physics of Solar Cells*. Imperial College Press, 1st edition, September 2003.

[20] A. Luque and A. Martí. Increasing the efficiency of ideal solar cells by photon induced transitions at intermediate levels. *Physical Review Letters*, 78(26):5014, 1997.

[21] A. Luque and S. Hegedus. *Handbook of photovoltaic science and engineering*. John Wiley and Sons, 2011.

[22] C. H. Henry. Limiting efficiencies of ideal single and multiple energy gap terrestrial solar cells. *Journal of Applied Physics*, 51(8):4494–4500, 1980.

[23] K. A. Bertness, D. J. Friedman, and J. M. Olson. Tunnel junction interconnects in GaAs-based multijunction solar cells. In *Photovoltaic Energy Conversion, 1994., Conference Record of the Twenty Fourth. IEEE Photovoltaic Specialists Conference-1994, 1994 IEEE First World Conference on*, volume 2, pages 1859–1862. IEEE, 1994.

[24] A. Willoughby. *Solar Cell Materials: Developing Technologies*. John Wiley & Sons, 2014.

[25] J. Burdick and T. Glatfelter. Spectral response and i-v measurements of tandem amorphous-silicon alloy solar cells. *Solar Cells*, 18(3):301–314, 1986.

[26] S. P. Philipps, W. Guter, E. Welser, J. Schöne, M. Steiner, F. Dimroth, and A. W. Bett. Present status in the development of III-V multi-junction solar cells. In *Next Generation of Photovoltaics*, pages 1–21. Springer, 2012.

[27] R. R. King, D. C. Law, K. M. Edmondson, C. M. Fetzer, G. S. Kinsey, H. Yoon, R. A. Sherif, and N. H. Karam. 40 % efficient metamorphic GaInP/GaInAs/Ge multijunction solar cells. *Applied Physics Letters*, 90(18):183516–183516, 2007.

[28] D. J. Friedman, J. F. Geisz, S. R. Kurtz, and J. M. Olson. 1ev solar cells with GaInNAs active layer. *Journal of Crystal Growth*, 195(1):409–415, 1998.

[29] R. R. King, D. Bhusari, D. Larrabee, X-Q. Liu, E. Rehder, K. Edmondson, H. Cotal, R. K. Jones, J. H. Ermer, C. M. Fetzer, D. C. Law, and N. H. Karam. Solar cell generations over 40 % efficiency. *Progress in Photovoltaics: Research and Applications*, 20(6):801–815, 2012.

[30] E. V. K. Rao, A. Ougazzaden, Y. Le Bellego, and M. Juhel. Optical properties of low band gap $GaAs_{1-x}N_x$ layers: Influence of post-growth treatments. *Applied Physics Letters*, 72(12):1409–1411, 1998.

[31] S. Francoeur, M-J. Seong, A. Mascarenhas, S. Tixier, M. Adamcyk, and T. Tiedje. Band gap of $GaAs_{1-x}Bi_x$, $0 < x < 3.6$ %. *Applied Physics Letters*, 82(22):3874–3876, 2003.

[32] U. Tisch, E. Finkman, and J. Salzman. The anomalous bandgap bowing in GaAsN. *Applied Physics Letters*, 81(3):463–465, 2002.

[33] K. W. J. Barnham and G. Duggan. A new approach to high-efficiency multi-band-gap solar cells. *Journal of Applied Physics*, 67(7):3490–3493, 1990.

[34] P. R. Griffin, J. Barnes, K. W. J. Barnham, G. Haarpaintner, M. Mazzer, C. Zanotti-Fregonara, E. Gränbaum, C. Olson, C. Rohr, J. P. R. David, J. S. Roberts, R. Grey, and M. A. Pate. Effect of strain relaxation on forward bias dark currents in GaAs/InGaAs multiquantum well p-i-n diodes. *Journal of Applied Physics*, 80(10):5815–5820, 1996.

[35] J. Barnes, J. Nelson, K. W. J. Barnham, J. S. Roberts, M. A. Pate, R. Grey, S. S. Dosanjh, M. Mazzer, and F. Ghiraldo. Characterization of GaAs/InGaAs quantum wells using photocurrent spectroscopy. *Journal of Applied Physics*, 79(10):7775–7779, 1996.

[36] N. J. Ekins-Daukes, K. W. J. Barnham, J. P. Connolly, J. S. Roberts, J. C. Clark, G. Hill, and M. Mazzer. Strain-balanced GaAsP/InGaAs quantum well solar cells. *Applied Physics Letters*, 75(26):4195–4197, 1999.

[37] B. Browne, J. Lacey, T. Tibbits, G. Bacchin, T-C. Wu, J. Q. Liu, X. Chen, V. Rees, J. Tsai, and J-G. Werthen. Triple-junction quantum-well solar cells in commercial production. In *9th International Conference on Concentrator Photovoltaics Systems: CPV-9*, volume 1556, pages 3–5. AIP Publishing, 2013.

[38] S. P. Bremner, R. Corkish, and C. B. Honsberg. Detailed balance efficiency limits with quasi-Fermi level variations [QW solar cell]. *Electron Devices, IEEE Transactions on*, 46(10):1932–1939, 1999.

Chapter 2

Experimental methods

2.1 Molecular beam epitaxy

2.1.1 Vacuum deposition method

Molecular beam epitaxy (MBE) is a vacuum deposition process which was first developed in the 1970s [1]. The technology is conceptually very simple; a substrate is held in an ultra-high vacuum (UHV) ($\sim 10^{-10}$ mBar) environment and subjected to atomic fluxes from the tuneable evaporation of high purity elements in effusion cells. The high crystal purity and sub-monolayer composition control made possible by this technique led to unprecedented advances in semiconductor technology [2]. While there are other semiconductor growth technologies which can be scaled more readily from research to industry level production, such as metal-organic vapour phase epitaxy (MOVPE) [3], MBE is still a valuable research tool. Whereas technologies such as MOVPE are chemically driven and require sufficient sample temperatures to facilitate surface chemical reactions, the simplicity of MBE allows growth to be performed at comparatively low sample temperatures [4]. By limiting the temperature of the sample it is possible to prevent the propagation of dislocations through the deposited structure, making it possible to grow highly strained structures using novel material systems [5]. These capabilities mean that MBE growth maintains its status as a cutting edge technique for the development of new material systems.

2.1.2 Growth Modes

There are three main modes of epitaxial growth: Frank-van der Merwe (FvdM), Volmer-Weber (VW) and Stransky-Krastanow (SK). Which growth mode is observed depends on the interfacial free energies of the system [6]. There are three free energies of interest: that of the epilayer/vacuum interface (γ_e), that of the epilayer/substrate interface (γ_i) and that of the substrate/vacuum interface (γ_s). The interfaces relevant to these three free energies are shown in figure 2.1. By considering the sum of γ_e and γ_s one can determine the energetically favourable growth mode.

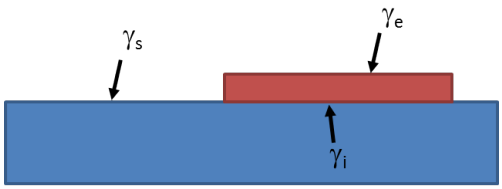

Figure 2.1: The surface free energies in MBE.

2.1.2.1 FvdM growth

FvdM growth is favoured if equation 2.1 is true. In this case it is energetically favourable for incident atoms to bind to the substrate rather than binding to each other.

$$\gamma_e + \gamma_i < \gamma_s \tag{2.1}$$

FvdM growth is a two dimensional, layer by layer growth mode which produces extremely perfect material. This growth mode can only be accessed when growing epitaxial layers of the same material as the substrate (homoepitaxy) or when growing a different material (heteroepitaxy) with a very similar lattice constant to the substrate. The growth must also be conducted at a high temperature to allow the atoms adsorbed onto the growth surface enough thermal energy to migrate to appropriate lattice sites. These constraints can be partially relaxed by the use of a surfactant, as discussed in section 2.1.4. The principles of FvdM growth are shown in figure 2.2.

In this growth mode incident atoms are adsorbed onto the sample surface and migrate until they find a step edge, where their potential energy is minimised [7]. At this point the atom is

incorporated into the lattice. Note that most semiconductor substrates are offcut by a small angle to produce a sufficient density of step edges and that step edges can be formed at dislocations. The build-up of strain due to the growth of lattice mismatched materials will eventually lead to this growth process becoming energetically unfavourable.

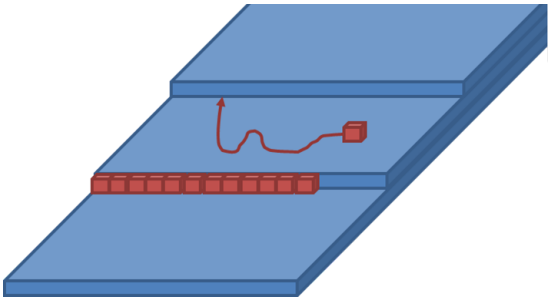

Figure 2.2: The concept of FvdM growth. Atoms incident on the surface migrate until they come into contact with a step edge. At this point they bind to an appropriate lattice position. In this way the step edges propagate across the growth surface.

2.1.2.2 VW growth

VW growth is favoured if equation 2.2 is true. In this case it is energetically favourable for the incident atoms to bind to each other rather than the substrate.

$$\gamma_e + \gamma_i > \gamma_s \tag{2.2}$$

During VW growth the incident atoms form three dimensional islands as shown in figure 2.3. As growth continues, the islands will grow and coalesce to form a full layer, although these layers tend to be polycrystalline [8].

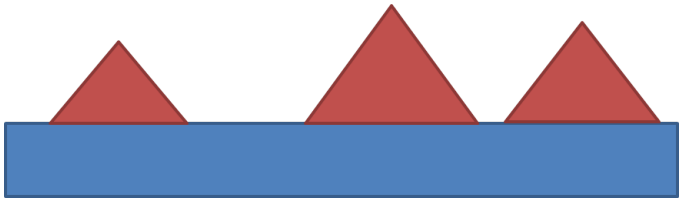

Figure 2.3: VW growth. Atoms incident on the surface form into three dimensional structures rather than two dimensional layers.

2.1.2.3 SK growth

SK growth occurs for epitaxial layers of large lattice mismatch. In this regime equation 2.1 is true initially; however, after a certain thickness, the build-up of internal strain energy (see section 2.1.3) causes the continuation of FvdM growth to be energetically unfavourable and growth then proceeds via three dimensional islanding [9, 10]. This is shown in figure 2.4.

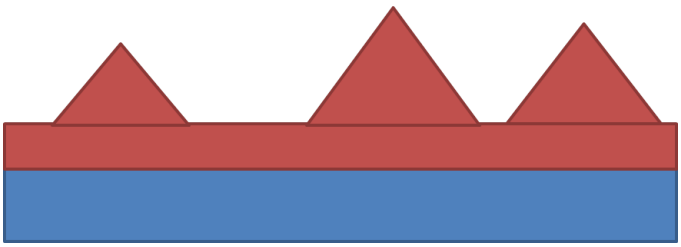

Figure 2.4: SK growth. Initially growth proceeds via the FvdM growth mode, forming a wetting layer. The build-up of strain then causes the growth mode to switch to three dimensional islanding.

2.1.3 Internal strain energy

One can consider a semiconductor to comprise many non-overlapping clusters of semiconductor material [11]. Consider reversibly removing one of these clusters and allowing the cluster and host lattice to relax. The internal energy of that semiconductor cluster is the total energy required to reinsert that cluster into the host lattice. The total internal strain energy of a semiconductor system can be calculated by summing over all of the clusters that comprise that semiconductor.

2.1.4 Surfactant mediated growth

The term surfactant was coined by Copel et al. in 1989 [12] by contracting the term ”surface-active compound”. A surfactant is an element which segregates from the growing layer and alters the surface free energy of an adsorbed atom on a growth surface. A surfactant modifies the average migration lengths of adsorbed atoms; whether the migration length is increased or decreased depends on the surfactant used [13]. In the case of low temperature growth, a surfactant can be used to promote FvdM growth by increasing the migration length of the adsorbed atoms. In the case of highly mismatched growth, a surfactant can be used to reduce the migration length in order to prevent three dimensional

islanding.

2.1.5 Importance of a good vacuum

In order to maintain high quality in epitaxial layers, the MBE environment must be held at UHV as the growing layer will readily incorporate any impurity atoms which are present in the growth chamber [1, 14]. Keeping the system at UHV requires the use of a specialised MBE chamber fitted with several different UHV pumps, each with a specific function during operation or maintenance. The MBE system used in this work and the associated in situ analytical equipment and vacuum pumps are discussed in the following sections.

2.1.6 Molecular beam epitaxy-scanning tunnelling microscopy machine

All samples produced in this work were grown using an Omicron molecular beam epitaxy - scanning tunnelling microscopy (MBE-STM) system. This system comprises an MBE chamber connected to a separate scanning tunnelling microscopy (STM) chamber. Samples can be transferred from the MBE chamber to the STM chamber without being exposed to air. The STM unit is capable of performing microscopy while growing to observe changes in surface structure during growth. These capabilities are of great scientific interest but are not within the scope of the current project. The use of the MBE-STM machine for this purpose is covered in detail in the PhD thesis produced by Dr Faebian Bastiman [15]. Throughout this project the MBE-STM system was only used for its MBE capabilities. As such the remaining discussion will focus on MBE.

2.1.6.1 Machine description

The main growth chamber of the MBE-STM system used in this project is shown in figure 2.5.

Sample loading and unloading is achieved via the fast entry lock (FEL) which is isolated from the MBE chamber by a manual gate valve. The FEL can be quickly vented to atmosphere and pumped down to UHV to allow rapid sample transfer. The sample's temperature is controlled with a heating element inbuilt to the heater stage and its surface structure is monitored using reflection high energy electron diffraction (RHEED). The atomic fluxes

required for growth are provided by the shuttered effusion cells at the base of the machine, these fluxes are monitored using a movable ion gauge (MIG). The operation of each of the component parts of the MBE machine is discussed in sections 2.1.6.2, 2.1.6.3 and 2.1.6.4.

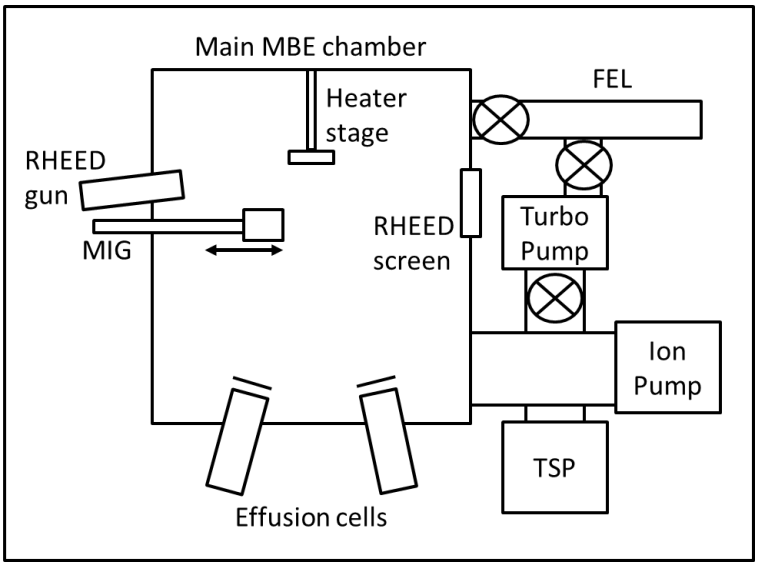

Figure 2.5: Schematic of the MBE machine used in this work.

2.1.6.2 Pumps

There are four pumps used to produce and maintain UHV conditions inside the MBE chamber: A turbomolecular pump, an ion pump, a titanium sublimation pump (TSP) and a liquid nitrogen (LN_2) cooling shroud.

The turbomolecular pump on the MBE chamber is backed by a rotary vane pump to provide a rough vacuum ($\sim 10^{-3}$ mBar) at the turbomolecular pump's exhaust. A turbomolecular pump comprises several rotors which strike the atoms in the vacuum and propel them to the pump's exhaust. The turbomolecular pump is used for pumping the main chamber when re-establishing a vacuum after maintenance and for pumping the FEL prior to sample loading. During normal operation the turbomolecular pump is isolated from the main chamber and is only used to pump the FEL. The turbomolecular pump is very good for quickly producing a vacuum around $10^{-8} - 10^{-9}$ mBar starting from atmosphere, however, it cannot reach pressures as low as 10^{-10} mBar and, as it exhausts to atmosphere, it can cause a potential leak if it fails.

The UHV in the chamber is maintained during operation by an ion pump and a cooling shroud. Ion pumps work by maintaining a strong electric potential (~5 kV) between two electrodes. Molecules entering the electric field between the electrodes are ionised and collected on the electrodes. Ion pumps are only effective at pressures lower than 10^{-6} mBar but can maintain vacuums as low as 10^{-10} mBar. Because they do not exhaust to atmosphere they cannot leak; however, they need to be regenerated periodically to maintain efficient operation.

The cooling shroud is an LN_2 cooled copper plate. The low temperature of the shroud causes molecules from the chamber to adhere to its surface, effectively removing them from the vacuum. To be at its most effective, the cooling shroud should be permanently cold except for outgassing during maintenance. The shroud on the MBE-STM machine is fed by LN_2 from a dewar which needs to be refilled every 48 h, limiting its effectiveness.

The final pump used is the TSP which operates by subliming Ti from a filament. The Ti binds to the chamber walls and getters reactive elements such as oxygen from the vacuum. The TSP is only used when re-establishing UHV conditions after maintenance. Due to the positioning of the TSP in the MBE-STM system it has optical access to the sample holder and could contaminate samples if used during routine operation.

2.1.6.3 Effusion cells

The atomic fluxes required for growth are provided by evaporating elemental material in Knudsen effusion cells. There are several types of cell used in the MBE machine. The Al is heated in a single filament cold lip effusion cell and the In and Ga are heated in standard hot lip effusion cells [16]. In the effusion cells, the source material is heated in pyrolytic boron nitride (PBN) crucibles. PBN is a III-V material and it is used due to its temperature stability (stable up to ~ 1400 °C), its chemical stability and the extremely smooth, non-porous crucible walls which can be achieved with this material. Within the cell, the PBN crucible is surrounded by a Ta or W heating element and contacted at its

base by a thermocouple. Hot lip cells have extra coils of heating element around the top of the cell; these extra coils produce a temperature gradient across the cell and reduce spitting. The temperature of the crucible is regulated by a proportional-integral-derivative loop which applies current to the heater element and receives feedback from the thermocouple. The Bi cell used in this work is a dual filament cell, the crucible being heated by different elements and monitored by separate thermocouples at the base and at the top. This design reduces spitting and also allows for precise control over the temperature gradient across the cell. The dopants in this work (Si and Be) are supplied by a dual dopant source. The dual source comprises two small effusion cells designed to fit into a single effusion cell port. As is supplied by a valved As cracker cell. The cracker cell comprises an As reservoir and a cracker section. As_4 tetramers sublime from the reservoir and pass through the cracker which can be heated to crack the As_4 tetramers and produce As_2 dimers if desired. The cracker was held at 650 °C to produce As_4 or at 1000 °C to produce As_2. In either case the flux will not be purely As_2 or As_4, but will contain a small fraction of the other species due to the cracking efficiency of the cracker cell [17]. This effect was ignored throughout this work and the cracker efficiency was assumed to be perfect. The maximum As flux is determined by the temperature of the reservoir and can be adjusted through several orders of magnitude by an adjustable needle valve between the reservoir and the cracker.

2.1.6.4 Movable Ion Gauge (MIG)

The atomic flux from the cells is measured by a MIG which can be moved into the beam path during measurements and retracted during growth. The MIG comprises a single filament collector cathode surrounded by a cylindrical shaped anode cage. Electrons are produced by passing a constant current through a third filament, which is outside the cage. The electrons are accelerated towards the cage and most pass through into the cage. Here the electrons ionise a fraction of the particles within the cage. The positive ions produced during this process impact the collector cathode and produce a small current. The current observed by the MIG is directly proportional to the beam equivalent pressure of the species being detected [2]. The MIG response is also dependent on the ionisation potential of the species being monitored; however, the MIG cannot differentiate between species and can only be used to measure combined background pressure or the absolute flux of one element at a

time.

2.1.7 Bonding and reconstructions

The surface structure of a semiconductor during growth can provide important information about the growth conditions. Although we are interested in the inter-atomic bonds on a semiconductor surface, it is instructive to first consider the inter-atomic bonding in bulk semiconductors. Section 2.1.7.1 discusses the inter-atomic bonding in bulk GaAs and section 2.1.7.2 discusses the formation of surface reconstructions on GaAs.

2.1.7.1 Bonding in Bulk Semiconductors

As MBE growth is driven by atomic interactions on the growth surfaces it is instructive to consider the physics of the semiconductor surface. In order to understand the physics of the semiconductor surface one must first consider the bonding in a bulk semiconductor such as GaAs. GaAs forms a zincblende structure as shown in figure 2.6. Neighbouring atoms are bonded by two spin-paired electrons. The number of electrons donated to bonding by each element is dictated by the valency of the element. Group III atoms (e.g. Ga) have 3 electrons to donate to bonding, whereas group V atoms (e.g. As) have 5 electrons to donate to bonding. Each atom is bonded to 4 nearest neighbours, shown as part of a GaAs unit cell in figure 2.6. Therefore, the Ga atoms contribute 0.75 electrons per bond and the As atoms contribute 1.25 electrons per bond.

2.1.7.2 Surface reconstructions

At the semiconductor surface, the lack of further atoms to which to bond leaves some of the valence electrons of the terminating layer unsatisfied. The resulting ”dangling bonds” are shown in figure 2.7. In order to minimise the surface energy, the dangling bonds will be used to form surface reconstructions. A reconstructed semiconductor surface is one whose symmetry is lower than that of the bulk crystal. In other words, a reconstructed surface comprises a repeating arrangement of atoms with a period which is greater than that of the unit cell of the bulk crystal. The periodicity of the reconstructed surface is labelled as $(n \times m)$ where n and m are the periodicities of the reconstruction in the $[1\bar{1}0]$ and [110]

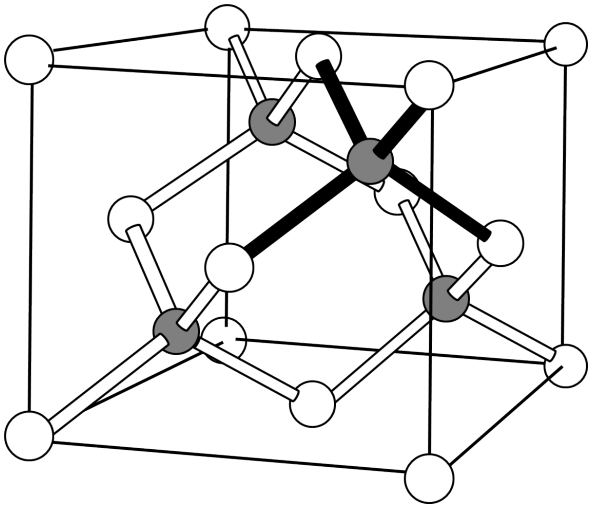

Figure 2.6: The zincblende structure of GaAs. The white circles represent cations (Ga) and the grey circles represent anions (As). The rods connecting the balls represent bonding. The filled rods are included to show the tetrahedral shape of the bonds. Adapted from [18]

directions respectively (on a (100) surface) in terms of the interatomic spacing of the crystal.

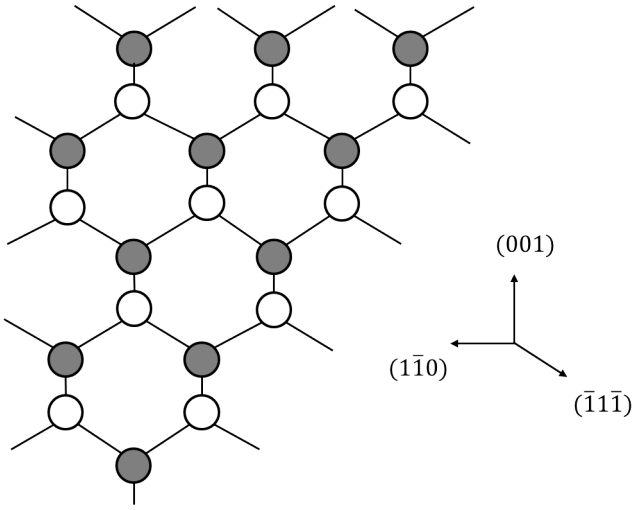

Figure 2.7: The dangling bonds resulting from the termination of the crystal lattice in GaAs. The white circles represent cations (Ga) and the grey circles represent anions (As). Adapted from [15].

As this thesis is concerned with growth on the (100) surface of GaAs based compounds, the discussion here will be limited to the reconstructions observed on such surfaces. A more comprehensive overview of semiconductor surface reconstructions can be found in [19].

A reconstructed surface region does not necessarily share the stoichiometry of the bulk

crystal and it is helpful to consider it as an epitaxial layer of a different compound. The surface reconstructions on (100) GaAs obey the following principles:

1. The observed surface structure will represent the lowest surface energy which is kinetically accessible.

2. The surface must be semiconducting.

3. The surface energy is lowered through hybridisation.

The first principle arises from the fact that there are several surface energy minima corresponding to different surface reconstructions. The observed surface reconstruction will be dependent not only on the ambient conditions but also on the previous ambient conditions.
The second principle requires that all dangling bonds which fall in the valence band are filled and all that fall within the conduction band are empty. In this case it requires that all of the As dangling bonds are filled and the Ga dangling bonds are empty [18] as shown in figure 2.8. This is achieved by the Ga valence electrons transferring onto the As atoms. Thus, the second principle can be restated as: "The number of surface electrons in the reconstruction must exactly fill all of the available dangling bonds". This is known as the electron counting model.
The third principle says that the exact position of the surface atoms, in the arrangements allowed by the second principle, is determined by lowering the energy of the surface bonds through hybridisation.

The three stable reconstructions on a GaAs (0 0 1) surface are $c(4\times4)$, (2×4) and (4×2). Atomic diagrams of these reconstructions are shown in figures 2.9, 2.10 and 2.11. There have been many other reconstructions observed which seem to be transient reconstructions between the three mentioned above ([20] and references therein).
A final note on the GaAs (001) reconstructions is that the first principle dictates that the observed reconstruction is dependent on the preparation conditions. The surface As population decreases as the surface follows the progression (of increasing temperature):

$$c(4\times4) \rightarrow \beta2(2\times4) \rightarrow \alpha(2\times4) \rightarrow \beta2(4\times2)$$

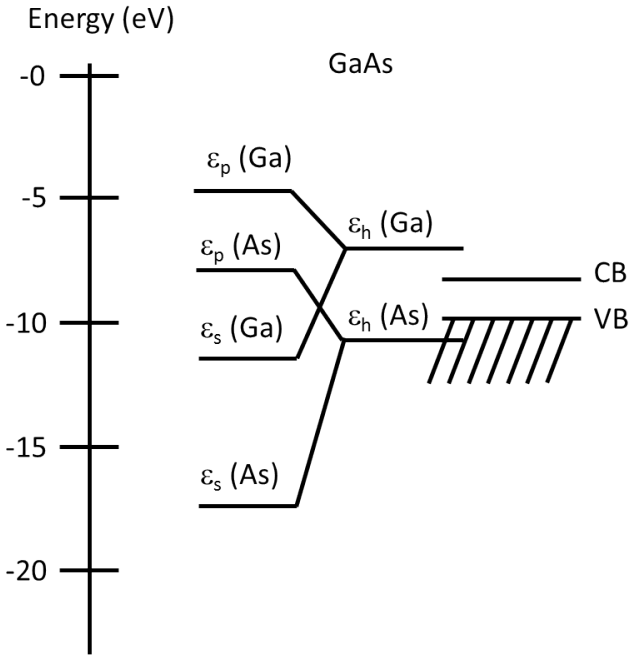

Figure 2.8: The hybridisation of the Ga and As atomic orbitals in GaAs. As the hybridised As bond energies are within the conduction band, these bonds will be occupied by electrons. The hybridised Ga bonds, which have energy levels in the conduction band, will be empty. Adapted from [18].

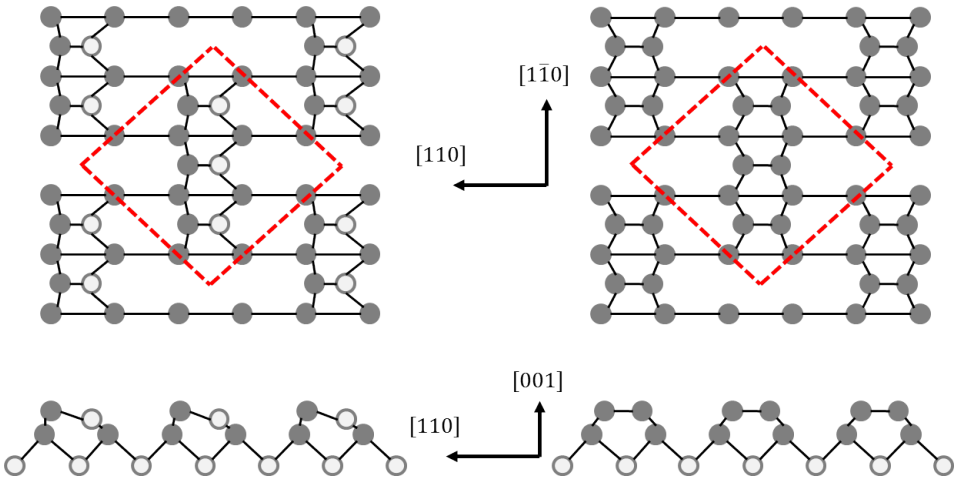

Figure 2.9: The α (left) and β (right) variants of the $c(4\times4)$ reconstruction. Adapted from [21]. The white circles represent Ga atoms and the grey circles represent As atoms. The red, dashed boxes indicate the unit cell of the surface reconstruction.

Therefore, in a perfect vacuum, one can raise the surface temperature to obtain different reconstructions. However, to reverse this procedure requires an external As flux. This has been widely utilised in surface studies by producing the desired surface reconstruction, terminating the As flux on the sample and then lowering the temperature to preserve the

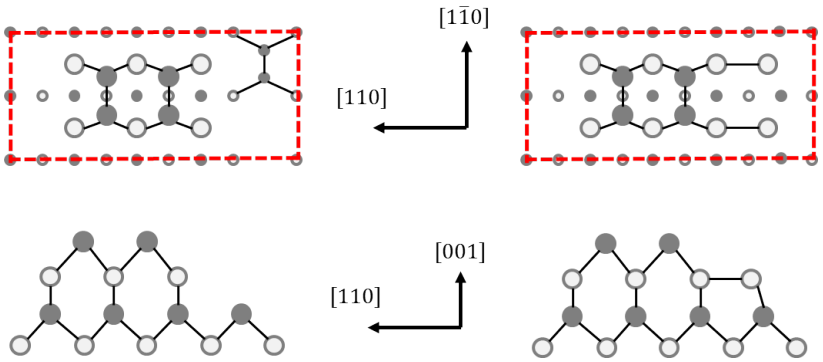

Figure 2.10: The $\beta 2$ (left) and α (right) atomic configurations of the GaAs (2×4) reconstruction. The white circles represent Ga atoms and the grey circles represent As atoms. The smaller circles represent atoms from the monolayer beneach the larger circles. The red, dashed boxes represent the unit cells of the two surface reconstructions. Adapted from [22].

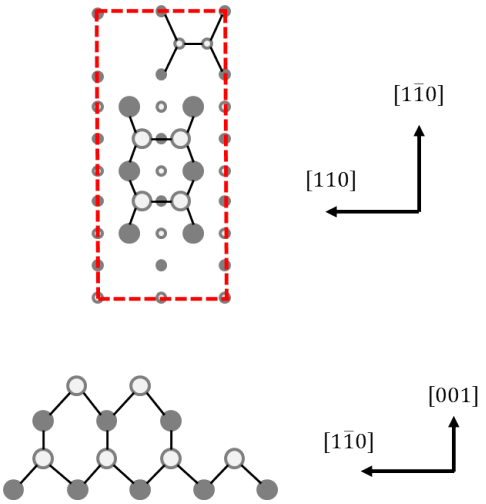

Figure 2.11: The Ga rich $\beta 2c(8\times2)$ reconstruction. Note that it is very similar to the $\beta 2(2\times4)$ but rotated through 90°and the terminating layer comprises Ga atoms. The white circles represent Ga atoms and the grey circles represent As atoms. The smaller circles represent atoms from the monolayer beneach the larger circles. The red, dashed box indicates the unit cell of the reconstruction. Adapted from [23].

reconstruction for subsequent investigation [24, 25].

2.1.8 Reflection high energy electron diffraction (RHEED)

RHEED is an in-situ technique for monitoring the surface reconstruction of a sample during growth [26]. It is an extremely powerful technique, allowing for the measurement of sample temperature (see section 2.1.9.1), growth rate (see section 2.1.9.2) and atomic fluxes (see section 2.1.9.3) as well as being an indicator of the sample surface quality.

The RHEED system used in this thesis works in the following way. A collimated beam of electrons is produced by an electron gun and is incident on the sample at a grazing angle (1 - 3 °). The electrons are diffracted by the top few monolayers of the sample and the diffraction pattern is observed on a phosphorescent screen. The resulting diffraction pattern can be understood by considering the diffraction criteria due to the reciprocal space lattice and the Ewald sphere [14]:

The first consideration is that of the diffraction condition. Each point of the reciprocal space lattice of the sample indicates an angle and wavevector for which the Bragg condition (see section 2.3.1) is satisfied and constructive interference will occur. Only the top few monolayers contribute to diffraction in the case of RHEED and, as such, there is no Bragg condition perpendicular to the sample surface. The reciprocal space lattice in this case comprises rods which start at reciprocal space lattice points and extend to infinity perpendicular to the sample surface. For constructive interference to occur, the diffracted wavevector must terminate on one of the reciprocal lattice rods.

The second consideration is of the conservation of momentum. The scattering in RHEED is mainly elastic. As such the scattered wavevectors are of equal magnitude to the incident electron wavevector. Thus, if all possible scattered wavevectors were given a common origin then the termini of all of these wavevectors would describe a sphere in reciprocal space. This sphere is known as an Ewald sphere [27].

Diffraction occurs at angles where the reciprocal space rods and the Ewald sphere intersect. In other words, where the Bragg condition and conservation of momentum are both satisfied. This is shown diagrammatically in figures 2.12 and 2.13. Note that the angle of the diffracted electron beam is conserved when transforming between real space and reciprocal space so it is valid to determine the angles at which constructive interference occurs in reciprocal space.

The points labelled as constructive interference in figures 2.12 and 2.13 comprise the diffraction pattern arising from the interatomic spacing of the lattice. They are known as zero order rods. If the sample surface has formed a reconstruction, as described in section 2.1.7.2, then there will be a separate diffraction pattern due to the periodicity of the surface reconstruction. As the period of the surface reconstruction is, by definition, larger than the atomic spacing, the period of its diffraction pattern will be smaller. Also, as the reconstruction is an

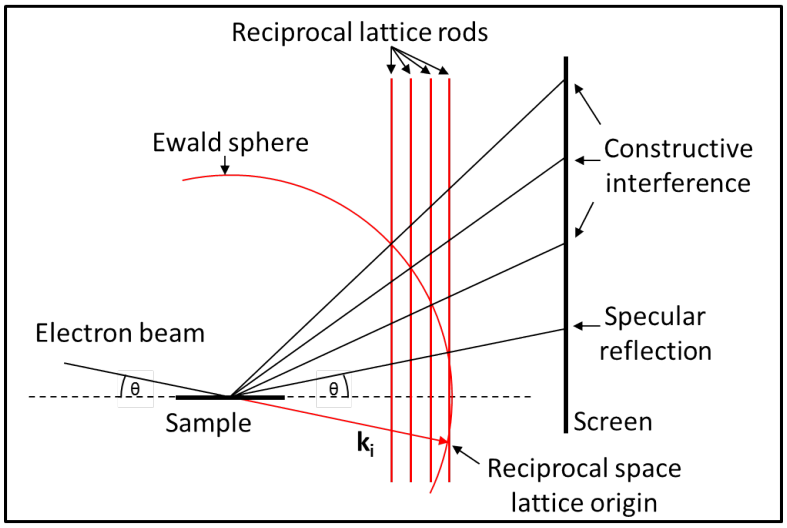

Figure 2.12: Side view of the diffraction pattern produced by RHEED. Note that the lines in red are in reciprocal space. Adapted from [14].

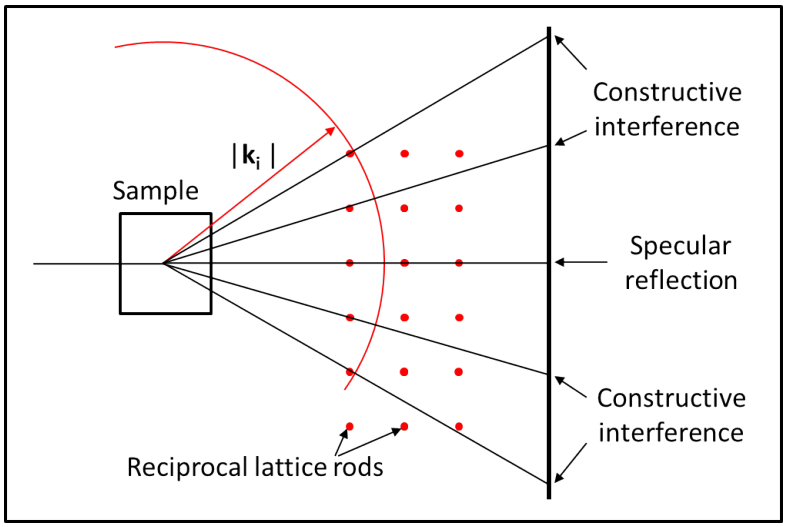

Figure 2.13: Top down view of the diffraction pattern caused by RHEED. Note that the diagram only shows the horizontal great circle of the Ewald sphere and all of the reciprocal lattice rods intersect the sphere twice at different altitudes. Adapted from [14].

integer number of atomic spacings in size, its diffraction pattern will be centred on the zero order rods. The superposition of the two diffraction patterns causes the zero order rods to appear brighter than the other rods in the pattern. Two examples of the diffraction patterns produced by RHEED are shown in figure 2.14.

RHEED offers valuable insight into the conditions on the sample surface. The real time, in situ sample surface analysis provided by this technique is invaluable for controlling the

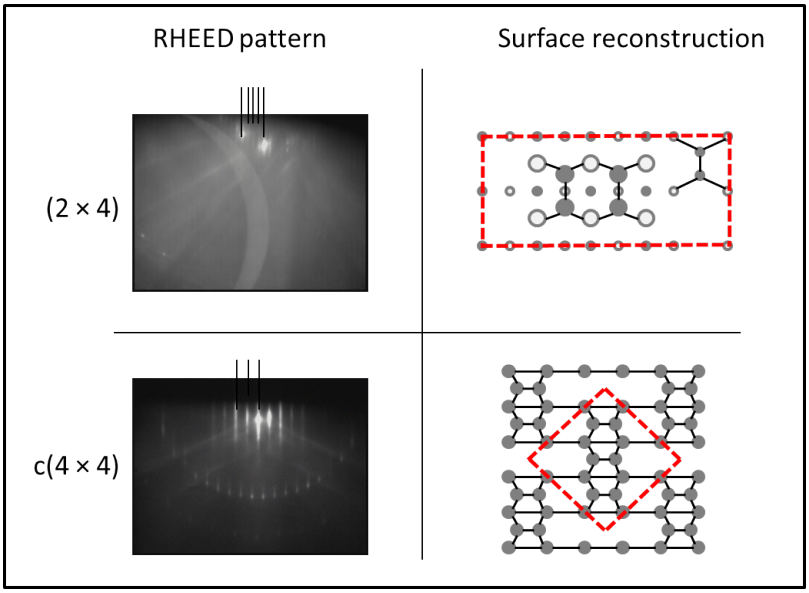

Figure 2.14: RHEED images and the surface reconstructions from which they arise. The reconstruction rods have been highlighted for clarity in the RHEED images. The white circles represent Ga atoms and the grey circles represent As atoms. The smaller circles represent atoms from the monolayer beneach the larger circles. The reconstruction unit cells are represented by the red dashed boxes.

conditions during growth, as will be seen in section 2.1.9.

2.1.9 Calibrations

The measurements required to control the growth conditions throughout this work are described in this section. The experimental uncertainties which arise from these measurements are then discussed.

2.1.9.1 Substrate temperature calibration

The MBE system used in this work is not equipped with an optical thermometry unit and although a thermocouple is attached to the sample heater stage, its distance from the sample renders it ineffective for sample temperature monitoring. It is necessary, therefore, to estimate the sample temperature during growth based on the current passed through the heater filament. This temperature estimation is calibrated against three well defined, temperature dependent RHEED transitions.

The three RHEED transitions used were as follows:

- The thermal desorption of native surface oxide at 580 ± 10 °C [28]
- The $c(4\times4) \rightarrow (2\times4)$ transition in the absence of an As flux at 410 ± 10 °C [29]
- The sublimation of As from an amorphous capping layer at 300 ± 20 °C [30]

Note that an amorphous As cap will remain on a sample surface up to 350 ± 10 °C on vicinal (offcut) surfaces due to its affinity with the step edges [31, 32]; however, the surfaces produced in this work have a very shallow offcut (~ 0.1 °) so the RHEED pattern is assumed to change from an amorphous haze to c(4 × 4) at 300 ± 20 °C. The calibration must be repeated for different sample thicknesses and doping concentrations because, while the temperature of the RHEED transition remains the same, the relationship between heater element current and sample temperature changes. The calibration for undoped GaAs, as described above, is shown in figure 2.15.

2.1.9.2 Growth rate calibration

RHEED can be used to measure the growth rate of a sample by observing periodic variations in the intensity of the specular reflection from the surface. The oscillations in the specular intensity can be understood by considering the following process. A completed monolayer on the sample surface is atomically flat, which gives a high intensity specular RHEED reflection. When growth commences the incident atoms bind onto the surface and form small islands, these islands cause a roughening of the surface and, consequently, a reduction in the specular beam intensity. As the islands grow, the average surface roughness increases and the specular beam intensity drops to a minimum. When the island surface coverage exceeds 50 % the islands begin to coalesce and form a new surface layer which is roughened by the gaps between islands. As these gaps are filled the surface becomes less rough and the specular beam intensity increases, reaching a maximum when the monolayer is completed and an atomically flat surface is restored. This process is illustrated in figure 2.16. Due to the random positioning of the islands during growth, new islands will form, commencing growth of a new monolayer before the previous monolayer is completed. Thus the RHEED pattern will never regain its full specular intensity. This process causes the decay observed

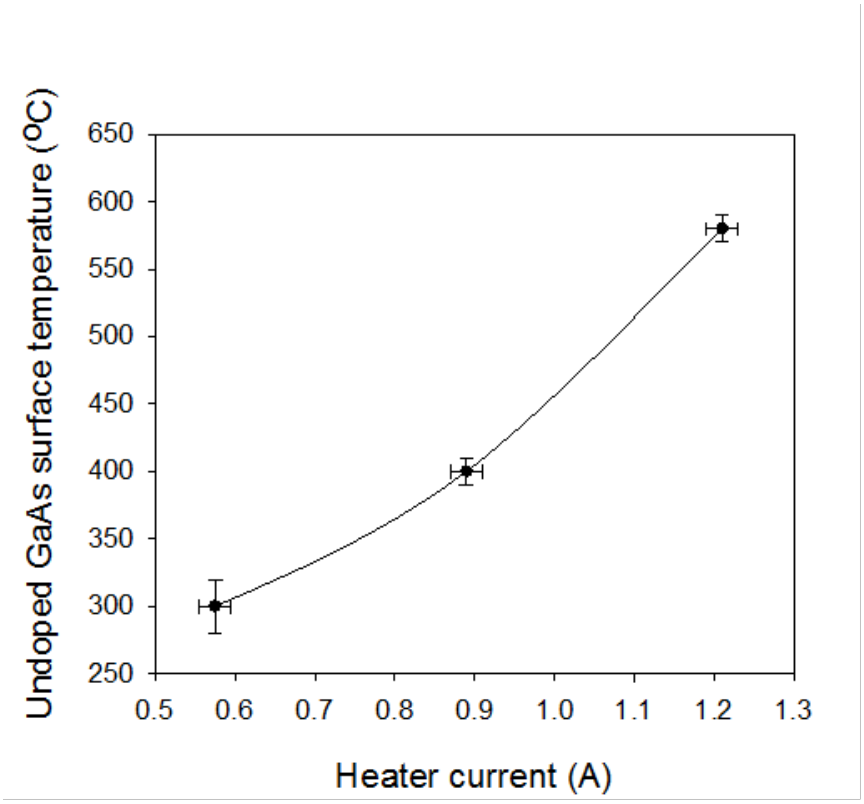

Figure 2.15: Graph of undoped GaAs sample temperature plotted against heater element current. A spline curve has been added to guide the eye.The uncertainty in the heater current is based on the variation in the current required to achieve each transition from day to day.

in growth rate oscillations as shown in figure 2.17. Each period of oscillation in the RHEED intensity corresponds to the deposition of one new monolayer. Thus the growth rate can be calculated by counting oscillations over a fixed time scale.

2.1.9.3 Flux Calibration

Ga Flux Measurement Once the growth rate is known, the Ga flux can be calculated by assuming a unity incorporation coefficient in the presence of surface As [33]. The calculation is as follows:

Figure 2.18 shows the Ga terminated face of a GaAs unit cell. As there are two Ga atoms on this face of each unit cell, the deposition of one monolayer of GaAs is equivalent to the deposition of 2 Ga atoms in an area of a^2_{GaAs}. The Ga flux can, therefore, be calculated from the measured growth rate as shown in equation 2.3:

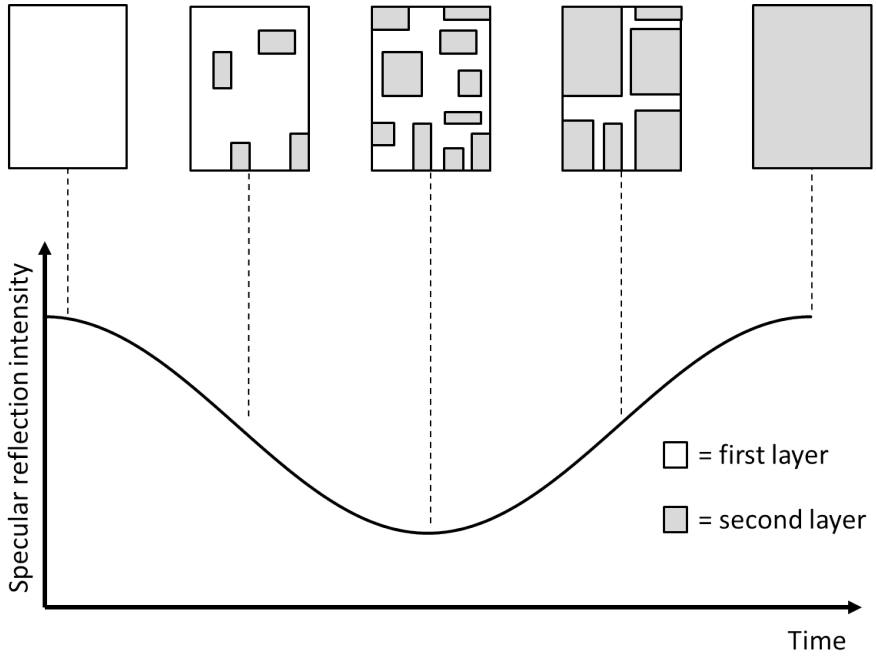

Figure 2.16: The oscillation of the specular RHEED intensity during the growth of a single monolayer. Adapted from [26]

$$F_{Ga} = \frac{2}{a^2_{GaAs} t_{ML}} = \frac{2}{0.5653^2 t_{ML}} \approx \frac{6.26}{t_{ML}} atoms.nm^{-2} s^{-1} \tag{2.3}$$

where F_{Ga} is the Ga flux in atoms.nm^{-2}s^{-1}; t_{ML} is the monolayer growth time in seconds.

Al flux measurement The Al flux can be determined in the same way as the Ga flux. However, during growth of the structures in this work, the material composition required was $Al_{0.3}Ga_{0.7}As$. Therefore, the calibration was performed as follows. The Ga flux was calculated first using the method described above and then the Al flux was calculated by growing AlGaAs and subtracting the known GaAs growth rate from the total growth rate. As the AlGaAs lattice constant perpendicular to growth is constrained by the GaAs substrate, the GaAs lattice constant is still used to determine the Al flux assuming a unity sticking coefficient of Al [34].

As flux measurement The sticking coefficient of As is not unity in the absence of surface Ga [35]. This means that the As flux cannot be calibrated in the same way as the Ga flux. Instead the As flux must be found by comparison to the Ga flux. In the case

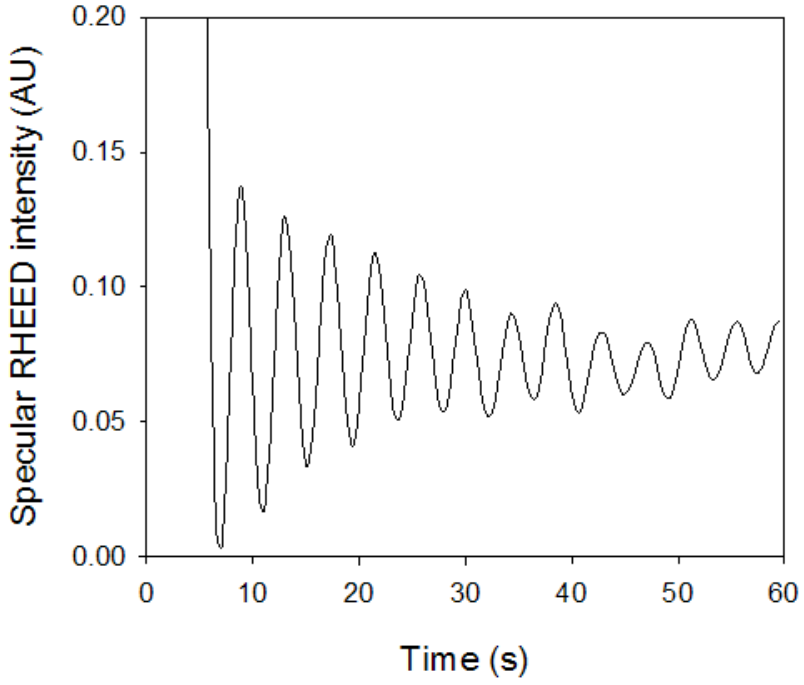

Figure 2.17: RHEED intensity oscillation damping. Image taken from the MBE-STM machine used in this work.

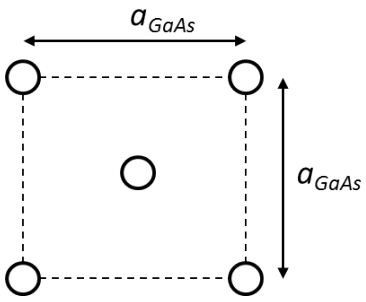

Figure 2.18: Ga atoms on one face of a GaAs unit cell. $a_{GaAs} \approx 0.5653$ nm at room temperature.

of GaAs there is a RHEED transition during growth at an As:Ga flux ratio of 1:1 when growing with As_2 [36]. The transition is between the As terminated (2×4) reconstruction (figure 2.10) and the Ga terminated (4×2) reconstruction (figure 2.11). The growth temperature must be low enough to neglect the contribution of thermal As desorption from the top monolayers of the growth surface at the growth rate used for the measurement. By tuning the As_2 flux during growth to a 1:1 ratio with Ga, i.e. to the transition between

the (2×4) and (4×2) reconstructions, the As flux can be determined by equating it to the Ga flux as calculated from RHEED oscillations. By performing this experiment at several different growth rates one can determine the relationship between As valve position and As atomic flux. As_4 does not exhibit a unity sticking coefficient in the presence of surface Ga [33], meaning that calibrating As_4 in the same way as As_2 is not possible. It was assumed that the atomic flux from the As source was not affected by the temperature of the cracker zone. Therefore the As_2 calibration was extended to As_4 by assuming that, for any given valve position and As bulk temperature, As_4 atomic flux = As_2 atomic flux, or equivalently, $2\times As_4$ molecular flux = As_2 molecular flux.

Bi flux measurement The Bi flux cannot be measured using the same method as the As flux as the compound GaBi has never been successfully grown. The method used to calculate the flux was to grow a polycrystalline Bi cap on a GaAs surface and measure its thickness using scanning electron microscopy. By growing the cap at $\sim0\,^{\circ}C$ the sticking coefficient can be assumed to be unity and, by knowing the density and atomic weight of Bi, the flux of Bi during growth can be estimated.

Dopant flux measurement The dopant fluxes were measured by growing a GaAs sample at a known growth rate and doping it using several different dopant cell temperatures to produce a stepped doping profile. This profile was characterized using a capacitance-voltage profiler to yield the doping density at each step. By assuming a unity sticking coefficient, the observed doping densities can be used to calculate the dopant fluxes in atoms.nm^{-2}s^{-1}.

Flux measurement using the movable ion gauge In the interests of expedience, MIG readings were used to estimate the cell fluxes on a daily basis. The measurements described above were performed at several different growth rates and the measured atomic fluxes were plotted against MIG readings to yield a relationship between MIG reading and atomic flux. The MIG must be calibrated regularly as its collection efficiency changes over time as it is coated by the growth elements used.

2.1.9.4 Experimental uncertainties

The calibrations for the atomic fluxes and substrate temperature as mentioned above are all subject to experimental uncertainty. Interpretation of RHEED patterns is the dominant source of uncertainty in this work. Transitions between RHEED patterns are rarely abrupt; most transitions are gradual with respect to time and temperature. Ascertaining the exact transition point between two RHEED patterns is very difficult and leads to significant uncertainty. Hence, the temperature and As flux calibrations are not very precise. The Ga flux calibration is much more accurate, the only uncertainty being in timing the oscillations. The uncertainty in dopant flux calibrations is dominated by the uncertainty in the capacitance-voltage measurement. The Bi flux measurement is dependent on the assumption of a unity sticking coefficient during the amorphous Bi layer deposition and also the assumption that the deposited Bi layer is truly amorphous. The uncertainties in each measurement as used throughout this work are listed here:

Temperature ± 10 °C; Ga flux ± 1%; As flux ± 10%; Dopant flux ± 10%; Bi flux ± 10%.

2.1.10 Sample preparation

The samples used in this work were cleaved from 3″ GaAs wafers into samples of 11.3 mm × 11.8 mm using a Loomis scribe and break machine. The rectangular shape of the samples allows the [110] and [1$\bar{1}$0] crystallographic directions in the samples to be identified. The samples were then cleaned using n-butyl acetate to clear the surface of any contamination from the cleaving process before being stored under vacuum in a desiccator prior to loading.

Samples are loaded into the MBE chamber via the FEL. This requires the FEL to be opened to atmosphere. In order to maintain the UHV in the MBE chamber the FEL must be pumped by the turbomolecular pump after sample loading for about 30 minutes before the sample can be transferred to the MBE chamber sample holder. Once the sample is in the sample holder it is outgassed at 450 °C for 30 minutes to remove any moisture from the sample surface. The sample is then heated to 600 °C to remove the native surface oxide [28]. Significant As dissociation from GaAs is observed above ~ 575 °C [37], hence an external

As flux must be used to prevent the GaAs surface from becoming As deficient during oxide removal. The condition of the sample surface after oxide removal is dependent on the age of the sample [38–40]. After production, GaAs substrates quickly form a layer of As_2O_3 on the surface several monolayers thick. This process is shown in equation 2.4.

$$4GaAs + 3O_2 \rightarrow 2As_2O_3 + 4Ga \tag{2.4}$$

This surface oxide is highly volatile and can easily be thermally removed with minimal surface damage as the As lost during oxide desorption is replaced by the external As flux. However, over the course of about 3 months this oxide reacts with the lattice to form the more stable oxide Ga_2O_3. This process is shown in equation 2.5.

$$2GaAs + As_2O_3 \rightarrow 4As + Ga_2O_3 \tag{2.5}$$

This oxide is more problematic as removing it also removes Ga and As atoms from the GaAs matrix by the process shown in equation 2.6 [41].

$$Ga_2O_3 + 4GaAs(bulk) \rightarrow 3Ga_2O + 4As \tag{2.6}$$

The desorption of Ga_2O removes Ga from the host matrix and leaves so called "μpits" [39, 42] in the substrate surface. In order to restore an atomically flat surface, a buffer layer of at least 100 nm must be grown [41]. The growth of the 100 nm buffer layer also buries any impurities left on the substrate surface by the polishing process. This is especially important when growing electrical devices where such impurities are extremely damaging to the depletion width of the device.

2.2 Photoluminescence

Photoluminescence (PL) is a non-destructive material characterisation technique [43]. PL offers insight into the band structure and material quality of semiconductor layers.

2.2.1 Radiative recombination

During a measurement, carriers are excited within the test sample by monochromatic light from a laser. The carriers then thermalise to the material's band edges before radiatively recombining. These steps are shown in figure 2.19. This technique is usually only used on direct band gap materials as indirect band gap materials require the excited carriers to simultaneously emit a photon and interact with a phonon to relax as discussed in section 1.2.5. The required interaction with a phonon makes the relaxation process a second order process and reduces the radiative efficiency of indirect band gap materials.

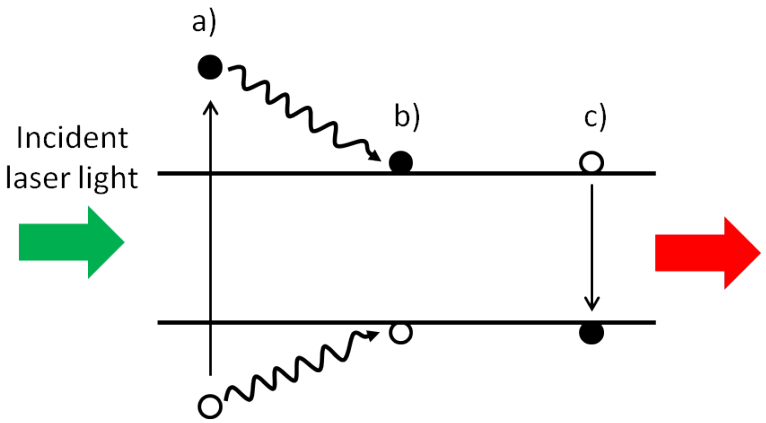

Figure 2.19: The processes involved in PL: a) Carriers are excited to the energy of the incident light. b) The excited carriers thermalise to the band edges by emitting phonons. c) The carriers recombine, emitting light at the energy of the band gap.

The process shown in figure 2.19 is radiative recombination. Radiative recombination is an inherent carrier loss mechanism in all semiconductors.

2.2.2 Non-radiative recombination

There are several non-radiative loss mechanisms which also contribute to carrier relaxation [44]; two of these mechanisms are shown in figure 2.20. Carriers can recombine via trap states within the band gap, either by emitting photons or phonons to discard their energy,

this is known as Shockley-Read-Hall (SRH) recombination. SRH recombination is caused by imperfections in the semiconductor crystal lattice, as such it can be reduced by improving crystal quality. Excited carriers can also recombine by giving their energy to other carriers, this is known as Auger recombination.

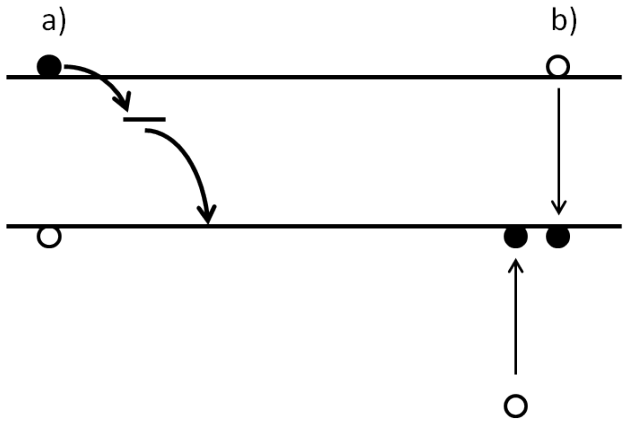

Figure 2.20: Non-radiative carrier relaxation mechanisms in semiconductors: a) Recombination via a trap state in the band gap (SRH recombination). b) Recombination transferring energy to another carrier (Auger recombination).

Each form of recombination has its own characteristic lifetime and the total carrier lifetime in the sample is given by the sum of the reciprocals of the lifetime of each mechanism. This is shown mathematically in equation 2.7:

$$\frac{1}{\tau_c} = C_R + C_{NR}N_c + C_A N_c^2 \tag{2.7}$$

where τ_C is the carrier lifetime; C_R, C_{NR} and C_A are the radiative, non-radiative and Auger recombination coefficients and N_c is the carrier density. This relationship holds for the relaxation of minority carriers. The rate of carrier recombination is equal to the number of carriers divided by the average carrier lifetime.

Clearly, the longer the non-radiative lifetime, the longer the average carrier lifetime. This means that there are more carriers available to radiatively recombine, increasing the intensity of the PL signal. Long carrier lifetimes are very important for solar cells. Hence the slightly counter-intuitive result that the greater the observed rate of radiative recombination (a loss mechanism in solar cells), the better the material is for solar cell use.

2.2.3 Experimental setup

For the PL experiments performed during this work, the laser light was produced by a 532 nm diode pumped solid state laser. The laser light was passed through a band pass filter to remove any harmonics from the laser signal before being incident on the sample. The PL was collected by a cassegrain telescope and focussed onto the entrance slit of a monochromator after passing through a long pass filter to remove any stray laser light. The monochromator used a 900 grooves/mm (850 nm blazed wavelength) diffraction grating to give good response for the wavelengths of interest (850 - 1400 nm). The signal was then detected by an LN_2 cooled Ge detector. The signal from the detector was passed to a lock-in amplifier which used a phase sensitive measurement technique in order to filter background signal from the measurement. This technique required the laser light to be chopped. The chopping frequency was chosen to be 180 Hz to avoid interference from the mains power supply (multiples of 50 Hz). A schematic of the setup is shown in figure 2.21.

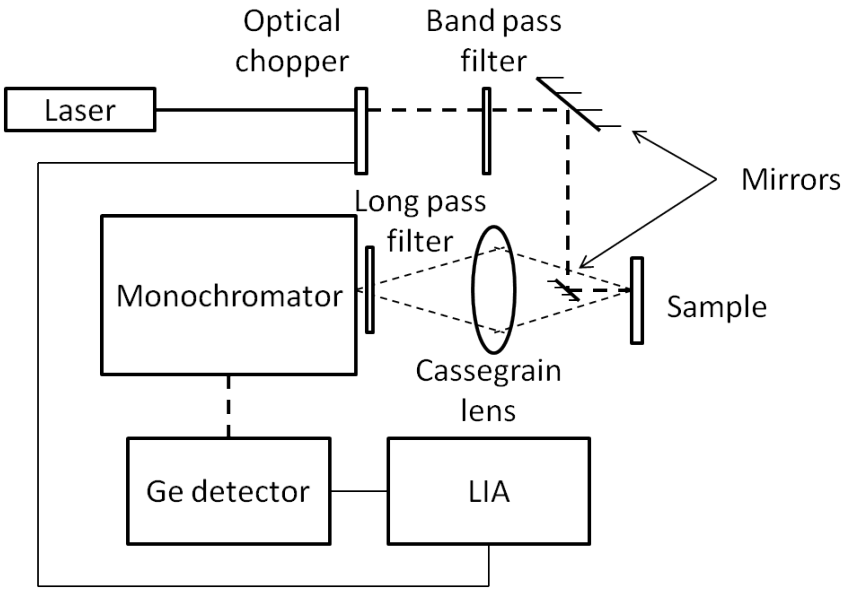

Figure 2.21: Schematic of the experimental PL setup used in this work.

2.3 X-ray diffraction

X-Ray diffraction (XRD) is a non-destructive crystal characterisation tool which was first developed in the early 20th century [45]. X-rays are electromagnetic waves in the wavelength range $10^{-8} - 10^{-12}$ m, these distances are comparable to the interatomic spacing in semiconductor crystals ($\sim 5 \times 10^{-10}$ m). By probing a sample with a monochromatic, collimated X-ray beam, a diffraction pattern is produced which yields information about the sample structure, as is discussed in this section.

2.3.1 Bragg's law

The angles at which X-rays diffracted from a crystalline solid will constructively interfere can be determined from Bragg's law. Note that Bragg's law can be applied to the formation of a RHEED pattern from a reconstructed surface, as discussed in section 2.1.8.

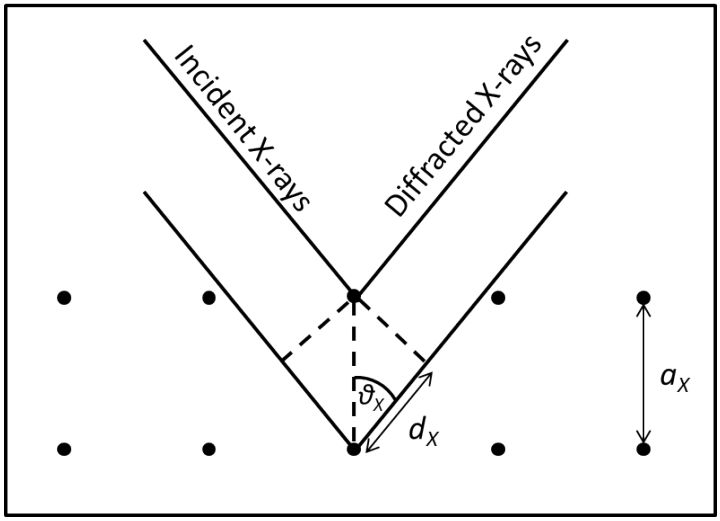

Figure 2.22: Bragg's law is only satisfied if the path length difference between the two X-rays ($2d_x$) is equal to an integer number of wavelengths.

Bragg's law states that the path length difference between two parallel diffracted beams must be an integer number of wavelengths, otherwise the beams will destructively interfere and no signal will be observed. This is illustrated in figure 2.22 and is expressed mathematically in the Bragg equation equation [46]:

$$n\lambda_x = 2d_x = 2a_x \cos\theta_x \tag{2.8}$$

where n is an integer; λ_x is the X-ray wavelength; d_x is the difference in X-ray path length between two diffracted beams; a_x is the reflecting plane spacing; θ_x is the angle of incidence of the X-rays relative to the normal of the reflecting plane. This criterion can be fulfilled for any lattice plane (e.g. (0 0 1) or (1 1 5) etc...) meaning that there are many different possible target planes which yield different information about the crystal.

2.3.2 Equipment

2.3.2.1 X-Ray production and beam conditioning

X-rays are produced by accelerating electrons towards a metal target, in this case Cu. If the electrons possess sufficient kinetic energy upon impact, then they can displace electrons from the inner shells of the target atoms. The radiation emitted by the outer electrons relaxing into the vacated electron orbitals produces very sharp, intense peaks in the luminescence spectrum of the target material. This produces a divergent, polychromatic source of X-rays. In order to produce collimated, monochromatic X-rays, the beam is diffracted by several beam conditioning crystals, aligned such that the Bragg condition is only fulfilled at all reflections for a single wavelength [47]. In this work the selected wavelength is the standard Cu Kα_1 line at 1.54 Å [48].

2.3.2.2 Double and triple axis designs

XRD systems are classified by the number of axes involved in the measurement. The most common forms are the double and triple axis setups. The double axis setup comprises a beam conditioning section and a wide aperture detector; the wide aperture detector offers increased signal but the signal is integrated over a range of reciprocal space [49]. The alternative is the triple axis setup, which incorporates a detector with a very narrow acceptance angle. This offers increased resolution at the expense of signal intensity. Mapping a sample's XRD pattern in reciprocal space necessitates the use of a triple axis system. Diagrams of the two types of experimental setup are shown in figure 2.23.

The XRD scans in this thesis were performed using the triple axis setup as sufficient signal was detected from the samples in this mode to allow rapid characterisation without the need to increase the detector acceptance angle.

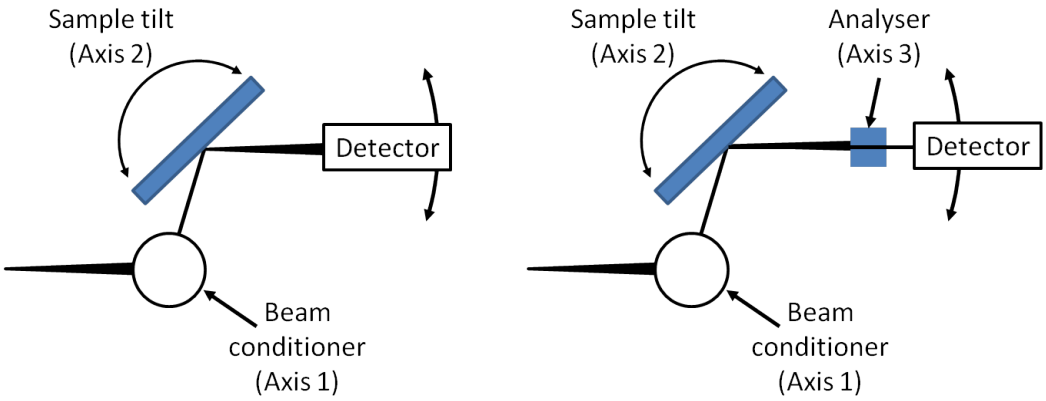

Figure 2.23: Double and triple axis XRD setups. The Axes refer to the parameters which are measured during an experiment. In reality the equipment will have many more axes for sample alignment and positioning etc... but these are not considered as experimental axes.

2.3.3 Bulk spectra

2.3.3.1 Substrate peak

Figure 2.24 shows a rocking curve measurement of a GaAs substrate. In a double axis setup, a rocking curve is measured by fixing the wide angle detector at the expected Bragg angle and tilting ("rocking") the sample in the X-ray beam (axis 2 in figure 2.23). As the triple axis setup was used throughout this work, the small angle detector was moved such that the angle of X-ray incidence and angle of detection with respect to the sample surface were equal. This measurement yields very similar data to the rocking curve for a symmetric scan and is known as an $\omega - 2\theta$ scan. The terms rocking curve and $\omega - 2\theta$ scan will be used interchangably throughout this thesis. The angular position of the peak can be used with Bragg's law and the known wavelength of the incident X-rays to find the lattice parameter of the substrate. The full width at half maximum (FWHM) of the diffracted X-ray peak is indicative of the crystal quality of the layer. There are several factors which can contribute to this broadening and these factors are outlined in section 2.3.3.3.

2.3.3.2 Determination of composition and thickness

Figure 2.25 shows a simulated rocking curve for an InGaAs layer grown on a GaAs substrate. Such a rocking curve can yield information about the composition, thickness and crystal quality of such a layer.

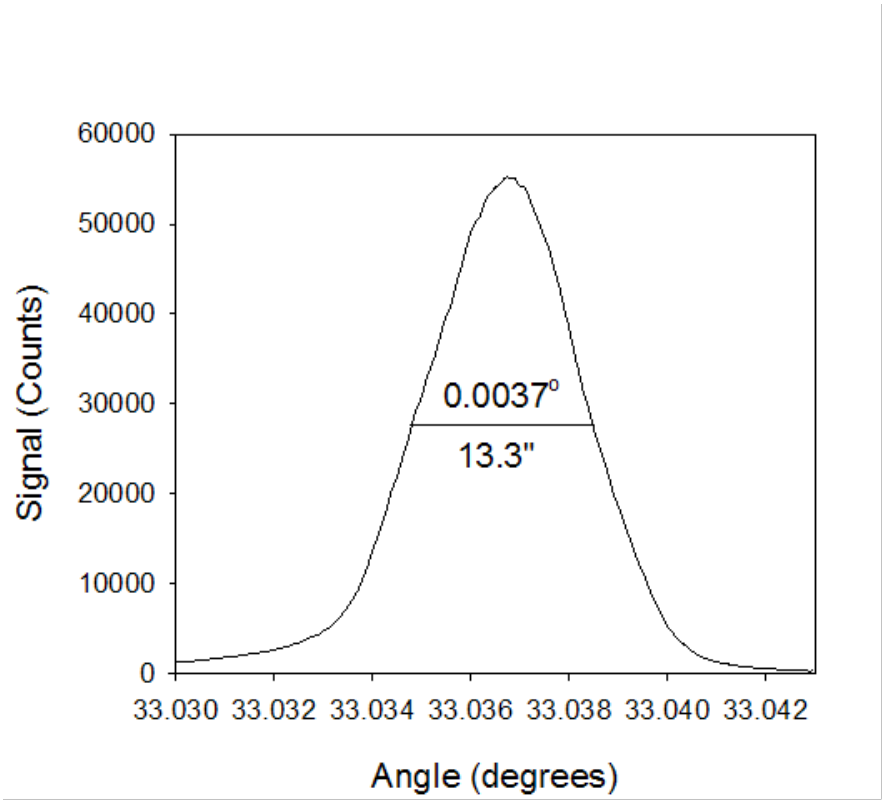

Figure 2.24: Rocking curve of a GaAs substrate. Note the very small FWHM, which is indicative of high crystal quality.

When using the (004) reflection, the peak splitting can be related to the difference in lattice parameter between the substrate and epitaxial layer by the following method: First, rearrange equation 2.8 in terms of a_x, which is identical to the lattice paramter normal to the substrate surface in this case (equation 2.9), then differentiate with respect to θ_x (equation 2.10):

$$a_x = 2n\lambda_x \csc\theta_x \tag{2.9}$$

$$\frac{\delta a_x}{\delta\theta_x} = 2n\lambda_x \frac{\delta \csc\theta_x}{\delta\theta_x} = 2n\lambda_x(-\csc\theta_x \cot\theta_x) \tag{2.10}$$

Thus, if the epitaxial layer is not tilted with respect to the substrate then one can calculate the difference in lattice parameter between the substrate and epitaxial layer simply by finding the peak splitting ($\delta\theta_x$). Using this method one can measure the difference between the

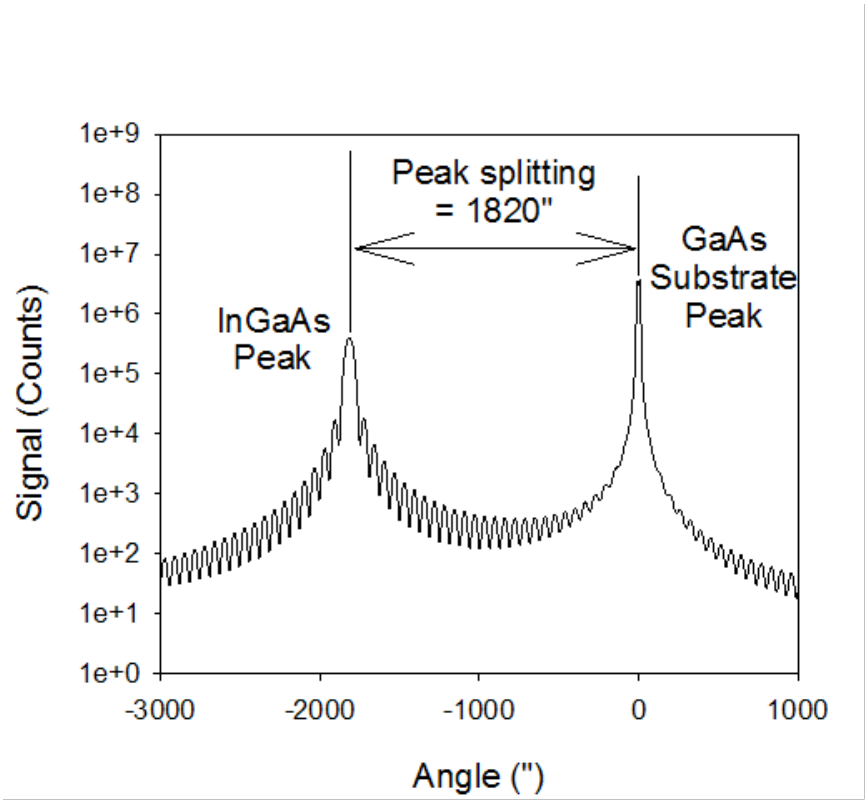

Figure 2.25: Simulated rocking curve of a 300 nm $In_{0.1}Ga_{0.9}As$ layer on top of a GaAs substrate.

substrate and overgrown layer lattice parameters normal to the sample surface. However, the lattice parameter of the epitaxial layer is modified by strain as shown in figure 2.26.

In this example, an epilayer of cubic lattice parameter a_2 has been grown on a substrate of cubic lattice parameter a_1, where $a_2 > a_1$. When grown, the epilayer assumes the lattice parameter of the substrate in the growth plane, compressively straining the layer. The strain is relieved by the epilayer increasing its lattice parameter perpendicular to the growth plane. This is known as tetragonal distortion. If a_2 were smaller than a_1 then the tensile strain in the system would be relieved by the epilayer reducing its lattice parameter perpendicular to the growth plane. In either case the measured epilayer lattice parameter is not the same as that of a free standing lattice of that material. Instead, the peak splitting of the two layers gives the "effective mismatch" as discussed in [47], which is shown in equation 2.11:

$$\frac{\delta a_x}{a_x} = m_x^* \tag{2.11}$$

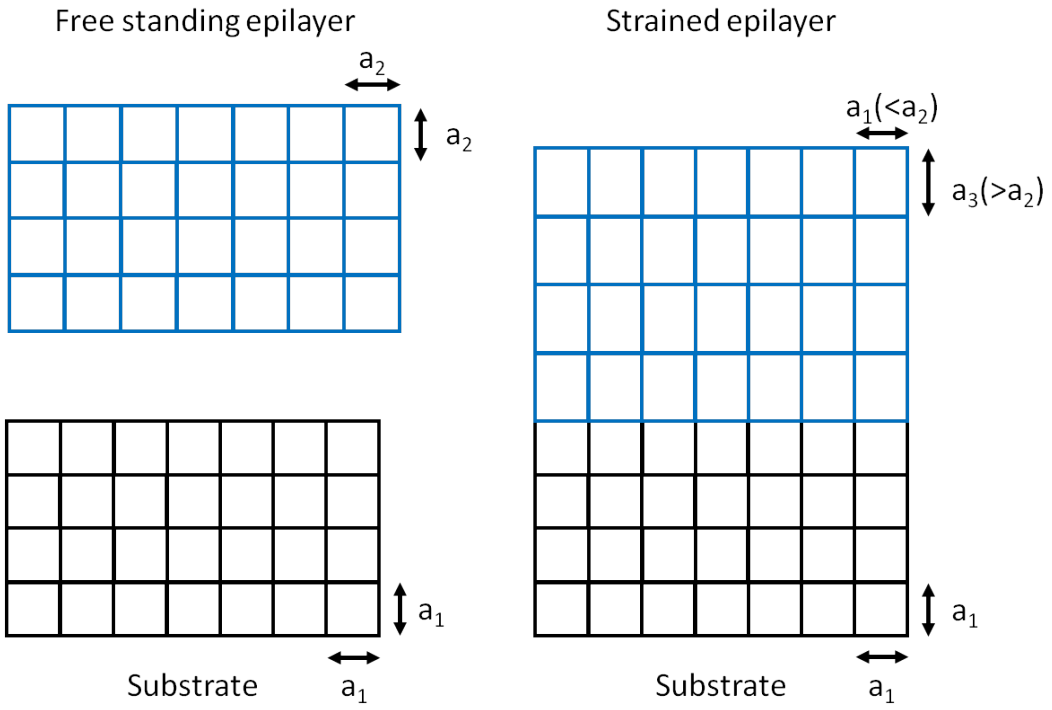

Figure 2.26: When a strained layer is grown on a substrate, it assumes the lattice parameters of the substrate in the growth plane. This causes tetragonal distortion of the epitaxial layer.

where m_x^* is related to the actual mismatch m_x by the Poisson ratio as shown in equation 2.12:

$$m_x = m_x^* \left[\frac{1 + \nu_p}{1 - \nu_p} \right] \tag{2.12}$$

where ν_p is the Poisson ratio, which can vary with material composition.

Having calculated the free standing lattice constant of the epilayer, the composition of that layer can be estimated by using Vegard's law [50]. Vegard's law was introduced in section 1.3.2 and it states that the lattice parameter of a compound varies linearly with composition between its binary endpoints. This is expressed mathematically in equation 2.13:

$$a_{ABC} = x a_{AC} + (1 - x) a_{BC} \tag{2.13}$$

where a_{ABC} is the lattice parameter of compound of material ABC; a_{AC} is the lattice parameter of material AC; a_{BC} is the lattice parameter of material BC; x is the proportion of material AC in the compound. The same principal applies to quaternary compounds.

However, in this case there are two degrees of freedom which determine the lattice constant, meaning that another measurement, such as PL is required in order to determine the composition.

The thickness of an epilayer can be found from the fringes surrounding the bulk peaks using equation 2.14 [49, 51]:

$$\Delta\theta_t = \frac{\lambda_x \sin(\theta_{Br} \pm \phi)}{t_l \sin 2\theta_{Br}} \tag{2.14}$$

where $\Delta\theta_t$ is the fringe spacing, ϕ is the offcut of the layer; t_l is the layer thickness; θ_{Br} is the Bragg angle.

So, for a simple layer it is, in principle, possible to determine the composition and thickness of the layer just from a rocking curve scan.

2.3.3.3 FWHM broadening

The FWHM of the diffracted peaks can yield information about the crystalline quality of a structure [52]. For thin layers, the FWHM of the Bragg peaks are limited by the thickness of the layers [52, 53]. However, for thicker layers the Bragg peak FWHM are limited by other factors such as individual crystal defects with strain fields which do not overlap and inhomogeneous strain [52]. Both of these effects cause inhomogeneity of the lattice constant throughout the layer, broadening the peak as the incident X-rays cover a large area of the sample. These effects are also indicative of strain relaxation within the sample.

2.3.4 Superlattice spectra

Superlattices (SLs) produce very distinctive rocking curves, as seen in figure 2.27.

Provided that the SL is thicker than ~ 300 nm there are several parameters which can, in principle, be gathered from a SL rocking curve without fitting using dynamical theory [49].

The SL can be considered as a one dimensional repeating structure. As such it will have an associated one dimensional reciprocal space structure as shown in figure 2.28.

The SL peaks shown in figure 2.27 are explained by this reciprocal space pattern. The larger the period of the SL, the more closely spaced the reciprocal lattice points are and the smaller the splitting between the SL peaks in the rocking curve. The period of the SL can

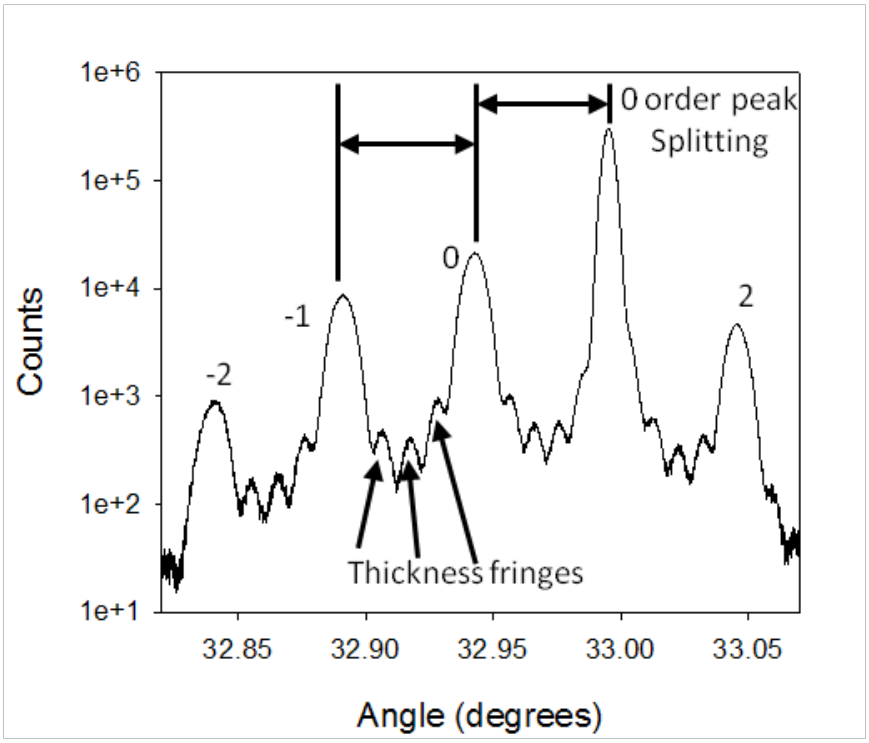

Figure 2.27: Rocking curve from a 5 period AlAs/GaAs SL. The SL peaks are labelled with their peak numbers.

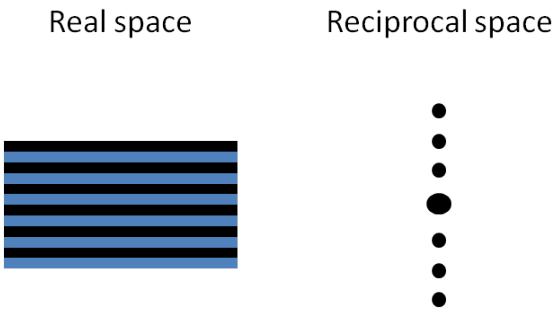

Figure 2.28: Real and reciprocal space representaions of a SL.

be determined using equation 2.15 [47]:

$$\Delta\theta_{SL} = \frac{\lambda_x \sin(\theta_{Br} \pm \phi)}{t_{SL} \sin 2\theta_{Br}} \tag{2.15}$$

where $\Delta\theta_{SL}$ is the SL fringe spacing; t_{SL} is the periodicity of the SL.

The equation for the total thickness of the layer is still valid so the number of periods of a SL can be determined using equations 2.14 and 2.15 as follows:

$$N = \frac{t_l}{t_{SL}} = \frac{\left(\frac{\lambda_x \sin(\theta_{Br} \pm \phi)}{\Delta\theta_t \sin 2\theta_{Br}}\right)}{\left(\frac{\lambda_x \sin(\theta_{Br} \pm \phi)}{\Delta\theta_{SL} \sin 2\theta_{Br}}\right)} = \frac{\Delta\theta_{SL}}{\Delta\theta_t} \tag{2.16}$$

2.3.5 Modelling XRD curves

The above methods of calculating parameters directly from the XRD curve of a sample provide reasonable estimates but do not take into account the full dynamical diffraction from a complicated structure. Therefore, the most reasonable approach in most cases is to simulate the sample structure using specialised XRD software [49]. Simulating XRD data is a powerful way of determining the structure and composition of a sample. It is necessary to use the dynamical treatment of Takagi and Taupin [54, 55] to simulate a rocking curve for a defined structure and to iterate the parameters of that structure to match the measured rocking curve.

2.3.6 Asymmetric reflections

It is sometimes impossible to determine all of the necessary information about a sample using a single rocking curve. For example, if a sample has relaxed with respect to the substrate then the method of deriving the composition as mentioned in section 2.3.3.2 becomes invalid. In this case it is necessary to take two measurements to determine the level of relaxation and the composition of the layer. By taking a symmetric reflection (e.g. 0 0 4) and an asymmetric reflection (e.g. 5 1 1), one can determine the size and shape of the unit cell and, therefore, the extent of the relaxation within the structure.

2.3.7 Reciprocal space maps

It is sometimes instructive to take a reciprocal space map (RSM) of a sample. An RSM is produced by taking many $\omega - 2\theta$ scans around the substrate peak with small offsets between ω and 2θ. Thus, if the epilayer has relaxed and is tilted with respect to the substrate then this tilting will manifest as an offset between the substrate and epilayer peaks in ω [49].

2.4 Nomarski digital interference contrast microscopy

Nomarski digital interference constrast microscopy is an optical imaging technique that highlights regions of gradiented optical path length on a sample [56]. The principle of operation of a Nomarski microscope is shown in figure 2.29 and described below.

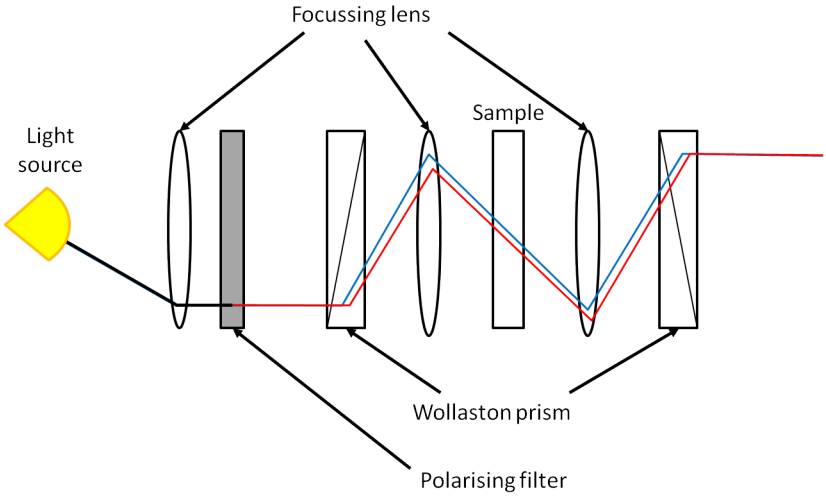

Figure 2.29: The optics involved in a Nomarski microscope. The red and blue lines represent light of 0 and 90 ° polarisation. Note that they are spacially separated before passing through the sample, so the way in which they interfere when recombined depends on the thickness and refractive index variation across that section of the sample.

A light source produces unpolarised light which is then polarised at 45 ° by the first polarising filter. This light is then passed through a Wollaston prism which separates the light into two beams, one 0 ° polarised and the other 90 ° polarised. The two beams are spacially separated by the Wollaston prism and focussed onto the sample. The two beams pass through the sample in close proximity ($\sim 0.2\,\mu$m) to each other. After passing through the sample the light is recombined using the reverse of the process described above. As the two components of the light travel along different paths through the sample, any difference in sample thickness or refractive index along the two paths will change the phase of the recombining light and cause interference. The resulting image highlights local variations in sample thickness and refractive index and appears as high contrast image of an obliquely illuminated three dimentional surface. While the image produced is not necessarily an accurate representation of the topography of the surface, it does provide a measure of the sample's compositional uniformity and surface roughness.

2.5 Transmission electron microscopy

Transmission electron microscopy (TEM) is a destructive imaging technique which can yield extremely high resolution images of a sample [57]. Prior to imaging, the sample must be thinned to a thickness of a few nm. This is achieved by thinning the sample into a wedge shape, meaning that the thinning need not be controlled to nm precision as the range of thicknesses across the sample will provide one region of the sample at the correct thickness. There are several types of measurements, some of which give atomic resolution over a very small area and others which give lower resolution over a larger area. In this work the lower resolution bright field (BF) and dark field (DF) measurement types were employed. The sample is mounted in a vacuum chamber and illuminated by a beam of electrons. The electron beam is transmitted through the sample and monitored using a phosphorescent screen or charge coupled device. The measurement is either BF or DF depending on where the electron beam is observed. This is shown in figure 2.30. In the BF position the detector measures the attenuation of the transmitted electron beam, in the DF position it measures the scattering of the electron beam. In both cases the scattering is proportional to the atomic number of the atoms within the sample. TEM can be used to directly observe defect densities and layer quality in samples.

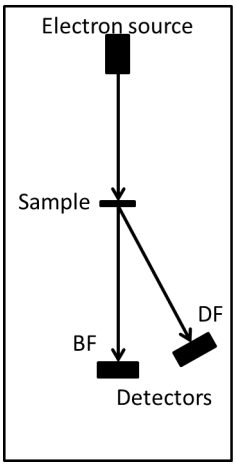

Figure 2.30: Cross-section of a transmission electron microscope.

Bibliography

[1] A. Cho and J. Arthur. Molecular beam epitaxy. *Progress in Solid State Chemistry*, 10:157–191, 1975.

[2] B. A. Joyce. Molecular beam epitaxy. *Reports on Progress in Physics*, 48(12):1637, 1985.

[3] A. G. Thompson, R. A. Stall, W. Kroll, E. Armour, C. Beckham, P. Zawadzki, L. Aina, and K. Siepel. Large scale manufacturing of compound semiconductors by MOVPE. *Journal of Crystal Growth*, 170(1):92–96, 1997.

[4] F. W. Smith, A. R. Calawa, C-L. Chen, M. J. Manfra, and L. J. Mahoney. New MBE buffer used to eliminate backgating in GaAs MESFETs. *Electron Device Letters, IEEE*, 9(2):77–80, 1988.

[5] S. Tixier, M. Adamcyk, T. Tiedje, S. Francoeur, A. Mascarenhas, P. Wei, and F. Schiettekatte. Molecular beam epitaxy growth of $GaAs_{1-x}Bi_x$. *Applied Physics Letters*, 82(14):2245–2247, 2003.

[6] K. Barnham and D. Vvedensky. *Low-dimensional semiconductor structures: fundamentals and device applications*. Cambridge University Press, 2008.

[7] F. C. Frank and Jan. H. van der Merwe. One-dimensional dislocations. I. Static theory. *Proceedings of the Royal Society of London. Series A. Mathematical and Physical Sciences*, 198(1053):205–216, 1949.

[8] S. C. Seel, C. V. Thompson, S. J. Hearne, and J. A. Floro. Tensile stress evolution during deposition of Volmer-Weber thin films. *Journal of Applied Physics*, 88(12):7079–7088, 2000.

[9] Y-W. Mo, D. E. Savage, B. S. Swartzentruber, and M. G. Lagally. Kinetic pathway in Stranski-Krastanov growth of Ge on Si (001). *Physical Review Letters*, 65(8):1020, 1990.

[10] A. G. Cullis, D. J. Norris, M. A. Migliorato, and M. Hopkinson. Surface elemental segregation and the Stranski-Krastanow epitaxial islanding transition. *Applied Surface Science*, 244(1):65–70, 2005.

[11] A-B. Chen, A. Sher, and M. A. Berding. Semiconductor alloy theory: Internal strain energy and bulk modulus. *Physical Review B*, 37(11):6285, 1988.

[12] M. Copel, M. C. Reuter, E. Kaxiras, and R. M. Tromp. Surfactants in epitaxial growth. *Physical Review Letters*, 63(6):632, 1989.

[13] J. Massies and N. Grandjean. Surfactant effect on the surface diffusion length in epitaxial growth. *Physical Review B*, 48(11):8502, 1993.

[14] G. Bauer and G. Springholz. Molecular beam epitaxyaspects and applications. *Vacuum*, 43(5):357–365, 1992.

[15] F. Bastiman. *In Situ Surface Studies of III-V Semiconductor Compounds*. PhD thesis, University of Sheffield, June 2010.

[16] Dr. Eberl MBE-Komponenten GmbH. Effusion cells. Web page, September 2014. www.mbe-komponenten.de/products/mbe-components/effusion-cells.php.

[17] Evan. H. C. Parker. *The technology and physics of molecular beam epitaxy*. Plenum Press New York, 1985.

[18] M. D. Pashley. Electron counting model and its application to island structures on molecular-beam epitaxy grown GaAs (001) and ZnSe (001). *Physical Review B*, 40(15):10481, 1989.

[19] C. B. Duke. Semiconductor surface reconstruction: The structural chemistry of two-dimensional surface compounds. *Chemical Reviews*, 96(4):1237–1260, 1996.

[20] V. P. LaBella, M. R. Krause, Z. Ding, and P. M. Thibado. Arsenic-rich GaAs (0 0 1) surface structure. *Surface Science Reports*, 60(1):1–53, 2005.

[21] A. Ohtake and N. Koguchi. Two types of structures for the GaAs (001)-c (4× 4) surface. *Applied Physics Letters*, 83(25):5193–5195, 2003.

[22] V. P. LaBella, H. Yang, D. W. Bullock, P. M. Thibado, P. Kratzer, and M. Scheffler. Atomic structure of the GaAs (001)-(2× 4) surface resolved using scanning tunneling microscopy and first-principles theory. *Physical Review Letters*, 83(15):2989, 1999.

[23] D. K. Biegelsen, R. D. Bringans, J. E. Northrup, and L-E. Swartz. Surface reconstructions of GaAs (100) observed by scanning tunneling microscopy. *Physical Review B*, 41(9):5701, 1990.

[24] B. G. Orr, C. W. Snyder, and M. Johnson. A combined molecular-beam epitaxy and scanning tunneling microscopy system. *Review of Scientific Instruments*, 62(6):1400–1403, 1991.

[25] M. Itoh, G. R. Bell, A. R. Avery, T. S. Jones, B. A. Joyce, and D. D. Vvedensky. Island nucleation and growth on reconstructed GaAs (001) surfaces. *Physical Review Letters*, 81(3):633, 1998.

[26] J. H. Neave, B. A. Joyce, P. J. Dobson, and N. Norton. Dynamics of film growth of GaAs by MBE from RHEED observations. *Applied Physics A*, 31(1):1–8, 1983.

[27] P. P. Ewald. Introduction to the dynamical theory of X-ray diffraction. *Acta Crystallographica Section A: Crystal Physics, Diffraction, Theoretical and General Crystallography*, 25(1):103–108, 1969.

[28] J. H. Neave and B. A. Joyce. Structure and stoichiometry of {100} GaAs surfaces during molecular beam epitaxy. *Journal of Crystal Growth*, 44(4):387–397, 1978.

[29] K. Regiński, J. Muszalski, V. V. Preobrazhenskii, and D. I. Lubyshev. Static phase diagrams of reconstructions for MBE-grown GaAs (001) and AlAs (001) surfaces. *Thin Solid Films*, 267(1):54–57, 1995.

[30] M. C. Gallagher, R. H. Prince, and R. F. Willis. On the atomic structure and electronic properties of decapped GaAs (001)(2× 4) surfaces. *Surface Science*, 275(1):31–40, 1992.

[31] U. Resch, N. Esser, Y. S. Raptis, W. Richter, J. Wasserfall, A. Förster, and D. I. Westwood. Arsenic passivation of MBE grown GaAs (100): structural and electronic properties of the decapped surfaces. *Surface Science*, 269:797–803, 1992.

[32] R. W. Bernstein, A. Borg, H. Husby, B-O. Fimland, and J. K. Grepstad. Capping and decapping of MBE grown GaAs(001), $Al_{0.5}Ga_{0.5}As$(001), and AlAs(001) investigated with ASP, PES, LEED, and RHEED. *Applied Surface Science*, 56-58, Part 1(0):74 – 80, 1992.

[33] C. T. Foxon and B. A. Joyce. Interaction kinetics of As_4 and Ga on {100} GaAs surfaces using a modulated molecular beam technique. *Surface Science*, 50(2):434–450, 1975.

[34] T. H. Chiu and S. N. G. Chu. Is the cation sticking coefficient unity in molecular beam epitaxy at low temperature? *Applied Physics Letters*, 57(14):1425–1427, 1990.

[35] C. T. Foxon and B. A. Joyce. Interaction kinetics of As_2 and Ga on {100} gaas surfaces. *Surface Science*, 64(1):293–304, 1977.

[36] A. Y. Cho. Bonding direction and surface-structure orientation on GaAs (001). *Journal of Applied Physics*, 47(7):2841–2843, 1976.

[37] C. T. Foxon, J. A. Harvey, and B. A. Joyce. The evaporation of GaAs under equilibrium and non-equilibrium conditions using a modulated beam technique. *Journal of Physics and Chemistry of Solids*, 34(10):1693–1701, 1973.

[38] Z. R. Wasilewski, J-M. Baribeau, M. Beaulieu, X. Wu, and G. I. Sproule. Studies of oxide desorption from GaAs substrates via Ga_2O_3 to Ga_2O conversion by exposure to Ga flux. *Journal of Vacuum Science & Technology B*, 22(3):1534–1538, 2004.

[39] D. A. Allwood, S. Cox, N. J. Mason, R. Palmer, R. Young, and P. J. Walker. Monitoring epiready semiconductor wafers. *Thin Solid Films*, 412(1):76–83, 2002.

[40] D. Allwood, N. Mason, A. Mowbray, and R. Palmer. MOVPE homoepitaxial growth used to study the effect of aging and chemical treatment on GaAs substrates. *Journal of Crystal Growth*, 248:108–113, 2003.

[41] Y. Asaoka. Desorption process of GaAs surface native oxide controlled by direct Ga-beam irradiation. *Journal of Crystal Growth*, 251(1):40–45, 2003.

[42] F. Bastiman, R. Hogg, M. Skolnick, A. G. Cullis, and M. Hopkinson. Temperature dependence of Ga-assisted oxide desorption on GaAs (001). In *Journal of Physics: Conference Series*, volume 209, page 012066. IOP Publishing, 2010.

[43] M. A. Fox. *Optical properties of solids*. Oxford University Press, 2 edition, 2010.

[44] P. T. Landsberg. Non-radiative transitions in semiconductors. *physica Status Solidi (b)*, 41(2):457–489, 1970.

[45] W. J. Bartels, J. Hornstra, and D. J. W. Lobeek. X-ray diffraction of multilayers and superlattices. *Acta Crystallographica Section A: Foundations of Crystallography*, 42(6):539–545, 1986.

[46] W. L. Bragg. The diffraction of short electromagnetic waves by a crystal. In *Proceedings of the Cambridge Philosophical Society*, volume 17, page 4, 1913.

[47] D. K. Bowen and B. K. Tanner. *High resolution X-ray diffractometry and topography*. CRC Press, 2005.

[48] P. J. Mohr and B. N. Taylor. CODATA recommended values of the fundamental physical constants: 1998. *Reviews of Modern Physics*, 72(2):351, 2000.

[49] P. F. Fewster. X-ray diffraction from low-dimensional structures. *Semiconductor Science and Technology*, 8(11):1915, 1993.

[50] L. Vegard. Die konstitution der mischkristalle und die raumfüllung der atome. *Zeitschrift für Physik A Hadrons and Nuclei*, 5(1):17–26, 1921.

[51] W. T. Stacy and M. M. Janssen. X-ray pendellösung in garnet epitaxial layers. *Journal of Crystal Growth*, 27:282–286, 1974.

[52] C. Ryang Wie. High resolution X-ray diffraction characterization of semiconductor structures. *Materials Science and Engineering: R: Reports*, 13(1):1–56, 1994.

[53] P. F. Fewster and C. J. Curling. Composition and lattice-mismatch measurement of thin semiconductor layers by x-ray diffraction. *Journal of Applied Physics*, 62(10):4154–4158, 1987.

[54] S. Takagi. Dynamical theory of diffraction applicable to crystals with any kind of small distortion. *Acta Crystallographica*, 15(12):1311–1312, 1962.

[55] S. Takagi. A dynamical theory of diffraction for a distorted crystal. *Journal of the Physical Society of Japan*, 26(5):1239–1253, 1969.

[56] W. Lang. *Nomarski differential interference-contrast microscopy*. Oberkochen, Carl Zeiss, 1982.

[57] P Goodhew. *General Introduction to Transmission Electron Microscopy (TEM)*, pages 1–19. John Wiley and Sons, Ltd, 2011.

Chapter 3

Growth of bulk GaAsBi using As_2 and As_4

3.1 Introduction

The previous chapters have introduced solar cell device physics, solar cell design and the experimental methods used throughout this work. It was mentioned in sections 1.3.2 and 1.5.7.3 that GaAsBi exhibits a large band gap reduction per unit strain and is potentially a strong candidate material for multijunction photovoltaics. In this chapter the characteristics and growth of GaAsBi are discussed in detail and an investigation of the growth temperature, As flux and As species dependence of Bi incorporation into GaAs is presented.

3.1.1 Review of previous bulk GaAsBi growth

Incorporating Bi into GaAs could be expected to be difficult; Bi has been used as a surfactant for GaAs growth for a long time because of its very low incorporation at standard MBE growth temperatures [1–3].

The first report of GaAsBi growth in the literature was in 1998 when Oe et al. [4] produced GaAsBi by MOVPE. The first report of GaAsBi grown by MBE was by Tixier et al. in 2003 [5]. In that work, samples with up to 3.1 % Bi were grown and their Bi contents were measured by Rutherford back-scattering. By correlating the lattice constants, as determined by XRD, with the Bi contents, a GaBi lattice constant of 6.33 Å was estimated. GaBi is

expected to be semi-metallic [6, 7] and, to date, has never been successfully synthesised. Over the past eleven years, there have been many demonstrations of the MBE growth of GaAsBi [8–19] and several attempts to estimate the GaBi lattice constant. These estimates are shown in table 3.1. It is not clear which of the estimates in table 3.1 is the most accurate. The value marked with * was used throughout this thesis for consistency.

Table 3.1: Estimates of the GaBi lattice constant

Reference	Type of estimate	Estimated lattice constant (Å)
Janotti 2002 [6]	Theoretical	6.324
Tixier 2003 [5]	Experimental	6.33
Ferhat 2006 [20]	Theoretical	6.46
Ferhat 2006 [20]	Theoretical	6.31
Takehara 2006 [21]	Experimental	6.23
Achour 2008 [22]	Theoretical	6.304
Achour 2008 [22]*	Theoretical	6.275
Belabbes 2008 [23]	Theoretical	6.186
Madouri 2008 [7]	Theoretical	6.442
Abdiche 2010 [24]	Theoretical	6.46
Abdiche 2010 [24]	Theoretical	6.30
Mbarki 2011 [25]	Theoretical	6.45
Usman 2011 [26]	Theoretical	6.328
Rajpalke 2014 [27]	Experimental	6.272

To date, the largest Bi fraction incorporated into GaAs is $\sim 20\,\%$ [12]. The difficulties involved in growing good quality GaAsBi are twofold. Firstly, the miscibility gap between GaAs and GaBi requires that the samples be grown at very low temperatures ($< 450\,^{\circ}$C [5]), with higher Bi fractions requiring even lower temperatures. The second issue is that near stoichiometric flux ratios must be used during growth [10, 12, 18]. The incorporation of Bi is dramatically reduced by an excess As flux, such as is used for conventional arsenide based III-V epitaxy . As such, the flux ratio during growth must be carefully controlled to maximise the incorporation of Bi without allowing the formation of Ga or Bi droplets - a problem which is commonly encountered when using a low As flux during growth [14, 28, 29].

The effects of Bi incorporation on the band structure of GaAs and its potential technological applications will be overviewed in sections 3.1.2.1 - 3.1.2.3. The growth models and previous work investigating growth parameter optimisation for GaAsBi will be discussed in section 3.1.3.

3.1.2 Band Structure of GaAsBi

3.1.2.1 The modified valence band anticrossing model

The anomalous bowing coefficient of GaAsBi was mentioned in section 1.3.2; this bowing coefficient can be expained using the band anticrossing model as follows. The incorporation of Bi into GaAs introduces localised states into the band structure very close to the valence band edge [30–32]. The hybridisation of these states causes the valence band edges to split into two bands [33], resulting in E+ and E- variants of the heavy-hole, light-hole and spin-orbit (SO) bands. This lifting of the valence band degeneracy causes a dramatic reduction in the band gap of GaAsBi. This model was named the valence band anticrossing model (VBAC) after the analogous band anticrossing model which is used to describe the effect of localised N induced states on the conduction band of GaAs [34]. Initially it was believed that the large reduction in the band gap of GaAs with Bi incorporation (70 - 90 meV/% [4, 5, 17, 18, 35–39]) could be entirely attributed to the VBAC interaction with a negligible contribution from the offsetting of the conduction band. However, more recent work has shown that this model overestimates the band gap of alloys with large Bi fractions [40]. The current consensus is that the effect of Bi on the band gap of GaAs must be modelled with a modified form of the VBAC (mVBAC) which takes into account a linear reduction in conduction band energy of ~ 28 meV/% [26, 40].

For GaAs based ternaries, the rate of change of band gap per unit strain on a GaAs substrate is 750 meV/% strain with Bi [36], 750 meV/% strain with N [41] and 200 meV/% strain with In [42]. The dramatic reduction in band gap with strain suggests that GaAsBi is a promising material for photovoltaic applications.

3.1.2.2 Temperature dependence of the GaAsBi band structure

The temperature dependence of the band gap of GaAsBi has been shown to be weak compared to that of GaAs, with estimates of the band gap temperature coefficient ranging from -0.12 meV/K to 0.4 meV/K [36–38, 43–46]. This behaviour, along with the relatively temperature insensitive refractive index of GaAsBi [47], makes it a very promising material for optical telecommunications.

3.1.2.3 Effect of Bi incorporation on the spin-orbit (SO) band

The calculated SO splitting of GaBi is 2.2 eV [31], which is very large compared to that of GaAs (0.34 eV). The rate of change of the SO splitting with incorporation of Bi into GaAs has been determined to be 80 meV/% for Bi fractions less than 2 % [48]. This implies a very large SO bowing parameter of -6 eV. Further work has determined the spin orbit splitting out to around 10 % [33, 49, 50] at which point it is approximately 0.8 eV. At this fraction, the band gap and SO splitting are equal as shown in figure 3.1.

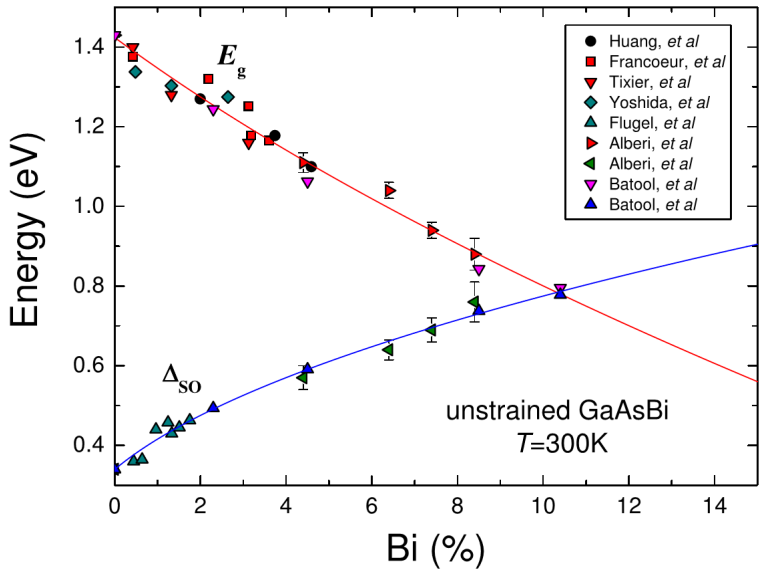

Figure 3.1: The modification of the band gap and SO splitting of GaAs with Bi incorporation, based on several reports in the literature.
Reprinted with permission from: [S. J. Sweeney and S. R. Jin. Bismide-nitride alloys: promising for efficient light emitting devices in the near-and mid-infrared. *Journal of Applied Physics*, 113(4):043110, 2013] Copyright [2013], AIP Publishing LLC.

When the SO splitting of a material exceeds its band gap, the Auger loss mechanism mentioned in section 2.2.2 is effectively suppressed as shown in figure 3.2.

3.1.3 Growth models

The complicated nature of GaAsBi growth means that there are very few models which describe the incorporation of Bi into GaAs. The most comprehensive models are those by Lu et al. [18] and Lewis et al. [12], which will be discussed in section 3.1.3.1. These models advocate stoichiometric flux ratios for the growth of high Bi content GaAsBi layers.

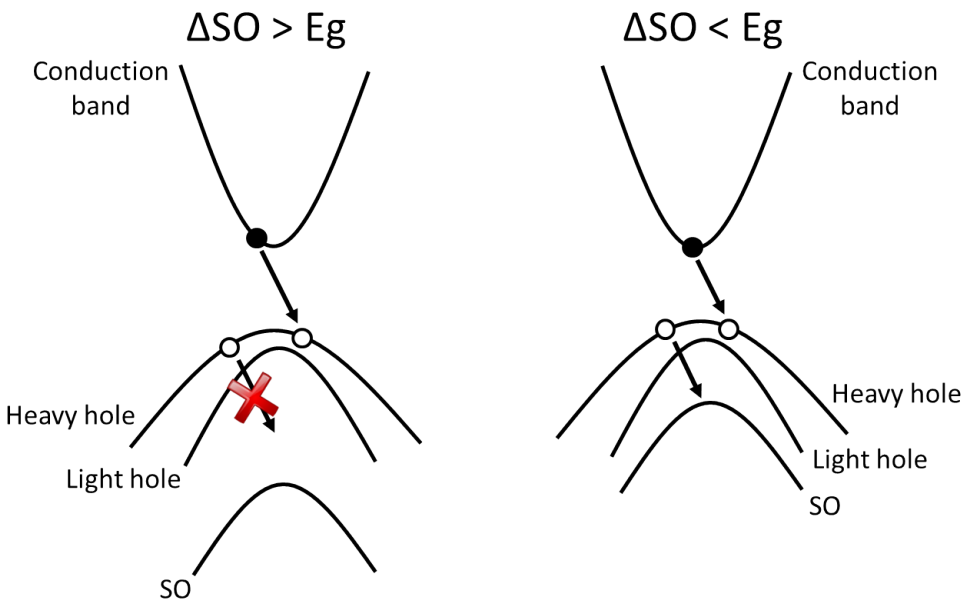

Figure 3.2: Illustration of the suppression of Auger recombination. When the SO splitting is larger than the band gap (left) there are no available states in the SO band accessible which can conserve energy during the Auger recombination process. This lack of available states is highlighted by the red cross in the diagram. Adapted from [49].

However, the optical quality of the layers is not discussed in these papers. Therefore, other work describing the optimum conditions for maximising material optical quality will be discussed in section 3.1.3.2.

3.1.3.1 The Lu et al. and Lewis et al. growth models

The model produced by Lu et al. [18] suggests that Bi forms a surface layer and then incorporates into the lattice from this surface layer. However, the Lu model fails to adequately describe the As flux dependence of Bi incorporation. According to the Lu model, Bi incorporation should be inversely proportional to As flux; however, this effect is not observed at low As fluxes. Lewis et al. [12] proposed that Bi incorporation is purely limited by the relative surface coverages of Bi, Ga and As. They suggest that the rate of change of Bi incorporation with time can be described by equation 3.1:

$$\frac{dx}{dt} \propto \theta_{Ga}\theta_{Bi} - a_1 x F_{Ga} - a_2 x e^{\left(\frac{-U_1}{k_B T}\right)} \tag{3.1}$$

where x is the Bi incorporation, assumed to be equal to the proportion of Bi in the termination layer; θ_{Ga} is the proportion of Ga in the termination layer; θ_{Bi} is the surface Bi coverage (which is assumed to lie on top of the termination layer); a_1 and a_2 are constants; F_{Ga} is the Ga flux; U_1 is the free energy difference between an incorporated Bi atom and a surfactant Bi atom; T is the sample temperature. The three terms in equation 3.1 are shown in figure 3.3.

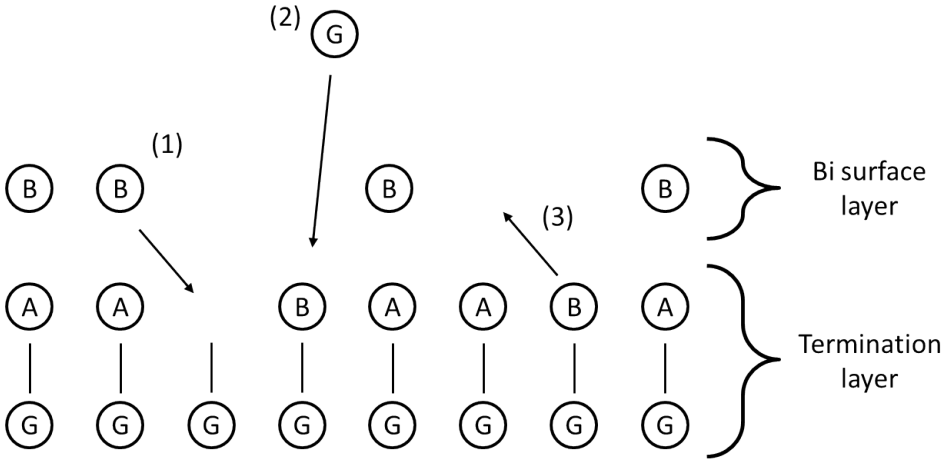

Figure 3.3: The processes considered in the Lewis model: 1) Bi binding to a surface Ga atom. 2) Ga binding to a surface Bi atom. 3) Bi being thermally displaced from the termination layer. Adapted from [12].

The second term in equation 3.1 is ignored in the paper because it is assumed to be much smaller than the other terms. As such, the rate of Bi incorporation in this model is only affected by the following: the probability of a Bi atom in the surface layer encountering a Ga atom in the termination layer and the rate of thermal Bi desorption from the termination layer. In this model, while As does not directly displace Bi from the termination layer, an increased As flux reduces the Ga content of the termination layer and, hence, reduces the Bi content of the sample.

At low temperatures and As fluxes the third term in equation 3.1 becomes very small compared to the first term and the Bi incorporation coefficient approaches unity, more accurately reflecting the observed Bi incorporation. The Bi incorporation coefficient is roughly proportional to the Ga surface coverage which is shown as a function of As:Ga atomic flux ratio in figure 3.4.

Lewis et al. employed XRD to measure the Bi content in their layers. The scans shown

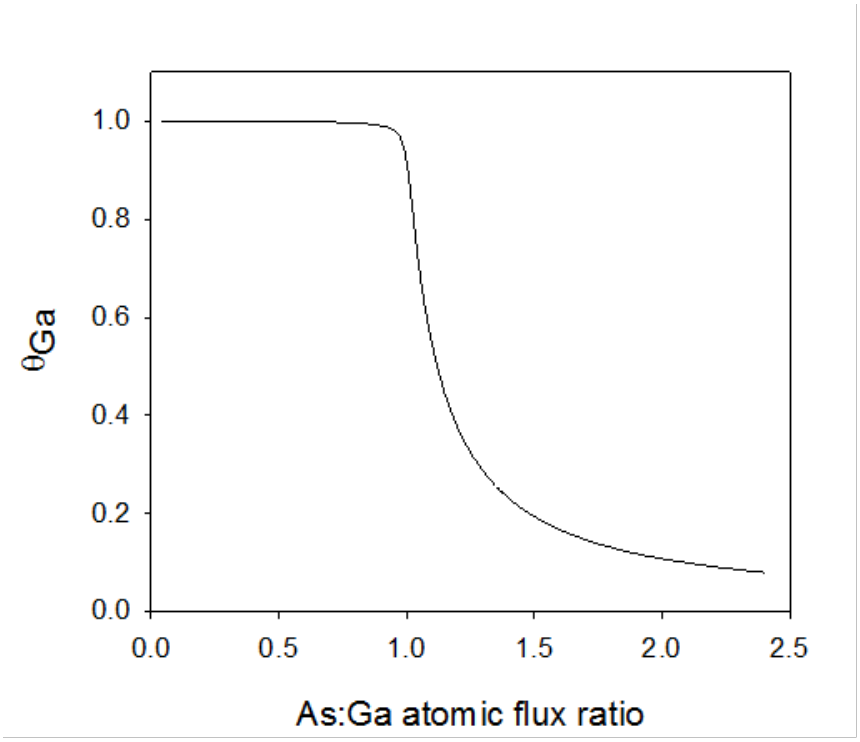

Figure 3.4: Termination layer Ga content as a function of the As:Ga atomic flux ratio. This plot was produced using the equations and parameters in [12].

in their paper exhibit good interference fringes, implying abrupt interfaces for the Bi layer. However, no reference is made to the optical quality of the samples and the formation of surface Bi droplets is noted for samples with near unity Bi incorporation coefficients.

3.1.3.2 The kinetically limited growth regime

In 2012, Ptak et al. [10] published a paper describing the optimum growth parameters for high optical quality GaAsBi. Ptak argued that by growing at a slightly lower temperature than the miscibility limiting temperature for the desired Bi content, growth can proceed in the kinetically limited regime. In this regime the Bi content is proportional to the Bi flux and the Bi incorporation coefficient approaches unity without droplet formation. However, care must be taken to ensure there is an adequate supply of Bi to act as a surfactant and prevent the growth surface from roughening due to the low growth temperature. The onsets of the insufficient flux and droplet formation effects are shown in figure 3.5.

Ptak et al. advocated growing at high growth rates in order to produce the best quality

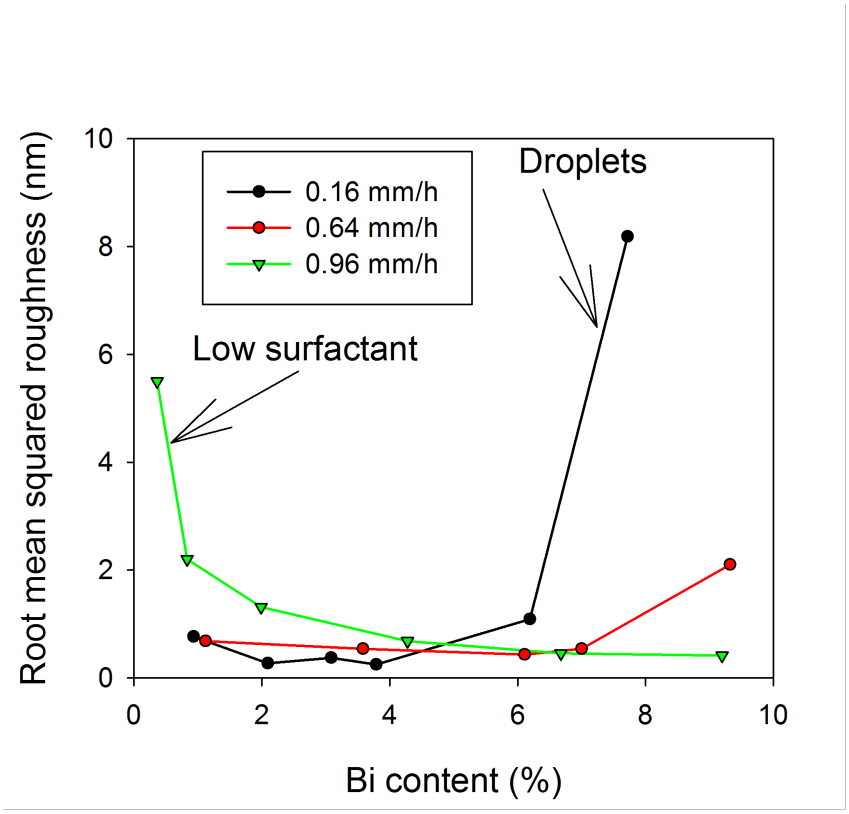

Figure 3.5: The effect of growth rate on surface roughness and droplet formation. The samples grown with a high growth rate and low Bi flux exhibited low Bi contents and high surface roughness as the Bi flux was insufficient to produce the surfactant effect. The samples grown with a low growth rate and a high Bi flux exhibited large Bi contents but also formed surface Bi droplets as the Bi content approached the miscibility limit for the growth temperature. Adapted from [10].

material. This effect is likely due to the fact that the margin for error in Bi flux becomes larger at higher growth rates, making the optimum growth conditions easier to achieve. This is in contrast with the findings of Lu et al. [18] who suggest that low growth rates produce the best samples. These conflicting reports highlight the complicated nature of Bi incorporation.

3.1.4 Surface reconstructions

A common theme throughout the GaAsBi growth literature is the observation that good quality GaAsBi growth requires the surface to exhibit a (2×1) reconstruction [9, 11–13, 15, 51]. This reconstruction is only found at near stoichiometric flux ratios [11] and comprises Bi dimer pairs on the growth surface [15] as shown in figure 3.6.

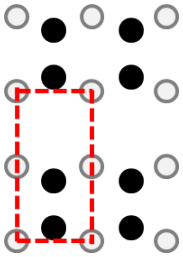

Figure 3.6: The Bi terminated (2×1) reconstruction on GaAs. The white circles represent Ga atoms and the black circles represent Bi atoms. Adapted from [15].

Mapping of the Bi terminated GaAs surface reconstructions was performed by Masnadi-Shirazi et al. [11] and Bastiman et al. [15]. The results are shown in figure 3.7.

The (2×1) reconstruction is only observed on a growing surface. While an early report claimed it was observed as a static reconstruction, the samples in that report were held at moderate temperatures without an incident As flux, meaning that As desorption probably caused the Bi surface layer to come into direct contact with Ga, as in the case of growth [52]. It seems likely that the (2×1) reconstruction is necessary for good quality GaAsBi growth as this reconstruction contains the highest proportion of Bi-Ga bonds on the growth surface.

3.1.5 The effect of thermal annealing on GaAsBi

There have been several studies into thermal annealing of GaAsBi layers. While some groups have investigated rapid thermal annealing [53–56] and others have investigated long term annealing [46, 57–59], there is a consensus that the PL intensity of the samples is improved by up to a factor of 5 for good quality samples. Note that Rodrigo et al. [58] showed an improvement of 120× in their PL intensity with a 3 h anneal at 200 °C; however, the PL signal from their un-annealed sample was very weak and it is likely that a much smaller improvement in PL signal would have been observed for better quality samples.

It has been shown that annealing can improve the Bi homogeneity in GaAsBi samples [55], although it has also been shown that similar improvements can be obtained by optimisation of the growth parameters [56]. The improvement in PL intensity from annealing has been attributed to an improvement of the host GaAs matrix quality rather than an improvement in Bi homogeneity [56].

The diffusion of Bi within GaAsBi/GaAs structures appears to be very small for annealing

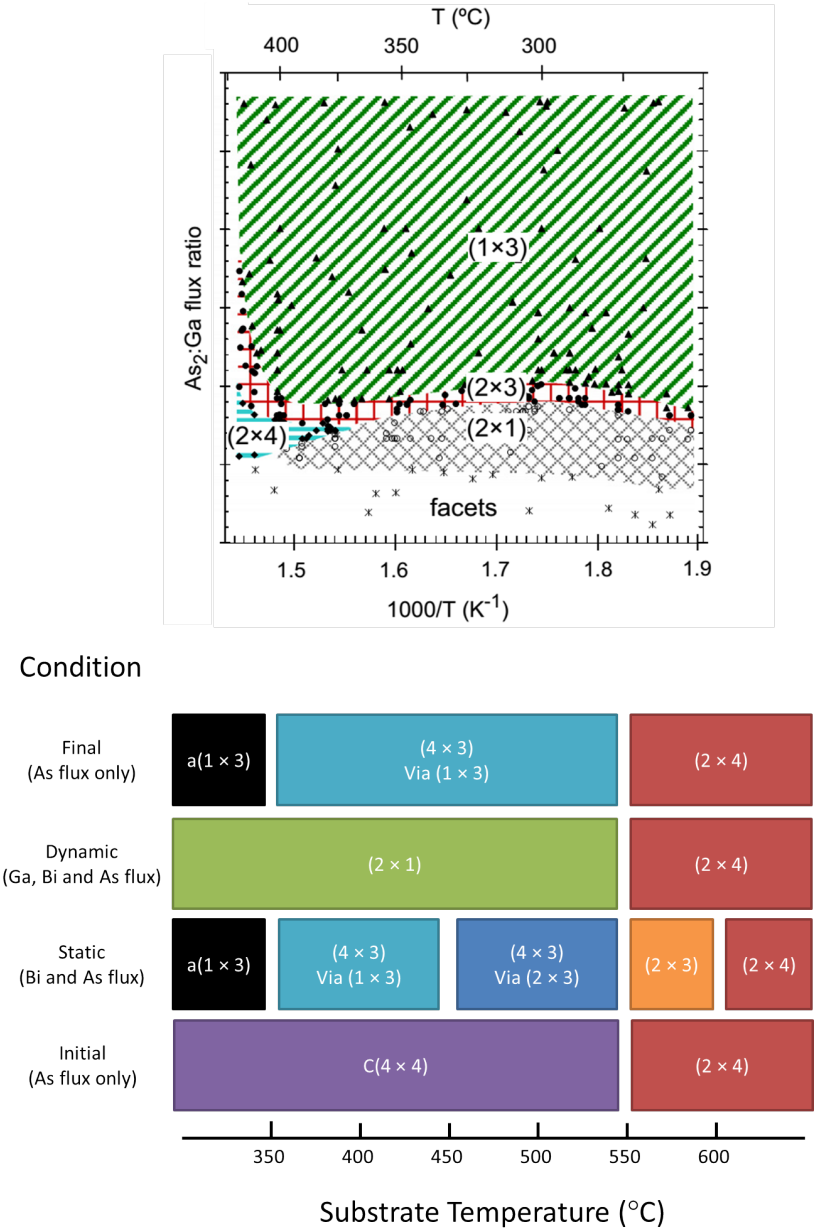

Figure 3.7: Static and dynamic Bi terminated reconstructions on GaAs.
Reprinted from Journal of Crystal Growth, volume 338/1, M. Masnadi-Shirazi, D. A. Beaton, R. B. Lewis, X. Lu, and T. Tiedje, Surface reconstructions during growth of $GaAs_{1-x}Bi_x$ alloys by molecular beam epitaxy, pages 80-84, Copyright (2012), with permission from Elsevier. [11]. Adapted from [15].

temperatures of up to ~ 650 °C as observed by XRD [46, 57]. The optimum temperature for thermal annealing appears to be a function of Bi content. The optimum annealing temperature decreases as the Bi content of the layer increases [56]. This is shown in figure 3.8.

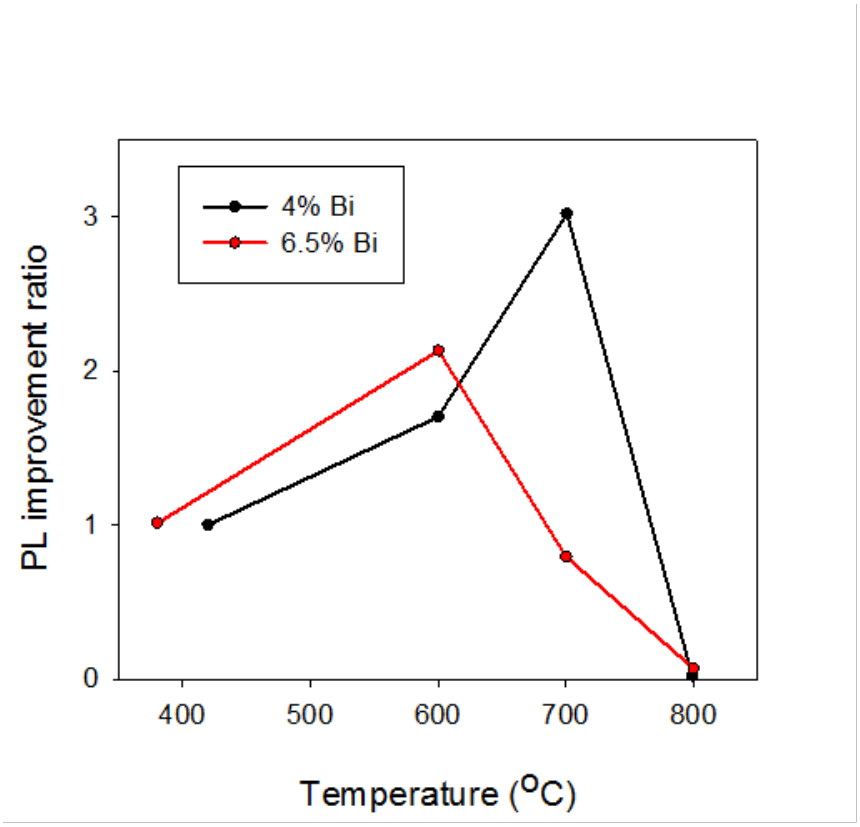

Figure 3.8: The room temperature PL intensity improvement observed as a function of annealing temperature for two different Bi fractions. Adapted from [56].

3.1.6 Effect of As species on the growth of GaAs

Most groups growing GaAsBi use As_2 rather than As_4. This is because As_2 has been shown to produce better quality GaAs at low growth temperatures [60], leading to the suppression of the EL2 defect. However, the dependence of Bi incorporation on As:Ga beam equivalent pressure ratio has been shown to be different for samples grown using As_2 and As_4 [14]. Specifically, the range of As_4 beam equivalent pressures that allows significant Bi incorporation has been shown to be much larger than that of As_2. This observation is difficult to justify as, throughout the literature, elemental fluxes during growth are quoted in a variety of different units. Sometimes fluxes are quoted in atoms.nm^{-2}s^{-1} [61], sometimes in mBar [62] or, in some cases, not directly mentioned at all [10]. As a result it was not clear whether the Bi incorporation dynamics were truly different when growing with As_2 compared to As_4. The work presented in this chapter aimed to clarify this apparent discrepancy and investigate the growth parameters of this material system.

3.1.7 Chapter layout

The aim of the work in this chapter was to ascertain the relationship between the maximum Bi content achievable and sample growth temperature. Also, to explore and justify the effect of As species on Bi incorporation and sample characteristics. Improving our understanding of the growth conditions necessary for good quality GaAsBi will enable this technology to make an impact as a material for solar cells and other devices.

3.2 Growth of bulk GaAsBi

3.2.1 Experimental details

The samples grown in this work were grown on undoped semi-insulating on-axis $\pm 0.1\,^{\circ}$ (001) GaAs substrates using a Ga flux of 6.26 atoms.nm^{-2}s^{-1}, equivalent to 1 μm/h. The clean-up procedure prior to growth is discussed in section 2.1.10. After thermal oxide desorption, a 100 nm GaAs buffer was grown using As_2. Upon completion of the buffer growth the sample was annealed at 610 °C for 20 minutes before the sample temperature was lowered to the desired growth temperature. The required As flux and species were selected by varying the As needle valve position and changing the As cracker temperature. The reason that the buffer growth was completed using As_2 is that it has been shown that GaAs produced by MBE using As_2 exhibits better optical and electrical properties than that grown using As_4 [60, 63]. Prior to GaAsBi growth the sample surface was exposed to a Bi flux for 30 s. During this time the surface reconstruction as observed by RHEED changed from $c(4\times4)$ or (2×4) to $(n\times3)$ or $c(n\times8)$. This transition is indicative of the formation of a surface layer of Bi [15]. The justification for this Bi pre-layer is that other groups have noted that the onset of Bi incorporation is slowed by the need to produce a surface Bi coverage before the maximum Bi incorporation can be realised [13, 18]. The Bi pre-layer was left for 30 s to equilibrate before the Ga and Bi shutters were opened and growth was commenced. The Bi flux used throughout this work was 0.31 atoms.nm^{-2}s^{-1}. Some samples were grown with a Bi flux of 0.49 atoms.nm^{-2}s^{-1} for comparison and these samples are indicated in the text and figure captions. The bismide layers grown in these samples were 100 nm thick. After bismide growth the sample was capped with 20 nm of GaAs using the same substrate

temperature and As species as the bismide layer. The same temperature was used to protect the sample from in situ annealing; such annealing has been shown to alter the optical quality of GaAsBi as discussed in section 3.1.5 and would obfuscate any conclusions drawn from the PL intensity of the samples grown in this work. The structure of the samples grown during this work is shown in figure 3.9.

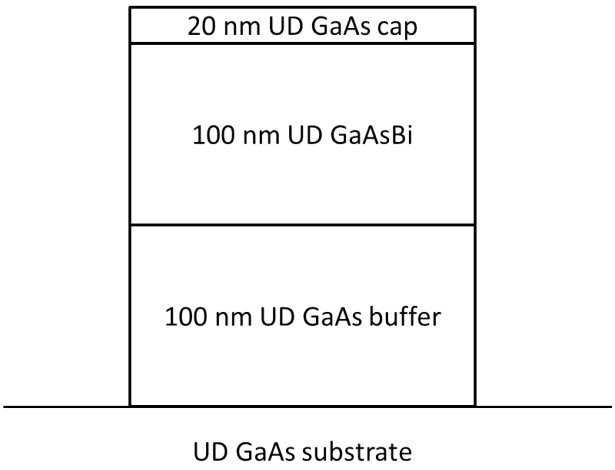

Figure 3.9: Sample structure used throughout this work. UD denotes undoped layers.

3.2.1.1 Sample characterisation

XRD The samples were initially characterised using XRD. The XRD measured spectra were then compared with simulated spectra assuming an abrupt GaAs-GaAsBi interface and a constant Bi content throughout the bismide layers. A typical example of this comparison is shown in figure 3.10.

It is obvious from the poor fit of the experimental and simulated data that the model does not accurately reflect the structure of the layer. This issue has been previously reported in the literature [64] although the exact cause for the non-uniformity of the GaAsBi layers remains unclear. A recent report by Reyes et al. [65] suggests that the non-uniformity is brought about by the onset of CuPt ordering in the layers. Other recent work has indicated that the onset of Bi droplet formation removes Bi from the growth surface, reducing the Bi content of the layer [66]. An example of a non-uniform GaAsBi layer is shown in figure 3.11.

Another attempt was made to model the structure using several layers of different Bi con-

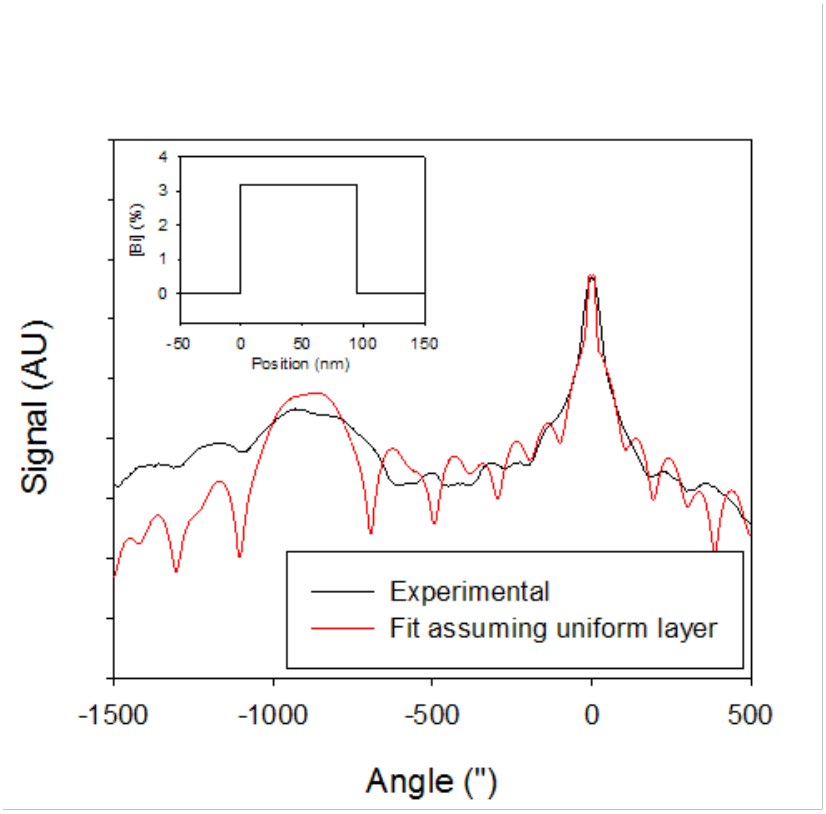

Figure 3.10: XRD spectrum from a bulk GaAsBi layer, modelled by assuming a uniform Bi concentration and a GaBi lattice constant of 6.28 Å. The inset shows the Bi profile of the simulated layer.

tents as suggested by Mazur et al. [64]. This is shown in figure 3.12.

This model more closely matches the observed XRD spectrum. Therefore, it seems that the Bi content of the layers is not uniform, making it difficult to determine the Bi content accurately by XRD.

PL The issue of non-uniform Bi content raises the question of which Bi content should be quoted for a sample when investigating GaAsBi growth conditions. It was decided that the region with the highest (optically active) Bi incorporation should be taken as the Bi content of the sample, as this is the parameter of most interest for devices such as detectors and light emitting diodes. Therefore it was decided to use PL to determine the Bi content of the layers.

The Bi contents of the samples were estimated from their peak PL wavelengths using the mVBAC model. The Bi contents associated with the Bi PL peak half maximum wavelengths

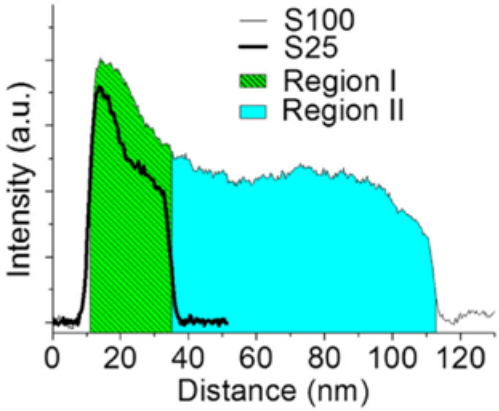

Figure 3.11: Bi profile of a nominally uniform bulk GaAsBi sample as determined by TEM image analysis. Note that the Bi content changes dramatically over the first ~ 20 nm of the GaAsBi layer and then appears to remain constant.
Reprinted from the open access journal article: (D. F. Reyes, F. Bastiman, C. J. Hunter, D. L. Sales, A. M. Sanchez, J. P. R. David, and D. González. Bismuth incorporation and the role of ordering in GaAsBi/GaAs structures. In this work S25 and S100 refer to samples with 25 nm and 100 nm Bi layers respectively. Regions I and II are identified by Reyes et al. as regions of decreasing Bi content and uniform Bi content respectively. Published in *Nanoscale Research Letters* by Springer, 9(1):18, 2014.) [65].

were considered to be the limits of the experimental uncertainty of the Bi content. This is demonstrated for a typical sample in figure 3.13.

The broad peaks of the PL spectra are likely due to alloy fluctuations both on a large scale and as a result of atomic Bi clustering [44, 45, 67–70].

3.2.2 Results

3.2.2.1 Effect of growth temperature on Bi incorporation

Data from all of the samples grown using a Bi flux of 0.31 atoms.nm^{-2}s^{-1} are shown in figure 3.14.

This plot highlights two phenomena: there is a trend of increasing Bi incorporation with decreasing temperature and the Bi content saturates at low temperatures. Note that there is a range of Bi contents observed at each temperature. Because of this, the maximum Bi incorporation observed at any given temperature was taken as the value for Bi incorporation at that temperature. Figure 3.15 shows the maximum Bi incorporation observed over a range of growth temperatures. Included in figure 3.15 are data for samples grown under an increased Bi flux of 0.49 atoms.nm^{-2}s^{-1}.

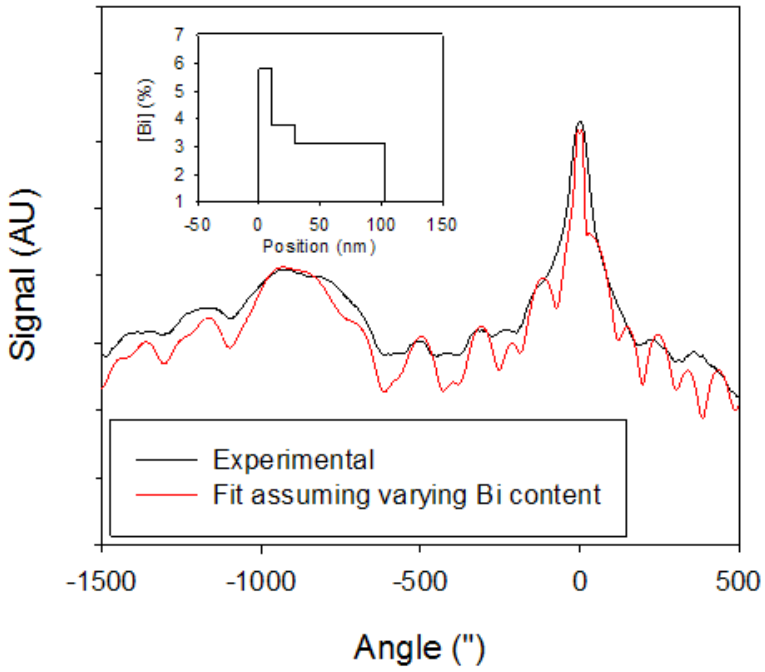

Figure 3.12: XRD spectrum from a bulk GaAsBi layer, modelled using several layers of different Bi concentration and a GaBi lattice constant of 6.28 Å. The inset shows the Bi profile of the simulated layer.

Two distinct growth regimes are visible from figure 3.15: a temperature limited regime ($> 370\,^{\circ}C$) and a Bi flux limited regime ($< 370\,^{\circ}C$). These regimes are in qualitative agreement with the literature. The temperature dependence is qualitatively consistent with that reported by Lu et al. [18] and Lewis et al. [12]. The Bi flux limited regime is qualitatively consistent with the kinetically limited regime reported by Ptak et al. [10]. In the Bi flux limited regime the Bi incorporation coefficient appears to tend towards unity (as shown by the dashed line in figure 3.15); however, the experimental uncertainty in the Bi contents of these samples prevents this from being conclusively demonstrated. Importantly, there is no discernable difference between the trends of the As_2 grown samples and the As_4 grown samples. Evidently the As species used does not affect the temperature limited miscibility or the Bi content achievable in the kinetically limited regime. It is also interesting to note that

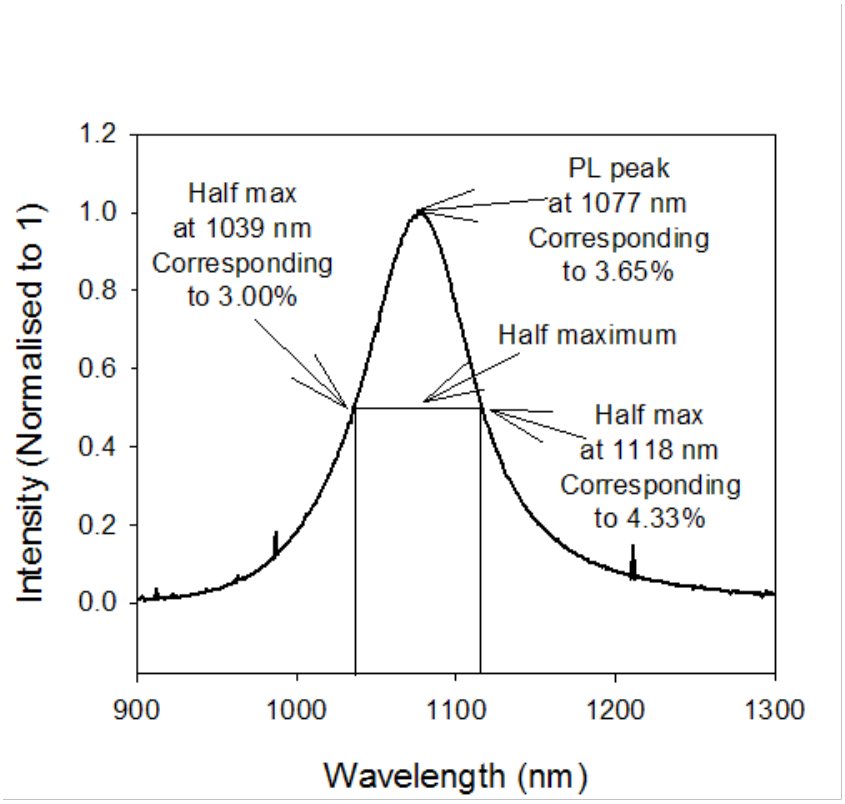

Figure 3.13: The method of Bi content estimation. The sample shown here is recorded as containing 3.65 % Bi with error bars extending down to 3 % and up to 4.33 %.

the samples grown with the higher Bi flux appear to follow the same temperature limited miscibility trend as those grown with the lower Bi flux. This suggests that the temperature limited miscibility is not affected by Bi flux. However, further work would be required to draw firm conclusions on this subject.

3.2.2.2 Effect of As flux on Bi incorporation

The next stage of the work was to investigate the As flux dependence of Bi incorporation. Samples with growth temperatures ranging between 350 °C and 380 °C were selected to be analysed. From the data in figure 3.15 it was estimated that the temperature limited Bi incorporation in this temperature range varied between 4.6 % and 4.9 %, which was deemed a small enough variation to allow conclusions to be drawn from the data. As with the temperature dependent data, the samples grown under each As:Ga flux ratio demonstrated a range of Bi incorporations and the highest Bi observed at each flux ratio was taken to be the

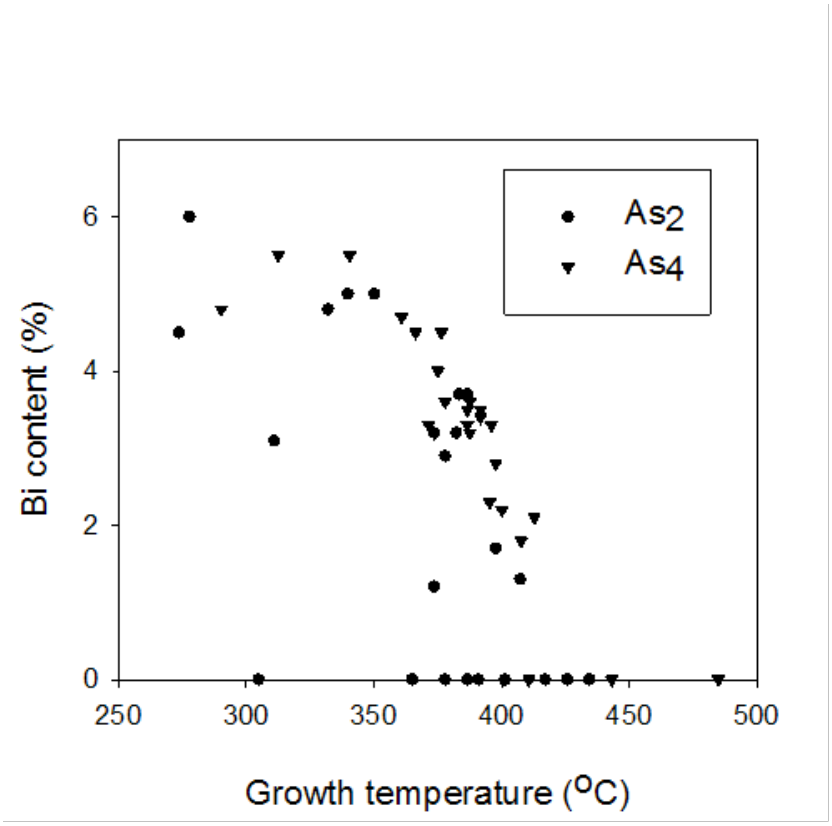

Figure 3.14: Bi incorporation vs growth temperature for all samples grown under the same Bi flux. For clarity, the error bars have been omitted from this figure.

As flux limited Bi content. The maximum Bi incorporation observed at each As:Ga atomic flux ratio is shown in figure 3.16

It is clear that the range of As_4 fluxes which allows significant Bi incorporation is much larger than that of As_2. The upper limit of the range of As_4 fluxes shown in figure 3.16 was set by the range of the As cracker valve. In order to investigate higher As_4 fluxes, it would have been necessary to raise the As reservior temperature (see section 2.1.6.3) and this was not attempted. Note that in both cases the Bi content appears to drop to 0 % as the As flux is reduced. This is in contrast with the Lu et al. and Lewis et al. models, which suggest that the Bi content should saturate at low As fluxes. This discrepancy can be reconciled by noting that the method for determining Bi content used in the previous studies is different to that used in this study. In the previous studies, the Bi content was determined by XRD, which takes no account of the optical quality of the material. However, this work uses PL. The low material quality produced at very low As:Ga flux ratios inhibits the PL

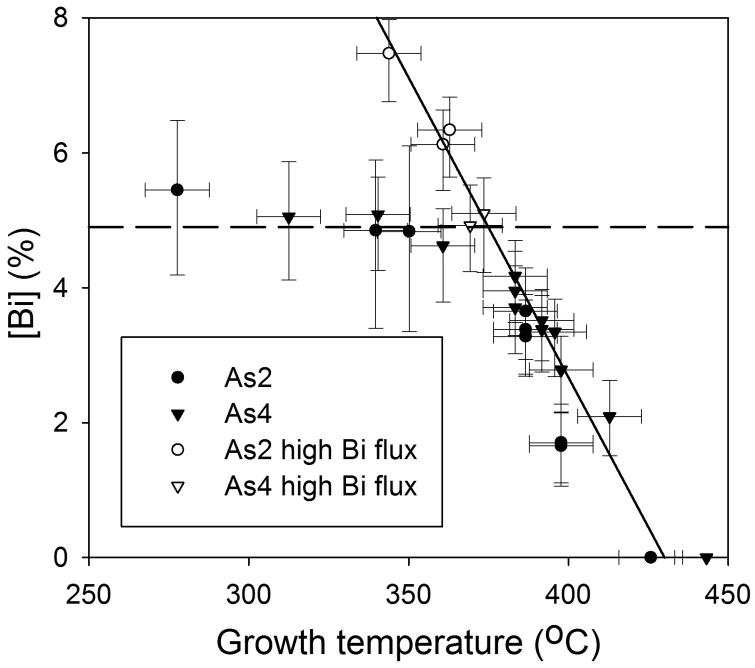

Figure 3.15: Maximum Bi incorporation observed over a range of growth temperatures. The solid line has been added to guide the eye. The dashed line represents the Bi content expected for a unity incorporation coefficient.
Reprinted from the Journal of Crystal Growth, volume 390, R. D. Richards, F. Bastiman, C. J Hunter, D. F. Mendes, A. R. Mohmad, J. S. Roberts, and J. P. R. David, Molecular beam epitaxy growth of GaAsBi using As_2 and As_4, pages 120-124, Copyright (2014), with permission from Elsevier. [71].

from these layers and leads to the false result that the Bi content drops at low As:Ga fluxes. While this result may not indicate the precise Bi content of the layers, it does indicate the optically active Bi content of the layers, a parameter of great importance for detectors, solar cells, light emitting diodes and lasers. Also, as the purpose of this work is to compare the incorporation of Bi grown using As_2 and As_4, this method is valid as it provides a fair comparison of the two species.

The data in figure 3.16 show that there is a clear difference between the incorporation of Bi under As_2 and As_4. In order to determine the origin of this difference it is necessary to understand the previous work on GaAs growth using As_2 and As_4. Foxon et al. [61, 72] investigated the incorporation dynamics of As_2 and As_4 on GaAs. Their work was later verified by other groups [73, 74] and is outlined below.

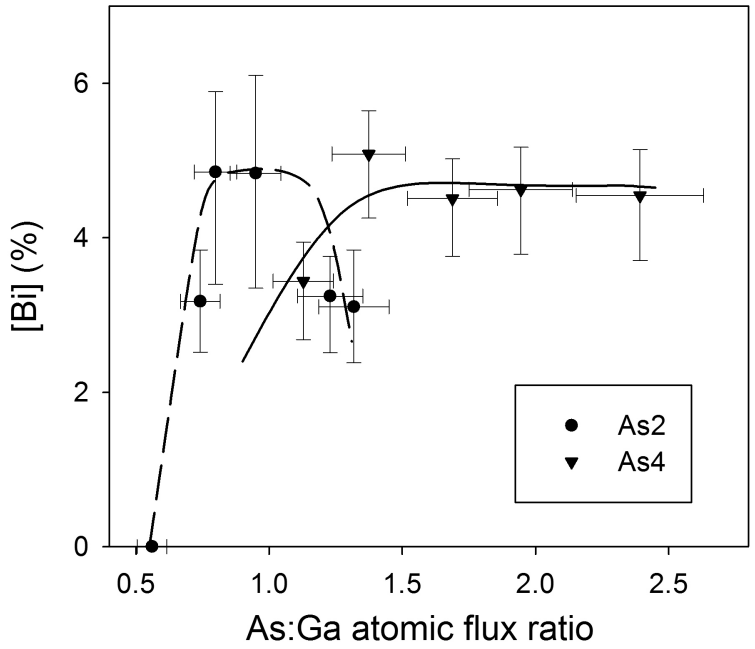

Figure 3.16: The As flux limited Bi incorporation for samples grown between 350 °C and 380 °C. The lines are added as a guide to the eye.
Reprinted from the Journal of Crystal Growth, volume 390, R. D. Richards, F. Bastiman, C. J Hunter, D. F. Mendes, A. R. Mohmad, J. S. Roberts, and J. P. R. David, Molecular beam epitaxy growth of GaAsBi using As_2 and As_4, pages 120-124, Copyright (2014), with permission from Elsevier. [71].

The sticking coefficient of As_2 on a GaAs surface varies between 0 and 1 depending on the temperature and surface Ga population as shown in figure 3.17. At the temperatures where GaAsBi growth proceeds, the sticking coefficient of As_2 is 1 in the presence of surface Ga. The sticking coefficient of As_4 on GaAs can never exceed 0.5 as shown in figure 3.18.
This is because of the more complicated incorporation dynamics of As_4 compared to As_2. Whereas As_2 can directly incorporate into the lattice upon finding exposed surface Ga, As_4 cannot; two As_4 tetramers must interact on the surface producing two As_2 dimers and necessarily causing the desorption of an As_4 tetramer before incorporating. This desorption process is what limits the sticking coefficient of As_4 to 0.5 and is shown in figure 3.19.
If this process is responsible for the observed difference in Bi incorporation under As_2 and As_4 then it would be expected that the data from both species in figure 3.16 would coincide if the As_4 fluxes were halved. This plot is shown in figure 3.20.

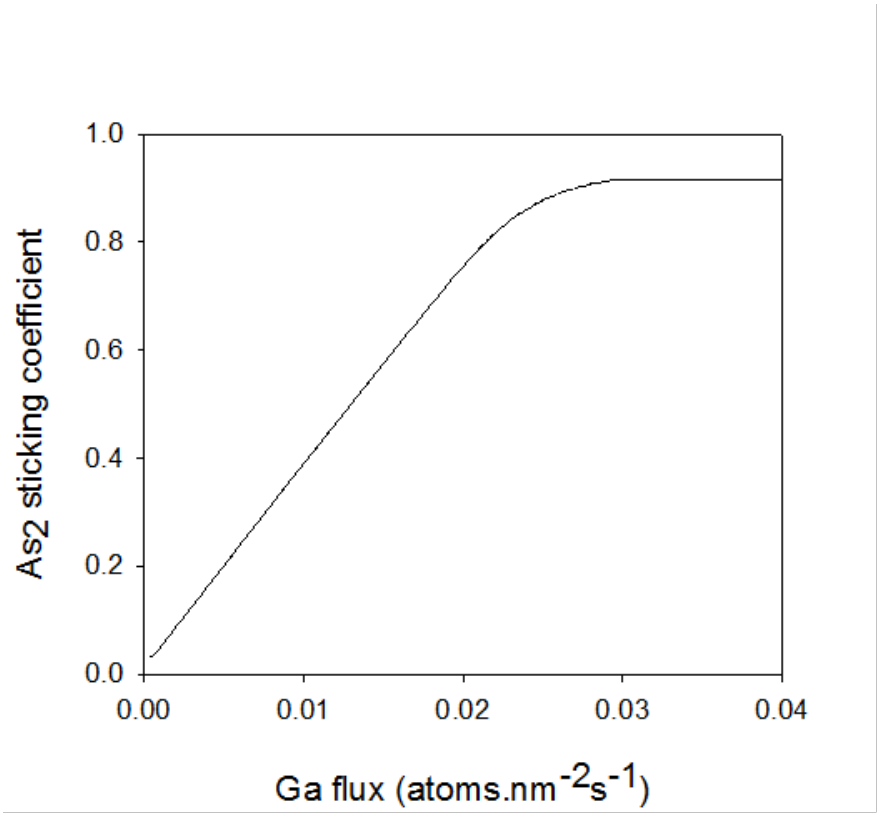

Figure 3.17: As_2 sticking coefficient as a function of Ga flux.
The As flux was $\approx$ 0.02 atoms.nm^{-2}s-1. The As_2 sticking coefficient does not reach unity in this plot but tends towards this value at higher Ga fluxes. Adapted from [61].

The data from the two As species are now coincident. It seems likely, therefore, that the observed difference in figure 3.16 can be solely attributed to the interaction kinetics of the two As species on GaAs, rather than any difference in the Bi incorporation kinetics during growth using each species. While there is no inherent advantage to using As_4 in preference to As_2 for bismide growth, the necessary desorption of half of the incident As_4 tetramers means that the range of As valve positions which allows significant Bi incorporation is doubled when using As_4 compared to that using As_2. This suggests that high Bi content GaAsBi growth can be more easily achieved using As_4 at the expense of the lifetime of the As charge. Therefore, a favourable growth development protocol would be to conduct preliminary growth parameter investigations using As_4 before switching to As_2 for the remainder of the research.

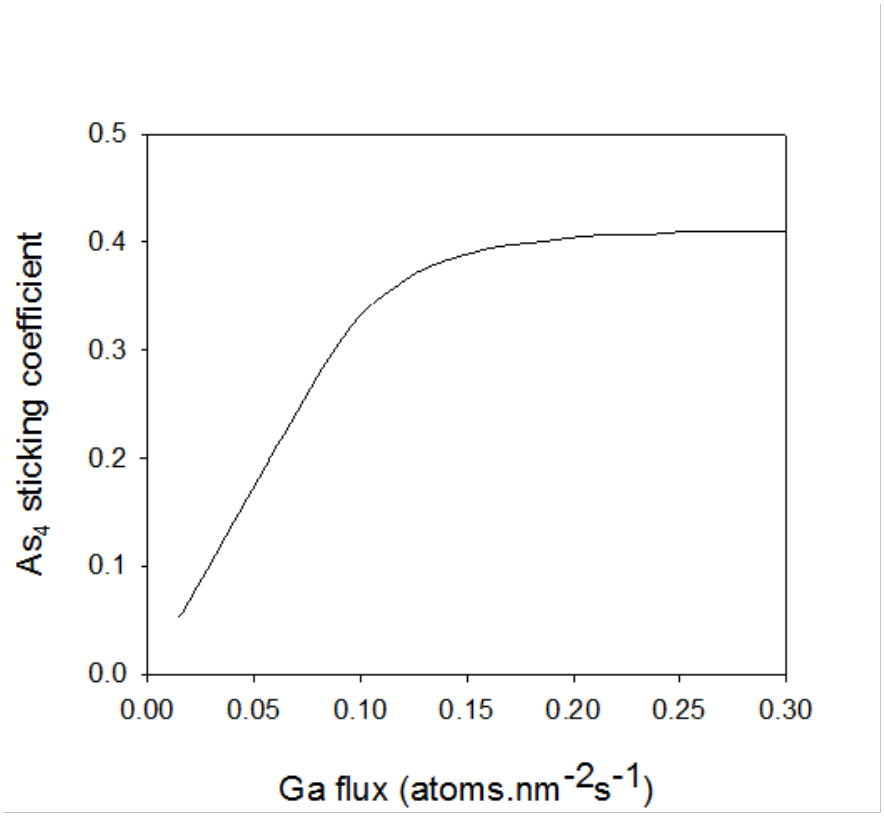

Figure 3.18: As_4 sticking coefficient as a function of Ga flux.
The As flux was $\approx$ 0.18 atoms.nm^{-2}s-1. The As_4 sticking coefficient does not reach 0.5 in this plot but it tends towards this value at higher Ga fluxes. Adapted from [72].

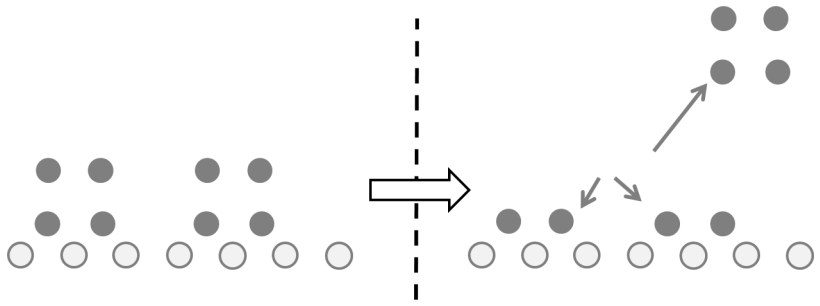

Figure 3.19: The incorporation kinetics of As_4 on GaAs. The black dots represent Ga atoms and the grey dots represent As atoms. Two As_4 tetramers on the surface must interact to produce two As_2 dimers and cause the desorption of one As_4 tetramer in order to allow any As incorporation.

3.2.2.3 Effect of Bi incorporation on PL peak intensity

The conclusion that Bi incorporation is unaffected by As species is supported by the observation that the As species has no impact on the brightness of the PL as a function of Bi content, as shown in figure 3.21.

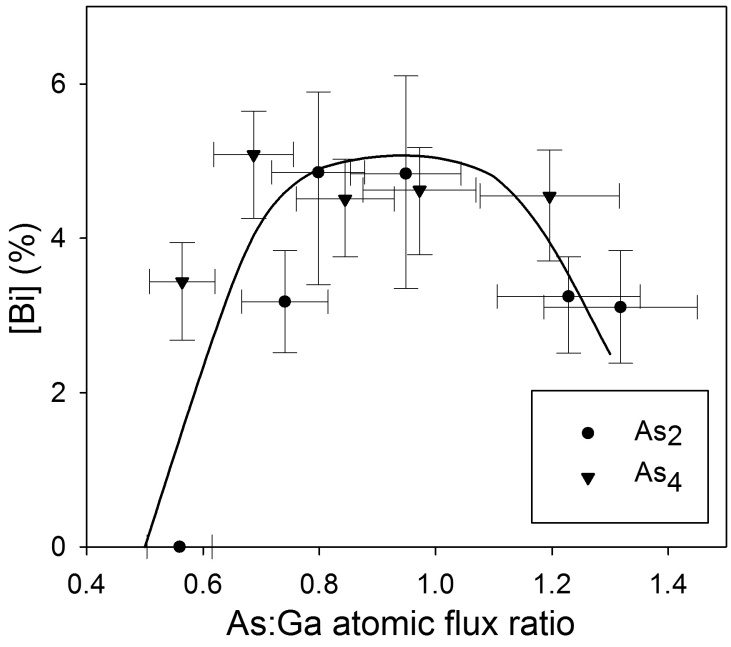

Figure 3.20: As flux limited Bi composition taking account of the necessary desorption of 50 % of the incident As_4.
Reprinted from the Journal of Crystal Growth, volume 390, R. D. Richards, F. Bastiman, C. J Hunter, D. F. Mendes, A. R. Mohmad, J. S. Roberts, and J. P. R. David, Molecular beam epitaxy growth of GaAsBi using As_2 and As_4, pages 120-124, Copyright (2014), with permission from Elsevier. [71].

From figure 3.21 it is clear that there are two regimes: increasing PL intensity with increasing Bi content for Bi < 4 % and decreasing PL intensity with increasing Bi content for Bi > 4 %. The factors which could explain the increase in PL intensity up to 4 % Bi are an increased Bi surfactant effect due to the increased surface lifetime of Bi at the lower temperatures required for higher Bi content and an increase in the band offset with the surrounding GaAs layers. These effects would improve the material quality and reduce the surface recombination velocity of the samples respectively. The region of decreasing PL intensity with increasing Bi can probably be attributed to a deterioration of the material quality due to the build-up of strain. It should be noted, however, that the samples grown during this work were grown using a range of substrate temperatures. The samples in figure 3.21 with high Bi content were grown at lower temperature than those with low Bi content. It is possible, therefore, that the decreasing PL intensity with increasing Bi content in figure 3.21 is caused by the lower temperatures necessary for the growth of these layers.

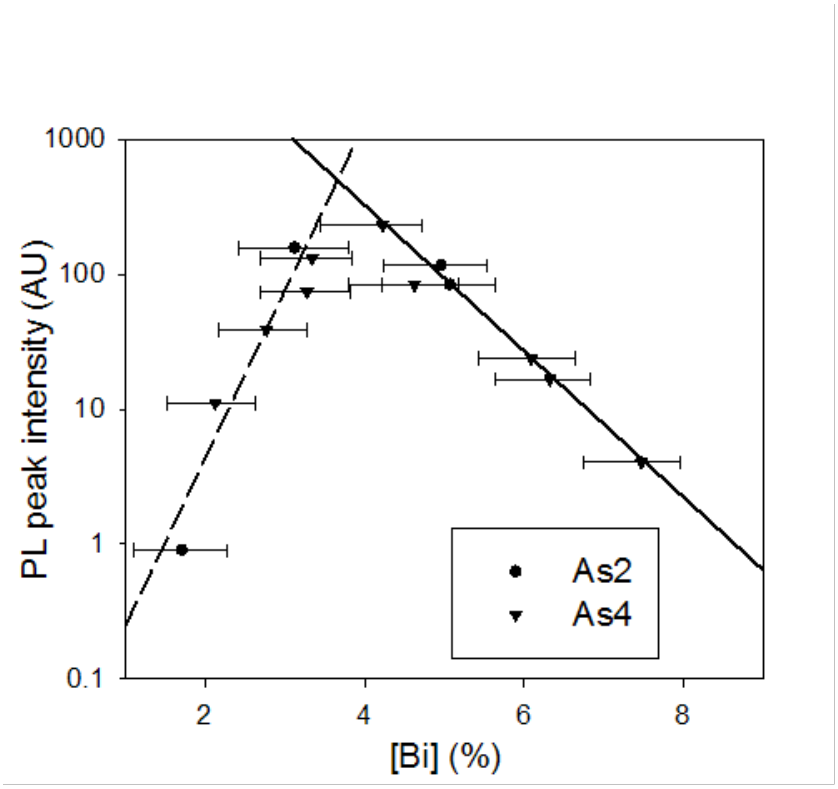

Figure 3.21: Peak room temperature PL intensity as a function of Bi content. The dashed and solid lines have been added to guide the eye.
Reprinted from the Journal of Crystal Growth, volume 390, R. D. Richards, F. Bastiman, C. J Hunter, D. F. Mendes, A. R. Mohmad, J. S. Roberts, and J. P. R. David, Molecular beam epitaxy growth of GaAsBi using As_2 and As_4, pages 120-124, Copyright (2014), with permission from Elsevier. [71].

3.2.2.4 As assisted Bi desorption

As Bi incorporates from a Bi terminated reconstruction layer on the GaAs surface, an experiment was devised to investigate the extent to which an As overpressure aids in the desorption of Bi from a Bi terminated reconstruction. This experiment was performed in the following way. A GaAs sample was loaded into the chamber, outgassed and heated to remove surface oxide as described in section 2.1.10. A 100 nm GaAs buffer was grown on the sample to provide an atomically flat As terminated surface. The sample temperature was set to the desired value and the sample was exposed to a Bi flux until the surface reconstruction changed from an As terminated reconstruction ((2×4) or $c(4\times4)$) to a Bi terminated reconstruction ($(n\times3)$ or $c(n\times8)$). Once this reconstruction was observed the Bi flux was terminated and the sample was held either under vacuum, under an As_2 flux or

under an As_4 flux (both As fluxes equivalent to 6.26 atoms.nm^{-2}s^{-1}) until the As terminated reconstruction was recovered. The process was monitored by recording the intensity of a RHEED reconstruction rod which is present in the As terminated reconstruction but not in the Bi terminated reconstruction. The time taken for the rod's intensity to reach half of its original intensity was taken as a characteristic time for the reconstruction recovery. The data from this experiment performed at 415 °C are shown in figure 3.22.

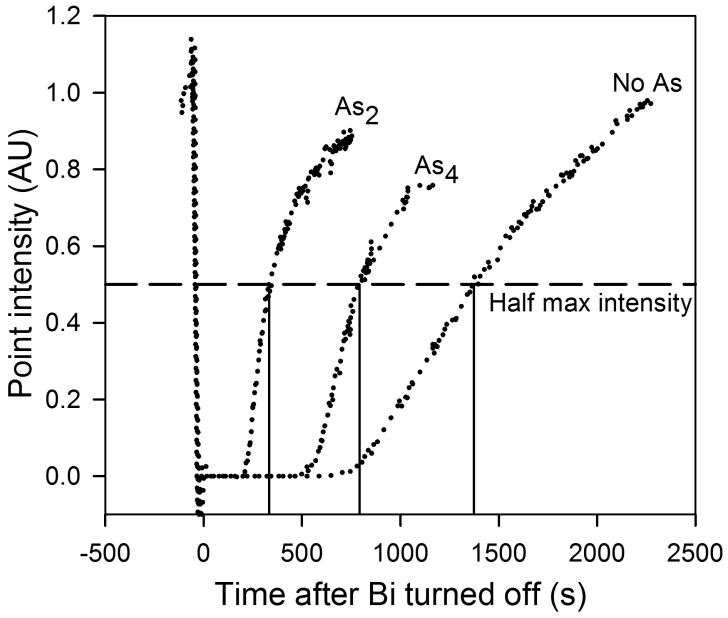

Figure 3.22: As reconstruction recovery as monitored by RHEED. The Bi flux was terminated at time 0 in each case. The dashed line represents half of the normalised starting intensity. The solid lines show the times recorded as the characteristic recovery time in each test.
Reprinted from the Journal of Crystal Growth, volume 390, R. D. Richards, F. Bastiman, C. J Hunter, D. F. Mendes, A. R. Mohmad, J. S. Roberts, and J. P. R. David, Molecular beam epitaxy growth of GaAsBi using As_2 and As_4, pages 120-124, Copyright (2014), with permission from Elsevier. [71].

The data in figure 3.22 show that an As overpressure significantly reduces the time taken to recover an As terminated reconstruction. This suggests that As has an active role in displacing Bi from the sample surface and that As_2 is more aggressive in displacing Bi than As_4. The characteristic desorption times recorded in each case are many hundreds of seconds, whereas the monolayer growth time in this work is 1 s. This suggests that, while As is active in removing Bi from the Bi surface reconstruction layer, the As assisted

desorption of Bi from the surface layer has little impact on the Bi incorporation observed in this work. Care must be taken with this result, however, as this test was performed on a static surface, rather than a growing surface. This conclusion supports the assumption in the model by Lewis et al. [12] that the role of As in limiting the Bi incorporation into GaAs is one of limiting the available surface Ga population rather than one of desorbing Bi from the surface.

3.3 Conclusions

Two distinct GaAsBi growth regimes were observed: a Bi flux independent, temperature limited regime where Bi content increases with decreasing temperature; a Bi flux limited regime where the Bi incorporation coefficient approaches unity.

This work has demonstrated that the observed differences between the As flux dependence of Bi incorporation under As_2 and As_4 can be solely attributed to the necessary desorption of 50 % of the incident As_4 during growth as observed by Foxon and Joyce [72]. This conclusion is supported by the observation that the temperature dependence of Bi incorporation is independent of As species, as is the PL intensity of GaAsBi samples as a function of Bi content. The PL intensity improves with Bi content up to 4 %. It is hypothesised that this is due to the improvement in carrier confinement within the GaAsBi layer and the increased Bi surfactant effect as the Bi surface lifetime increases as the sample temperature reduces. Above 4 % the PL intensity deteriorates, which is possibly due to a deterioration in material quality induced by strain. However, it is also possible that this effect is caused by the lower growth temperatures required for higher Bi contents.

As was shown to play an active role in desorbing Bi from a Bi terminated GaAs surface, with As_2 being more aggressive in desorbing Bi than As_4. However, the rate of assisted desorption is low enough to suggest that this effect has little impact on the incorporation of Bi in GaAs even at relatively low growth rates.

It seems that As species has no fundamental impact on the material quality or Bi incorporation achievable in MBE grown GaAsBi. However, growth with As_4 may provide a more forgiving growth parameter space in which to grow GaAsBi. The growth and structural characterisation of GaAsBi/GaAs MQW p-i-n diodes is discussed in chapter 4.

Bibliography

[1] M. R. Pillai, S-S. Kim, S. T. Ho, and S. A. Barnett. Growth of $In_xGa_{1-x}As$/GaAs heterostructures using Bi as a surfactant. *Journal of Vacuum Science & Technology B*, 18(3):1232–1236, 2000.

[2] A. J. Ptak, D. A. Beaton, and A. Mascarenhas. Growth of BGaAs by molecular-beam epitaxy and the effects of a bismuth surfactant. *Journal of Crystal Growth*, 351(1):122–125, 2012.

[3] S. Tixier, M. Adamcyk, E. C. Young, J. H. Schmid, and T. Tiedje. Surfactant enhanced growth of GaNAs and InGaNAs using bismuth. *Journal of Crystal Growth*, 251(1):449–454, 2003.

[4] K. Oe and H. Okamoto. New semiconductor alloy $GaAs_{1-x}Bi_x$ grown by metal organic vapor phase epitaxy. *Japanese Journal of Applied Physics*, 37(11A):L1283, 1998.

[5] S. Tixier, M. Adamcyk, T. Tiedje, S. Francoeur, A. Mascarenhas, P. Wei, and F. Schiettekatte. Molecular beam epitaxy growth of $GaAs_{1-x}Bi_x$. *Applied Physics Letters*, 82(14):2245–2247, 2003.

[6] A. Janotti, S-H. Wei, and S. B. Zhang. Theoretical study of the effects of isovalent coalloying of Bi and N in GaAs. *Physical Review B*, 65(11):115203, 2002.

[7] D. Madouri, A. Boukra, A. Zaoui, and M. Ferhat. Bismuth alloying in GaAs: a first-principles study. *Computational Materials Science*, 43(4):818–822, 2008.

[8] K. Forghani, A. Anand, L. J. Mawst, and T. F. Kuech. Low temperature growth of $GaAs_{1-y}Bi_y$ epitaxial layers. *Journal of Crystal Growth*, 380(0):23 – 27, 2013.

[9] D. Fan, P. C. Grant, S-Q. Yu, V. G. Dorogan, X. Hu, Z. Zeng, C. Li, M. E. Hawkridge, M. Benamara, Y. I. Mazur, G. J. Salamo, S. R. Johnson, and Z. M. Wang. Mbe grown GaAsBi/GaAs double quantum well separate confinement heterostructures. *Journal of Vacuum Science & Technology B*, 31(3):03C105, 2013.

[10] A. J. Ptak, R. France, D. A. Beaton, K. Alberi, J. Simon, A. Mascarenhas, and C-S. Jiang. Kinetically limited growth of GaAsBi by molecular-beam epitaxy. *Journal of Crystal Growth*, 338(1):107–110, 2012.

[11] M. Masnadi-Shirazi, D. A. Beaton, R. B. Lewis, X. Lu, and T. Tiedje. Surface reconstructions during growth of $GaAs_{1-x}Bi_x$ alloys by molecular beam epitaxy. *Journal of Crystal Growth*, 338(1):80–84, 2012.

[12] R. B. Lewis, M. Masnadi-Shirazi, and T. Tiedje. Growth of high Bi concentration $GaAs_{1-x}Bi_x$ by molecular beam epitaxy. *Applied Physics Letters*, 101(8):082112, 2012.

[13] D. Fan, Z. Zeng, X. Hu, V. G. Dorogan, C. Li, M. Benamara, M. E. Hawkridge, Y. I. Mazur, S-Q. Yu, S. R. Johnson, Z. M. Wang, and G. J. Salamo. Molecular beam epitaxy growth of GaAsBi/GaAs/AlGaAs separate confinement heterostructures. *Applied Physics Letters*, 101(18):181103, 2012.

[14] F. Bastiman, A. R. B. Mohmad, J. S. Ng, J. P. R. David, and S. J. Sweeney. Non-stoichiometric GaAsBi/GaAs (100) molecular beam epitaxy growth. *Journal of Crystal Growth*, 338(1):57–61, 2012.

[15] F. Bastiman, A. G. Cullis, J. P. R. David, and S. J. Sweeney. Bi incorporation in GaAs (100)-2× 1 and 4× 3 reconstructions investigated by RHEED and STM. *Journal of Crystal Growth*, 341(1):19–23, 2012.

[16] Y. Tominaga, Y. Kinoshita, G. Feng, K. Oe, and M. Yoshimoto. Growth of $GaAs_{1-x}Bi_x$/GaAs multi-quantum wells by molecular beam epitaxy. *Physica Status Solidi (c)*, 5(9):2719–2721, 2008.

[17] V. Pačebutas, K. Bertulis, G. Aleksejenko, R. Adomavičius, G. Molis, and A. Krotkus. Growth and characterization of GaBiAs epilayers. *Optical Materials*, 30(5):756–758, 2008.

[18] X. Lu, D. A. Beaton, R. B. Lewis, T. Tiedje, and M. B. Whitwick. Effect of molecular beam epitaxy growth conditions on the Bi content of $GaAs_{1-x}Bi_x$. *Applied Physics Letters*, 92(19):192110–192110–3, May 2008.

[19] M. Henini, J. Ibanez, M. Schmidbauer, M. Shafi, S. V. Novikov, L. Turyanska, S. I. Molina, D. L. Sales, M. F. Chisholm, and J. Misiewicz. Molecular beam epitaxy of GaBiAs on (311) B GaAs substrates. *Applied Physics Letters*, 91(25):251909–251909, 2007.

[20] M. Ferhat and A. Zaoui. Structural and electronic properties of III-V bismuth compounds. *Physical Review B*, 73(11):115107, 2006.

[21] Y. Takehara, M. Yoshimoto, W. Huang, J. Saraie, K. Oe, A. Chayahara, and Y. Horino. Lattice distortion of GaAsBi alloy grown on GaAs by molecular beam epitaxy. *Japanese Journal of Applied Physics*, 45(1R):67, 2006.

[22] H. Achour, S. Louhibi, B. Amrani, A. Tebboune, and N. Sekkal. Structural and electronic properties of GaAsBi. *Superlattices and Microstructures*, 44(2):223–229, 2008.

[23] A. Belabbes, A. Zaoui, and M. Ferhat. Lattice dynamics study of bismuth III-V compounds. *Journal of Physics: Condensed Matter*, 20(41):415221, 2008.

[24] A. Abdiche, H. Abid, R. Riane, and A. Bouaza. Structural and electronic properties of zinc blend $GaAs_{1-x}Bi_x$ solid solutions. *Physica B: Condensed Matter*, 405(9):2311–2316, 2010.

[25] M. Mbarki and A. Rebey. First-principles calculation of the physical properties of $GaAs_{1-x}Bi_x$ alloys. *Semiconductor Science and Technology*, 26(10):105020, 2011.

[26] M. Usman, C. A. Broderick, A. Lindsay, and E. P. OReilly. Tight-binding analysis of the electronic structure of dilute bismide alloys of GaP and GaAs. *Physical Review B*, 84(24):245202, 2011.

[27] M. K. Rajpalke, W. M. Linhart, M. Birkett, K. M. Yu, J. Alaria, J. Kopaczek, R. Kudrawiec, T. S. Jones, M. J. Ashwin, and T. D. Veal. High Bi content GaSbBi alloys. *Journal of Applied Physics*, 116(4):043511, 2014.

[28] G. Vardar, S. W. Paleg, M. V. Warren, M. Kang, S. Jeon, and R. S. Goldman. Mechanisms of droplet formation and Bi incorporation during molecular beam epitaxy of GaAsBi. *Applied Physics Letters*, 102(4):–, 2013.

[29] E. C. Young, M. B. Whitwick, T. Tiedje, and D. A. Beaton. Bismuth incorporation in $GaAs_{1-x}Bi_x$ grown by molecular beam epitaxy with in-situ light scattering. *Physica Status Solidi (c)*, 4(5):1707–1710, 2007.

[30] R. N. Kini, A. Mascarenhas, R. France, and A. J. Ptak. Low temperature photoluminescence from dilute bismides. *Journal of Applied Physics*, 104(11):113534–113534, 2008.

[31] Y. Zhang, A. Mascarenhas, and L-W. Wang. Similar and dissimilar aspects of III-V semiconductors containing Bi versus N. *Physical Review B*, 71(15):155201, 2005.

[32] S. Francoeur, S. Tixier, E. Young, T. Tiedje, and A. Mascarenhas. Bi isoelectronic impurities in GaAs. *Physical Review B*, 77(8):085209, 2008.

[33] K. Alberi, O. D. Dubon, W. Walukiewicz, K. M. Yu, K. Bertulis, and A. Krotkus. Valence band anticrossing in $GaBi_xAs_{1-x}$. *Applied Physics Letters*, 91(5):051909, 2007.

[34] W. Shan, W. Walukiewicz, J. W. Ager III, E. E. Haller, J. F. Geisz, D. J. Friedman, J. M. Olson, and S. R. Kurtz. Band anticrossing in GaInNAs alloys. *Physical Review Letters*, 82(6):1221, 1999.

[35] K. Oe. Characteristics of semiconductor alloy $GaAs_{1-x}Bi_x$. *Japanese Journal of Applied Physics*, 41(5R):2801, 2002.

[36] S. Francoeur, M-J. Seong, A. Mascarenhas, S. Tixier, M. Adamcyk, and T. Tiedje. Band gap of $GaAs_{1-x}Bi_x$, $0 < x < 3.6$ %. *Applied Physics Letters*, 82(22):3874–3876, 2003.

[37] M. Yoshimoto, W. Haung, G. Feng, and K. Oe. GaNAsBi semiconductor alloy with temperature-insensitive bandgap. In *MRS Proceedings*, volume 891, pages 0891–EE11. Cambridge Univ Press, 2005.

[38] M. Yoshimoto, W. Huang, G. Feng, and K. Oe. New semiconductor alloy GaNAsBi with temperature-insensitive bandgap. *Physica Status Solidi (b)*, 243(7):1421–1425, 2006.

[39] W. Huang, K. Oe, G. Feng, and M. Yoshimoto. Molecular-beam epitaxy and characteristics of $GaN_yAs_{1-x-y}Bi_x$. *Journal of Applied Physics*, 98(5):053505, 2005.

[40] A. R. Mohmad, F. Bastiman, C. J. Hunter, R. D. Richards, S. J. Sweeney, J. S. Ng, J. P. R. David, and B. Y. Majlis. Localization effects and band gap of GaAsBi alloys. *Physica Status Solidi (b)*, 251:1276–1281, 2014.

[41] U. Tisch, E. Finkman, and J. Salzman. The anomalous bandgap bowing in GaAsN. *Applied Physics Letters*, 81(3):463–465, 2002.

[42] S. M. Sze. *Physics of semiconductor devices*. John Wiley and Sons, Inc, 2nd edition, 1981.

[43] Y. Tominaga, K. Oe, and M. Yoshimoto. Low temperature dependence of oscillation wavelength in $GaAs_{1-x}Bi_x$ laser by photo-pumping. *Applied Physics Express*, 3(6):062201, 2010.

[44] A. R. Mohmad, F. Bastiman, J. S. Ng, S. J. Sweeney, and J. P. R. David. Photoluminescence investigation of high quality $GaAs_{1-x}Bi_x$ on GaAs. *Applied Physics Letters*, 98(12):122107, 2011.

[45] S. Imhof, A. Thränhardt, A. Chernikov, M. Koch, N. S. Köster, K. Kolata, S. Chatterjee, S. W. Koch, X. Lu, S. R. Johnson, D. A. Beaton, T. Tiedje, and O. Rubel. Clustering effects in Ga(AsBi). *Applied Physics Letters*, 96(13):131115, 2010.

[46] Z. Chine, H. Fitouri, I. Zaied, A. Rebey, and B. El Jani. Photoreflectance and photoluminescence study of annealing effects on GaAsBi layers grown by metalorganic vapor phase epitaxy. *Semiconductor Science and Technology*, 25(6):065009, 2010.

[47] K. Yamashita, M. Yoshimoto, and K. Oe. Temperature-insensitive refractive index of GaAsBi alloy for laser diode in WDM optical communication. *physica Status Solidi (c)*, 3(3):693–696, 2006.

[48] B. Fluegel, S. Francoeur, A. Mascarenhas, S. Tixier, E. C. Young, and T. Tiedje. Giant spin-orbit bowing in $GaAs_{1-x}Bi_x$. *Physical Review Letters*, 97(6):067205, 2006.

[49] S. J. Sweeney and S. R. Jin. Bismide-nitride alloys: promising for efficient light emitting devices in the near-and mid-infrared. *Journal of Applied Physics*, 113(4):043110, 2013.

[50] Z. Batool, K. Hild, T. J. C. Hosea, X. Lu, T. Tiedje, and S. J. Sweeney. The electronic band structure of GaBiAs/GaAs layers: Influence of strain and band anti-crossing. *Journal of Applied Physics*, 111(11):113108, 2012.

[51] Y. Tominaga, Y. Kinoshita, K. Oe, and M. Yoshimoto. Structural investigation of $GaAs_{1-x}Bi_x$/GaAs multiquantum wells. *Applied Physics Letters*, 93(13):131915, 2008.

[52] S. Horng and A. Kahn. Epitaxial growth of Bi on GaAs (100) surfaces. *Journal of Vacuum Science & Technology B*, 7(4):931–935, 1989.

[53] R. Butkutė, V. Pačebutas, B. Čechavičius, R. Adomavičius, A. Koroliov, and A. Krotkus. Thermal annealing effect on the properties of GaBiAs. *physica Status Solidi (c)*, 9(7):1614–1616, 2012.

[54] B. Čechavičius, R. Adomavičius, A. Koroliov, and A. Krotkus. Thermal annealing effect on photoexcited carrier dynamics in $GaBi_xAs_{1-x}$. *Semiconductor Science and Technology*, 26(8):085033, 2011.

[55] S. Mazzucato, P. Boonpeng, H. Carrère, D. Lagarde, A. Arnoult, G. Lacoste, T. Zhang, A. Balocchi, T. Amand, X. Marie, and C. Fontaine. Reduction of defect density by rapid thermal annealing in GaAsBi studied by time-resolved photoluminescence. *Semiconductor Science and Technology*, 28(2):022001, 2013.

[56] A. R. Mohmad, F. Bastiman, C. J. Hunter, R. Richards, S. J. Sweeney, J. S. Ng, and J. P. R. David. Effects of rapid thermal annealing on $GaAs_{1-x}Bi_x$ alloys. *Applied Physics Letters*, 101(1):012106, 2012.

[57] I. Moussa, H. Fitouri, Z. Chine, A. Rebey, and B. El Jani. Effect of thermal annealing on structural and optical properties of the $GaAs_{0.963}Bi_{0.037}$ alloy. *Semiconductor Science and Technology*, 23(12):125034, 2008.

[58] J. F. Rodrigo, D. L. Sales, M. Shafi, M. Henini, L. Turyanska, S. Novikov, and S. I. Molina. Effect of annealing on the structural and optical properties of (311)B GaAsBi layers. *Applied Surface Science*, 256(18):5688–5690, 2010.

[59] O. M. Lemine, A. Alkaoud, H. V. Avanço Galeti, V. Orsi Gordo, Y. Galvão Gobato, H. Bouzid, A. Hajry, and M. Henini. Thermal annealing effects on the optical and structural properties of (1 0 0) $GaAs_{1-x}Bi_x$ layers grown by Molecular Beam Epitaxy. *Superlattices and Microstructures*, 65(0):48 – 55, 2014.

[60] H. Künzel and K. Ploog. The effect of As_2 and As_4 molecular beam species on photoluminescence of molecular beam epitaxially grown GaAs. *Applied Physics Letters*, 37(4):416–418, 1980.

[61] C. T. Foxon and B. A. Joyce. Interaction kinetics of As_2 and Ga on {100} gaas surfaces. *Surface Science*, 64(1):293–304, 1977.

[62] F. Bastiman, A. G. Cullis, and M. Hopkinson. GaAs (001)(2× 4) to c (4× 4) transformation observed in situ by STM during As flux irradiation. *Surface Science*, 603(16):2398–2402, 2009.

[63] H. Künzel, J. Knecht, H. Jung, K. Wünstel, and K. Ploog. The effect of arsenic vapour species on electrical and optical properties of GaAs grown by molecular beam epitaxy. *Applied Physics A*, 28(3):167–173, 1982.

[64] .Y I Mazur, V. G. Dorogan, M. Benamara, M. E. Ware, M. Schmidbauer, G. G. Tarasov, S. R. Johnson, X. Lu, S. Q. Yu, T. Tiedje, and G. J. Salamo. Effects of spatial confinement and layer disorder in photoluminescence of $GaAs_{1-x}Bi_x$/GaAs heterostructures. *Journal of Physics D: Applied Physics*, 46(6):065306, 2013.

[65] D. F. Reyes, F. Bastiman, C. J. Hunter, D. L. Sales, A. M. Sanchez, J. P. R. David, and D. González. Bismuth incorporation and the role of ordering in GaAsBi/GaAs structures. *Nanoscale Research Letters*, 9(1):1–8, 2014.

[66] J. M. Millunchick, N. Modine, and A. Duzik. Ab initio studies of atomic surface structure of Bi-containing III-V compound semiconductor alloys. In *5th International Workshop on Bismuth-Containing Semiconductors*, July 2014.

[67] S. Mazzucato, H. Lehec, H. Carrère, H. Makhloufi, A. Arnoult, C. Fontaine, T. Amand, and X Marie. Low-temperature photoluminescence study of exciton recombination in bulk GaAsBi. *Nanoscale Research Letters*, 9(1):1–5, 2014.

[68] X. Lu, D. A. Beaton, R. B. Lewis, T. Tiedje, and Y. Zhang. Composition dependence of photoluminescence of $GaAs_{1-x}Bi_x$ alloys. *Applied Physics Letters*, 95(4):041903, 2009.

[69] G. Pettinari, A. Polimeni, M. Capizzi, J. H. Blokland, P. C. M. Christianen, J. C. Maan, E. C. Young, and T. Tiedje. Influence of bismuth incorporation on the valence and conduction band edges of $GaAs_{1-x}Bi_x$. *Applied Physics Letters*, 92(26):262105–262105, 2008.

[70] R. Kudrawiec, M. Syperek, P. Poloczek, J. Misiewicz, R. H. Mari, M. Shafi, M. Henini, Y. G. Gobato, S. V. Novikov, J. Ibáñez, M. Schmidbauer, and S. I. Molina. Carrier localization in GaBiAs probed by photomodulated transmittance and photoluminescence. *Journal of Applied Physics*, 106(2):023518, 2009.

[71] R. D. Richards, F. Bastiman, C. J Hunter, D. F. Mendes, A. R. Mohmad, J. S. Roberts, and J. P. R. David. Molecular beam epitaxy growth of GaAsBi using As_2 and As_4. *Journal of Crystal Growth*, 390(0):120 – 124, 2014.

[72] C. T. Foxon and B. A. Joyce. Interaction kinetics of As_4 and Ga on {100} GaAs surfaces using a modulated molecular beam technique. *Surface Science*, 50(2):434–450, 1975.

[73] E. S. Tok, J. H. Neave, J. Zhang, B. A. Joyce, and T. S. Jones. Arsenic incorporation kinetics in GaAs (001) homoepitaxy revisited. *Surface Science*, 374(1):397–405, 1997.

[74] J. Y. Tsao, T. M. Brennan, and B. E. Hammons. Reflection mass spectrometry of As incorporation during GaAs molecular beam epitaxy. *Applied Physics Letters*, 53(4):288–290, 1988.

Chapter 4

Growth and characterisation of GaAsBi/GaAs multiple quantum wells

4.1 Introduction

In the previous chapter, the effects of growth temperature, As flux and As species on MBE grown bulk GaAsBi were presented. In this chapter the physics of MQW solar cells is outlined and previous work on GaAsBi/GaAs MQW structures is reviewed before the growth and structural characterisation of strained GaAsBi/GaAs MQWs with large well numbers is reported.

4.1.1 Concept of MQW solar cells

The topic of MQW solar cells was introduced in section 1.5.7.3. In this chapter, the topic will be discussed in greater detail, with specific reference to previous work on the effects of strain and relaxation in MQW structures.

In 1990 Barnham et al. [1] suggested that a decoupling of the V_{oc} and I_{sc} in single junction solar cells could be achieved by introducing quantum wells (QWs) into a cell. In a conventional bulk cell, the band gap of the cell determines both V_{oc} and I_{sc}. However, by introducing QWs into a bulk cell, the effective band gap for absorption is lowered while

maintaining the carrier energies upon extraction, as shown in figure 4.1. Photons with energy greater than E_{well} are absorbed and extracted at an energy of $E_{barrier}$. In practice the V_{oc} produced by an MQW solar cell is slightly lower than that produced by an equivalent cell comprising the barrier material [2, 3].

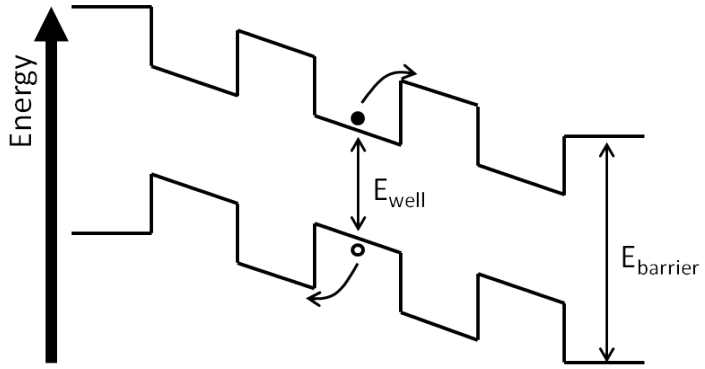

Figure 4.1: Band diagram of an MQW p-i-n junction.

Initial results investigating GaAs/AlGaAs MQW solar cells showed that an increase in efficiency could be achieved with the inclusion of the wells [4]. However, it was argued by some [5, 6] that MQW cells could not offer any inherent increase in efficiency over bulk cells. They suggested that the observed increase in efficiency was due to the GaAs QWs reducing the effective band gap of the AlGaAs cell and bringing it closer to the single junction optimum band gap of $\sim$ 1.2 eV. These groups argued that, while the wells provided another possible route for carrier excitation, they also produced another possible route for carrier recombination which limited the maximum theoretical MQW cell efficiency to that of a bulk single junction cell. This is shown in figure 4.2.

As can be seen from figure 4.2, incorporating QWs into a solar cell introduces two new transitions for carrier excitation (transitions 1 and 3). However, these transitions are reversible, giving rise to transitions 2 and 4. According to the Shockley-Queisser detailed balance model [7], unless there is a driving force preventing recombination through transitions 2 and 4, they will act as carrier sinks and limit the efficiency of the device at that of a bulk single junction cell.

The reason that MQWs offer a theoretical maximum efficiency enhancement over bulk cells is that the carrier escape from the QWs is not reversible [8, 9]. In a p-i-n MQW structure

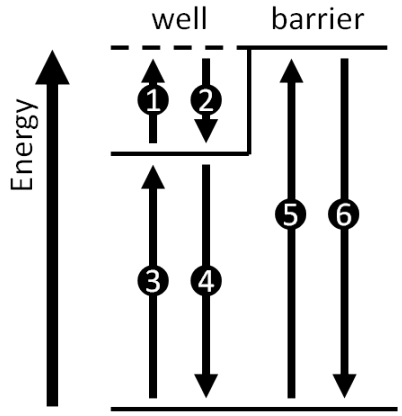

Figure 4.2: Simplified band structure of a QW. The possible carrier transitions are denoted by the black arrows.

the inbuilt field across the i-region sweeps carriers away from the wells, meaning that, once excited from a well, a carrier is highly unlikely to be trapped again by the same well. In figure 4.2 the irreversibility of carrier escape gives rise to an inequality between the rates of transition 1 and transition 2, which leads to an inequality between the rates of transition 3 and transition 4.

The increased photocurrent collected by an MQW solar cell compared to a bulk solar cell is highlighted in figure 4.3. It is clear from this figure that the incorporation of QWs provides a contribution to the current generated by the cell from long wavelength light.

4.1.2 Strain in bulk heteroepitaxial layers

Initial research into MQW solar cells was hindered by strain relaxation in the samples [11, 12]. The strain f_s in a heteroepitaxial bulk semiconductor is given by equation 4.1:

$$f_s = \frac{a_l - a_s}{a_s} \tag{4.1}$$

where a_l is the free standing heteroepitaxial layer lattice constant; a_s is the substrate lattice constant.

According to Matthews and Blakeslee [13] for any given strain there will be a critical thickness of heteroepitaxial growth at which point it will become energetically favourable for dislocations in the material to propagate to the sample surface. There have been many ex-

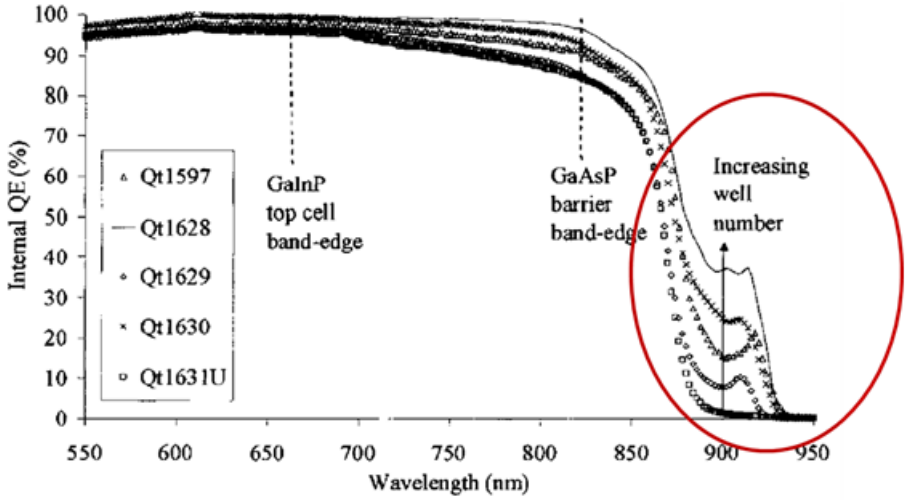

Figure 4.3: The external quantum efficiency of an InGaAs/GaAsP solar cell. The region circled in red highlights the main contribution to the absorption from the QWs.
Reprinted with permission from [D. B. Bushnell, T. N. D. Tibbits, K. W. J. Barnham, J. P. Connolly, M. Mazzer, N. J. Ekins-Daukes, J. S. Roberts, G. Hill, and R. Airey. Effect of well number on the performance of quantum-well solar cells. *Journal of Applied Physics*, 97(12):124908, 2005]. Copyright [2005], AIP Publishing LLC. [10]

perimental studies into the critical thickness of heteroepitaxial layers [14–16]. The results from these studies are varied, with some authors claiming that the Matthews-Blakeslee critical thickness accurately predicted the onset of dislocation propagation [17, 18] and other authors claiming that this critical thickness could be greatly exceeded before the onset of dislocation propagation [15, 16, 19]. The results depended on the method used to observe the presence of dislocations [20]. Certain techniques, such as photoluminescence microscopy or cathodoluminescence (CL) are sensitive to individual dislocations; whereas, techniques such as PL and XRD are sensitive to bulk crystal properties and can only detect the onset of dislocation generation.

The strain driven dislocation propagation does not result in significant relaxation of strain [11]. To relieve strain in the material, the generation of dislocations is required. The generation of dislocations occurs at greater thicknesses than the Matthews-Blakeslee critical thickness. There are several models which describe the onset of dislocation generation [13, 21–26]; however, it is not clear which of these should be adopted as a working model.

4.1.3 Strain in MQW heteroepitaxial layers

The initial theories on the build-up of strain in MQW systems suggested that, provided the width of each well was below its critical thickness, the strain in the layer would be fully compensated by the overgrowth of a barrier region [18]. However, it was shown by other authors [27–29] that strain builds up throughout the MQW region and catastrophic lattice relaxation can occur even if each well does not individually exceed its critical thickness.
In an MQW layer the average strain $\langle f_s \rangle$ is given by equation 4.2 [12]:

$$\langle f_s \rangle = \frac{a_l - a_s}{a_s} \frac{N_{qw} t_{qw}}{N_{qw} t_{qw} + (N_{qw} - 1) t_b} \tag{4.2}$$

where N_{qw} is the number of wells; t_{qw} is the thickness of a single well; t_b is the thickness of a single barrier. Dislocations are generated at the interfaces between the MQW region and the surrounding cladding layers [11, 12].
In 1996 Griffin et al. [12] conducted a study into relaxation in MQW p-i-n diode structures. Selected data from this study is shown in figure 4.4. The Matthews-Blakeslee critical thickness for the onset of dislocation propagation is shown as a dashed line in figure 4.4 and an estimate for the onset of dislocation generation is shown as a solid line.
The samples which showed high dark line densities in figure 4.4 were taken to be relaxed as this feature is indicative of the generation of dislocations at the lower MQW interface. Based on this plot there appears to be good agreement between the predicted and observed values for the onset of dislocation generation. Of the samples with high dark line densities, some showed a further increase in dark line density as the misfit between the relaxed MQW layer and the capping layer became sufficient to cause the generation of dislocations at the upper MQW interface.
In the work by Griffin et al. [12] and other studies [27, 30], strain relaxation in MQW samples was linked to an increase in forward bias dark current, which indicates that the formation of dislocations in MQW solar cells has a negative impact on their performance.

4.1.4 Strain balancing in MQW structures

In 1999, Ekins-Daukes et al. [31] reported the successful application of the technique of strain-balancing to the i-region of an MQW solar cell. Strain-balancing is a technique which

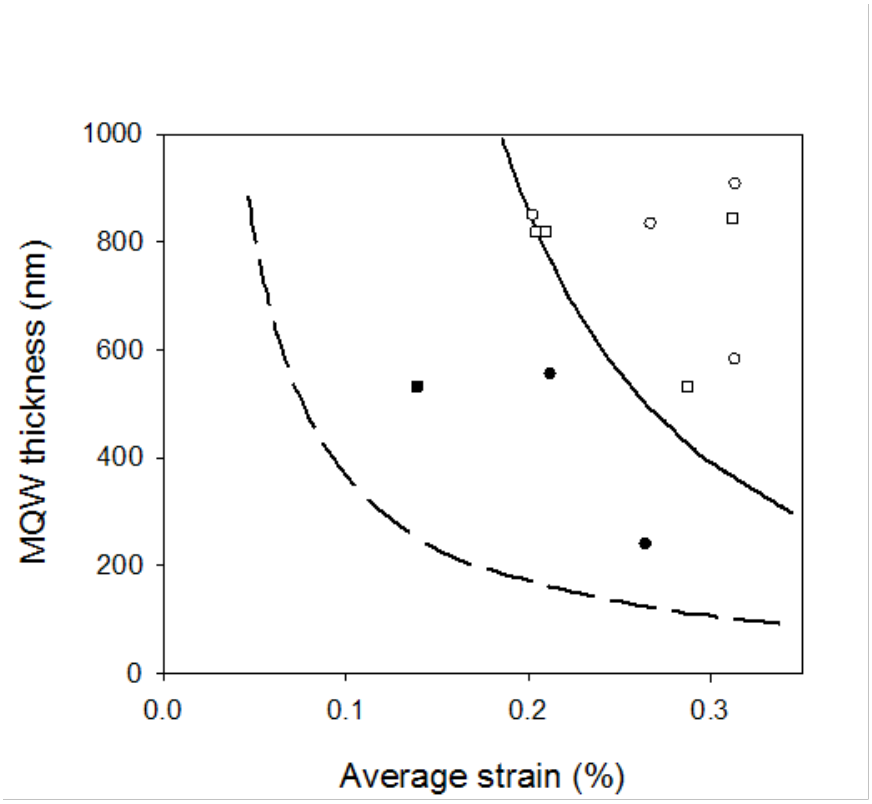

Figure 4.4: Data from [12]. The data points represent a series of MQW samples grown by MBE (squares) and MOVPE (circles). The dashed line represents the Matthews-Blakeslee critical thickness [13] and the solid line represents the critical thickness for dislocation generation, estimated from Drigo et al. [11]. The solid symbols represent samples which show low dark line densities under CL and the empty symbols represent samples which show high dark line densities under CL. Adapted from [12].

had been used for many years in MQW lasers [32, 33] and involves growing layers of alternating tensile and compressive strain. This is shown in figure 4.5.

Determining the average strain in a strain-balanced MQW is not as simple as finding it in a strained MQW. First the average lattice constant $\langle a_{MQW} \rangle$ must be calculated using equation 4.3 [31]:

$$\langle a_{MQW} \rangle = \frac{t_b a_b + t_{qw} a_{qw}}{t_b + t_{qw}} \tag{4.3}$$

where a_b is the free standing lattice constant of the barrier material and a_w is the free standing lattice constant of the well material. The average strain can then be calculated as for bulk heterostructures using equation 4.4.

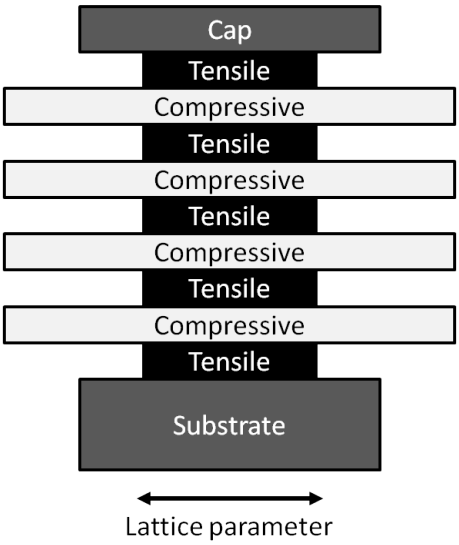

Figure 4.5: Sequencing of layers under alternating compressive and tensile strain in a strain-balanced MQW.

$$\langle f_s \rangle = \frac{\langle a_{MQW} \rangle - a_s}{a_s} \tag{4.4}$$

From equation 4.3 it can be seen that the average lattice constant can be tuned by changing the compositions of the wells and barriers and also by varying the thicknesses of the wells and barriers. By careful optimisation of these parameters the band gaps of the wells and barriers and the average lattice constant of the MQW layer can be tuned independently.

The first report of strain-balanced MQW p-i-n diodes demonstrated an order of magnitude decrease in forward bias dark current compared to the best strained MQW p-i-n diodes at that time [31].

4.1.5 Previous MQW solar cell results

In 2010, Adams et al. [34] reported a world record single junction efficiency of 28.3 % using the InGaAs/GaAsP material system. The record was subsequently retaken by a pure GaAs cell [35], but it was an important demonstration of the competitiveness of the MQW technology.

In 2013, Browne et al. [36] reported the production of commercial multi-junction cells with top and middle junctions comprising InGaAsP/GaInP and InGaAs/GaAsP strain-balanced

MQWs respectively. The median efficiencies of these devices were above 41 %.

4.1.6 Previous work on GaAsBi/GaAs QWs

There have been several studies investigating the growth and characterisation of GaAsBi/GaAs QWs [37–42]. Tominaga et al. [37] demonstrated the growth of 24 period GaAsBi/GaAs MQWs which showed good interfaces as measured by TEM. They investigated the effects of 10 minute thermal annealing cycles on the structural and optical properties of the MQWs as measured by XRD and PL and showed that annealing temperatures below 600 °C had little effect on the PL peak wavelength of the sample. This suggests that overgrowing GaAsBi/GaAs MQWs with material grown at standard MBE growth temperatures (550 - 600 °C) should not adversely affect the MQW region. Tominaga et al. went on to demonstrate the growth of GaAsBi wells with > 10 % Bi content [38] and show the relative temperature insensitivity of the PL emission from the wells [39].

Fan et al. [41] investigated the growth of samples with one and two QWs. Using PL data they demonstrated that the first well in the series was thinner than expected. As the growth conditions were nominally identical for both wells, they argued that the difference must be due to the accumulation of a surface layer of Bi; the first well is thinner because it takes a finite time to build up a surface Bi layer from which Bi can incorporate. They argued that the Bi layer remained on the surface throughout the growth of the intermediate GaAs and AlGaAs layers in their structure, meaning that Bi incorporation could commence immediately as the Bi shutter was opened for subsequent wells. This argument was supported by the observation of a (1×3) surface reconstruction during the intervening GaAs and AlGaAs layers which was not observed in the earlier GaAs and AlGaAs layers [40]. They suggested that the Bi layer acted as a surfactant and improved the material quality of the low temperature grown GaAs and AlGaAs.

Ludewig et al. [42] investigated the MOVPE growth of GaAsBi/GaAs MQWs. Their data also indicated that the first well in the MQW sequence can be smaller than the subsequent wells. When they increased the Bi precursor flux during growth this issue was mitigated, at the expense of the formation of Bi droplets on the growth surface. Although this test was performed using MOVPE, it suggests that raising the Bi flux for MBE grown GaAsBi/GaAs MQWs could produce more uniform QWs. However, the potential issue of droplet forma-

tion reduces the appeal of this technique.

The highest number of GaAsBi wells grown in any previous study is 24 [37]. For photovoltaics, a large well number is required to maximise absorption; it has been suggested that well numbers in excess of 50 should be investigated for multi-junction MQW photovoltaics [10].

4.1.7 Motivation for investigating GaAsBi/GaAs MQWs for solar cell applications

The constraint that each individual layer within the MQW region of a strain-balanced solar cell must not exceed its critical thickness has limited the absorption edge of the InGaAs/GaAsP system to wavelengths < 1000 nm [43]. This is a significantly shorter wavelength than the optimum wavelength for the middle junction in Ge based triple junction photovoltaics (1240 - 1300 nm [44]). The increased rate of band gap reduction in GaAsBi compared to InGaAs (750 meV/% strain for Bi [45], 200 meV/% strain for In [46] (as discussed in section 3.1.2.1)) suggests that GaAsBi may be a more effective material for middle junction MQWs. This chapter aims to investigate the material properties of strained GaAsBi/GaAs MQWs and compare the results to those from the strained InGaAs/GaAs material system.

4.2 Growth and characterisation of GaAsBi/GaAs MQWs

4.2.1 Preliminary growth optimisation

The growth conditions for the QWs grown in this work were selected based on the PL characteristics of preliminary GaAsBi/GaAs 3×8 nm QW samples with 20 nm barriers, grown by Dr Abdul Rahman Mohmad. The samples were grown using a growth rate of 0.6 μm/h and are discussed in more detail in appendix A. The room temperature PL from these samples is shown in figure 4.6 as a function of growth temperature and in figure 4.7 as a function of Bi flux.

Figure 4.6 shows that GaAsBi growth temperatures below ~ 360 °C produce material which does not show room temperature PL. The two spectra that do show good room temperature

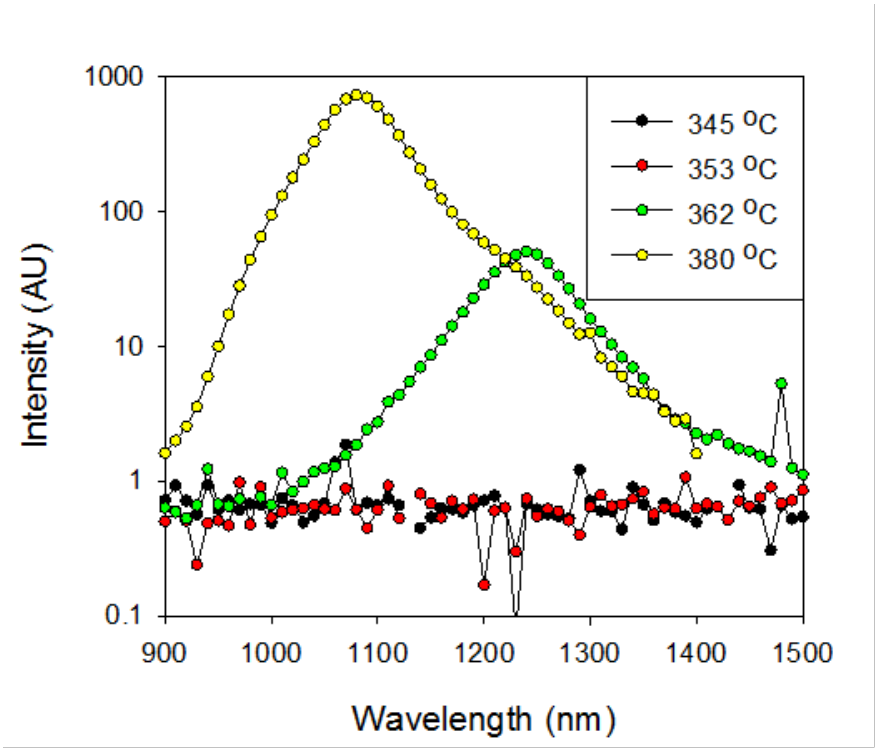

Figure 4.6: Room temperature PL from a series of 3×8 nm QW samples grown at different temperatures using a Bi flux of 0.29 atoms.nm^{-2}s^{-1}.

PL also show a strong dependence of peak wavelength and intensity on growth temperature, suggesting that the Bi content of these samples was limited by the growth temperature. It was decided to grow the MQW diode samples using a growth temperature of 380 °C as the PL from this sample was an order of magnitude brighter than that of the sample grown at 362 °C. The data from figure 4.7 show that the highest PL intensity is achieved at a Bi flux of 0.29 atoms.nm^{-2}s^{-1}. The blueshift of the sample grown using 0.19 atoms.nm^{-2}s^{-1} suggests that, under these conditions, the kinetically limited regime ends at a Bi flux between 0.19 and 0.29 atoms.nm^{-2}s^{-1}. The blueshift of the sample grown with a Bi flux of 0.42 atoms.nm^{-2}s^{-1} indicates that this sample was grown in the temperature limited regime. It was decided to grow using a Bi flux of 0.24 atoms.nm^{-2}s^{-1}. This flux was selected to be sure that the samples were grown in the kinetically limited regime, thus ensuring the highest possible level of repeatability throughout the sample series.

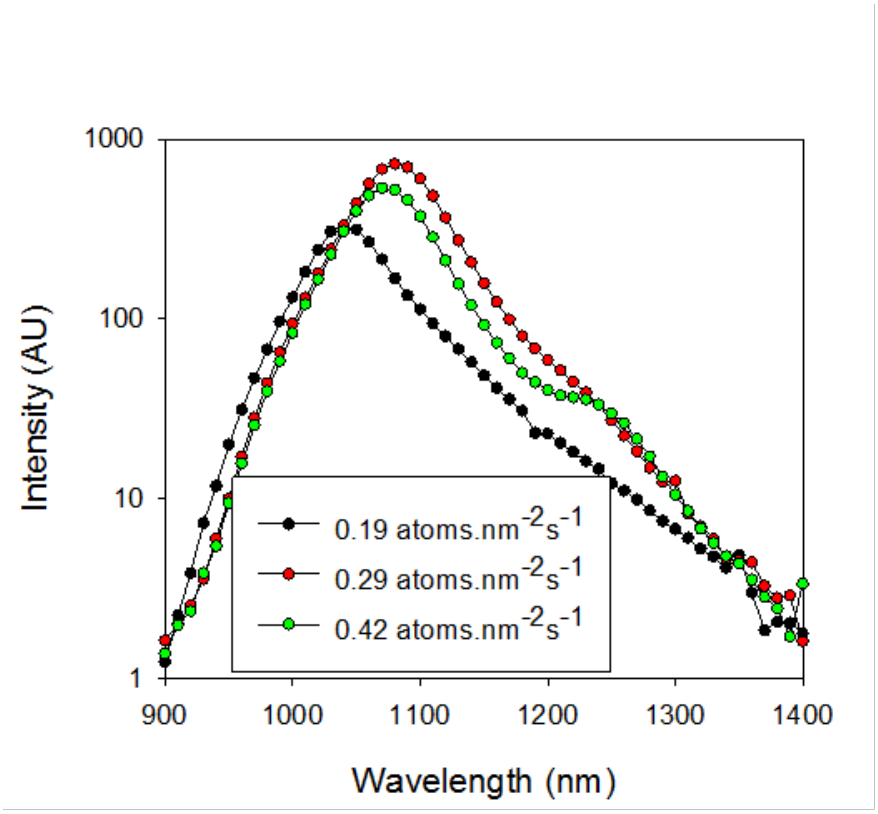

Figure 4.7: Room temperature PL from a series of 3×8 nm QW samples grown using different Bi fluxes at a substrate temperature of 380 °C

4.2.2 Experimental details

In this work a systematic series of GaAsBi/GaAs MQW p-i-n diodes were grown by MBE on GaAs:Si n+ (001) on axis $\pm$ 0.1 ° substrates. The nominal sample structures are shown in figure 4.8. The 200 nm n-type GaAs:Si buffer was grown at 580 °C using a Ga flux of 3.44 atoms.nm^{-2}s^{-1}, corresponding to a growth rate of 0.55 μm/h. This is slightly lower than the growth rate used for the growth parameter optimisation samples; however, as the uncertainty in the Bi flux in this work is $\pm$ 10 % and the uncertainty in the temperature is $\pm$ 10 °C , this difference was assumed to have no material effect on the growth parameters identified as optimal. The As_2 flux used for this region was 6 atoms.nm^{-2}s^{-1}. The n-type AlGaAs cladding region was also grown at 580 °C, using the same Ga flux, an As_2 flux of 7 atoms.nm^{-2}s^{-1} and an Al flux of 1.47 atoms.nm^{-2}s^{-1} to produce $Al_{0.3}Ga_{0.7}As$. After growth of the n-type AlGaAs region, growth was halted for 20 minutes to cool the substrate temperature to 380 °C and the As cracker to 650 °C to provide As_4 for GaAsBi growth.

The i-region comprised a ~620 nm GaAsBi/GaAs MQW with nominally 8 nm wells; the number of wells was varied throughout the series and the barrier thicknesses were designed to keep the i-region thickness constant. The GaAsBi wells were grown using an As_4 flux of 6 atoms.nm^{-2}s^{-1} and a Bi flux of 0.24 atoms.nm^{-2}s^{-1}. Prior to growth of the first well the sample surface was exposed to a Bi flux in the absence of a Ga flux for 30 s. During this time the sample surface reconstruction changed from $c(4\times4)$ to $(n\times3)$, this transition indicates the presence of a Bi layer on the sample surface [47]. This step was performed to prevent the compositional fluctuations in the first few nm of GaAsBi growth as reported by Fan et al. [41]. The sample was then held under the As_4 flux for 30 s to let any excess Bi desorb and to allow the Bi reconstruction layer to anneal before commencing growth of the first well. It was shown in section 3.2.2.4 that the characteristic Bi surface reconstruction lifetime at these temperatures is significantly longer than 30 s, so it was assumed that the reconstruction layer would remain intact during this time. The growth of each layer in the MQW region was separated by a 1 minute pause. These pauses were designed to allow the surface to anneal as it has been shown that growth of bulk GaAsBi leads to undulating surfaces which can adversely affect material quality [48, 49]. Growth was halted again after completion of the MQW region to heat the sample to 580 °C and to heat the As cracker to 1000 °C to produce As_2 for the subsequent layer growth. The p-type cladding and capping regions were grown using the same conditions as the n-type region, using Be as the p-type dopant.

Note that during the growth of the p-type layers, the MQW region is effectively being annealed at 580 °C for approximately 2 h. It seems unlikely this temperature will cause damage to the structure of any fully strained samples, although it will increase the PL intensity of these samples [37, 38, 50–52] and potentially cause degradation to the PL and structure of any partially relaxed samples [53].

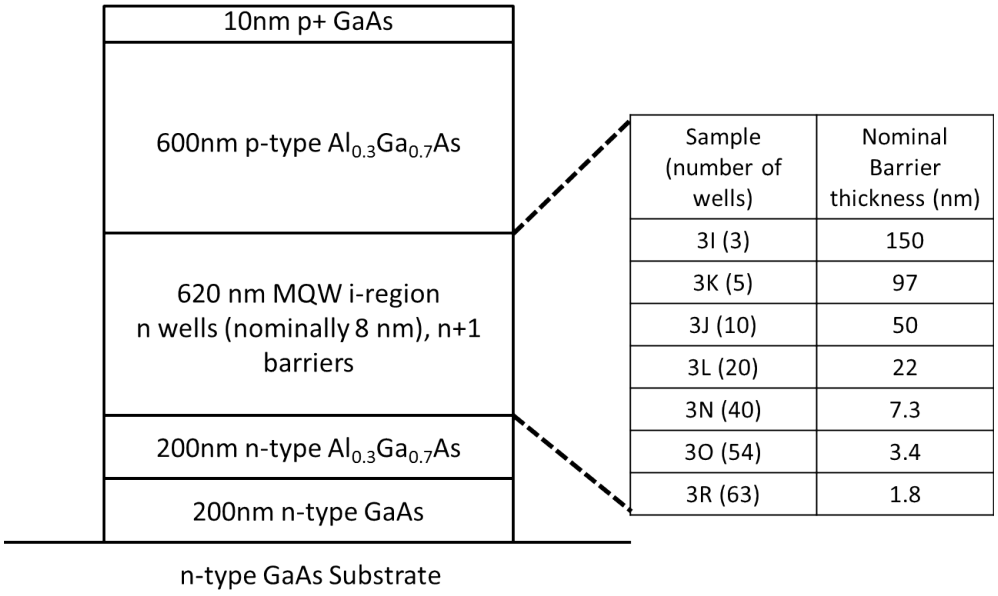

Figure 4.8: Sample structures grown during this work.

4.2.3 Surface profiles

Nomarski images of the surfaces of the MQW samples are shown in figures 4.9 - 4.15. All samples show indications of sub-surface damage with the samples containing more wells showing more damage lines up to 3N (40 wells). Few of the visible lines on the surfaces of the samples with up to 40 wells are orthogonal and are, therefore, not indicative of strain relaxation within the samples [54]. It is more likely that the sub-surface damage occurred as a result of the substrate preparation as described in section 2.1.10. Samples 3O (54 wells) and 3R (63 wells) show a high density of orthogonal sub-surface damage lines. These lines suggest that a relaxation event has occurred in these samples [54]. The image of sample 3R (63 wells) shows signs of significant contamination on the surface prior to growth as there are large regions of very high density metallic droplets on the surface. The edge of one such region is visible in the top right of figure 4.15.

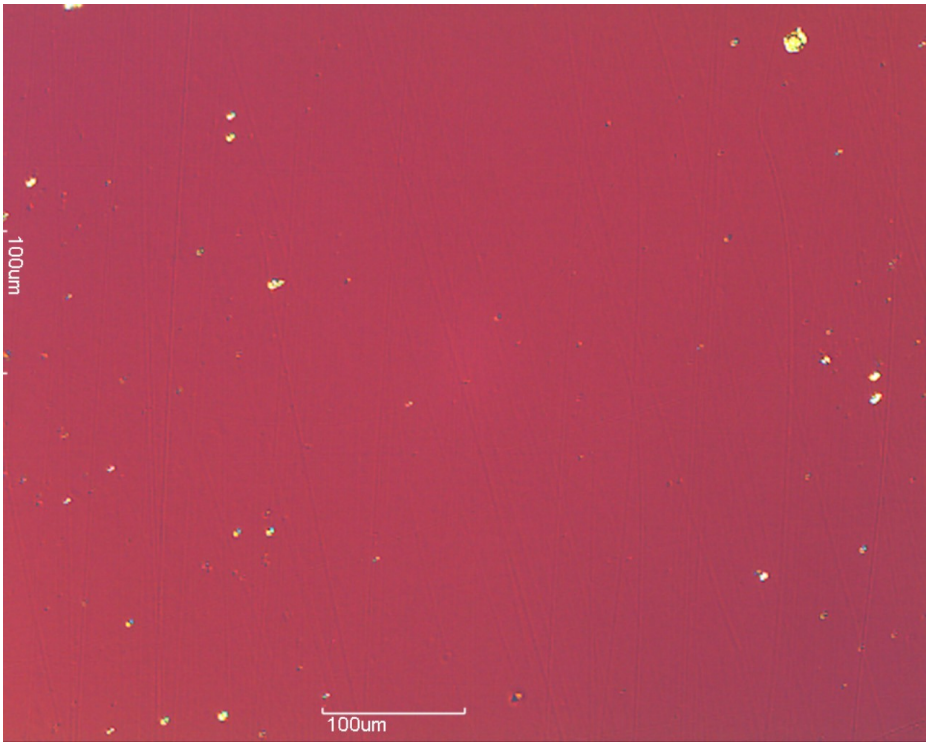

Figure 4.9: Nomarski image of sample 3I (3 wells).

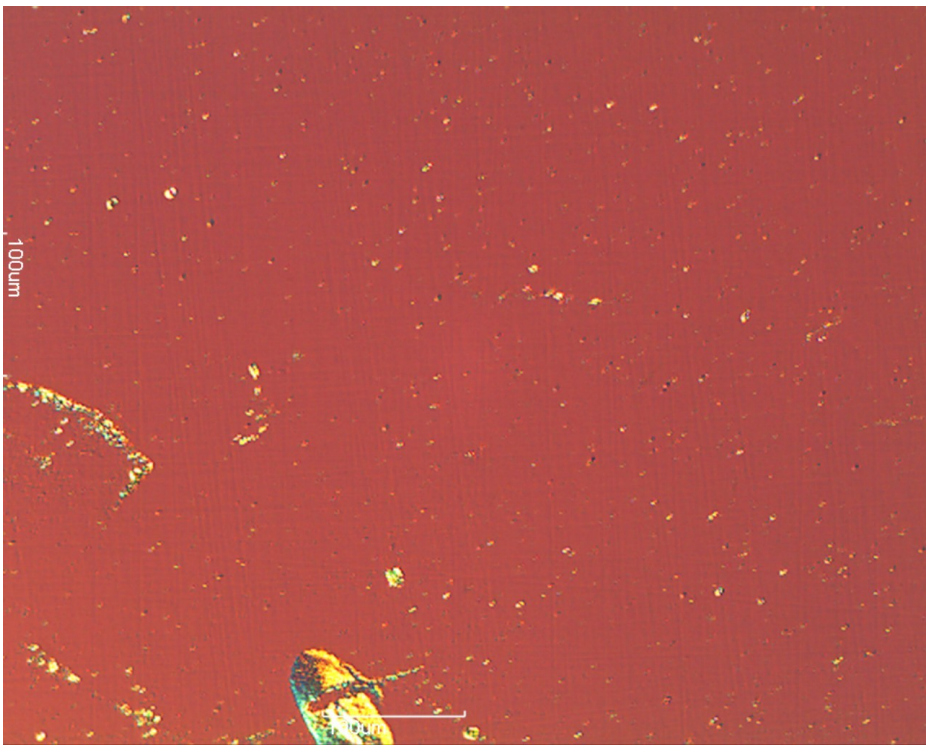

Figure 4.10: Nomarski image of sample 3K (5 wells).

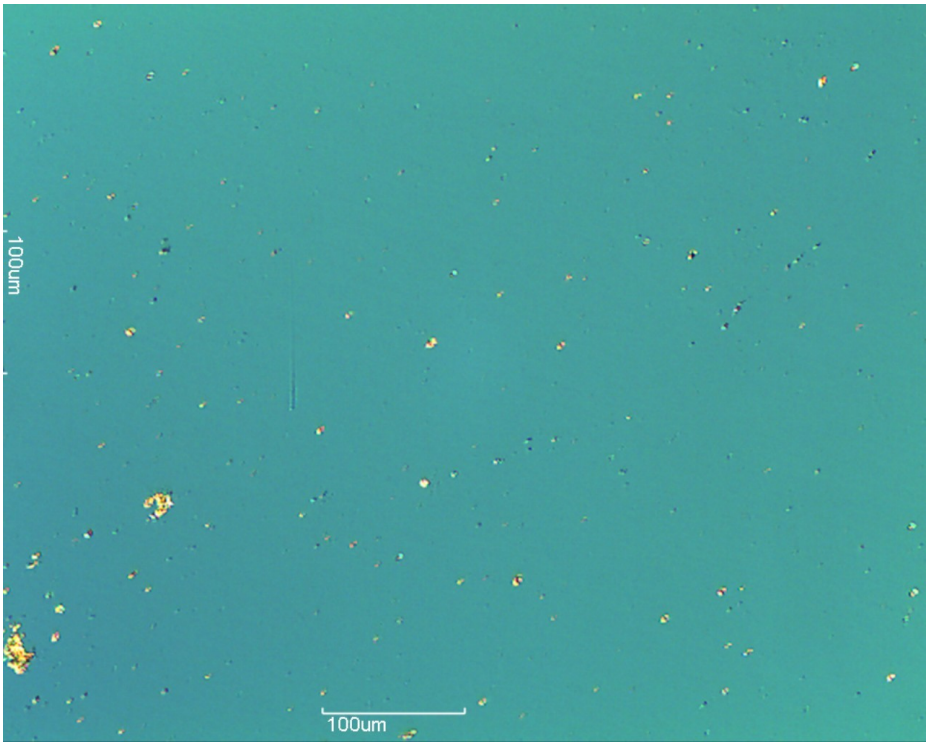

Figure 4.11: Nomarski image of sample 3J (10 wells).

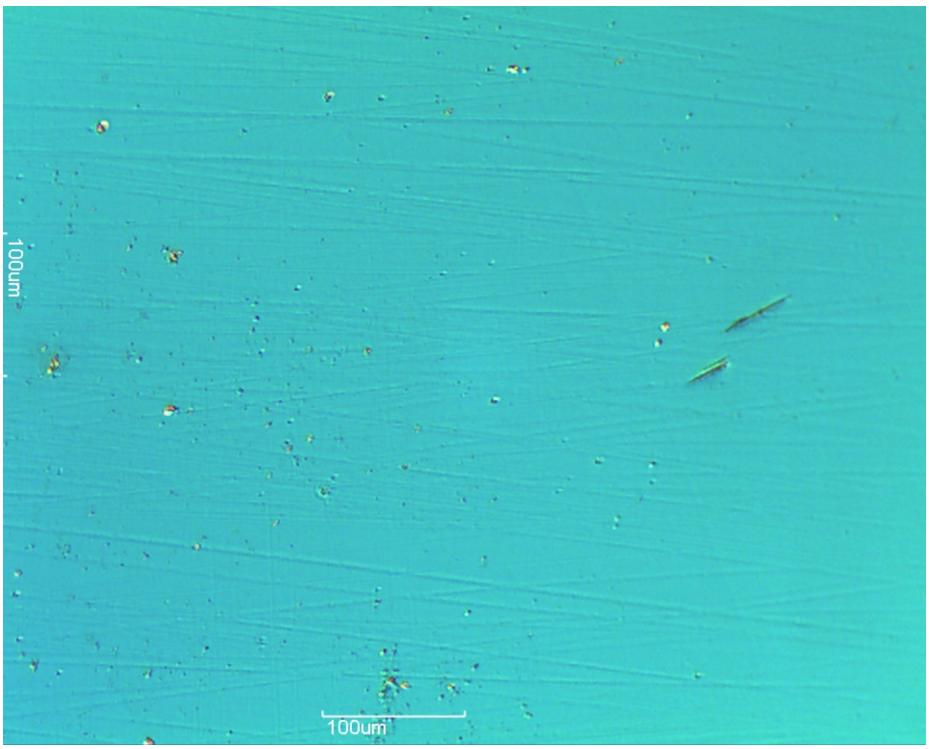

Figure 4.12: Nomarski image of sample 3L (20 wells).

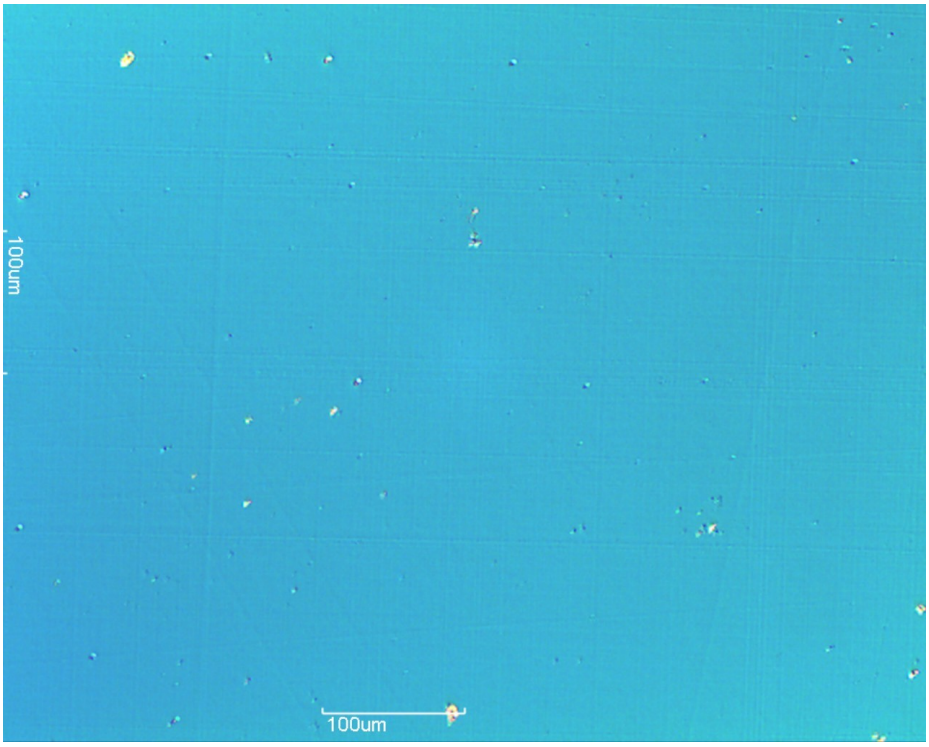

Figure 4.13: Nomarski image of sample 3N (40 wells).

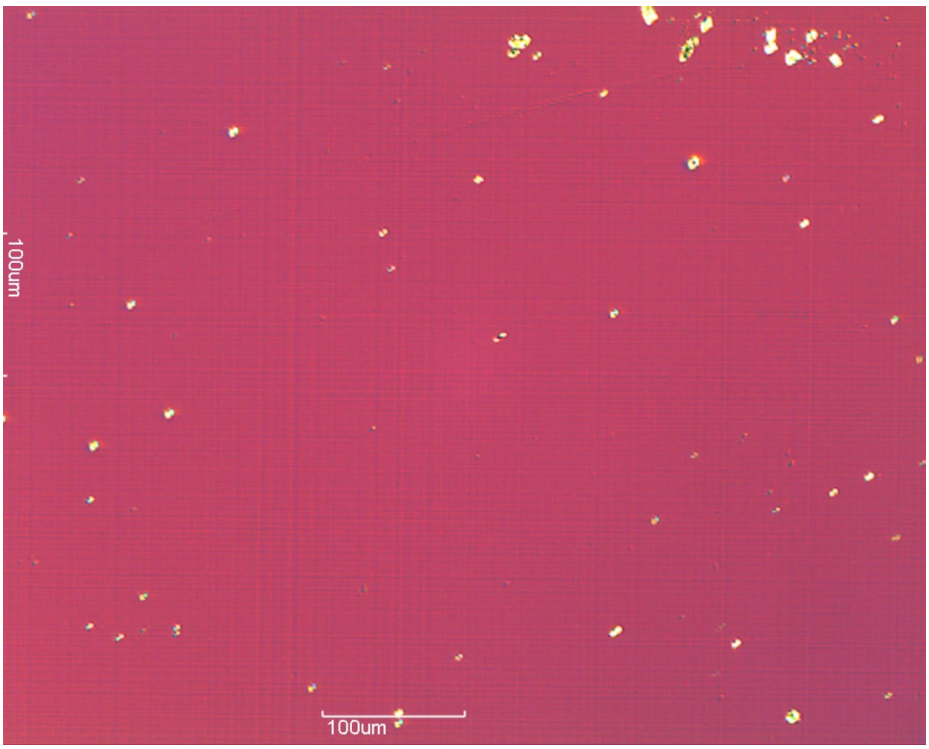

Figure 4.14: Nomarski image of sample 3O (54 wells).

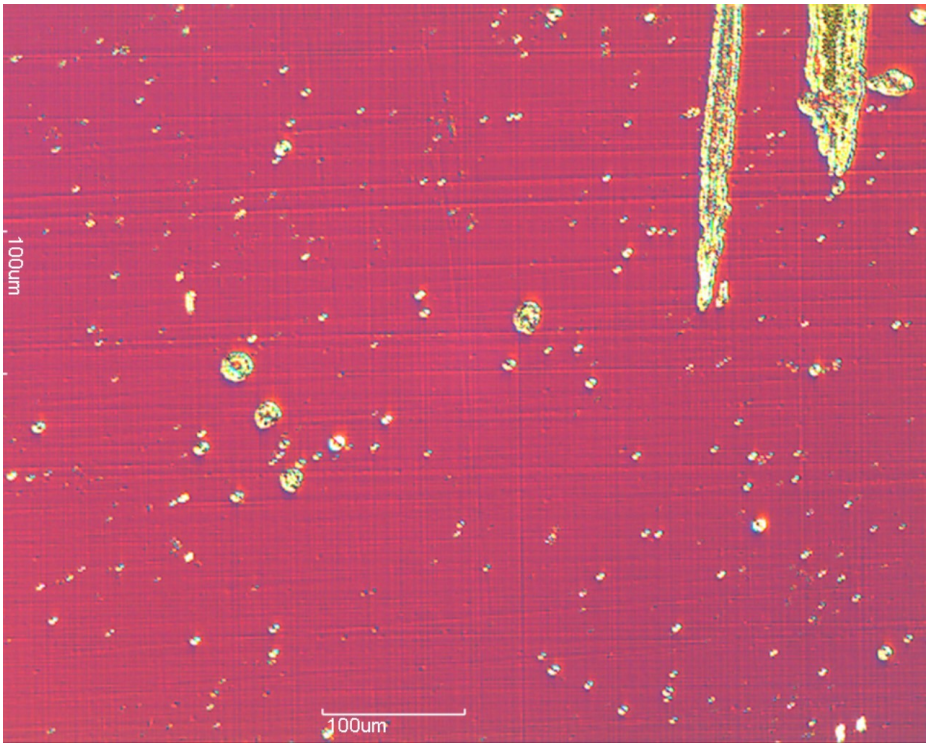

Figure 4.15: Nomarski image of sample 3R (63 wells).

4.2.4 XRD results

Symmetric $\omega - 2\theta$ scans were taken of the (004) reflection of each sample using Cu Kα_1 radiation. These preliminary scans are shown in figure 4.16. All scans show clear superlattice (SL) peaks indicating that MQW regions of good uniformity were grown.

The scans in figure 4.16 were modelled using RADS Mercury software assuming the nominal 8 nm square well profile and a GaBi lattice constant of 6.28 Å [55]. The structural parameters determined from this fitting are shown in table 4.1.

Table 4.1: Initial MQW parameters extracted from XRD data

Sample (number of wells)	Well Bi content (%)	Nominal barrier thickness (nm)	Period (nm)	Average Bi content (%)	SL Peak FWHM (″)
3I (3)	3.2	145	153	0.167	67
3K (5)	2.8	94	102	0.22	58
3J (10)	3.2	57	65	0.39	46
3L (20)	3.2	20.5	28.5	0.9	67
3N (40)	2.8	6.4	14.4	1.56	66
3O (54)	3.5	3.4	11.4	2.46	231
3R (63)	3.0	1.0	9.0	2.67	162

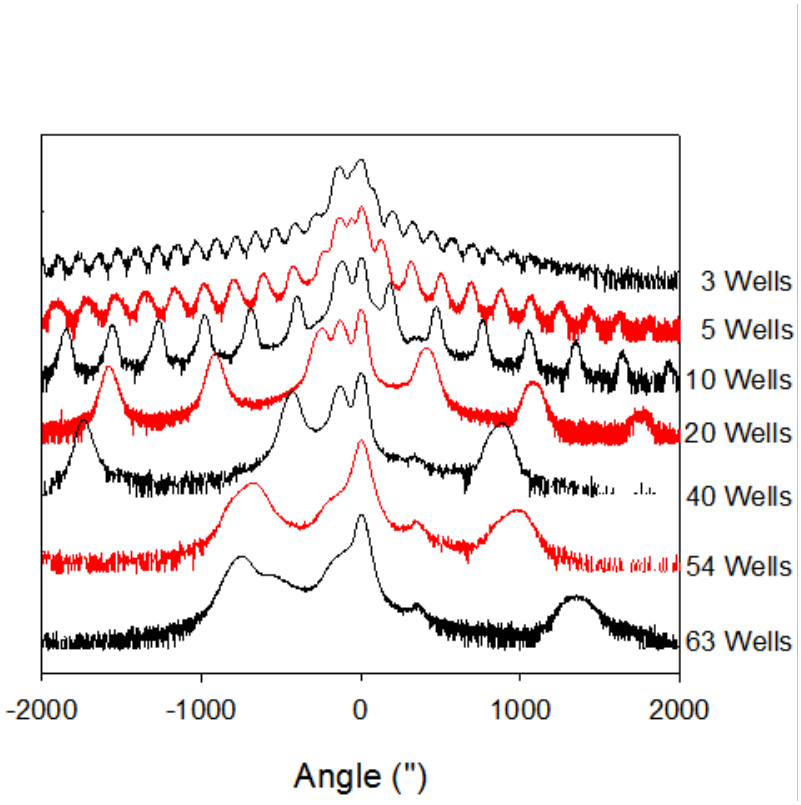

Figure 4.16: Preliminary (004) $\omega - 2\theta$ scans of the samples grown in this work using Cu Kα_1 radiation. The scans have been normalised and vertically offset for clarity.

In order to verify the consistency of the growth throughout this series of samples, the measured average Bi content is plotted against the estimated average Bi content of each sample assuming 8 nm square wells of 3.13 % Bi content as shown in figure 4.17. The Bi content is estimated by performing a least squares fit to the gathered data. The value of 3.13 % Bi is used to get the best fit to the experimental data; however, in practice the Bi content of the wells cannot be quoted to this level of accuracy so the value of 3.1 ± 0.5 % is taken as the value extracted from this plot.

Note that if one ignores the effects of quantum confinement, then the peak PL wavelength of the preliminary sample grown with a Bi flux of 0.29 atoms.nm^{-2}s^{-1} in figure 4.7 (1079 nm) suggests a Bi content of 3.7 % (calculated using the mVBAC model). If this Bi flux is in the kinetically limited regime then one can use the Bi flux ratio to calculate the predicted Bi content of the samples in the MQW series as shown in equation 4.5:

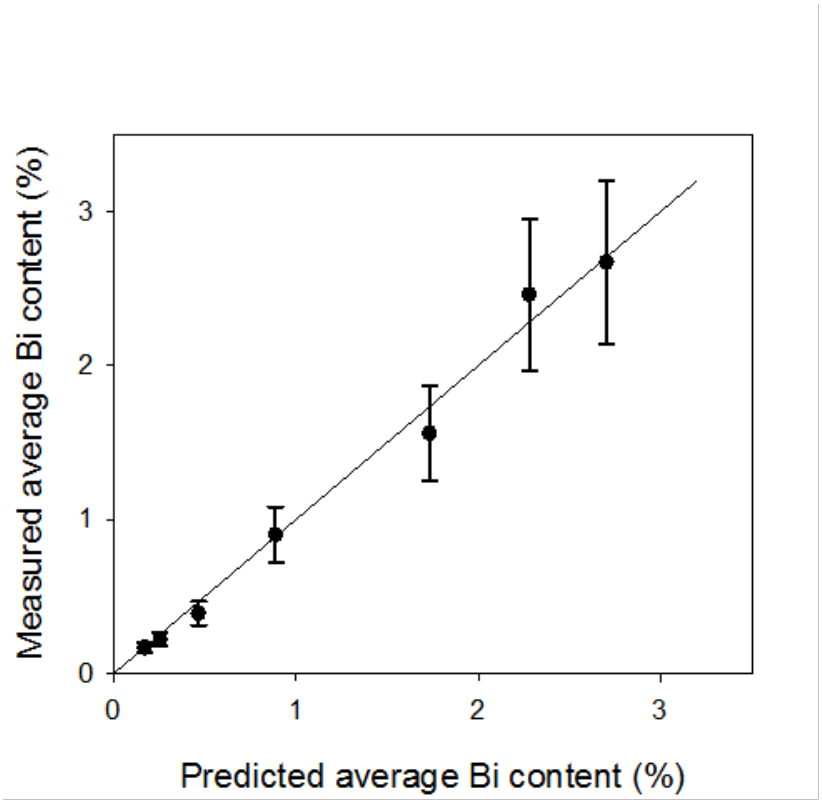

Figure 4.17: The Measured average Bi content of the layers in this work plotted against the predicted average Bi content assuming 8 nm wells of 3.13 % Bi. The error bars were estimated from the range of simulated Bi contents which produced a reasonable fit to the XRD data.

$$x_f = \frac{x_i \times F_f \times GR_i}{F_i \times GR_f} \tag{4.5}$$

$$= \frac{3.7\% \times 0.24 \times 0.6}{0.29 \times 0.55} \tag{4.6}$$

$$= 3.34\,\% \tag{4.7}$$

Where x_f is the Bi content of the QWs in the final sample series; x_i is the Bi content of the QWs in the initial sample series; F_f is the Bi flux used for the final sample series; F_i is the Bi flux used for the initial sample series; GR_i is the growth rate used in the initial sample series; GR_f is the growth rate used in the final sample series. The accuracy of the predicted Bi content is limited to ± 0.5 % but it is very close to the value of 3.13 % found by the least squares fit to the measured XRD data. This result suggests that the MQW samples were grown in the kinetically limited regime as expected and that the growth conditions were

well controlled throughout the series.

Throughout this analysis, the assumption is made that the wells have abrupt interfaces and uniform Bi contents. It has been shown that this assumption is not necessarily accurate [56]; however, in order to extract meaningful data from these layers without using advanced modelling techniques (for example [57]) this assumption is necessary.

4.2.4.1 Reciprocal space maps

The FWHM of each sample listed in table 4.1 is based on the first visible positive SL peak of each sample. The samples with 10 or more wells all have visible +1 SL peaks, whereas the +1 SL peak is obscured by the substrate peak in the 3I (3 wells) and 3J (5 wells) spectra, so the SL peak FWHM is measured from a higher peak in these samples. Any trend in the FWHM for the samples with small numbers of wells is difficult to discern; however, there is a clear increase in FWHM for the samples with 54 and 63 wells. Broadening of the XRD SL peaks is often an indication of roughening of the MQW interfaces [58]. In order to investigate the origin of this broadening, RSMs of the (004) reflections of samples 3N (40 wells) and 3O (54 wells) were performed at different substrate rotations (ϕ_s (see figure 4.24)) by Dr David Walker at Warwick University. The resulting scans are shown in figures 4.18 to 4.23.

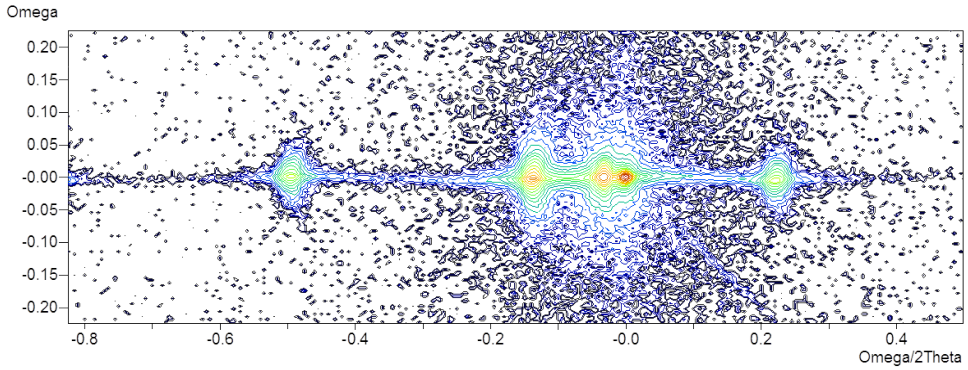

Figure 4.18: (004) RSM of sample 3N (40 wells) at $\phi_s = 0$.

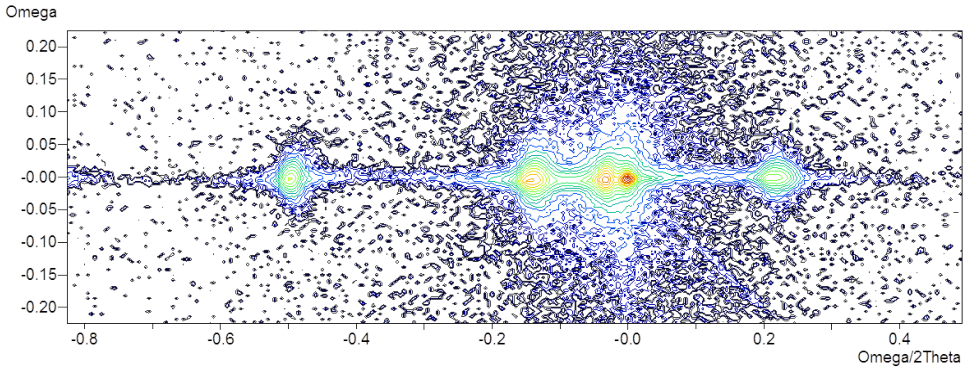

Figure 4.19: (004) RSM of sample 3N (40 wells) at $\phi_s = 45$.

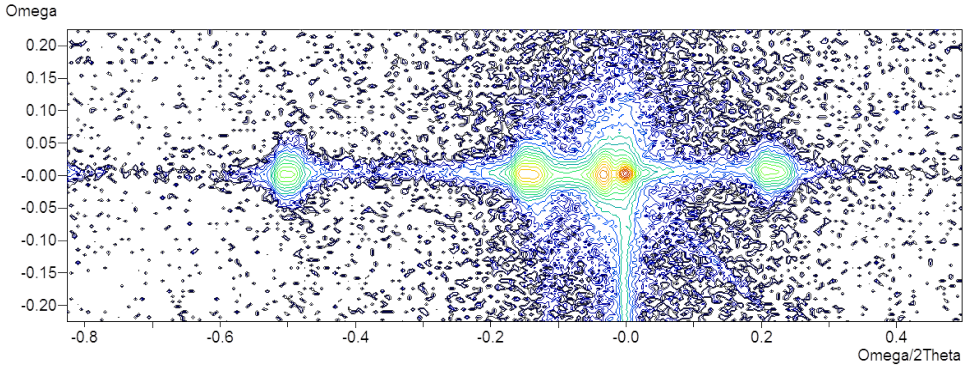

Figure 4.20: (004) RSM of sample 3N (40 wells) at $\phi_s = 90$.

It is clear from the RSMs shown in figures 4.18 to 4.23 that all of the peaks from 3O are much broader than those from 3N. The AlGaAs peak which is visible in the 3N spectra at -0.03 ° appears only as a slight skewing of the substrate peak in the spectra from 3O. What is also clear is that the SL peaks are offset from the substrate peak in omega in the 3O spectra but not in the 3N spectra. This is indicative of a tilting of the MQW layer with respect to the substrate [58, 59]. The tilting cannot be quantified from a single RSM as rotation of the substrate about its surface normal affects the observed tilt angle. The Tilt was quantified by fitting the apparent tilt from the three different substrate angles with a sine curve as shown in figure 4.24.

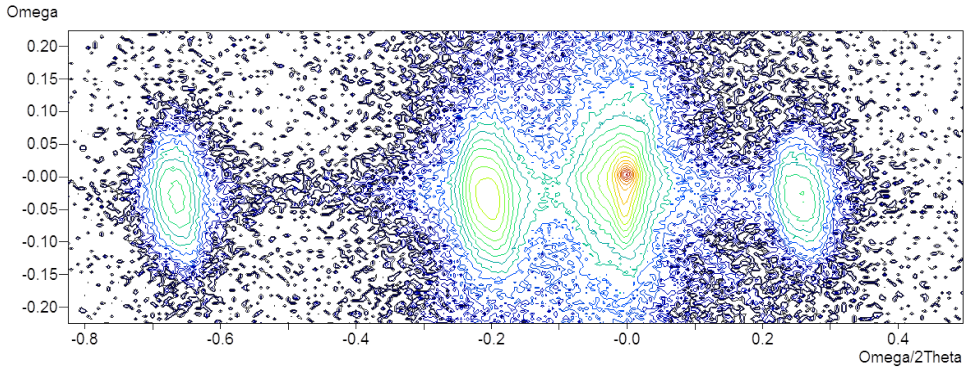

Figure 4.21: (004) RSM of sample 3O (54 wells) at $\phi_s = 0$.

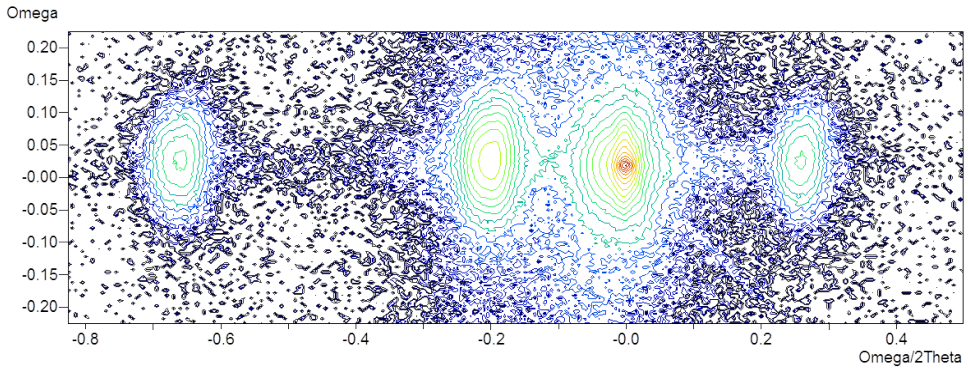

Figure 4.22: (004) RSM of sample 3O (54 wells) at $\phi_s = 45$.

The absolute tilt of sample 3O (54 wells) was determined to be 0.045 ± 0.005 °. The magnitude of the tilt measured for sample 3N (40 wells) is at least an order of magnitude smaller than that of 3O and the spread in the apparent tilt angles for the SL peaks in each scan means that no meaningful fit can be obtained.

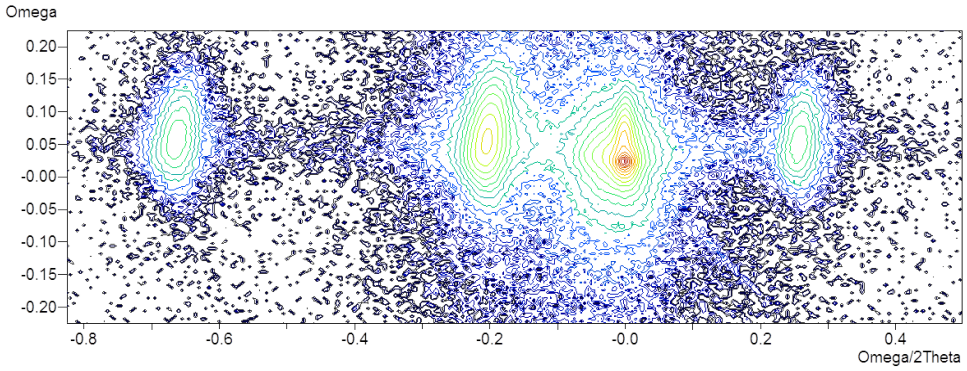

Figure 4.23: (004) RSM of sample 3O (54 wells) at $\phi_s = 90$.

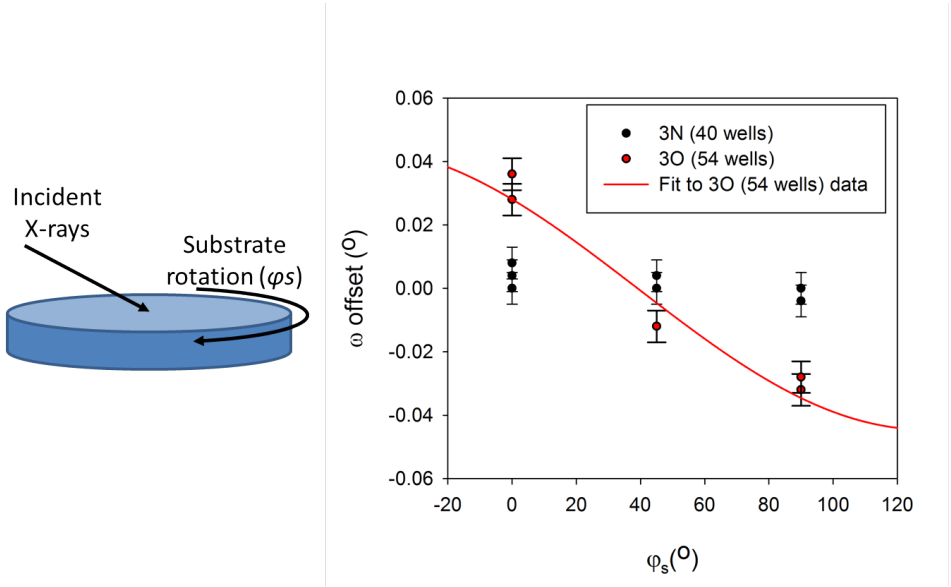

Figure 4.24: Measuring the absolute MQW tilt with respect to the substrate by fitting the apparent tilt as a function of substrate rotation with a sine curve. The black points represent the measured tilt in sample 3N (40 wells) and the red points represent the measured tilt in sample 3O (54 wells). The red curve represents the least squares fit to the 3O (54 wells) data; no fitting was attempted to the data from 3N (40 wells).

4.2.5 Transmission electron microscopy

TEM images were taken of each of the samples in this work by Dr Richard Beanland at Warwick University, with the exception of sample 3I (3 wells), which was not imaged. Images from each of the samples are shown in figures 4.25 - 4.31. Each image includes a scale bar and a label identifying it as either BF or DF and indicating the magnification of the image.

The thickness of the first well in each sample differs from the thickness of the subsequent wells. This issue has been shown by other groups [41, 42] and it was hoped that the Bi prelayer applied to the surface prior to growth would mitigate the effect. In each sample the first well is thicker than the subsequent wells except 3R (63 wells) in which the first well is thinner than the subsequent wells. It is possible that the measurement is disrupted by the poor material quality in sample 3R (63 wells), or that the thin barriers do not effectively remove the excess Bi from the surface, causing a significant Bi prelayer to be present at the start of the growth of subsequent wells.

The images show that each sample contains well defined QWs with a uniform QW period throughout.

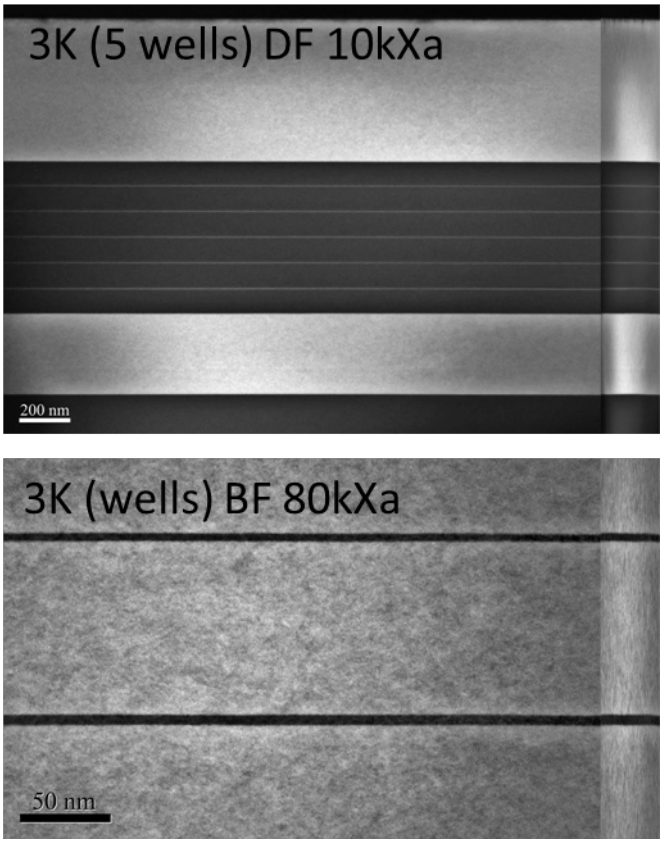

Figure 4.25: TEM images of sample 3K (5 wells). There are no visible dislocations in any of the images of this sample. The BF 80kXa image shows the first two wells grown in this sample. The first well is ~ 20 % thicker than the other wells in this sample.

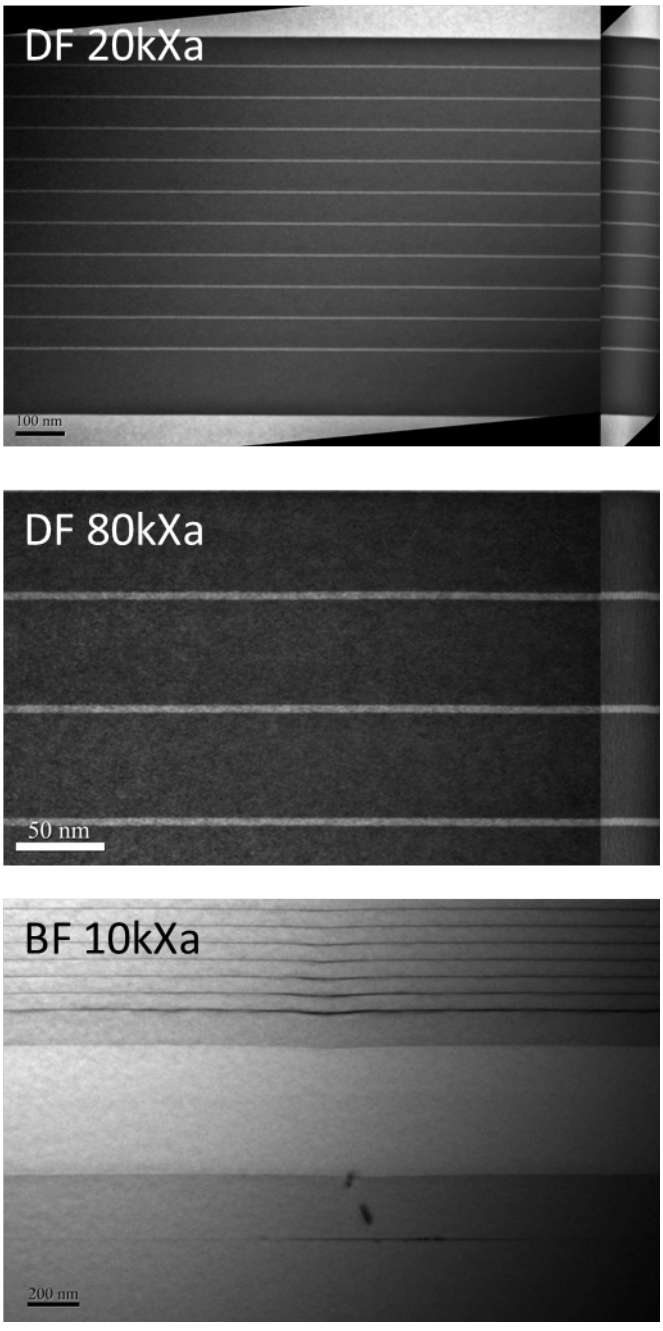

Figure 4.26: TEM images from sample 3J (10 wells). The DF 20kXa and DF 80kXa images show good material quality. It is clear that the first GaAs barrier is thicker than the other barriers, which is due to an error in programming the growth recipe for this sample. The BF 10kXa image shows that there is some structural damage in some areas of the sample, probably caused by the presence of contamination on the sample surface prior to growth. The first well in this sample is ~ 30 % thicker than the other wells.

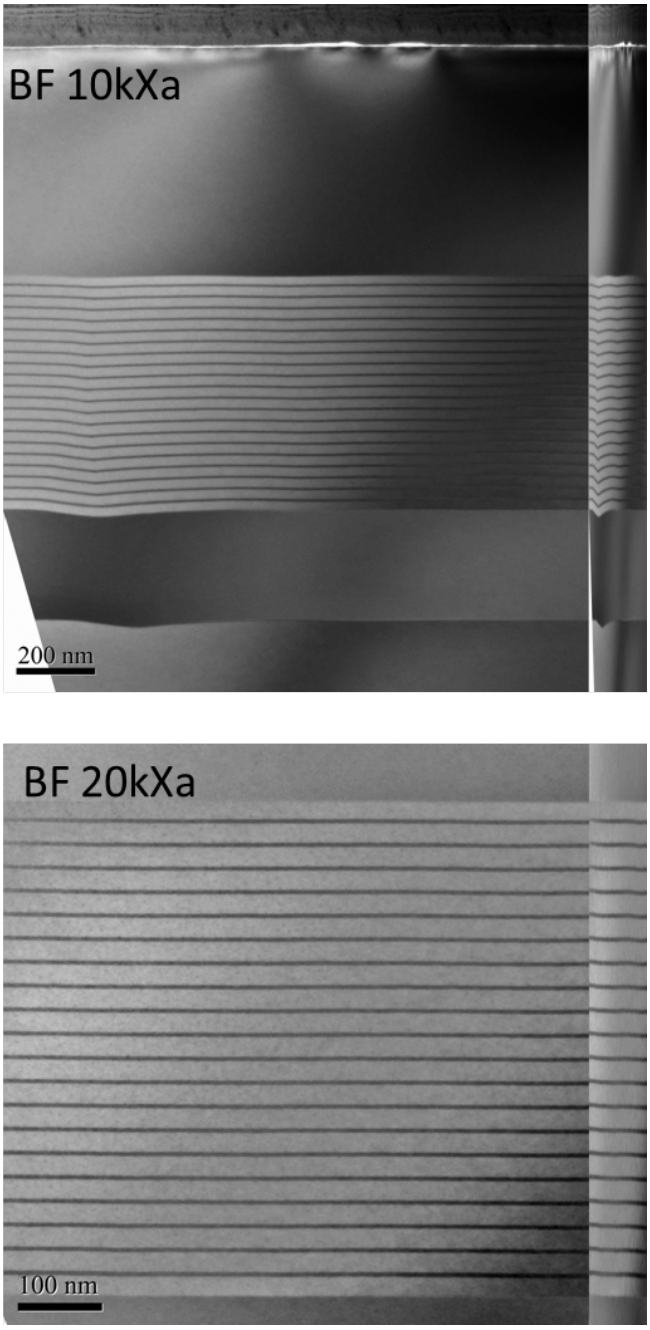

Figure 4.27: TEM from sample 3L (20 wells). The BF 10kXa image shows a significant deformation of the lower part of the MQW region, probably due to contamination of the substrate surface prior to growth. The first well in this sample is ~ 8 % thicker than the other wells.

The images of sample 3L (20 wells) in figure 4.27 show a significant distortion of the MQW region. As the lower AlGaAs cladding region shows a similar distortion, it seems that this is indicative of an issue with contamination on the sample surface prior to growth.

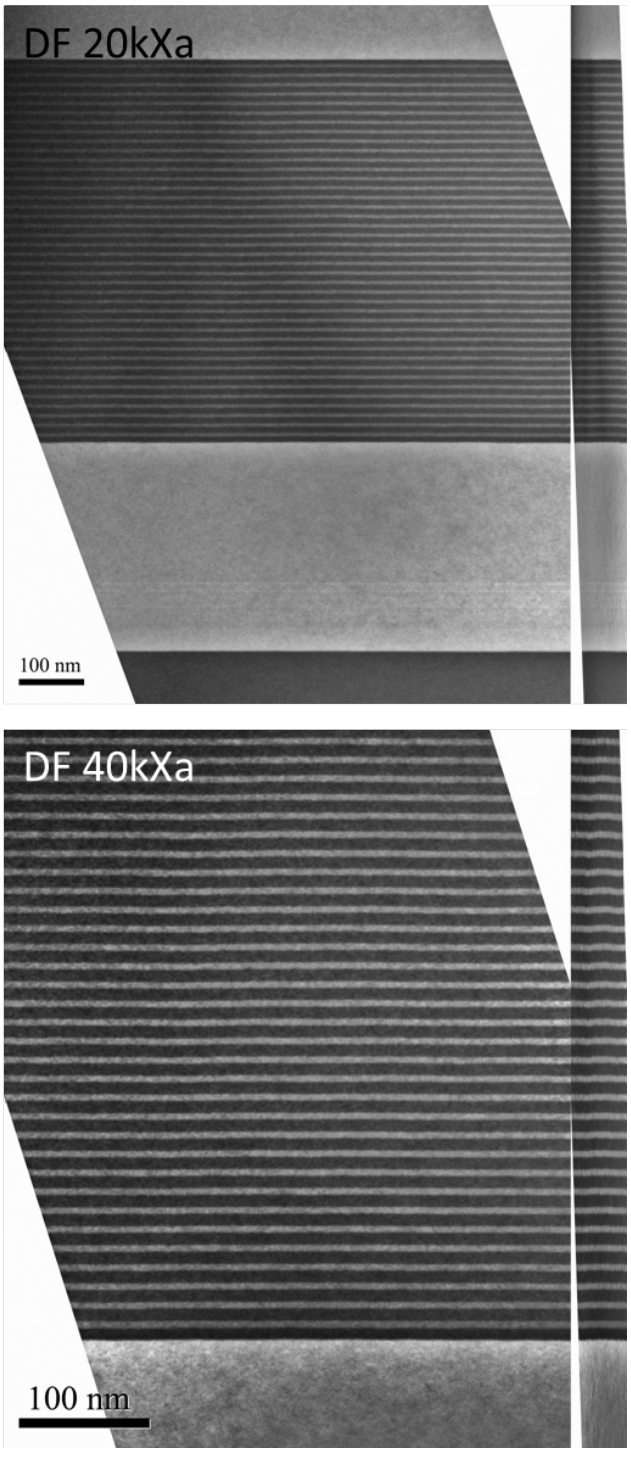

Figure 4.28: TEM from sample 3N (40 wells). None of the images of this sample show any sign of sample surface contamination during growth. The first well is ~ 10 % thicker than the subsequent wells.

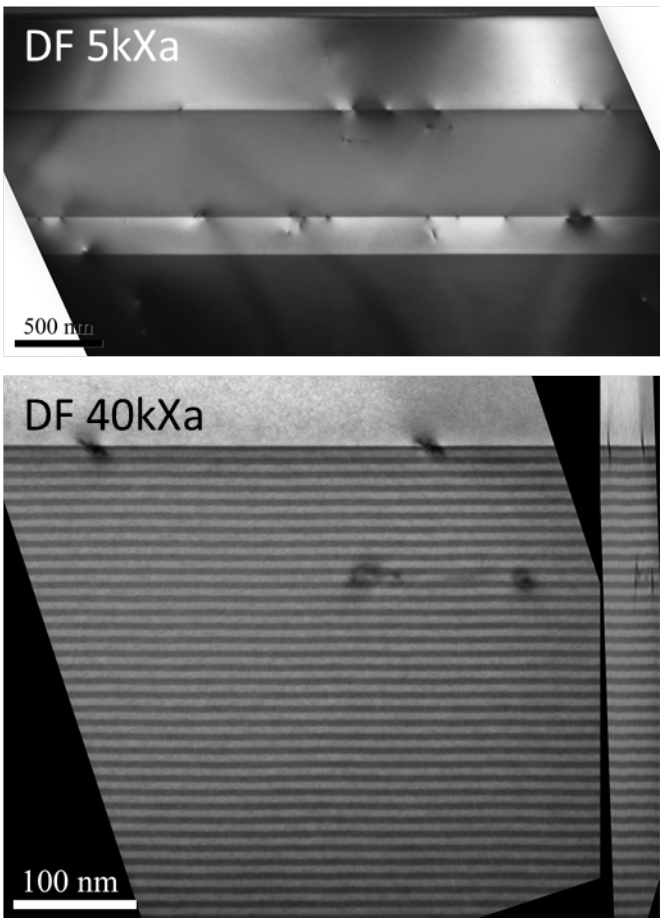

Figure 4.29: TEM from sample 3O (54 wells). There are a significant number of defects visible in this sample. The majority of the defects are located at the upper and lower interfaces of the MQW region. The first well is ~ 5 % thicker than the subsequent wells.

The images of sample 3O (54 wells) in figure 4.29 show a much higher defect density than the images of the samples containing fewer wells. The fact the the defects are mainly localised at the MQW-AlGaAs interfaces suggests that they are due to strain relaxation in the structure.

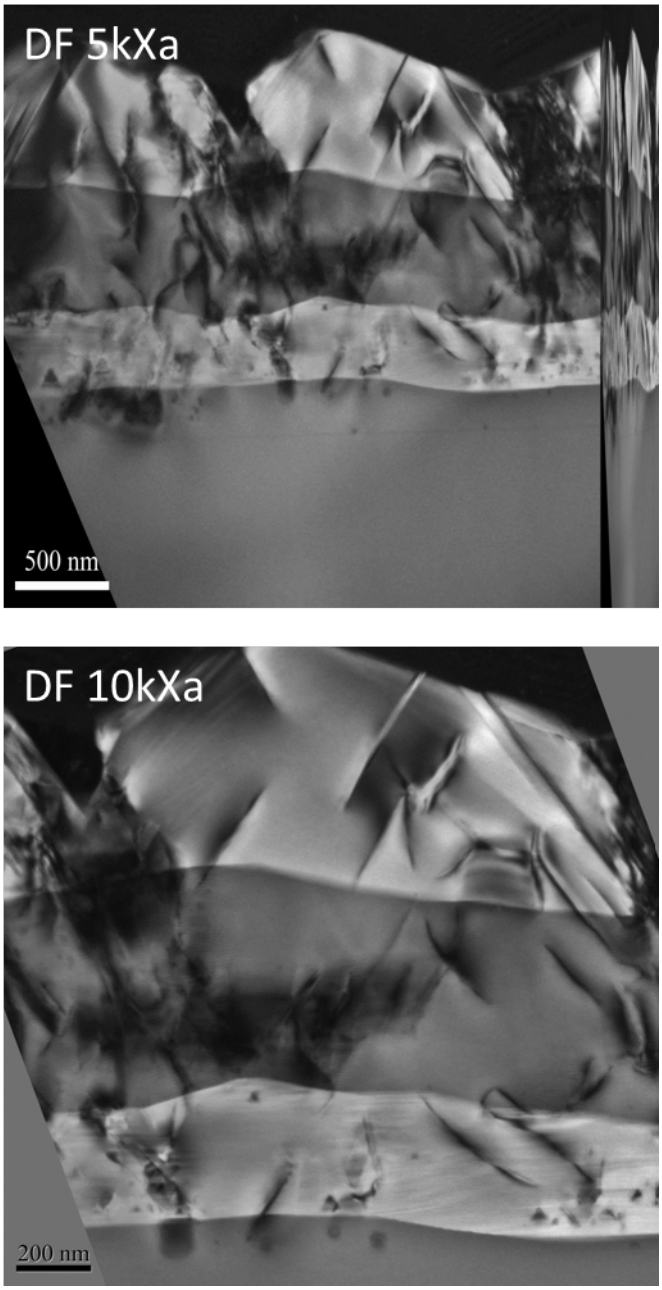

Figure 4.30: Initial TEM images of sample 3R (63 wells). The images from this region of the sample showed extremely poor material quality. The distortion of the lower AlGaAs region suggests that the reason for this poor material quality is contamination of the sample surface.

The images shown in figure 4.30 indicate extremely poor material quality in sample 3R (63 wells). It is probable that the poor quality is caused by contamination of the sample surface prior to growth. The sample was thinned again in order to image a different region of the sample. The subsequent images are shown in figure 4.31.

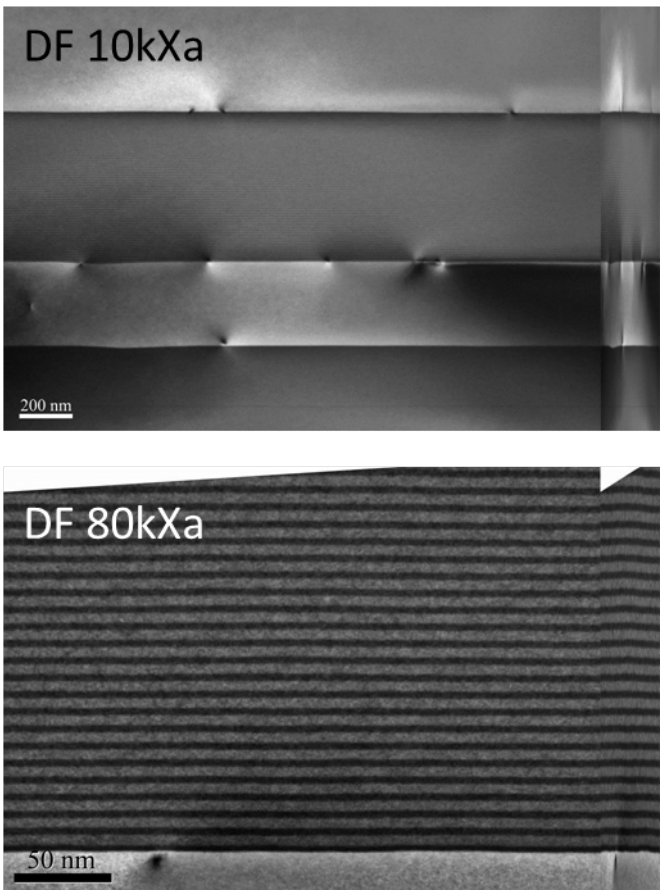

Figure 4.31: Further TEM images from sample 3R (63 wells). There are a significant number of defects visible in this sample. While there are some defects in the lower AlGaAs region suggesting that there was some contamination of the sample surface, the majority of the defects are visible at the upper and lower MQW interfaces. The first well is ~ 14 % thinner than the subsequent wells.

The presence of defects prior to the MQW region in many of the TEM images indicates that there was probably contamination on the sample surfaces prior to growth. However, the absence of dislocations at the MQW region interfaces indicates that dislocation generation has not occurred in samples with up to 40 wells. For samples 3O (54 wells) and 3R (63 wells), the densities of dislocations at the lower MQW interfaces indicate that the MQW region has relaxed with respect to the lower AlGaAs cladding region. The dislocation density at the interface between the MQW region and the upper AlGaAs cladding layer suggests that the AlGaAs cladding has relaxed to the relaxed MQW region.

4.2.6 Photoluminescence

The room temperature PL from the samples is shown in figure 4.32. The range of peak wavelengths and intensities observed in the samples with up to 40 wells is attributed to variations in the atomic fluxes, background pressure and ambient temperature in the MBE machine from growth run to growth run. There is a clear divide between the samples with up to 40 wells and 3O (54 wells) and 3R (63 wells). It is likely that the lattice relaxation observed in the TEM images for these samples (figures 4.29 and 4.31) is responsible for the attenuation of the PL from these samples. Lattice relaxation proceeds via the formation of dislocations which provide non-radiative recombination centres, increasing the rate of SRH recombination and reducing the radiative efficiency of the sample as discussed in section 2.2.2. Strain relaxation could also explain the redshift observed in the PL of these samples; compressive strain acts to increase the bandgap of the material [60]. An alternative explanation for the redshift and attenuation of the PL peaks from 3O (54 wells) and 3R (63 wells) is that the barriers in these samples are too thin to maintain effective quantum confinement (see table 4.1). If the electron wavefunctions are not effectively confined by the individual wells then the carrier confinement energy will be lost, redshifting the PL peak. Also, the electrons and holes would not be held in close proximity by the wells, reducing the wavefunction overlap and reducing the radiative efficiency.

The room temperature PL characteristics for each sample are listed in table 4.2.

Table 4.2: MQW sample PL characteristics.

Sample (number of wells)	Peak wavelength (nm)	Peak energy (eV)	FWHM (meV)	Peak intensity (normalised to 3N)	Integrated PL intensity (normalised to 3N)
3I (3)	1044	1.188	88	0.588	0.644
3K (5)	1046	1.186	77	0.714	0.690
3J (10)	1074	1.155	80	0.714	0.782
3L (20)	1060	1.171	80	0.385	0.405
3N (40)	1058	1.173	78	1	1
3O (54)	1112	1.116	79	0.018	0.020
3R (63)	1106	1.122	92	0.036	0.044

The average PL peak energy of the samples with up to 40 wells is 1.175 eV and the average peak energy of 3O (54 wells) and 3R (63 wells) is 1.119 eV. Meaning the average redshift between the two groups of samples is 56 meV. If the redshift is caused by strain relaxation

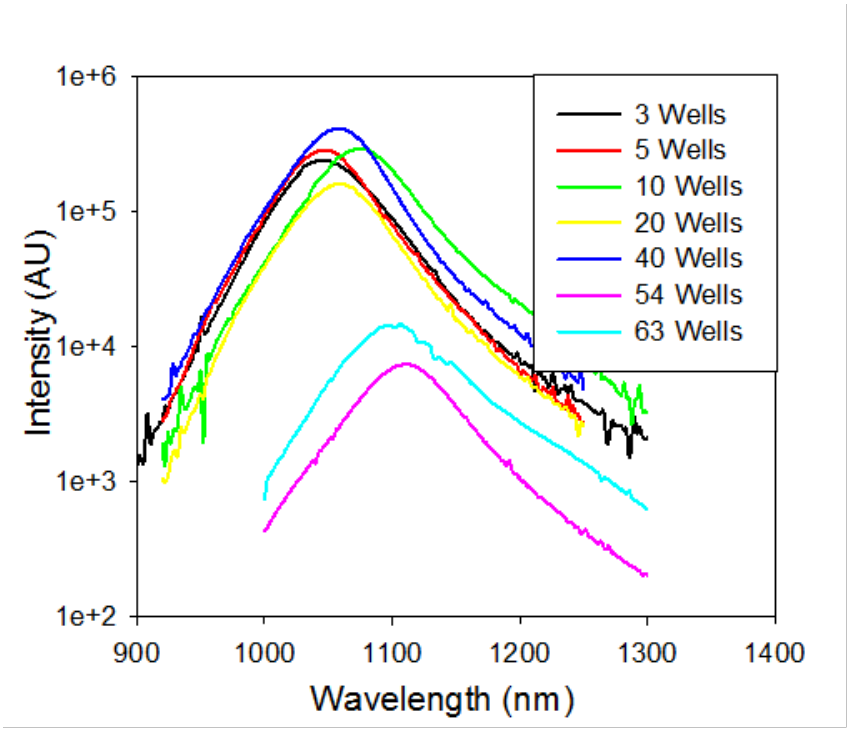

Figure 4.32: Room temperature PL from the MQW samples. The intensity axis has a logarithmic scale.

or loss of carrier confinement, then the theoretically calculated energies associated with these effects must be comparable to the observed redshift. In order to assess the feasibility of these effects being responsible for the redshift, the energy of each effect is calculated. These calculations are detailed in section 4.2.7.

4.2.7 Effect of strain and quantum confinement

4.2.7.1 Quantum confinement calculations

Singh [61] shows that the confinement energy of a finite QW can be approximated by equation 4.8:

$$E_q = \frac{\Delta E}{2} - \frac{\pi^2\hbar^2}{4m_c^* t_{qw}^2}\left[\sqrt{\left(1 + \frac{32\Delta E^2 t_{qw}^4 m_c^{*2}}{\pi^6\hbar^4}\right)} - 1\right] \tag{4.8}$$

where ΔE is the band offset; m_c^* is the carrier reduced mass; t_{qw} is the well width. For this calculation the electron and hole reduced masses were taken to be $0.06\,m_0$ [62] and $0.55\,m_0$

[63] respectively, where m_0 is the mass of a free electron. The values for well width and Bi content used in the calculations were varied to maintain the average Bi content in each sample as shown in table 4.1. The band offsets for a given well Bi fraction were calculated using the mVBAC model. By varying the well width and Bi content, the predicted transition energy (E_{GaAsBi} + $E_q(valence)$ + $E_q(conduction)$) was brought into coincidence with the observed PL peak energy for each sample. The results of this calculation are shown in table 4.3.

Table 4.3: QW parameters for each sample, determined by fitting the estimated first QW transition to the PL peak energy and using the average Bi content for each sample as derived from XRD.

Sample (number of wells)	Estimated well Bi content (%)	Estimated well width (nm)	Band gap estimated by mVBAC (eV)	Total confinement energy (meV)
3I (3)	3.6	7.0	1.156	52
3K (5)	3.6	7.0	1.156	52
3J (10)	4.4	5.5	1.106	68
3L (20)	4.0	6.3	1.131	60
3N (40)	4.0	6.3	1.131	60
3O (54)	5.4	4.6	1.047	86
3R (63)	5.2	4.8	1.058	82

For the samples with up to 40 wells the estimated Bi contents are all within 10 % (relative) of 4 % Bi, which is a reasonable variation given that the uncertainty in the growth conditions was ± 10 % for the group V fluxes, ± 1 % for the group III fluxes and ± 10 °C for the sample temperature as discussed in section 2.1.9.

The well widths are all within 13 % (relative) of 6.3 nm. This is significantly thinner than the nominal well width of 8 nm. The uncertainties mentioned above will have an effect on the real well width; however, it is likely that the main error in this value is derived from the assumption that the wells have square profiles. Previous work has shown that GaAsBi QWs do not necessarily have uniform Bi contents [42, 56]. If the QWs in these samples are not uniform then that will alter both the band gap and the confinement in the wells and lead to an error in the above calculations. As the purpose of this section is to estimate the confinement energy in these samples and compare it with the redshift observed in the PL spectra of samples 30 (54 wells) and 3R (63 wells), the mean of the estimated confinement energies in samples 3I - 3N is used (58 meV).

The results of the calculations for samples 3O (54 wells) and 3R (63 wells) are noticeably different to those of the other samples. If the PL peak wavelength is modified by a loss of confinement or lattice relaxation then the calculations will overestimate the Bi content in these samples to produce the right transition energy, which would explain the increase in the calculated Bi contents of these samples. This Bi content overestimate will cause an underestimation of the well widths. The well width and ground state transition energy in these calculations are plotted as functions of Bi content in figure 4.33 to highlight this point. It should be noted that Singh states that equation 4.8 cannot accurately predict the confinement energy of an MQW system with thin barriers; however, any deviation from the form of equation 4.8 must indicate the electron wavefunctions overlapping several wells and, hence, would suggest loss of confinement as a cause of the redshift and attenuation shown in figure 4.32.

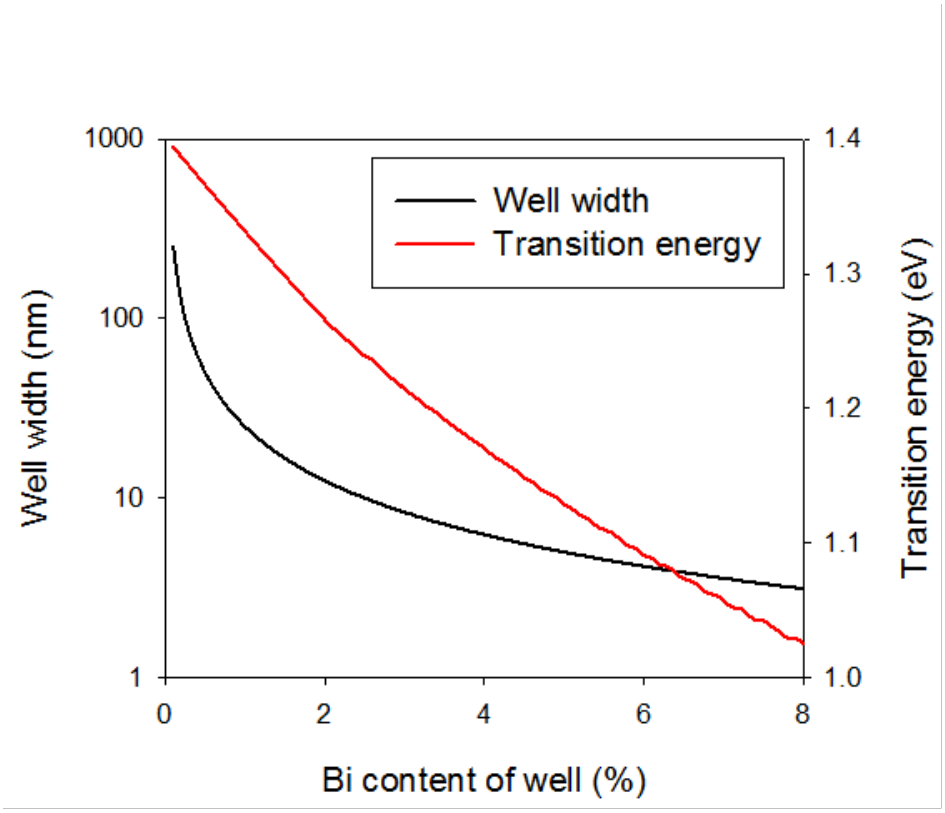

Figure 4.33: Well width and ground state transition energy as a function of Bi content in these calculations. This plot assumes that the total Bi content of the well is fixed and equal to the Bi content of a 1 nm well containing 24 % Bi.

4.2.7.2 Strain band gap modification calculations

The effect of strain on the heavy hole transition energy in these samples was calculated using the approach of Batool et al. [64]. The heavy hole transition energy (E_g^{HH+}) is given by equation 4.9:

$$E_g^{HH+} = E_{g0} + \delta E_H + \delta E_s \tag{4.9}$$

where E_{g0} is the unstrained transition energy; δE_H is the band gap modification due to hydrostatic strain; δE_s is the band gap modification due to shear strain. The band gap modifications due to hydrostatic and shear strain are given by equations 4.10 and 4.11:

$$\delta E_H = P_H(2\epsilon_{xx} + \epsilon_{zz}) \tag{4.10}$$

$$\delta E_s = P_S(\epsilon_{zz} - \epsilon_{xx}) \tag{4.11}$$

where ϵ_{xx} is the in plane biaxial strain; ϵ_{zz} is the strain in the growth direction; P_H and P_S are the hydrostatic and shear deformation potentials respectively. The shear deformation potential was calculated using equation 4.12:

$$P_S = 2000 + (163 \times x)meV \tag{4.12}$$

as deduced by Batool et al. [64]. The hydrostatic deformation potential was calculated using equation 4.13:

$$P_H = P_{Hc} + P_{Hv} \tag{4.13}$$

where P_{Hc} and P_{Hv} are the the conduction band and valence band hydrostatic deformation potentials respectively. These values were assumed to be the same as those of GaAs ($P_{Hc} = -7.17\,\text{eV}$; $P_{Hv} = -1.16\,\text{eV}$) [65]. The values of ϵ_{xx} and ϵ_{zz} are given by equations 4.14 and 4.15 respectively:

$$\epsilon_{xx} = \frac{(a_{GaAs} - a_{GaAsBi})}{a_{GaAsBi}} \tag{4.14}$$

$$\epsilon_{zz} = -\left(\frac{2c_{12}}{c_{11}}\right)\epsilon_{xx} \tag{4.15}$$

where a_{GaAs} is the GaAs lattice constant; a_{GaAsBi} is the GaAsBi lattice constant; c_{11} and c_{12} are the elastic constants of GaAsBi. c_{11} and c_{12} are assumed to be the same as for GaAs ($c_{11} = 12.21 \times 10^{11} \frac{\text{dyn}}{\text{cm}^2}$; $c_{12} = 5.66 \times 10^{11} \frac{\text{dyn}}{\text{cm}^2}$ [65]). a_{GaAsBi} was calculated using Vegard's law assuming a GaBi lattice constant of 6.28 Å [55], using the results from the quantum confinement calculations shown in table 4.3. The band gap modification due to strain for each sample is shown in table 4.4 along with the modification of the ground state transition energy due to strain (see figure 4.34) and the average strain throughout each sample's MQW region.

Table 4.4: Effect of strain on the first QW transition of each sample.

Sample (number of wells)	Band gap modification due to strain (meV)	Ground state transition modification due to strain (meV)	Average strain (%)
3I (3)	56	32	0.026
3K (5)	56	30	0.033
3J (10)	69	49	0.052
3L (20)	62	40	0.097
3N (40)	62	42	0.185
3O (54)	87	69	0.244
3R (63)	83	64	0.284

The samples with up to 40 wells show ground state transition modifications of 30 - 42 meV, this is not enough to account for the redshift seen in samples 3O (54 wells) and 3R (63 wells) in figure 4.32. The larger values of strain induced transition energy change calculated for samples 3O (54 wells) and 3R (63 wells) are probably due to the overestimation of the Bi content as shown in table 4.3; this would cause the calculated strain induced band gap modification in these samples to be unrealistically large.

The values in table 4.3 and table 4.4 represent upper limits on the confinement energy and effect of strain on the ground state transition energy. Given the evidence from Nomarski, XRD and TEM for significant relaxation in samples 3O (54 wells) and 3R (63 wells) and that relaxation of strain is not enough to fully account for the PL redshift of these samples, it seems likely that strain relaxation and loss of confinement contribute to that redshift. Note

that the effect of strain on the PL peak position will be enhanced if there is no quantum confinement as quantum confinement acts to reduce the impact of band gap on PL peak position, as shown in figure 4.34.

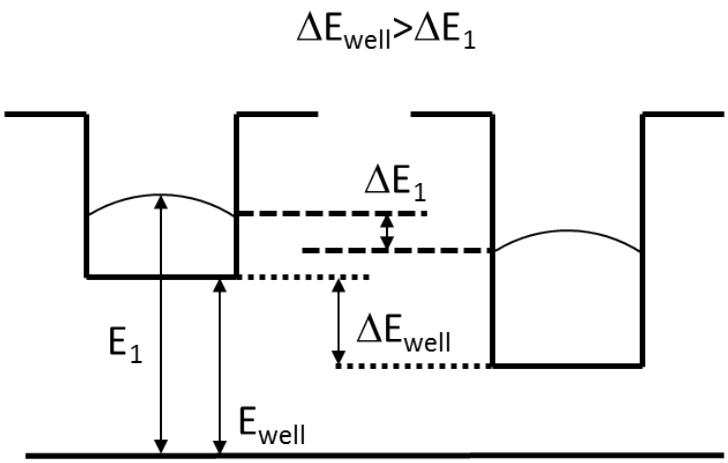

Figure 4.34: Simplified band diagram showing how quantum confinement causes the PL peak position to vary sub-linearly with respect to the bandgap.

4.3 Comparison of GaAsBi/GaAs and InGaAs/GaAs MQWs

The results of Griffin et al. [12] are shown in figure 4.35 along with the two estimated critical thickness lines of Matthews and Blakeslee [13] and Drigo et al. [11] and the results from this work.

The results from this work appear to be consistent with the predicted dislocation generation line of Drigo et al. However, it must be noted that there is a large difference in average strain between samples 3N (40 wells) (strained) and 3O (54 wells) (relaxed), so it is difficult to determine how well the samples from this work agree with the prediction of Drigo et al. Another point to note is that Griffin et al. used cathodoluminescence to detect regions of non-radiative recombination in their MQWs, allowing for a very sensitive determination of the defect density. In this work the most sensitive technique used to detect defects was TEM, which is not sensitive to areas of non-radiative recombination. The technique used to determine the onset of relaxation has been shown to be of critical importance [20], so care must be taken when comparing results. However, this result suggests that InGaAs and

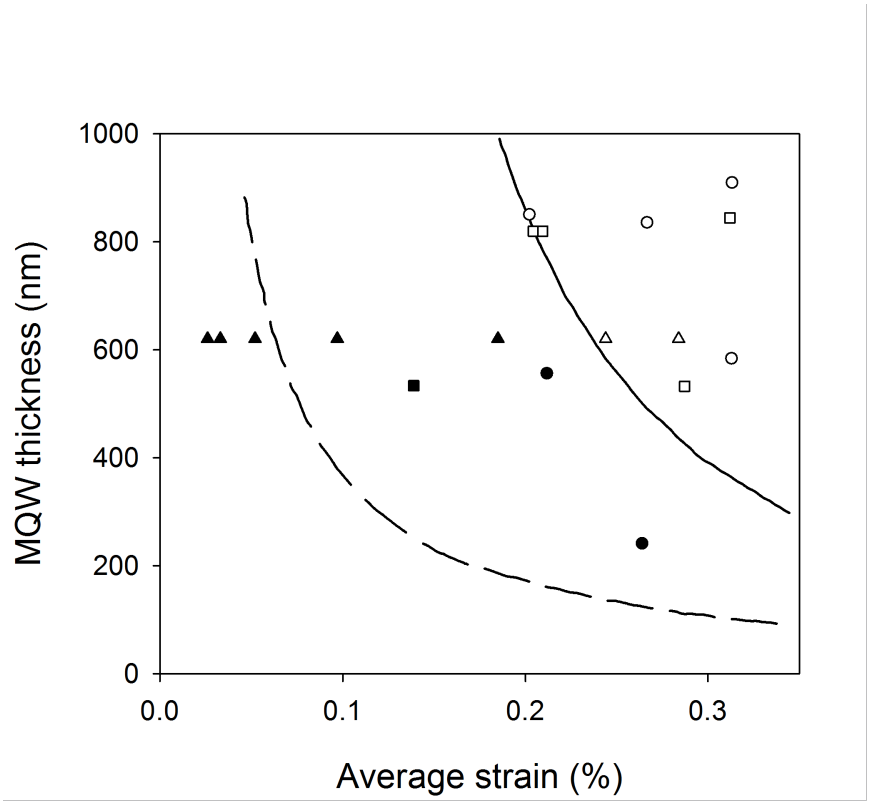

Figure 4.35: The results from [12] along with the Matthews and Blakeslee critical thickness (dashed line) and the dislocation generation thickness (solid line). The circles represent MOVPE grown InGaAs/GaAs MQWs; the squares represent MBE grown InGaAs/GaAs MQWs; the triangles represent the GaAsBi/GaAs MQWs grown in this work. Empty symbols represent samples in which significant strain relaxation appears to have taken place. Adapted from [12].

GaAsBi may exhibit lattice relaxation at similar values of average strain.

To compare the GaAsBi/GaAs material system with the InGaAs/GaAs material system, a calculation of the ground state transition for an InGaAs/GaAs QW was performed. To make a fair comparison with the samples in this work, an InGaAs/GaAs structure with 54 wells, a QW width of 6.4 nm (the calculated average for the samples with up to 40 wells) and a barrier width of 5.0 nm (the period of 3O (54 wells) minus the assumed well width). At an In content of 6 % this sample would have an average strain of 0.243 % (close to the predicted dislocation generation limit for this thickness) and a ground state transition of 1.36 eV. This is significantly higher than the average transition energy of 1.18 eV from the samples in this work. The larger reduction in band gap before the onset of lattice relaxation in GaAsBi compared to InGaAs suggests that GaAsBi may be a strong candidate material for MQW photovoltaics.

4.4 Conclusions

GaAsBi/GaAs MQW p-i-n diodes have been grown by MBE. Throughout the series the number of wells was varied and the barrier thickness was altered to maintain the i-region thickness. The nominal well thickness was 8 nm. Preliminary ω - 2θ XRD scans indicated that good structural quality was achived. For samples with more than 40 wells, a strain relaxation event appears to have occurred as evidenced by the onset of high density cross-hatching on the sample surface observed by Nomarski, a tilting of the MQW region with respect to the substrate measured by XRD, the appearance of visible dislocations imaged by TEM and a redshift and attenuation of the PL spectra. Calculations were performed to estimate the contributions of strain and quantum confinement to the PL peak wavelength. It seems that both strain relaxation and loss of quantum confinement contributed to the redshift of the PL signal. Further work would be required to conclusively demonstrate the individual effects of strain relaxation and loss of quantum confinement on this material system.

The results from the GaAsBi/GaAs MQWs in this work were compared to those gathered from similar InGaAs/GaAs MQWs. For a similar MQW thickness the onset of relaxation appears to occur at around the same average strain in both material systems. However, a series of samples with smaller increments of well number would be required to conclusively determine the critical thickness in the GaAsBi/GaAs material system. The results from this work indicate that GaAsBi/GaAs could potentially offer a competetive alternative to InGaAs/GaAs for PV applications.

Bibliography

[1] K. W. J. Barnham and G. Duggan. A new approach to high-efficiency multi-band-gap solar cells. *Journal of Applied Physics*, 67(7):3490–3493, 1990.

[2] K. W. J. Barnham, B. Braun, J. Nelson, M. Paxman, C. Button, J. S. Roberts, and C. T. Foxon. Short-circuit current and energy efficiency enhancement in a low-dimensional structure photovoltaic device. *Applied Physics Letters*, 59(1):135–137, 1991.

[3] K. Barnham, J. Connolly, P. Griffin, G. Haarpaintner, J. Nelson, E. Tsui, A. Zachariou, J. Osborne, C. Button, G. Hill, M. Hopkinson, M. Pate, J Roberts, and T. Foxon. Voltage enhancement in quantum well solar cells. *Journal of Applied Physics*, 80(2):1201–1206, 1996.

[4] K. Barnham, I. Ballard, J. Barnes, J. Connolly, P. Griffin, B. Kluftinger, J. Nelson, E. Tsui, and A. Zachariou. Quantum well solar cells. *Applied Surface Science*, 113:722–733, 1997.

[5] S. M. Ramey and R. Khoie. Modeling of multiple-quantum-well solar cells including capture, escape, and recombination of photoexcited carriers in quantum wells. *Electron Devices, IEEE Transactions on*, 50(5):1179–1188, 2003.

[6] G. L. Araújo and A. Martí. Absolute limiting efficiencies for photovoltaic energy conversion. *Solar Energy Materials and Solar Cells*, 33(2):213–240, 1994.

[7] W. Shockley and H. J. Queisser. Detailed balance limit of efficiency of p-n junction solar cells. *Journal of Applied Physics*, 32(3):510–519, 1961.

[8] B. Kluftinger, K. Barnham, J. Nelson, T. Foxon, and T. Cheng. Temperature-dependent study of the quasi-Fermi level separation in double quantum well P-I-N structures. *Microelectronic Engineering*, 51:265–274, 2000.

[9] N. J. Ekins-Daukes, J. Nelson, J. Barnes, K. W. J. Barnham, B. G. Kluftinger, E. S. M. Tsui, C. T. Foxon, T. S. Cheng, and J. S. Roberts. Radiative currents in quantum-well solar cells. *Physica E: Low-dimensional Systems and Nanostructures*, 2(1):171–176, 1998.

[10] D. B. Bushnell, T. N. D. Tibbits, K. W. J. Barnham, J. P. Connolly, M. Mazzer, N. J. Ekins-Daukes, J. S. Roberts, G. Hill, and R. Airey. Effect of well number on the performance of quantum-well solar cells. *Journal of Applied Physics*, 97(12):124908, 2005.

[11] A. V. Drigo, A. Aydinli, A. Carnera, F. Genova, C. Rigo, C. Ferrari, P. Franzosi, and G. Salviati. On the mechanisms of strain release in molecular-beam-epitaxy-grown $In_xGa_{1-x}As$/GaAs single heterostructures. *Journal of Applied Physics*, 66(5):1975–1983, 1989.

[12] P. R. Griffin, J. Barnes, K. W. J. Barnham, G. Haarpaintner, M. Mazzer, C. Zanotti-Fregonara, E. Gränbaum, C. Olson, C. Rohr, J. P. R. David, J. S. Roberts, R. Grey, and M. A. Pate. Effect of strain relaxation on forward bias dark currents in GaAs/InGaAs multiquantum well p-i-n diodes. *Journal of Applied Physics*, 80(10):5815–5820, 1996.

[13] J. W. Matthews and A. E. Blakeslee. Defects in epitaxial multilayers: I. Misfit dislocations. *Journal of Crystal Growth*, 27:118–125, 1974.

[14] T. G. Andersson, Z. G. Chen, V. D. Kulakovskii, A. Uddin, and J. T. Vallin. Variation of the critical layer thickness with in content in strained $In_xGa_{1-x}As$-GaAs quantum wells grown by molecular beam epitaxy. *Applied Physics Letters*, 51(10):752–754, 1987.

[15] P. J. Orders and B. F. Usher. Determination of critical layer thickness in $In_xGa_{1-x}As$/GaAs heterostructures by X-ray diffraction. *Applied Physics Letters*, 50(15):980–982, 1987.

[16] D. J. Lockwood, M. W. C. Dharma-Wardana, W. T. Moore, and R. L. S. Devine. Raman scattering study of folded acoustic phonons in GaAs/$In_xGa_{1-x}As$ strained-layer superlattices. *Applied Physics Letters*, 51(5):361–363, 1987.

[17] P. L. Gourley, R. M. Biefeld, and L. R. Dawson. Elimination of dark line defects in lattice-mismatched epilayers through use of strained-layer superlattices. *Applied Physics Letters*, 47(5):482–484, 1985.

[18] I. J. Fritz, S. T. Picraux, L. R. Dawson, T. J. Drummond, W. D. Laidig, and N. G. Anderson. Dependence of critical layer thickness on strain for $In_xGa_{1-x}As$/GaAs strained-layer superlattices. *Applied Physics Letters*, 46(10):967–969, 1985.

[19] R People. Physics and applications of Ge_xSi_{1-x}/Si strained-layer heterostructures. *IEEE Jounal OF Quantum Electronics*, 22(9):1696–1710, SEP 1986.

[20] P. L. Gourley, I. J. Fritz, and L. R. Dawson. Controversy of critical layer thickness for InGaAs/GaAs strained-layer epitaxy. *Applied Physics Letters*, 52(5):377–379, 1988.

[21] J. H. Van Der Merwe and W. A. Jesser. An exactly solvable model for calculating critical misfit and thickness in epitaxial superlattices: Layers of equal elastic constants and thicknesses. *Journal of Applied Physics*, 63(5):1509–1517, 1988.

[22] J. H. Van Der Merwe. Crystal interfaces. Part II. Finite overgrowths. *Journal of Applied Physics*, 34(1):123–127, 1963.

[23] F. R. N. Nabarro and M. S. Duesbery. *Dislocations in solids*, volume 11. Elsevier, 2002.

[24] B. W. Dodson and P. A. Taylor. Atomistic Monte Carlo calculation of critical layer thickness for coherently strained siliconlike structures. *Applied Physics Letters*, 49(11):642–644, 1986.

[25] J. W. Matthews, S. Mader, and T. B. Light. Accommodation of misfit across the interface between crystals of semiconducting elements or compounds. *Journal of Applied Physics*, 41(9):3800–3804, 1970.

[26] J. W. Matthews. Defects associated with the accommodation of misfit between crystals. *Journal of Vacuum Science and Technology*, 12(1):126–133, 1975.

[27] J. P. R. David, R. Grey, M. A. Pate, P. A. Claxton, and J. Woodhead. Barrier width dependence of leakage currents in InGaAs/GaAs multiple quantum well P-I-N diodes. *Journal of Electronic Materials*, 20(4):295–297, 1991.

[28] M. J. Ekenstedt, W. Q. Chen, T. G. Andersson, and J. Thordson. Mediation of strain from $In_{0.36}Ga_{0.64}As$ layers through gaas barriers in multiple quantum well structures. *Applied Physics Letters*, 65(25):3242–3244, 1994.

[29] R. Grey, J. P. R. David, P. A. Claxton, F. G. Sanz, and J. Woodhead. Relaxation of strain within multilayer InGaAs/GaAs pseudomorphic structures. *Journal of Applied Physics*, 66(2):975–977, 1989.

[30] N. J. Ekins-Daukes, J. M. Barnes, K. W. J. Barnham, J. P. Connolly, M. Mazzer, J. C. Clark, R. Grey, G. Hill, M. A. Pate, and J. S. Roberts. Strained and strain-balanced quantum well devices for high-efficiency tandem solar cells. *Solar Energy Materials and Solar Cells*, 68(1):71 – 87, 2001.

[31] N. J. Ekins-Daukes, K. W. J. Barnham, J. P. Connolly, J. S. Roberts, J. C. Clark, G. Hill, and M. Mazzer. Strain-balanced GaAsP/InGaAs quantum well solar cells. *Applied Physics Letters*, 75(26):4195–4197, 1999.

[32] G. Zhang and A. Ovtchinnikov. Strain-compensated InGaAs/GaAsP/GaInAsP/GaInP quantum well lasers ($\lambda \sim 0.98\,\mu$m) grown by gas-source molecular beam epitaxy. *Applied Physics Letters*, 62(14):1644–1646, 1993.

[33] H. Hillmer, R. Lösch, and W. Schlapp. Strain-balanced AlGaInAs/InP heterostructures with up to 50 QWs by MBE. *Journal of Crystal Growth*, 175:1120–1125, 1997.

[34] J. G. J. Adams, W. Elder, G. Hill, J. S. Roberts, K. W. J. Barnham, and N. J. Ekins-Daukes. Higher limiting efficiencies for nanostructured solar cells. volume 7597, pages 759705–759705–9, 2010.

[35] M. A. Green, K. Emery, Y. Hishikawa, and W. Warta. Solar cell efficiency tables (Version 34). *Progress in Photovoltaics: Research and Applications*, 17(5):320–326, 2009.

[36] B. Browne, J. Lacey, T. Tibbits, G. Bacchin, T-C. Wu, J. Q. Liu, X. Chen, V. Rees, J. Tsai, and J-G. Werthen. Triple-junction quantum-well solar cells in commercial production. In *9th International Conference on Concentrator Photovoltaics Systems: CPV-9*, volume 1556, pages 3–5. AIP Publishing, 2013.

[37] Y. Tominaga, Y. Kinoshita, G. Feng, K. Oe, and M. Yoshimoto. Growth of $GaAs_{1-x}Bi_x$/GaAs multi-quantum wells by molecular beam epitaxy. *Physica Status Solidi (c)*, 5(9):2719–2721, 2008.

[38] Y. Tominaga, Y. Kinoshita, K. Oe, and M. Yoshimoto. Structural investigation of $GaAs_{1-x}Bi_x$/GaAs multiquantum wells. *Applied Physics Letters*, 93(13):131915, 2008.

[39] Y. Tominaga, K. Oe, and M. Yoshimoto. Low temperature dependence of oscillation wavelength in $GaAs_{1-x}Bi_x$ laser by photo-pumping. *Applied Physics Express*, 3(6):062201, 2010.

[40] D. Fan, Z. Zeng, X. Hu, V. G. Dorogan, C. Li, M. Benamara, M. E. Hawkridge, Y. I. Mazur, S-Q. Yu, S. R. Johnson, Z. M. Wang, and G. J. Salamo. Molecular beam epitaxy growth of GaAsBi/GaAs/AlGaAs separate confinement heterostructures. *Applied Physics Letters*, 101(18):181103, 2012.

[41] D. Fan, P. C. Grant, S-Q. Yu, V. G. Dorogan, X. Hu, Z. Zeng, C. Li, M. E. Hawkridge, M. Benamara, Y. I. Mazur, G. J. Salamo, S. R. Johnson, and Z. M. Wang. Mbe grown GaAsBi/GaAs double quantum well separate confinement heterostructures. *Journal of Vacuum Science & Technology B*, 31(3):03C105, 2013.

[42] P. Ludewig, N. Knaub, W. Stolz, and K. Volz. Movpe growth of Ga(AsBi)/GaAs multi quantum well structures. *Journal of Crystal Growth*, 370:186–190, 2013.

[43] Y-P. Wang, S-J. Ma, K. Watanabe, M. Sugiyama, and Y. Nakano. Management of highly-strained heterointerface in InGaAs/GaAsP strain-balanced superlattice for pho-

tovoltaic application. *Journal of Crystal Growth*, 352(1):194 – 198, 2012. The Proceedings of the 18th American Conference on Crystal Growth and Epitaxy.

[44] S. R. Kurtz, D. Myers, and J. M. Olson. Projected performance of three-and four-junction devices using GaAs and GaInP. In *Conference Record IEEE Photovoltaic Specialists Conference*, volume 26, pages 875–878. IEEE INC, 1997.

[45] S. Francoeur, M-J. Seong, A. Mascarenhas, S. Tixier, M. Adamcyk, and T. Tiedje. Band gap of $GaAs_{1-x}Bi_x$, $0 < x < 3.6$ %. *Applied Physics Letters*, 82(22):3874–3876, 2003.

[46] S. M. Sze. *Physics of semiconductor devices*. John Wiley and Sons, Inc, 2nd edition, 1981.

[47] F. Bastiman, A. G. Cullis, J. P. R. David, and S. J. Sweeney. Bi incorporation in GaAs (100)-2× 1 and 4× 3 reconstructions investigated by RHEED and STM. *Journal of Crystal Growth*, 341(1):19–23, 2012.

[48] F. Bastiman, A. R. B. Mohmad, J. S. Ng, J. P. R. David, and S. J. Sweeney. Non-stoichiometric GaAsBi/GaAs (100) molecular beam epitaxy growth. *Journal of Crystal Growth*, 338(1):57–61, 2012.

[49] F. Bastiman, Y. Qiu, and T. Walther. GaAsBi atomic surface order and interfacial roughness observed by STM and TEM. In *Journal of Physics: Conference Series*, volume 326, page 012060. IOP Publishing, 2011.

[50] H. Makhloufi, P. Boonpeng, S. Mazzucato, J. Nicolai, A. Arnoult, T. Hungria, G. Lacoste, C. Gatel, A. Ponchet, and H. and Carrère. Molecular beam epitaxy and properties of GaAsBi/GaAs quantum wells grown by molecular beam epitaxy: effect of thermal annealing. *Nanoscale Research Letters*, 9(1):123, 2014.

[51] I. Moussa, H. Fitouri, Z. Chine, A. Rebey, and B. El Jani. Effect of thermal annealing on structural and optical properties of the $GaAs_{0.963}Bi_{0.037}$ alloy. *Semiconductor Science and Technology*, 23(12):125034, 2008.

[52] A. R. Mohmad, F. Bastiman, C. J. Hunter, R. Richards, S. J. Sweeney, J. S. Ng, and J. P. R. David. Effects of rapid thermal annealing on $GaAs_{1-x}Bi_x$ alloys. *Applied Physics Letters*, 101(1):012106, 2012.

[53] B. Čechavičius, R. Adomavičius, A. Koroliov, and A. Krotkus. Thermal annealing effect on photoexcited carrier dynamics in $GaBi_xAs_{1-x}$. *Semiconductor Science and Technology*, 26(8):085033, 2011.

[54] D. J. Dunstan. Strain and strain relaxation in semiconductors. *Journal of Materials Science: Materials in Electronics*, 8(6):337–375, 1997.

[55] H. Achour, S. Louhibi, B. Amrani, A. Tebboune, and N. Sekkal. Structural and electronic properties of GaAsBi. *Superlattices and Microstructures*, 44(2):223–229, 2008.

[56] .Y I Mazur, V. G. Dorogan, M. Benamara, M. E. Ware, M. Schmidbauer, G. G. Tarasov, S. R. Johnson, X. Lu, S. Q. Yu, T. Tiedje, and G. J. Salamo. Effects of spatial confinement and layer disorder in photoluminescence of $GaAs_{1-x}Bi_x$/GaAs heterostructures. *Journal of Physics D: Applied Physics*, 46(6):065306, 2013.

[57] S. R. Jin, K. Hild, I. P. Marko, Z. Batool, and S. J. Sweeney. Properties of GaAsBi/GaAs quantum well structures with different Bi-distribution profiles. In *5th International Workshop on Bismuth-Containing Semiconductors*, July 2014.

[58] P. F. Fewster. X-ray diffraction from low-dimensional structures. *Semiconductor Science and Technology*, 8(11):1915, 1993.

[59] J. Li, Z. Mai, S. Cui, J. Zhou, and W. Feng. X-ray characterization of strain relaxation in InGaAs/GaAs strained-layer superlattices. *Applied Physics Letters*, 63(24):3327–3329, 1993.

[60] H. Asai and K. Oe. Energy band-gap shift with elastic strain in $Ga_xIn_{1-x}P$ epitaxial layers on (001) GaAs substrates. *Journal of Applied Physics*, 54(4):2052–2056, 1983.

[61] J. Singh. Analytical closed form expressions for the effective band edges in shallow quantum wells. *Applied Physics Letters*, 64(20):2694–2696, 1994.

[62] B. Fluegel, R. N. Kini, A. J. Ptak, D. Beaton, K. Alberi, and A. Mascarenhas. Shubnikov-de Haas measurement of electron effective mass in $GaAs_{1-x}Bi_x$. *Applied Physics Letters*, 99(16):162108, 2011.

[63] J. Hwang and Jamie D. Phillips. Band structure of strain-balanced GaAsBi/GaAsN superlattices on GaAs. *Physical Review B*, 83(19):195327, 2011.

[64] Z. Batool, K. Hild, T. J. C. Hosea, X. Lu, T. Tiedje, and S. J. Sweeney. The electronic band structure of GaBiAs/GaAs layers: Influence of strain and band anti-crossing. *Journal of Applied Physics*, 111(11):113108, 2012.

[65] I. Vurgaftman, J. R. Meyer, and L. R. Ram-Mohan. Band parameters for III-V compound semiconductors and their alloys. *Journal of Applied Physics*, 89(11):5815–5875, 2001.

Chapter 5

Conclusions and future work

5.1 Conclusions

The effects of growth temperature, As flux and As species on the Bi content of MBE grown bulk GaAsBi has been investigated. The presence of temperature limited and Bi flux limited regimes has been demonstrated. The maximum Bi incorporation achievable in the temperature limited regime is set by the miscibility of GaAs and GaBi and appears to be independent of Bi flux. The Bi flux limited regime occurs when unity Bi incorporation results in a Bi content lower than the miscibility limit of GaAs and GaBi at the growth temperature. In the Bi flux limited regime, the incorporation coefficient of Bi approaches unity.

The observed difference between the Bi content dependence on As_2 and As_4 flux is explained by the necessary desorption of 50 % of the incident As_4 during GaAs growth as determined by Foxon and Joyce. This result suggests that Bi does not interact differently with the two As species. The PL intensity of GaAsBi is also shown to be independent of As species and is shown to peak at ~ 4 % Bi. The As assisted desorption of Bi from a static surface at a typical GaAsBi growth temperature was investigated. The results indicate that As_2 displaces Bi more aggressively than As_4; however, the characteristic desorption times are two orders of magnitude longer than the monolayer growth times used in this work, suggesting that As assisted surface Bi desorption does not affect Bi content.

GaAsBi/GaAs MQW p-i-n diodes were grown by MBE. XRD and TEM analyses show that structures of good uniformity were grown. Samples with more than 40 QWs exhibit

signs of structural relaxation as evidenced by surface cross-hatching observed by Nomarski, degradation and redshift in PL, dislocation lines visible in TEM images and a tilting of the layer observed by XRD RSMs. By calculating the contributions of strain and quantum confinement to the PL emission energy, it was shown that both effects probably contribute to the PL redshift and attenuation of the samples with large numbers of QWs. The onset of dislocation multiplication in these samples appears to occur at a similar average strain to InGaAs/GaAs MQW samples of similar thickness. The increased band gap reduction of the GaAsBi/GaAs samples compared to that calculated for a similar InGaAs/GaAs structure, suggests that GaAsBi is a strong candidate for multi-junction PV applications.

5.2 Future work

In order to better understand the relationship between Bi content and PL intensity, one could grow a series of samples at one growth temperature, varying the Bi flux. Such a series could verify the existance of the Bi flux limited and miscibility limited growth regimes. By comparing the PL spectra of such a series with the data in figure 3.21, one could ascertain the cause of the PL efficiency reduction above 4 % Bi.

The MQW diodes could be tested as devices. Assessing the electrical and opto-electronic characteristics of the samples would enable one to understand the suitability of GaAsBi for PV applications.

A further series of MQW diodes could be grown with peak PL emission wavelengths around 1.2 μm ($\sim$ 1 eV). This is an important wavelength for high efficiency multi junction PV. Analysis of the opto-electronic characteristics of these samples would be of great importance in demonstrating the applicability of GaAsBi for PV. By planning the growth series carefully, the analysis of the samples could be used, along with the results already gathered from the MQWs in this work, to verify the effects of strain relaxation and quantum confinement on the PL emission from GaAsBi/GaAs QWs.

Appendix A: Sample structures

Three sets of samples were grown and characterised throughout this work. The structures of these samples are described in this appendix.

5.3 Bulk GaAsBi sample structures.

The structures analysed in chapter 3 comprised a 100 nm undoped GaAsBi layer, capped with 20 nm of undoped GaAs, grown on a 100 nm undoped GaAs buffer on an undoped GaAs (001) on axis ± 0.1 ° substrate. This device structure is shown in figure 5.1. Throughout this series of samples, the growth rate was fixed at 1 μm/h and the Bi flux was fixed at 0.31 atoms.nm^{-2}s^{-1}. Some samples were grown using a Bi flux of 0.49 atoms.nm^{-2}s^{-1} for comparison and are indicated in the text and figure captions. The GaAsBi growth temperature, As species and As flux were varied as part of the investigation.

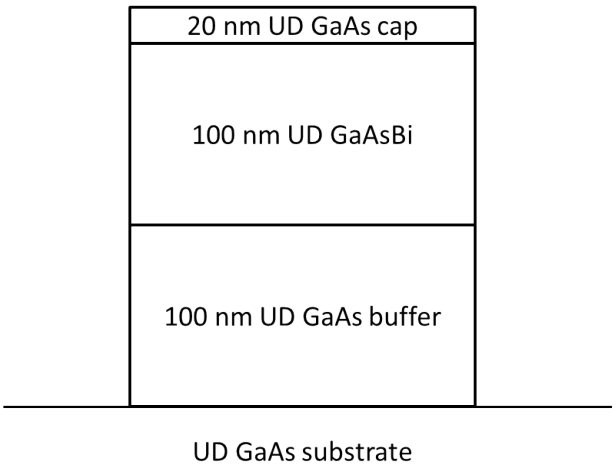

Figure 5.1: Bulk GaAsBi sample structure as used in chapter 3.

5.4 Quantum well growth optimisation structures.

The samples grown in order to optimise the growth parameters for GaAsBi/GaAs quantum wells in section 4.2.1 comprised 3×8 nm GaAsBi quantum wells separated by 20 nm GaAs barriers. The undoped quantum well region was grown on a 500 nm undoped GaAs buffer

on an undoped GaAs (001) on axis ± 0.1 ° substrate and was capped with 100 nm of undoped GaAs. This sample structure is shown in figure 5.2. Throughout this series the growth rate was 0.6 μm/h.

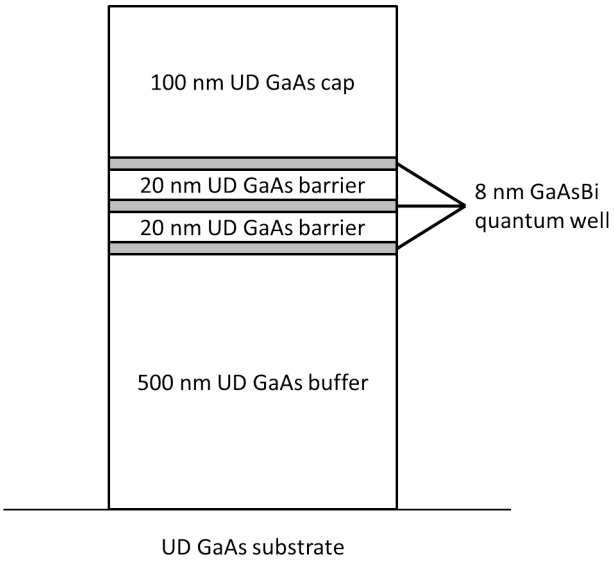

Figure 5.2: 3×8 nm quantum well growth optimisation sample structure as used in section 4.2.1.

5.5 Multiple quantum well diode structures.

The multiple quantum well structures that were the main focus of chapter 4 are shown in figure 5.3. These samples were grown on n+ GaAs:Si (001) on axis ± 0.1 ° substrates. The structure comprised a 200 nm n-type GaAs:Si buffer; a 200 nm n-type $Al_{0.3}Ga_{0.7}As$:Si cladding layer; a 620 nm GaAsBi/GaAs multiple quantum well i-region; a 600 nm p-type $Al_{0.3}Ga_{0.7}As$:Be cladding layer; a 10 nm p+ GaAs cap. The i-region of each sample contained a different number of evenly spaced, nominally 8 nm GaAsBi quantum wells and the thickness of the GaAs barriers was designed to maintain the i-region thickness at 620 nm. The growth rate used throughout this series was 0.55 μm/h for GaAs and 0.79 μm/h for AlGaAs. The As flux used for the i-region was 6 atoms.nm^{-2}s^{-1} and the Bi flux was 0.24 atoms.nm^{-2}s^{-1}.

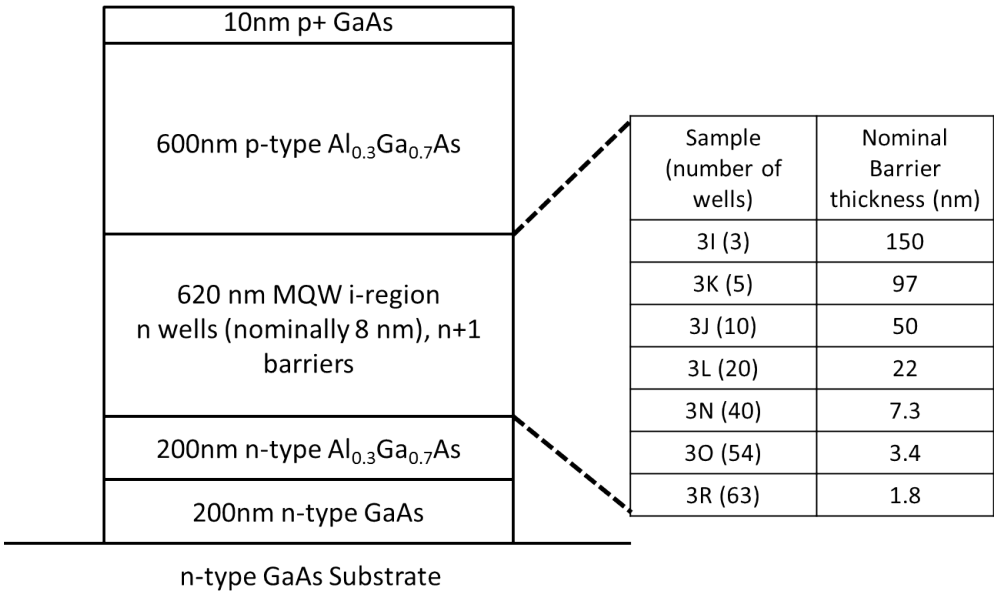

Figure 5.3: Multiple quantum well diode sample structure as used in chapter 4.

Appendix B: Glossary

Table 5.1: List of acronyms used throughout the thesis.

Acronym	Meaning
AM	Air mass
AU	Arbitrary units
BF	Bright field
CL	Cathodoluminescence
DF	Dark field
FEL	Fast entry lock
FF	Fill factor
FWHM	Full width at half maximum
LN_2	Liquid nitrogen
MBE	Molecular beam epitaxy
MBE-STM	Molecular beam epitaxy-scanning tunnelling microscopy
MIG	Movable ion gauge
MOVPE	Metal-organic vapour phase epitaxy
MQW	Multiple quantum well
mVBAC	Modified valence band anticrossing model
PBN	Pyrolytic boron nitride
PL	Photoluminescence
PV	Photovoltaic
QE	Quantum efficiency
QFL	Quasi-Fermi level
QW	Quantum well
RHEED	Reflected high energy electron diffraction
RSM	Reciprocal space map
SK	Stranski-Krastanow growth mode
SL	Superlattice
SO	Spin-orbit
SRH	Shockley-Read-Hall
STM	Scanning tunnelling microscopy
TEM	Transmission electron microscopy
TSP	Titanium sublimation pump
UHV	Ultra high vacuum
VBAC	Valence band anticrossing model
VW	Volmer-Weber growth mode
XRD	X-ray diffraction

Table 5.2: List of chapter 1 abbreviations.

Abbreviation	Meaning
γ_s	Angle of elevation of the sun
ν	Photon frequency
b	Bowing coefficient
e	The charge of a proton
E	Energy
E_F	Fermi level
E_{Fe}	Electron quasi-Fermi level
E_{Fh}	Hole quasi-Fermi level
E_g	Semiconductor band gap
$f(E)$	Fermi function
h	Planck's constant
I_m	Current at maximum power output
I_{sc}	Short circuit current
I	Current
I_0	Diode saturation current
$I_{0_{rec}}$	Recombination current scaling factor
k	Carrier momentum
k_B	Boltzmann's constant
k_{phonon}	Phonon momentum
n	Diode ideality factor
n_{AM}	Air mass index
P_s	Solar power incident on a solar cell
R_s	Series parasitic resistance
R_{sh}	Shunt parasitic resistance
T	Temperature
UD	Undoped
V_{bias}	Bias voltage
V_m	Voltage at maximum power output
V_{oc}	Open circuit voltage
x	Semiconductor alloying fraction

Table 5.3: List of chapter 2 abbreviations.

Abbreviation	Meaning
θ_{Br}	Bragg angle
$\Delta\theta_t$	Thickness fringe spacing
θ_x	Angle between incident X-rays and the normal of the reflecting plane
λ_x	Wavelength
ν_p	Poisson ratio
τ_c	Carrier lifetime
a_{GaAs}	GaAs lattice constant
a_x	Reflecting plane spacing
C_A	Auger recombination coefficient
C_{NR}	Non-radiative recombination coefficient
C_R	Radiative recombination coefficient
d_x	Difference in X-ray path length of beams diffracted from adjacent reflecting planes
F_{Ga}	Ga flux
m_x	Lattice mismatch
m_x^*	Effective lattice mismatch
N_c	Carrier density
t_l	Epitaxial layer thickness
t_{ML}	Monolayer growth time
t_{SL}	Superlattice period

Table 5.4: List of chapter 3 abbreviations.

Abbreviation	Meaning
θ_{Bi}	Bi surface coverage
θ_{Ga}	Ga surface coverage
a_1, a_2 and U_1	Fitting paramters in the Lewis model
E_g	Semiconductor band gap
F_{As}	As flux
F_{Bi}	Bismuth flux
F_{Ga}	Ga flux
t	Time
x	Semiconductor alloying fraction

Table 5.5: List of chapter 4 abbreviations.

Abbreviation	Meaning
ϵ_{xx}	In plane biaxial strain
ϵ_{zz}	Strain in the growth direction
ϕ_s	Sample rotation about its surface normal
a_l	Free standing epitaxial layer lattice constant
a_s	Substrate lattice constant
a_{qw}	Quantum well lattice constant
c_{11} and c_{12}	Elastic constants
ΔE	Conduction or valence band offset in a quantum well
E_1	Ground state transition energy in a quantum well
E_{well}	Conduction or valence band offset in a quantum well
E_{g0}	Transition energy in freestanding material
E_g^{HH+}	Heavy hole transition energy
E_{GaAsBi}	Band gap of GaAsBi
δE_H	Band gap modification due to hydrostatic strain
E_q	Quantum well confinement energy
δE_s	Band gap modification due to shear strain
E_{well}	Band gap of a quantum well
F_f	Bi flux used during the MQW sample series
F_i	Bi flux used for the preliminatry sample
f_s	strain in an epitaxial layer
$\langle f_s \rangle$	average strain in an epitaxial layer
GR_f	Growth rate used for the MQW sample series
GR_i	Growth rate used for the preliminary sample
$\hbar$	Planck's constant
I_{sc}	Short circuit current
m_0	Freestanding electron mass
m_c^*	Carrier reduced mass
N_{qw}	Number of quantum wells
P_H	Hydrostatic deformation potential
P_Hc	Conduction band hydrostatic deformation potential
P_Hv	Valence band hydrostatic deformation potential
t_b	Quantum well barrier thickness
t_{qw}	Quantum well thickness
V_{oc}	Open circuit voltage
x_f	Bi content in the quantum wells in the MQW sample series
x_i	Bi content in the quantum wells in the preliminary sample